Dielectron Production in Pb–Pb Collisions at $\sqrt{s_{NN}} = 5.02\,\text{TeV}$ with ALICE

Dissertation
zur Erlangung des Doktorgrades
der Naturwissenschaften

vorgelegt beim Fachbereich Physik
der Johann Wolfgang Goethe-Universität
in Frankfurt am Main

von

Carsten Klein
aus Seligenstadt

Frankfurt 2019
(D 30)

Vom Fachbereich Physik
der Johann Wolfgang Goethe-Universität als Dissertation angenommen.

Dekan:	Prof. Dr. Michael Lang
Gutachter:	Prof. Dr. Henner Büsching
	Prof. Dr. Harald Appelshäuser

Am Anfang wurde das Universum erschaffen. Das machte viele Leute sehr wütend und wurde allenthalben als Schritt in die falsche Richtung angesehen.
Per Anhalter durch die Galaxis, Douglas Adams

Dielektronenproduktion in Pb–Pb Kollisionen bei $\sqrt{s_{NN}} = 5.02\,\mathrm{TeV}$ mit ALICE

Die vorliegende Arbeit umfasst die Messung der Dielektronenproduktion in hochrelativistischen Blei-Blei-Kollisionen mit dem ALICE Experiment bei einer Schwerpunktsenergie von $\sqrt{s_{\mathrm{NN}}} = 5.02\,\mathrm{TeV}$. Erstmals wurde die Dielektronenproduktion in Schwerionenkollisionen am ALICE Experiment zentralitätsabhängig mit einem minimalen transversalen Elektronenimpuls von $p_{\mathrm{T}} > 0.2\,\mathrm{GeV}/c$ gemessen. Die Produktion wird in Abhängigkeit der invarianten Masse m_{ee} und des transversalen Impulses des Dielektrons $p_{\mathrm{T,ee}}$ dargestellt. Die gemessenen Spektren werden mit dem erwarteten Beitrag aus hadronischen Quellen und mit theoretischen Vorhersagen verglichen. Die Anzahl virtueller direkter Photonen als Funktion des transversalen Impulses wird extrahiert. Zusätzlich wird die kinematische Region mit einem Paartransversalimpuls $p_{\mathrm{T,ee}} < 0.15\,\mathrm{GeV}/c$ untersucht, welche durch photoninduzierte Produktion von Dielektronen dominiert wird.

Die gesamte Materie besteht nach heutigen Kenntnissen aus nur wenigen Grundbausteinen: Quarks und Leptonen. Zusammen mit den Eichbosonen, welche die einzelnen Wechselwirkungen zwischen den Teilchen vermitteln, können sie mit Hilfe des Standardmodells der Teilchenphysik beschrieben werden. Das Standardmodell umfasst drei der vier grundlegenden Kräfte: die elektromagnetische Kraft, sowie die schwache und starke Kernkraft. Die Gravitation spielt auf den mikroskopischen Skalen der Teilchenphysik eine untergeordnete Rolle und kann mit heutigen mathematischen Methoden nicht mit den übrigen Theorien der Fundamentalkräfte in Einklang gebracht werden. Während die Theorie des Elektromagnetismus und der schwachen Wechselwirkung gut verstanden ist und mit heutigen mathematischen Methoden berechenbar ist, ist eine vollständige analytische Lösung der zugrundeliegenden Theorie der starken Wechselwirkung, der Quantenchromodynamik (QCD), derzeit nicht bekannt. Dieser Umstand liegt zum einen an der Selbstwechselwirkung des Gluons als Vermittler der starken Kraft und an der Kopplungskonstanten α_s. Entgegen dem Namen zeigt die Kopplungskonstante der starken Wechselwirkung eine Abhängigkeit vom Impulsübertrag und somit auch vom Abstand der beteiligten Teilchen. Für große Impulsüberträge und somit kleine Abstände wird die Kopplungskonstante klein was zur sogenannten asymptotischen Freiheit von Quarks und Gluonen führt. Bei kleinen Impulsüberträgen und somit großen Abständen wächst α_s, was dazu führt, dass Quarks nicht im ungebundenen Zustand vorkommen können. Dieses Phänomen wird als Confinement bezeichnet.

Materie, welche einer sehr hohen Temperatur und/oder hohen Dichte ausgesetzt wird, kann diese Eigenschaft des Confinements verlieren und somit quasi-freie Quarks und Gluonen beinhalten. Dieser Zustand wird Quark-Gluon-Plasma (QGP) genannt. Ein QGP kann unter Laborbedingungen auf der Erde nur mittels einer ultrarelativistischen Schwerionenkollision erzeugt werden. Speziell um das QGP zu erforschen wurde das A Large Ion Collider Experiment (ALICE) am größten Teilchenbeschleuniger der Welt gebaut. Zwei Bleiionen werden auf nahezu Lichtgeschwindigkeit beschleunigt und im Zentrum des ALICE Experiments zur frontalen Kollision gebracht. Die Detektoren um diesen Kollisionspunkt herum messen die Spuren der in dieser Kollision produzierten Teilchen. Die direkte Messung von korrelierten Paaren aus Elektronen und Positronen, sogenannte Dielektronen, eignet sich hervorragend, um Rückschlüsse auf die dynamischen Vorgänge innerhalb des QGP zu schliessen. Im Gegensatz zu Teilchen, die aus Quarks zusammengesetzt sind, können Dielektronen das produzierte heiße Medium nahezu wechselwirkungsfrei durchqueren und somit die Informationen bezüglich ihres Ursprungs direkt nach außen tragen. Ebenso werden Dielektronen innerhalb aller Phasen einer solchen Schwerionenkollision erzeugt und können deshalb einzigartige Informationen über die zeitliche Entwicklung des Mediums geben.

ALICE eignet sich hervorragend zur Messung von Dielektronen, da es sehr niedrige transversale Impulse $p_{\mathrm{T}} > 0.15\,\mathrm{GeV}/c$ messen und gleichzeitig die entsprechende Teilchensorte identifizieren kann. In der vorliegenden Analyse wird die Elektronen- und Positronenidentifizierung mit Hilfe des inneren Spurfindungsdetektors (ITS), der Spurendriftkammer (TPC) und des Flugzeitdetektors (TOF) vorgenommen. Um möglichst präzise Ergebnisse zu erhalten, werden bestimmte Anforderungen an die einzelnen gemessenen Spuren gestellt. Diese Anforderungen stellen unter anderem sicher, dass die Spurqualität maximiert und gleichzeitig möglichst wenig relevanten Spuren verworfen werden. Um die für die Analyse benötigten Elektronen und Positronen zu selektieren, werden die Teilchenidentifizierungsinformationen der Subdetektoren ITS, TPC und TOF genutzt. ITS und TPC nutzen zur Identifizierung der Teilchenspuren den spezifischen Energieverlust dieser geladener Teilchen auf dem Weg durch das Detektormaterial. Der Energieverlust bei gegebenem Impuls unterscheidet sich in bestimmten Impulsbereichen für Hadronen und Elektronen, was eine Trennung zwischen beiden erlaubt. Zusätzlich wird mit dem TOF-Detektor die gemessene Flugzeit mit dem Impuls und der rekonstruierten Flugstrecke der Teilchen korreliert, um somit auf deren Masse rückzuschließen. Diese Informationen werden dann genutzt, um gleichzeitig die Anzahl der selektierten Elektronen und die Reinheit der Stichprobe zu maximieren.

Bei einer Dielektronenmessung ist a priori nicht bekannt, welches Elektron ein korreliertes Paar mit welchem Positron bildet. Aus diesem Grund wird eine statische Methode angewandt. Es werden Spektren als Funktion der invarianten Masse m_{ee} und des Transversalimpulses $p_{\mathrm{T,ee}}$ gebildet, bestehend aus allen möglichen Paarkombinationen aus Elektronen mit Positronen, das sogenannte Unlike-Sign Spek-

trum ULS. Dieses Spektrum beinhaltet das relevante Signal sowie kombinatorischen Untergrund, bestehend aus zufälligen, unkorrelierten Paarkombinationen. Zusätzlich beinhaltet das Spektrum Untergrund aus korrelierten Paaren aus Quellen, die in dieser Analyse nicht als Signal betrachtet werden, wie beispielsweise Paare aus Konversionen. Um diesen Untergrund abzuschätzen wird das Spektrum aller Kombinationen gleicher Ladung gebildet, das Like-Sign Spektrum, LS. Dieses Spektrum beinhaltet ebenso kombinatorische, sowie genau die korrelierten Paare, die nicht als Signal betrachtet werden sollen. Um Effekte durch die endliche Detektorakzeptanz zu berücksichtigen, wird der R-Faktor auf das LS angewendet. Durch Subtraktion des LS von dem ULS Spektrum ergibt sich nun das relevante Signal. Um die Signifikanz der Messung zu erhöhen, wird der Untergrund möglichst auf ein Minimum reduziert. Ein großer Teil des Untergrunds sind Dielektronen aus Photonkonversionen. Der Einfluss dieser Konversionen wird mittels zweier Methoden minimiert. Da Dielektronen aus Konversionen keine Masse besitzen, ist der Öffnungswinkel zwischen Elektron und Positron null. Dieser verschwindende Öffnungswinkel sorgt dafür, dass solche Elektronen- und Positronenspuren räumlich sehr nah sind und somit an der ersten Detektorlage des ITS gemeinsame Spurpunkte teilen. Durch das Abweisen genau dieser Spuren kann der Einfluss von Konversionen auf das Spektrum signifikant gesenkt werden. Weiterhin werden diese Konversionsdielektronen nur durch das magnetische Feld des Experiments aufgespalten. Diese Winkelkorrelation in Relation zum Magnetfeld kann genutzt werden um verbleibende Konversionspaare auszuschließen. Die unterschiedlichen Anforderungen an einzelne Spuren und Paare, zusammen mit defekten Teilen der Detektoren und weiteren Effekten, führen zu einem Verlust von Signaldielektronen. Um diesen Verlust zu korrigieren, werden aufwendige Simulationen durchgeführt mit dem Ziel diesen Verlust möglichst genau zu ermitteln. Die Ergebnisse dieser Simulationen können anschließend benutzt werden um diese Effekte zu korrigieren. Nach der Effizienzkorrektur können die Ergebnisse mit theoretischen Erwartungen verglichen werden. Zusätzlich werden die systematischen Unsicherheiten mittels einer pseudorandomisierten Änderung der Anforderungen an die einzelnen Spuren abgeschätzt. Diese Änderungen umfassen Variationen an die Anforderungen der Qualität der Spuren und zusätzliche grundlegende Änderungen an der Elektronenidentifizierung. Dies führt zu signifikant unterschiedlichen Signal-zu-Untergrund Verhältnissen, hervorgerufen durch eine unterschiedliche Anzahl an missidentifizierten Hadronen in der Elektronstichprobe und eine Variation der Anzahl von Dielektronen aus Photonkonversionen im Material. Nach der Effizienzkorrektur sollten alle diese unterschiedlichen Anforderungsschemata identische Dielektronenspektren ergeben. Die tatsächlich auftretenden Abweichungen werden dann in eine systematische Unsicherheit umgerechnet.

Die korrigierten Daten werden mit dem hadronischen Cocktail verglichen, welcher die erwarteten Beiträge zum Dielektronenspektrum durch den Zerfall von Hadronen in Dielektronen beschreibt. Dieser Cocktail basiert auf vorherigen Messungen von hadronischen Spektren wie den Transversalimpulsspektren des π^0. Aus diesem gemessenen Spektren wird der erwartete Beitrag des Zerfalls $\pi^0 \rightarrow e^+e^-\gamma$ zum Di-

elektronenspektrum mit Hilfe der Kroll-Wada-Gleichung errechnet. Um die großen statistischen und systematischen Unsicherheiten des π^0-Spektrum besonders bei kleinen transversalen Impulsen zu umgehen, wird in dieser Analyse auf das Spektrum geladener Pionen zurückgegriffen. Das K/π-Verhältnis wird als Annäherung an das η/π-Verhältnis zur Abschätzung des Beitrags des η Mesons genutzt. Die übrigen Beiträge durch η', ρ, ω und ϕ Mesonen zum Dielektronenspektrum werden aus dem sogenannten m_{T}-scaling abgeleitet. Der radiative und resonante Beitrag des J/ψ wird, basierend auf einer ALICE-Messung, durch eine Simulation ermittelt. Der Beitrag zum Dielektronenspektrum durch semileptonische Zerfälle der Fragmentationsprodukte aus $c\bar{c}$ und $b\bar{b}$ in korrelierte Dielektronen dominiert über große Bereiche das invariante Massenspektrum. Um diese Beiträge abzuschätzen wird eine Simulation basierend auf dem Pythia Ereignis-Generator durchgeführt. Diese Spektren werden anschließend auf den gemessenen Wirkungsquerschnitt in Proton-Proton-Kollisionen und die erwartete Anzahl an binären Partonkollisionen pro Ereignis normiert. Pythia beinhaltet keine Effekte welche durch die Kollision von schweren Atomkernen zustande kommen und somit auf die Produktionswahrscheinlichkeit und Kinematik von Hadronen mit Charm- oder Beautyquark wirken. Üblicherweise werden diese Effekte unterteilt in Effekte des kalten und heißen Mediums. Effekte des heißen Mediums beinhalten unter anderem den Energieverlust der initialen $c\bar{c}$ und $b\bar{b}$ Quarks durch elastische und inelastische Stöße sowie durch Abstrahlung von Gluonen. Die initiale Partonverteilung innerhalb der kollidierenden Atomkerne zählt zu den Effekten des kalten Mediums. In dieser Arbeit wurde der letztere Effekt auf die generierten $c\bar{c}$ Quarks angewandt und der Effekt auf den resultierenden Dielektronbeitrag untersucht. In einem zweiten Fall wurde der von ALICE gemessene nukleare Modifikationsfaktor R_{AA} von Elektronen aus c und b Quarks auf die generierten Elektronen und Positronen des Generators angewendet. Dieser nukleare Modifikationsfaktor enthält die Effekte, die durch das kalte und heiße Medium hervorgerufen werden.

Der Vergleich der vollkorrigierten Spektren mit dem hadronischen Cocktail zeigt, dass in dem Masseintervall, in dem der Beitrag von semileptonischen Zerfällen von Hadronen mit Charmquark $1.1 < m_{\mathrm{ee}} < 2.7\,\mathrm{GeV}/c^2$ dominiert, der hadronische Beitrag die Daten überwiegt. Dies deutet darauf hin, dass zur vollständigen Beschreibung der Daten die Modifikationen durch das Medium berücksichtigt werden müssen. Ein Vergleich mit den hadronischen Cocktails inklusive medium-modifizierter Charmkomponente zeigt eine bessere Übereinstimmung mit den Daten. Jedoch muss berücksichtigt werden, dass die systematische wie statistische Unsicherheit der Daten und die systematische Unsicherheit des Verzweigungsverhältnisses $c \to e$ eine genauere Quantifizierung nicht zulässt.

Weiterhin zeigt sich, dass sich die Dielektronenproduktion bei kleinen Massen $m_{\mathrm{ee}} < 0.14\,\mathrm{GeV}/c^2$ sowie in der Region des J/ψ mit den Erwartungen aus dem hadronischen Cocktail innerhalb der Sensitivität der Messung gut erklären lässt. Es zeigt sich ebenso, dass die Messung oberhalb des hadronischen Cocktails in der Massenregion $0.14 < m_{\mathrm{ee}} < 0.54\,\mathrm{GeV}/c^2$ liegt. Dieser Überschuss konnte in vorherigen Messungen

mit einem Beitrag durch ein medium-modifiziertes ρ Hadron erklärt werden. Zwei theoretische Rechnungen, basierend auf einem Feuerballmodell und einer Transportrechnung sind mit diesem gemessenen Überschuss verträglich. Allerdings lassen die derzeitigen statistischen sowie systematischen Unsicherheiten der experimentellen Daten keine quantitative Unterscheidung der beiden Szenarien zu. Zusätzlich werden zentralitätsabhängig die Spektren virtueller direkter Photonen extrahiert. Der Vergleich mit Spektren, die bei einer Schwerpunktsenergie $\sqrt{s_{\mathrm{NN}}} = 2.76\,\mathrm{TeV}$ gemessen wurden, zeigt eine sehr gute Übereinstimmung mit den hier extrahierten Spektren.

Letztlich wurde die kinematische Region mit einem Paartransversalimpuls $p_{\mathrm{T,ee}} < 0.15\,\mathrm{GeV}/c$ näher untersucht. Messung der STAR Kollaboration haben eine im Vergleich zum hadronischen Cocktail gesteigerte Produktion von Dielektronen in diesem Bereich ergeben. Theoretische Modelle, die diese Steigerung beschreiben können, basieren auf einer photoninduzierten Produktion von Dielektronen. Die kollidierenden Bleikerne erzeugen ein extremes elektromagnetisches Feld. Die von diesem Feld generierten Photonen können interagieren und Dielektronenpaare erzeugen. Die in dieser Arbeit gemessenen Spektren dieses zusätzlichen Beitrags zum Dielektronenspektrum sind in ihrer Form konsistent mit den Ergebnissen von STAR, zeigen aber insgesamt einen höheren Produktionsquerschnitt, was im Widerspruch zu einem theoretischen Model steht.

Contents

1. Introduction

According to cosmologic models, the Big Bang marks the beginning of the universe and therefore the creation of matter, energy, space and time about $\approx 13.8 \cdot 10^9$ years ago [1]. Subsequently during the next fractions of a second, the extremely hot universe expanded inflationary by several orders of magnitude and cooled down. After about $\approx 10^{-12}$ seconds, all four fundamental interactions, gravitation, electromagnetism, weak and strong force, have taken their current forms. However, the temperature of the matter in this early universe was too high to allow quarks and antiquarks to form mesons and baryons. This exotic phase of matter is called Quark-Gluon-Plasma (QGP).

The ALICE experiment [2, 3] located at the most powerful particle collider, LHC, at CERN in Geneva, Switzerland, was explicitely built to research this phase of matter. To investigate the QGP, heavy nuclei, like fully ionized lead ions, are accelerated to almost the speed of light and brought to collision in the center of ALICE. Eventually, the achieved high energy densities lead to the creation of a QGP. After cooling down of the plasma, quarks and antiquarks form mesons and baryons which fly towards the detectors of ALICE. The correlations between these measured particles allow for drawing conclusions on the dynamics of the QGP. Several observables were identified during the history of heavy-ion physics like the elliptic flow or the sequential suppression of quarkonia. One prime observable is the correlation of a pair of an electron with a positrons, called dielectron. Because electrons and positrons do not interact strongly, they can traverse the strongly-interacting QGP almost unaffected. Additionally, dielectrons are produced in every stage of the collision allowing to probe the full evolution of the medium from its early hot and dense stages to the later hadronic stages.

This thesis discusses the measurement of the production of dielectrons in lead-lead collisions with a center-of-mass energy of $\sqrt{s_{\mathrm{NN}}} = 5.02\,\mathrm{TeV}$. The data was recorded in the first heavy-ion period of the LHC in its second measurement campaign in 2015. For the first time at an LHC experiment, the dielectron production in heavy-ion collisions is measured with a minimal transverse momentum requirement of $p_{\mathrm{T}} > 0.2\,\mathrm{GeV/c}$, enabling to measure the soft production of dielectrons.

This document is structured in the following way. The first chapter introduces the concepts of the standard model of particle physics, the quark-gluon plasma and the theory of strong interactions: Quantum Chromo Dynamics (QCD). Additionally,

Quark	Electric charge	Mass
up	+2/3 e	$2.2^{+0.5}_{-0.4}$ MeV/c^2
down	−1/3 e	$4.7^{+0.5}_{-0.3}$ MeV/c^2
charm	+2/3 e	1275^{+25}_{-35} MeV/c^2
strange	−1/3 e	95^{+9}_{-3} MeV/c^2
top	+2/3 e	173000^{+400}_{-400} MeV/c^2
bottom	−1/3 e	4180^{+40}_{-30} MeV/c^2
e	−1 e	0.510 99 MeV/c^2
ν_e	0	< 2 eV/c^2
μ	−1 e	105.658 MeV/c^2
ν_μ	0	< 0.19 MeV/c^2
τ	−1 e	(1776.82 ± 0.16) MeV/c^2
ν_τ	0	< 18.2 MeV/c^2

Table 1.1.: Properties of quarks and leptons in the standard model [4].

the mechanism and impact of chiral symmetry breaking as an important concept of QCD is discussed because dielectrons are an excellent and potentially unique probe to understand the effect of chiral symmetry restoration in a QGP. The next chapter discusses the different sources of dielectron production in a heavy-ion collision and their potential modification in comparison to the production in elementary proton-proton collisions. The third chapter introduces the ALICE experiment. The next chapters discuss the event and track selection together with the electron identification process. After this, the extraction of the dielectron yield via combinatorial pairing, the calculation of the detector efficiency correction and the estimation of systematic uncertainties is shown in detail. The next chapter focuses on the calculation of the so-called hadronic cocktail which represents the best known estimate of the dielectron production based on different independent measurements. Afterwards, this hadronic cocktail is compared to the data and the results are discussed in great detail.

1.1. Standard Model

The standard model of particle physics describes the elementary particles which form matter and three out of four fundamental interactions: electromagnetism, weak and strong force. Up to now, theoreticians are not able to include gravitational force into the standard model to achieve a unified theory. However, gravitation plays only a negligible role in particle and heavy-ion physics. Particles within the standard model can be categorized into fermions with half-integer spin and bosons with integer spin.

Boson	Interaction	Couples to
Photon (γ)	electromagnetic	All charged particles
Gluon (g)	strong	Quarks and gluons
$Z^0, W^\pm$	weak	Quarks and leptons

Table 1.2.: Properties of bosons in the standard model [4].

The mediators of the interactions are bosons like the photon as mediator of the electromagnetic interaction or the gluon as mediator of the strong interaction. The fermions of the standard model can be further separated into quarks and leptons. Quarks themselves can be subdivided into three groups called family or generation. The first generation contains up- and down-quarks. These quarks are the lightest and make up almost all mass of the known universe. The up-quark has an electric charge of $q_{\text{up}} = +2/3e$ and a mass of $m_{\text{up}} \approx 2.3\,\text{MeV}/c^2$. The down-quark has an electric charge of $q_{\text{down}} = -1/3e$ and a mass of $m_{\text{down}} \approx 4.8\,\text{MeV}/c^2$. Quarks in the second and third generation have the same electric charge but their masses are significantly higher. The properties of all quarks are summarized in table 1.1. Analogous to the generations in the quark sector, leptons can also be categorized into generations which differ by their mass. More details on the properties of the leptons and bosons can be found in table 1.1 and table 1.2, respectively. The gluon as mediator of the strong force, in contrast to the photon, interacts with itself. This self-interaction is the crucial aspect in understanding QCD. The implications of this behaviour are explained in more detail in the following section.

1.2. Quantum Chromo Dynamics

The quantized field theory Quantum Chromo Dynamics (QCD) was first formulated by Murray Gell-Mann and Steven Weinberg in 1972-73 [5]. Similar to the Quantum Electro Dynamics (QED) for electromagnetically charged objects, QCD describes the strong interaction between color-charged objects, like quarks and gluons. The quantum number color charge can be expressed by three different colors (red, green and blue) which are carried by quarks, and the corresponding anti-colors which are carried by antiquarks. The concept of three color charges was initially introduced to explain the discovery of the Δ^{++} baryon [6].

In contrast to the almost constant electromagnetic coupling $\alpha_{em} = e^2/\hbar c \approx 1/137$, the coupling of the strong interaction α_s depends on the momentum transfer Q^2 of the interaction:

$$\alpha_s(Q^2) \propto \frac{1}{\ln(Q^2/\lambda_{\text{QCD}})} \tag{1.1}$$

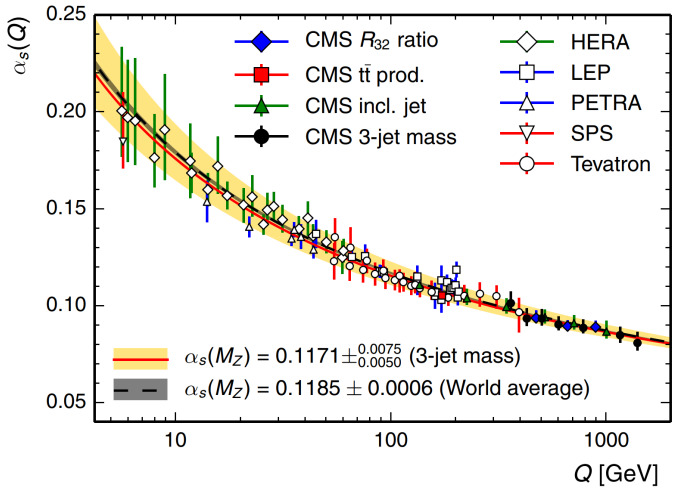

Figure 1.1.: Running coupling α_s as a function of the momentum transfer Q measured at different experiments [7].

with $\lambda_{\text{QCD}} \approx 0.2\,\text{GeV}$ as the typical scale of QCD. Figure 1.1 shows a summary of measurements of α_s as a function of Q. This property is called the *running coupling* of the QCD. This behaviour is reflected in the effective potential between two color-charged objects:

$$V_{\text{eff}}(r) = -\frac{\alpha_s}{r} + k \cdot r \tag{1.2}$$

with the distance r between to color-charged objects which is inversely proportional to the momentum transfer Q, the coupling constant of the strong interaction α_s and a constant k. For small distances $r < 1\,\text{fm}$ the potential is coulomb-like and describes the quasi-free regime of so-called *asymptotic freedom*. At large distances the linear $k \cdot r$ term is dominant and characterizes the experimentally observed *confinement* of color-charged objects in neutral hadrons. By increasing the distance between two colored particles the potential energy between both increases due to the attractive force up to the point that the stored potential energy surpasses the rest mass of a quark-antiquark pair which is created in the process.

Chiral Symmetry

Chiral symmetry in the context of particle physics means that a particle and its mirror particle are identical and are thus called chiral partners. Chiral partners in QCD are axial- and vector-mesons. In the limit of vanishing quark masses $m_q \to 0$ QCD shows a perfect chiral symmetry, meaning that the masses of chiral partners should be degenerate. Because of the small masses of u- and d quarks QCD can be regarded as approximately chiral symmetric [8]. However, measurements of chi-

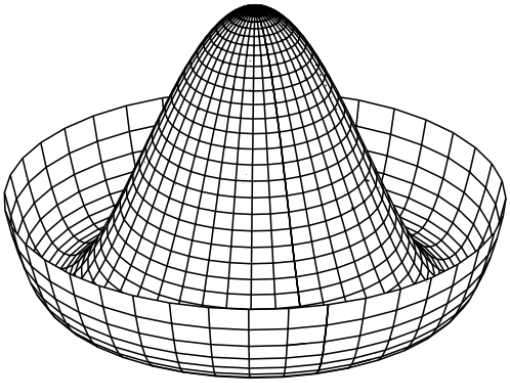

Figure 1.2.: Illustration of spontaneous chiral symmetry breaking [9].

ral partners like π and σ ($m_{\pi^0} = 0.135\,\mathrm{GeV}/c^2$, $m_\sigma = 400 - 550\,\mathrm{GeV}/c^2$) or ρ and a_1 show that their masses are different from each other ($m_\rho = 0.77\,\mathrm{GeV}/c^2$, $m_{a_1} = 1.26\,\mathrm{GeV}/c^2$). This mass difference can not be explained by the *explicit* chiral symmetry breaking originating from the non-vanishing quark masses of u- and d-quarks. The difference is an effect of the *spontaneous* symmetry breaking of the QCD where the Lagrangian is symmetric but the corresponding ground state is not. Figure 1.2 illustrates spontaneous chiral symmetry breaking with a so-called mexican hat potential. The potential is symmetric under rotations around the center but the ground state lies in finite distance from the symmetry point. If a ball would be put at the center of the potential it would eventually roll down to the rotational symmetric ground state. In this scenario the π field corresponds to rotations and the σ field corresponds to radial translations. Rotating the potential along the π field would not lead to an excitation of the field and therefore π mesons are expected to be massless. Excitations in the σ direction would lead to an overall excitation of the field, resulting in massive σ mesons. The measured mass of the π meson is a result of the explicit symmetry breaking due to non-vanishing quark masses.

The so-called quark condensate $\langle\bar{\psi}\psi\rangle$ acts like an order parameter for the process of spontaneous chiral symmetry breaking. Theoretical calculations [10] show that $\langle\bar{\psi}\psi\rangle$ can be melted by increasing the temperature and the density in the medium. If the quark condensate melts $\langle\bar{\psi}\psi\rangle \to 0$ chiral symmetry will be restored and the masses of chiral partners will degenerate.

In figure 1.3 the spectral functions of the vector meson ρ^0 and the axial-vector meson a_1 are shown as a function of invariant mass at increasing temperatures in an effective fireball model [11]. While for small temperatures the peaks of the vector and axial-vector spectral functions are clearly separated, at larger temperatures around the critical temperature of $T_c \approx 155\,\mathrm{MeV}$ the mass difference decreases until both spectral functions are degenerate. Heavy-ion collisions can be used to reach these temperatures and nuclear densities. The measurement of the vector meson ρ^0

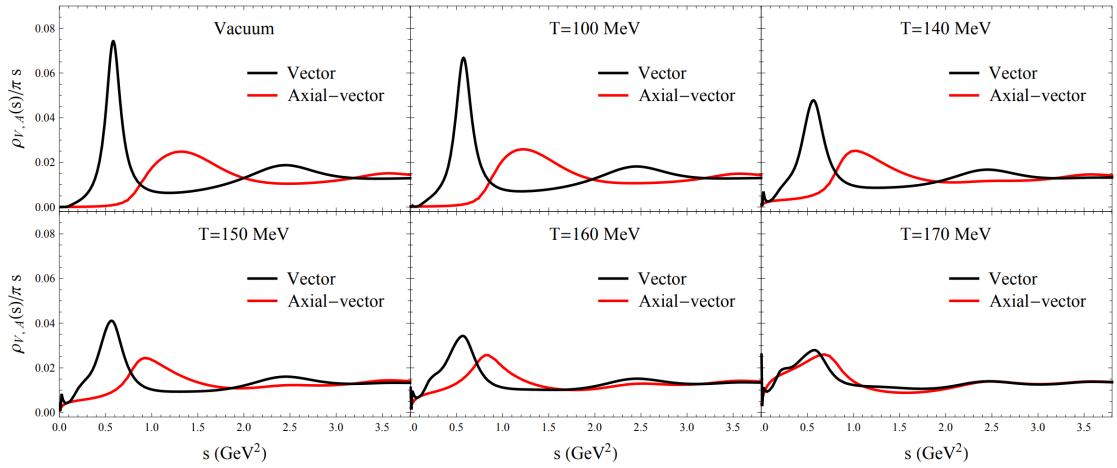

Figure 1.3.: Finite-temperature vector (black curve) and axial-vector (red curve) spectral functions at increasing temperatures T [11].

via the dielectron channel plays an important role to understand the phenomenon. Electrons do not interact with the produced strongly interacting matter and carry the information of the ρ^0 unaffected. Additionally, the ρ^0 meson has a typical decay time which is smaller than the life time of the medium. However, the experimental confirmation of chiral symmetry restoration remains challenging because both chiral partners have to be measured and the measurement of the a_1 stays difficult in the future because of the dominating hadronic decay channels which are all affected by the medium.

1.3. QCD Phase Diagram

Analogous to the phase diagram of water, the different phases of strongly-interacting matter can be depicted in the phase diagram of QCD. Figure 1.4 shows a schematic illustration of this phase diagram as a function of the baryon chemical potential μ_B and the temperature of the medium T. At small temperatures and small baryon chemical potentials quark matter is confined in hadrons. Increasing the temperature of a medium leads to more violent collisions of the quarks inside this medium and therefore the coupling α_s decreases. Eventually, the temperature rises across a certain temperature threshold T_c and the regime of asymptotic freedom of quarks and gluons is reached: a quark-gluon plasma is formed. Increasing the baryon number density and therefore the density of the medium at moderate temperatures leads to smaller distances between hadrons. This pressure also leads to the formation of a quark-gluon plasma. The hadronic phase and the quark-gluon plasma are separated by a first-order transition. At high temperatures and moderate densities this first-order transition ends with a critical point which is followed by a cross over region. At

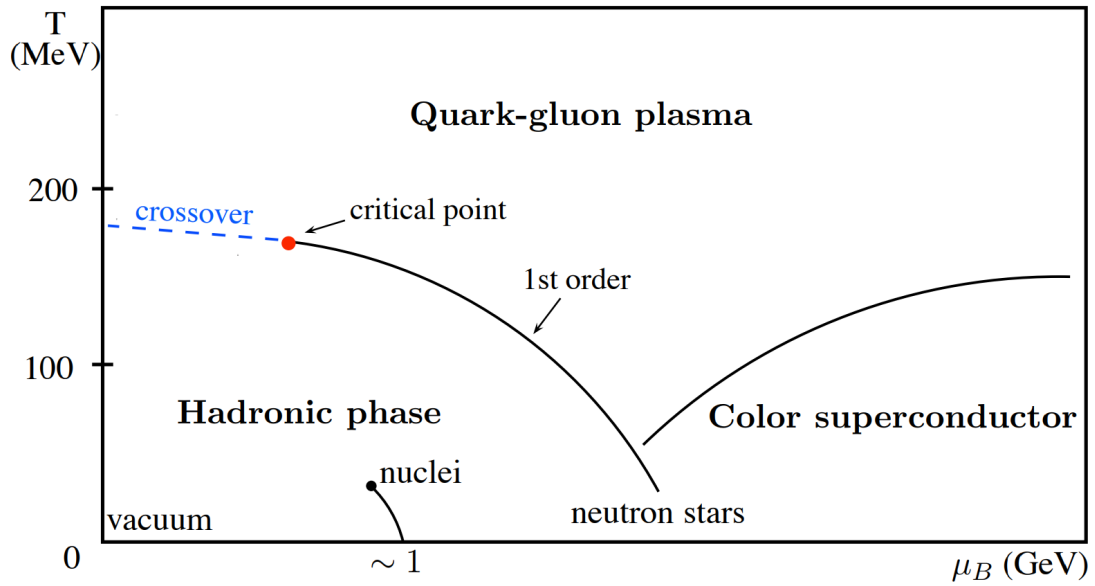

Figure 1.4.: QCD phase diagram as a function of temperature and baryon number density [12].

high μ_B and small temperatures an exotic color superconductor phase is expected [13] which is not relevant for this analysis. Ultrarelativistic heavy-ion collisions can be used to study the different thermodynamic states within this QCD phase diagram.

1.4. Heavy-Ion Collisions

The collision of two ultra-relativistic heavy ions is able to produce a QGP in a controlled environment. The space-time evolution of a typical heavy-ion collision is sketched in figure 1.5. The two colliding nuclei fly towards each other with almost the speed of light. The initial collisions of the nuclei are dominated by hard scatterings of the partons while the nuclei pass through each other. Multiple interactions of the partons with each other lead to the formation of a thermalized QGP with a temperature higher than the critical temperature $T_{\text{init}} > T_c$. This created medium expands rapidly and cools down until the quarks and gluons hadronize into mesons and baryons. The end of this hadronization phase is called chemical freeze-out where the chemical composition and therefore the abundances of all hadrons are fixed. This so-called hadron-gas expands further until elastic collisions cease to happen, leading to fixed particle kinematics, the so-called kinetic freeze-out. After this kinetic-freeze out the created particles fly towards the detectors of the experiments which typically surround the collision point. To study the properties of nuclear matter

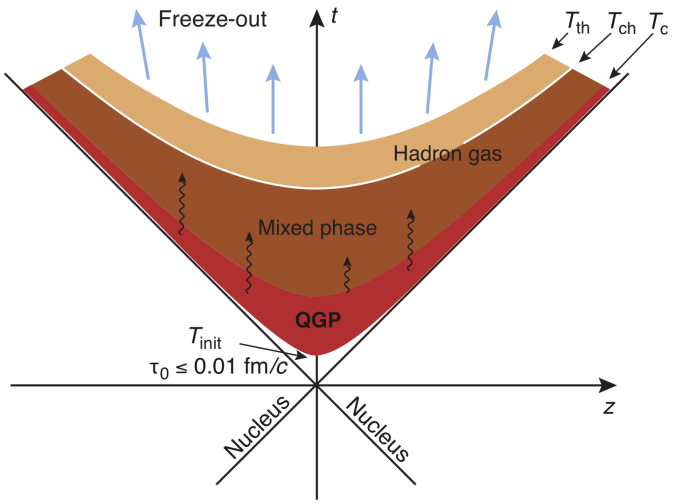

Figure 1.5.: Space-time evolution of a typical heavy-ion collision [14].

and the evolution of the QGP within a heavy ion collision, a range of dedicated experiments have been constructed. Heavy-ion collider experiments, like ALICE at the LHC or PHENIX and STAR at RHIC, give access to the thermodynamic region of the phase diagram at high temperature and low baryon number density. Heavy-ion fixed-target experiments, like HADES at GSI or CERES at SPS, allow to probe the region of the phase diagram in the vicinity of the first order transition.

1.5. Experimental Signatures of the QGP

With todays experimental means, the QGP can not be observed directly. Only the final products of the collision reach the detectors. These measured particles were either produced directly in the collision or they are the result of the decay of a produced particle. However, all measured particles are by some extent influenced by the dynamic of the different stages of a heavy-ion collision. This convolution of effects is extremely complex and makes the understanding of the properties of the QGP a challenging task. Over the years, several experimental signatures were identified to investigate certain aspects of the QGP. Experiments made large efforts to measure these signatures. The experimental results were interpreted by theoreticians and new theoretical models were created to describe the measurements and to gain a complete picture of the dynamic of the QGP. The following sections give an overview over selected experimental signatures of the QGP which affect directly the production mechanisms of dielectrons which is the main topic of this thesis. A detailed description of the dielectron production mechanisms can be found in section 2.

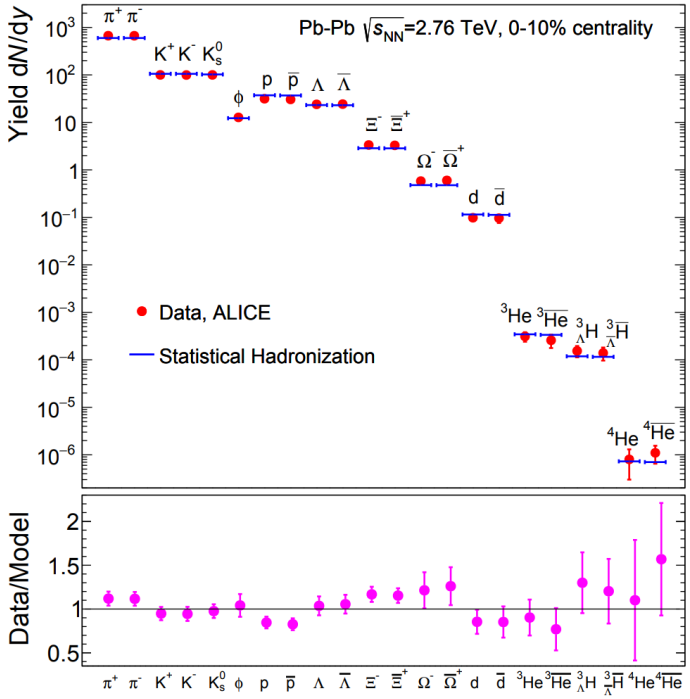

Figure 1.6.: Hadron yield at midrapidity in central Pb-Pb collisions at $\sqrt{s_{\mathrm{NN}}} = 2.76\,\mathrm{TeV}$ measured by the ALICE collaboration in comparison to the prediction of the Statistical Hadronization Model [15]. The lower panel shows the ratio of the data to the predictions. The uncertainty in the ratio originates purely from the uncertainty of the data.

1.5.1. Thermal Hadron Production

A key observable of heavy-ion collisions is the amount of produced hadrons per collision. Since most of the measured dielectrons originate from decays of hadrons, the amount of created hadrons is directly reflected in the dielectron production. To describe the abundance of hadrons within a heavy-ion collision a purely statistical approach without utilizing details of the underlying QCD can be found in the so-called Statistical Hadronization Model (SHM). In its simplest form, this effective model assumes that the medium is fully thermalized and the particle production happens instantaneous at the phase boundary. The model is able to predict the yield of produced particles in a heavy-ion collision with only 3 parameters: the temperature T at the chemical freeze-out, the baryochemical potential μ_B and the volume V of the medium. It is remarkable that this rather simple model is able to predict the production yields over several orders of magnitude. Figure 1.6 shows a comparison of the predicted to the measured hadron yield in the 10% most central Pb-Pb collisions at $\sqrt{s_{\mathrm{NN}}} = 2.76\,\mathrm{TeV}$ [15].

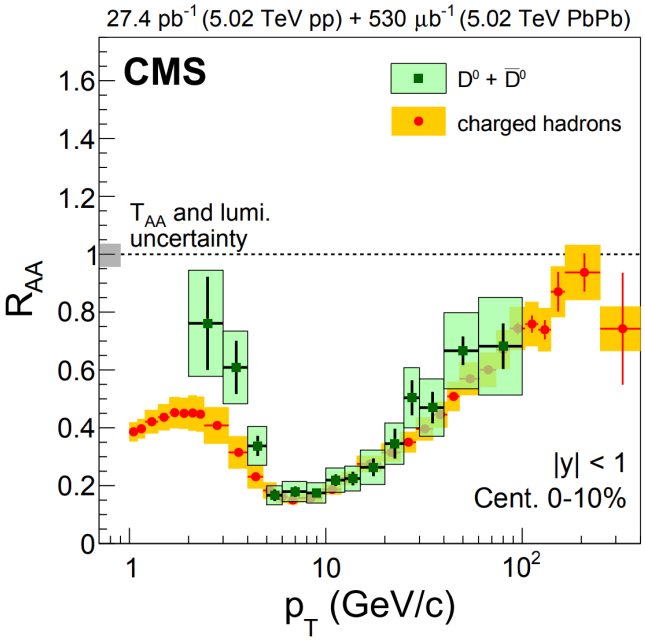

Figure 1.7.: Nuclear modification factor R_{AA} as a function of the transverse momentum of mesons containing charm and of all charged hadrons [16].

1.5.2. Parton Energy Loss

A color-charged parton traversing the hot and dense medium loses energy. This energy loss depends on the density of the QGP, the travelled length inside the medium and the type of parton. A quark typically loses less energy compared to a gluon because it carries only a single color charge instead of the two color charges of the gluon. Two mechanisms are responsible for the energy loss of the parton: the collisional and radiative energy loss. The collisional energy loss dominates at low transverse momenta and originates from elastic collisions of the relevant parton with other partons inside the medium. The higher the transverse momentum of the parton, the more relevant the radiative energy loss becomes. Whenever a parton is accelerated it emits a gluon. This phenomenon is called gluonstrahlung, similar to the bremsstrahlung of electromagnetic particles. The so-called dead cone effect suppresses small gluon radiation angles and therefore reduces the amount of radiated gluons. This effect depends on the respective quark mass divided by its energy.

The energy loss is typically measured with the nuclear modification factor R_{AA} as a function of the transverse momentum p_{T} of the particle:

$$R_{\mathrm{AA}}(p_{\mathrm{T}}) = \frac{\mathrm{d}N_{\mathrm{AA}}/\mathrm{d}p_{\mathrm{T}}}{\langle N_{\mathrm{coll}} \rangle \cdot \mathrm{d}N_{\mathrm{pp}}/\mathrm{d}p_{\mathrm{T}}} \tag{1.3}$$

with N_{AA}, N_{pp} and $\langle N_{\mathrm{coll}} \rangle$ as the yield measured in heavy-ion collisions, proton-

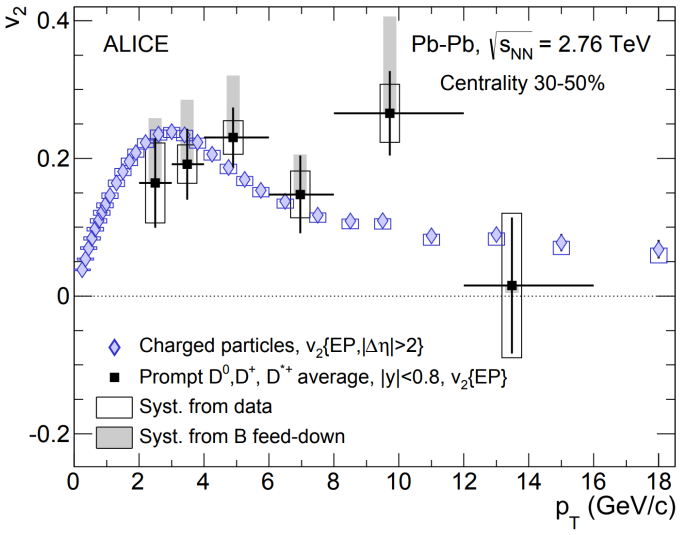

Figure 1.8.: Elliptic flow v_2 as a function of the transverse momentum for charged hadrons (blue) and hadrons carrying charm quarks (black) [18].

proton collisions and the mean number of binary nucleon-nucleon collisions, respectively. For a detailed explanation of $\langle N_{\mathrm{coll}} \rangle$ see section 6.4. If $R_{\mathrm{AA}} = 1$, a heavy-ion collision can be treated as a superposition of independent proton-proton collisions. $R_{\mathrm{AA}} < 1$ can be interpreted as either an energy loss of the particles or a suppression of their production. Due to gluonstrahlung and the dead-cone effect the nuclear modification factor of light quarks like u, d and s is expected to be smaller than for heavier quarks like c and b and therefore the energy loss is larger: $R_{\mathrm{AA}}(u,d,s) < R_{\mathrm{AA}}(c) < R_{\mathrm{AA}}(b)$. However, recent measurements show that this expected behavior can not be confirmed in heavy-ion collisions at the LHC. Figure 1.7 shows R_{AA} as a function of the transverse momentum for mesons containing a charm quark and for all charged hadrons which is dominated by the contribution of light mesons like pions and kaons [16]. At high transverse momenta both distributions are equally suppressed whereas at smaller transverse momenta charmed mesons seem to be less suppressed. The interpretation of this difference is not straightforward because of several effects like a different initial transverse momentum distribution or radial expansion of the medium which affects particles depending on their respective mass [17]. The energy loss of partons inside the medium affects the amount of producued hadrons and their kinematics and therefore it affects also the production of dielectrons as the decay products of these hadrons. The effect of the parton energy loss on the dielectrons originating from heavy-flavour hadron decays is described in more detail in section 11.2.

1.5.3. Collective Flow

Quarks and gluons are subject to collective motion inside the strongly coupled QGP. This collective motion can be expressed in terms of the azimuthal distribution $\mathrm{d}N/\mathrm{d}\phi$ of the measured hadrons in relation to the reaction plane Ψ_{RP} which is defined by the vector of the impact parameter of both incoming nuclei and the beam direction:

$$\frac{\mathrm{d}N}{\mathrm{d}\phi} = \frac{1}{2\pi}(1 + 2\sum^{n} v_n \cos(n(\varphi - \Psi_{\mathrm{RP}}))) \tag{1.4}$$

The harmonics v_n can be interpreted as different kinds of collective motions. v_0 can be identified with a radial expansion of the medium similar to a fireball or explosion and is typically largest when the two colliding nuclei hit each other with biggest possible overlap and therefore smallest impact parameter. The radial expansion velocity leads to an increase of the momentum of all particles, similar to a blue-shift. However, this fireball affects all produced particles mass dependent, i.e. the momentum distribution of lighter pions ($m_{\pi^0} = 0.135\,\mathrm{GeV}/c^2$) is affected differently than the distribution for heavier protons ($m_{\mathrm{p}} = 0.938\,\mathrm{GeV}/c^2$). The second harmonic v_2 is called elliptic flow and is typically created in collisions where the impact parameter is non-vanishing $b > 0\,\mathrm{fm}$ and therefore the collision geometry gets anisotropic. The amount of elliptic flow v_2 hints to the viscosity of the QGP. Results from LHC and RHIC experiments seem to indicate that the viscosity in the QGP is extremely small [19, 20]. Elliptic flow is typically explained with two mechanisms at different transverse momentum of the particles. At low transverse momenta elliptic flow can be described by the pressure gradient of the initial spatial anisotropy of the early stages of collision evolution [21, 22]. At higher transverse momenta the path-length dependent energy loss of particles traversing the medium dominates the v_2 generation [23, 24]. Heavy quarks, like the charm quark, are produced in the initial hard scatterings of the heavy-ion collision and therefore experience the whole dynamic of the collision. D mesons which contain a charm quark ($m_{\mathrm{q}} \approx 1.3\,\mathrm{GeV}/c$) offer the opportunity to test if heavy quarks participate in the collective expansion of the system [18]. Figure 1.8 shows the elliptic flow v_2 as a function of the transverse momentum p_{T} for charged hadrons and D mesons. Within uncertainty both distributions agree indicating that heavy charm quarks participate in the collective motion. However, for theoretical models it is challenging to describe simultaneously the nuclear modification factor and the elliptic flow of charmed mesons [25]. Collective flow affects the kinematics of dielectrons. Especially, the measurement of the collective flow of dielectrons coming from virtual direct photons can help to solve the so-called direct photon puzzle because dielectrons are sensitive to the production time of the direct photon. More details on the photon puzzle can be found in section 1.5.6.

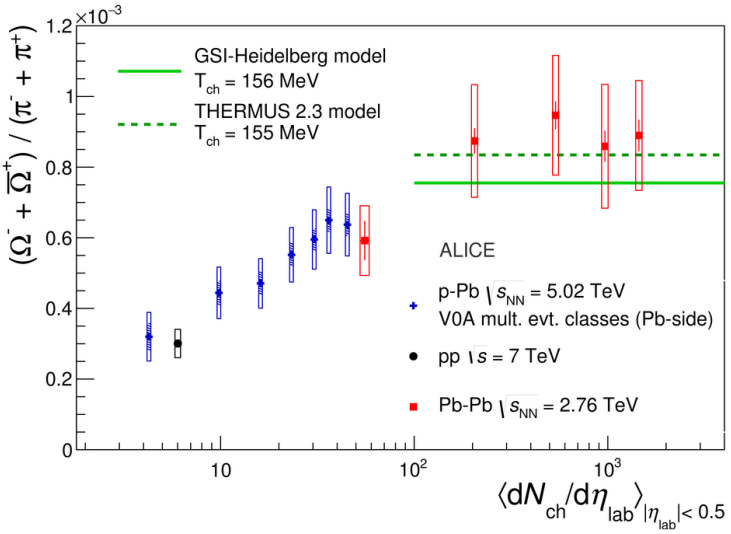

Figure 1.9.: Ratio of measured $\Omega^{\pm}$ mesons over $\pi^{\pm}$ as a function of the multiplicity density in an event for proton-proton, proton-lead and lead-lead collisions at $\sqrt{s} = 7\,\text{TeV}$, $\sqrt{s_{\text{NN}}} = 5.02\,\text{TeV}$ and $\sqrt{s_{\text{NN}}} = 2.76\,\text{TeV}$, respectively. The lines indicate predictions of two thermal models [26].

1.5.4. Strangeness Enhancement

The enhanced production of strange hadrons was proposed as one of the first signatures of the QGP [27, 28]. The colliding protons or ions do not carry net strangeness. This means, that the production of strange and anti-strange quarks happens during the collision process. In the vacuum, i.e. proton-proton collisions, the energy threshold for creating strange hadrons depends on the constituent mass of the strange quark inside the hadron which is substantially larger than the bare mass of the quark. In the QGP where quarks and gluons roam freely, only the energy equivalent of the bare quark masses of the strange/ anti-strange quark is required to form such a quark/anti-quark pair. The strangeness enhancement is expected to be smaller for higher collision energies and it is expected to increase with the number of constituent strange quarks inside the hadron. The points in figure 1.9 illustrate the ratio of measured $\Omega^{\pm}$ mesons over $\pi^{\pm}$ as a function of the multiplicity density in an event for proton-proton, proton-lead and lead-lead collisions at $\sqrt{s} = 7\,\text{TeV}$, $\sqrt{s_{\text{NN}}} = 5.02\,\text{TeV}$ and $\sqrt{s_{\text{NN}}} = 2.76\,\text{TeV}$, respectively. The lines indicate predictions of two thermal models, similar to the model described in more detail in section 1.5.1. The production of Ω, a state containing three strange quarks, in heavy-ion collisions is enhanced over the production in elementary proton-proton collisions. The enhancement depends on the produced multiplicity in the event which itself is a measure for the size of the QGP [29]. However in recent years the interpretation of the results is getting more challenging as new measurements in smaller collision systems, like proton-lead, seem to also show an enhanced strangeness production

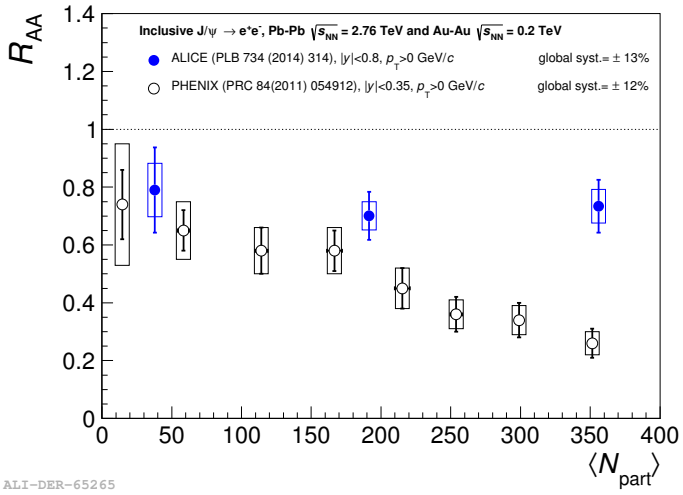

Figure 1.10.: Nuclear modification factor R_{AA} of J/ψ as a function of the number of nucleons participating in the collision. Black points are measured by PHENIX at a center-of-mass-energy $\sqrt{s_{\mathrm{NN}}} = 0.2\,\mathrm{TeV}$. Blue points are measured by ALICE at $\sqrt{s_{\mathrm{NN}}} = 2.76\,\mathrm{TeV}$ and show a decrease of the suppression at more central collisions [30].

where a priori no formation of a QGP is expected [26]. The strangeness enhancement affects the dielectron production since some of the mesons which decay into dielectrons contain strange quarks, like the ϕ meson.

1.5.5. Charmonium and Bottomium Suppression

In 1986, another signature for the QGP was proposed regarding the suppression of $c\bar{c}$ and $b\bar{b}$ states in the deconfined matter [31]. Because of the high gluon density inside the QGP the color field between a $q\bar{q}$ pair is modified leading to the destruction of these states. This process is analogous to the Debye screening of the electromagnetic field in a plasma [32]. The effective QCD potential between both quarks $V_{q\bar{q}}$ can be described as:

$$V_{q\bar{q}}(r,T) \propto -\frac{\alpha_s}{r}\exp(-r/r_D(T)) \tag{1.5}$$

with the Debye radius $r_D = \sqrt{kT/4\pi n_0 e^2}$. Therefore, the suppression factor of $q\bar{q}$ production depends on the temperature of the medium [33]. Figure 1.10 shows the nuclear modification factor R_{AA} of J/ψ mesons as a function of the number of nucleons N_{part} which participate in the collision for measurements with center-of-mass-energies $\sqrt{s_{\mathrm{NN}}} = 2.76\,\mathrm{TeV}$ (blue) and $\sqrt{s_{\mathrm{NN}}} = 0.2\,\mathrm{TeV}$ (black). The measurement at a smaller collision energy clearly shows a trend to a larger suppression of the J/ψ production at more central, and therefore hotter, collisions. However, the measured R_{AA} at $\sqrt{s_{\mathrm{NN}}} = 2.76\,\mathrm{TeV}$ indicates that the suppression does not increase anymore

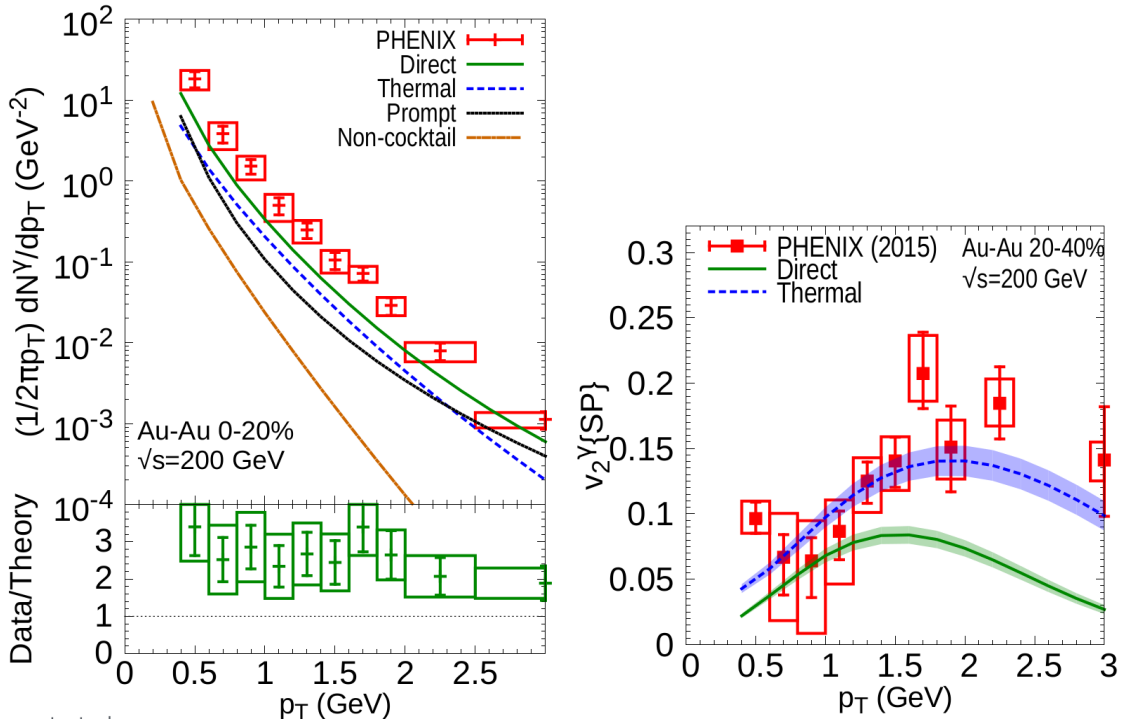

Figure 1.11.: Transverse momentum p_T and elliptic flow v_2 distribution of direct photons in Au-Au collisions with a center-of-mass-energy of $\sqrt{s_{NN}} = 0.2\,\text{TeV}$ measured by PHENIX in comparison to a theoretical model including a hydrodynamic approach to describe the QGP phase [35].

for more central events. One possible explanation for this behaviour is called color recombination [34]. At sufficiently high collision energies, the density of produced $c\bar{c}$ pairs is high enough that charm and anticharm quarks from different original pairs may combine to form a J/ψ meson. At LHC energies this effect can reduce the J/ψ suppression in very central collisions as shown in figure 1.10.

1.5.6. Direct Photon Puzzle

Direct photons are photons, which do not originate from decays of hadrons. The main sources of direct photons are hard scatterings in the initial stages of the heavy-ion collision, so called prompt photons, and thermally produced photons. A more detailed discussion of the separate production mechanisms can be found in section 2.6. Up to now, theoretical models are not able to describe the transverse momentum p_T distribution and the elliptic flow v_2 of direct photons. Figure 1.11 shows the p_T and v_2 distributions measured by the PHENIX collaboration in comparison to a theoretical model based on an hydrodynamic approach [35]. The model contains individual contributions from thermal, prompt and an additional third group of

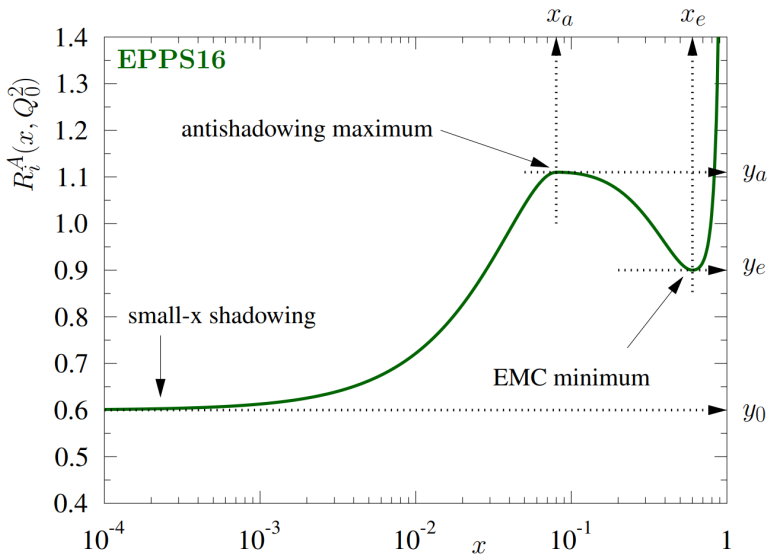

Figure 1.12.: Typical modification of the parton distribution function inside a nucleus as a function of the Bjorken-x [37].

photons from hadronic decays which were not subtracted beforehand and make up only a small fraction of the overall yield. The model underestimates the measured photon yield and predicts a smaller elliptic flow. Increasing the initial temperature and therefore the thermal direct photon yield could help to reduce the discrepancy with the measured yield. Most of these additional thermal direct photons would emerge at early times of the collision were the medium ist the hottest. However, at early stages the initial spatial anisotropy is not fully evolved into a anisotropy in the momentum space, leading to a small elliptic flow v_2 of these direct photons from the hottest stage. The discrepancy between the theoretical models and two independent measurements by ALICE and STAR is found to be not as large as the difference between the models and the discussed PHENIX measurement [36].

1.5.7. Cold Nuclear Matter Effects

Heavy-ion collisions are investigated to understand the properties of the QGP and to search for the phase transition from normal matter to the deconfined QGP. The signature described in the previous section rely on the presence of a QGP. However, some experimental observations can also be described by other mechanisms that do not involve the QGP but the presence of a nucleus [38]. These so-called cold nuclear matter effects can be studied in small collision systems, like p-Pb collisions, where no formation of the QGP is expected.

A crucial role plays the modification of the parton distribution function (PDF) inside

a nucleus. A PDF describes the probability density to find a gluon or quark with a certain fraction of the total momentum x (Bjorken-x) at a given energy scale Q^2 inside a hadron, like the proton. The probed Bjorken-x depends on the collision energy, the rapidity, the momentum and the mass of the produced particle. The PDF is an essential part of the calculation of cross sections within particle interactions. It can be measured via deep-inelastic scatterings of leptons off the hadron where the lepton acts as probe. The parton distribution of free protons is different to the distribution of partons of a proton inside a nucleus. This modification of the function is called nuclear parton distribution function (nPDF) and is typically illustrated as the modification of the underlying PDF as a function of the fraction of the total momentum x as shown in figure 1.12. This means that the production of quarks might be enhanced (antishadowing) or suppressed (shadowing, EMC minimum) in comparison to the production in elementary proton-proton collisions.

Several cold nuclear matter effects are able to modify the production of quarks within a collision, like initial-state multi parton scatterings or a modification of the particle density function inside a nucleus. Initial-state multi parton interactions, the so-called Cronin effect [39], occur when the partons of the projectile proton scatter softly off the partons of the nucleus before the actual hard scattering, resulting in a modification of their energy. This leads to a suppression of the particle production at low transverse momenta and to an enhancement at high transverse momenta in comparison to the particle production measured in proton-proton collisions.

2. Electromagnetic Probes

2.1. Dileptons as an electromagnetic probe

Dileptons consist of a pair of a lepton with its corresponding anti-lepton. This analysis focuses on the production of dielectrons, and therefore correlated pairs of electrons and positrons. Dielectrons are a fantastic probe to study the properties of the strongly interacting QGP created in heavy-ion collisions. They are produced in every phase of the collision and therefore allow for the study of the complete heavy-ion collision evolution. Additionally, the mean-free path of electrons[1] inside the medium is large because they do not carry any colour charge and interact only electromagnetically. This means that dielectrons are mostly unaffected by the medium and they are therefore able to carry information about their creation process without any modification by the medium. Contrary to the behaviour of electrons is the behaviour of strongly-interacting probes like quarks as carriers of colour charges. These color charges interact with the medium via the strong force and therefore lose the information about their origin. This property can be traced back to the strength of the respective coupling constant which is smaller for electromagnetic processes in comparison to strong interactions $\alpha_{em} < \alpha_s$. However, the small coupling strength α_{em} is also a disadvantage because it leads to a small production rate of dielectrons. This small rate and the typically large background render the dielectron analysis challenging.

The analysis of dielectrons in heavy-ion collisions offer a rich field of different observables. All of the phenomena which are described in sections 1.5.7 and 1.5, like the flow of the medium, partonic energy loss or cold-nuclear matter effects, directly affect the amount of produced dielectrons and can be measured via the dielectron channel. The most important sources of dielectrons and their possible modification by the medium are summarized here and then discussed in more details in the following sections. With a dielectron measurement it is possible to measure the invariant mass and pair transverse momentum distributions of several pseudo-scalar (π^0, η, η') and vector mesons (ω, ρ, ϕ, J/ψ, Υ). Especially the modification of the ρ meson production in comparison to the production in elementary proton-proton collisions is related to the concept of chiral symmetry restoration as it was introduced in more detail in section 1.2. The production of correlated dielectrons from semileptonic

[1] If not explicitely stated, the label 'electron' corresponds to electrons and positrons.

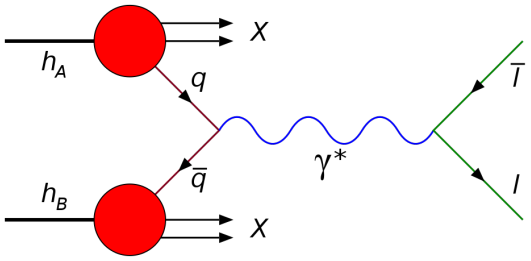

Figure 2.1.: Feynman diagram of the Drell-Yan process [40].

heavy-flavour hadron decays can give insight in the modification of heavy-flavour quarks via cold- and hot-nuclear matter effects. An additional important observable is the direct measurement of the temperature of the QGP and the production of direct photons from hard scatterings of partons in the initial phases of the collision.

2.2. Drell-Yan

The Drell-Yan process [41] describes the production of a dilepton at hard scatterings typically in the initial stages of hadron-hadron collisions, first seen at the AGS accelerator in 1970 [42]. The process is depicted in figure 2.1: A quark and an antiquark of the two colliding hadrons annihilate producing a virtual photon which further decays into a dilepton pair. This Drell-Yan process is purely electromagnetic and can be fully described by QED. At collision energies of the LHC accelerator which is used in this analysis, the Drell-Yan contribution to the dielectron spectrum dominates at large invariant masses $m_{\mathrm{ee}} \gg 15\,\mathrm{GeV}/c^2$ [43] and was found to be negligible at smaller invariant masses[2] [44]. Because this analysis focuses on the invariant mass range smaller than $m_{\mathrm{ee}} < 4\,\mathrm{GeV}/c^2$, the Drell-Yan production process is not further taken into account.

2.3. Light-flavour mesons

Sources of dielectrons in heavy-ion collisions are the Dalitz and resonance decay of so-called light-flavour mesons π^0, η, η', ω and ϕ into dielectrons. A direct measurement of these light-flavour mesons is not possible because of their short life time and therefore short decay length. The measurements are always performed via reconstructing their decay products, e.g. $\phi \to e^+e^-$. Therefore, the dielectron channel allows for an independent measurement of the production of these mesons

[2]More information on kinematic observables can be found in section A

and, additional, have the advantage that their decay products are not affected by the strongly interacting matter which is produced in heavy-ion collisions in contrast to hadronic decay channels, like $\phi \rightarrow K^+K^-$.

These light-flavour meson decays dominate the invariant mass spectrum below $m_{\mathrm{ee}} < 1.1\,\mathrm{GeV}/c^2$. The shape of the Dalitz decays as a function of the invariant mass m_{ee} and the pair transverse momentum $p_{\mathrm{T,ee}}$ can be described with the Kroll-Wada equation [45]:

$$\frac{\mathrm{d}^2N_{\mathrm{ee}}}{\mathrm{d}m_{\mathrm{ee}}\mathrm{d}p_{\mathrm{T,ee}}} = \frac{2\alpha_{\mathrm{EM}}}{3\pi} \cdot \sqrt{1-\frac{4m_{\mathrm{e}}^2}{m_{\mathrm{ee}}^2}} \cdot \left(1+\frac{2m_{\mathrm{e}}^2}{m_{\mathrm{ee}}^2}\right) \cdot \frac{1}{m_{\mathrm{ee}}} \cdot S(m_{\mathrm{ee}}, p_{\mathrm{T,ee}}) \cdot \frac{\mathrm{d}N_{\mathrm{hadr}}}{\mathrm{d}p_{\mathrm{T}}} \quad (2.1)$$

with α_{EM}, $\mathrm{d}N_{\mathrm{hadr}}/\mathrm{d}p_{\mathrm{T}}$ and m_{e} being the electromagnetic fine-structure constant, the real photon yield as function of transverse momentum and the electron rest mass, respectively. The factor $S(m_{\mathrm{ee}}, p_{\mathrm{T,ee}})$ includes the electromagnetic form factor and ensures that the spectral function ends at the rest mass of the decaying hadron. A recent measurement of the electromagnetic form factors was performed by the NA60 collaboration [46].

In the vacuum, e.g. in proton-proton collisions where no QGP or hadron gas is produced, the resonance decays of the vector mesons ω, ρ and ϕ show a peak-like structure as function of the invariant mass. In heavy-ion collisions, when the temperature of the QGP decreases below the critical temperature T_c the phase transition to the hadronic phase takes place. In the vicinity of this phase transition boundary, these vector mesons are expected to have broadened spectral functions compared to their vacuum expectations due to hadronic interactions inside the hadron gas [47]. These modifications can be related to a partially restored chiral symmetry. This chiral symmetry restoration process leads to the degeneration of the masses of chiral partners like the axial vector meson a_1 and the vector meson ρ. The ρ meson is especially interesting due to its short life-time of $\tau_\rho \approx 1.3\,\mathrm{fm}/c$. This short life-time ensures that the produced ρ mesons decay in the hot and dense hadron gas. This hot medium leads to a decrease of the order parameter of chiral symmetry $\langle\bar{\psi}\psi\rangle$ in comparison to the vacuum value and therefore to a partly restoration of chiral symmetry. More details on chiral symmetry can be found in section 1.2.

2.4. Heavy-flavour mesons

Charm and beauty quarks are typically categorized as so-called heavy-flavour quarks. The contribution of semileptonic decays of open heavy-flavour hadrons to the dielectron spectrum is dominant at LHC energies in the so-called intermediate mass range between the vector meson ϕ and the J/ψ in the mass interval $1.1 < m_{\mathrm{ee}} < 2.9\,\mathrm{GeV}/c^2$ and at higher masses up to the bottomium resonances, like the upsilon Υ.

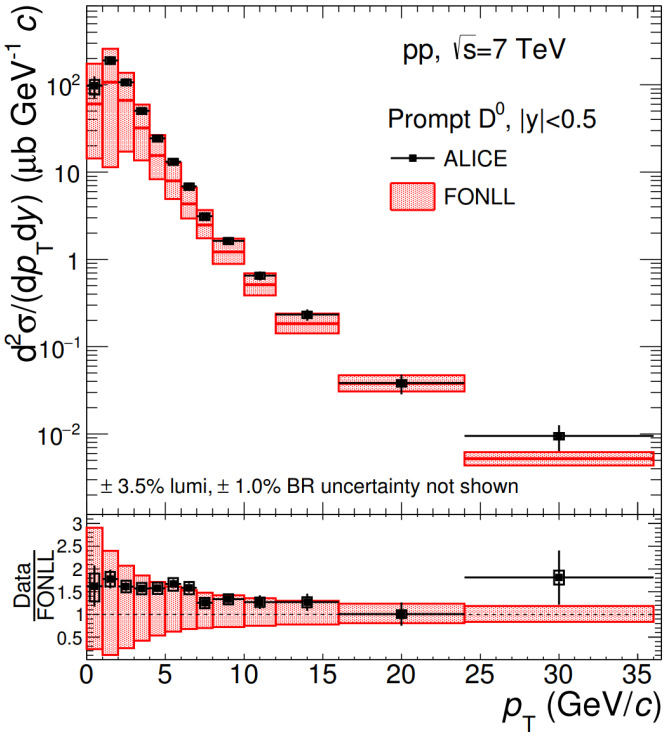

Figure 2.2.: Cross section of D^0 production as a function of the transverse momentum p_{T} in proton-proton collisions at $\sqrt{s} = 7\,\mathrm{TeV}$ measured by ALICE and compared to FONLL calculations [48].

Typically heavy quarks are produced in hard processes during the initial stages of the collision. Because of their early production time they serve as an interesting probe of the QGP because they are affected by the whole evolution of the hot and dense medium. The modification of the parton distribution function, which happens inside the nucleus, plays a crucial role in the production of heavy quarks and its suppression in comparison to the production cross section in elementary proton-proton collision. Typically at LHC energies the production of charm and anticharm quarks is suppressed by a factor of ≈ 0.6 as shown in section 11.2 where the effect of the so-called EPPS16 nuclear parton distribution function is applied to a simulation. Section 1.5.7 gives a more detailed description of these so-called cold-nuclear matter effects. Another important aspect in heavy-ion collisions is the radiative and collisional energy loss of heavy quarks traversing the QGP. This process, as well, leads to an overall modification of the produced yield. More detailed information about the production process and its modifications inside the QGP can be found in section 1.5.

The hadronization process at the end of the QGP phase eventually leads to open heavy-flavour hadrons meaning a composition of a heavy-flavour quark with lighter quarks like u, d and s. While open heavy-flavour mesons with a charm quark

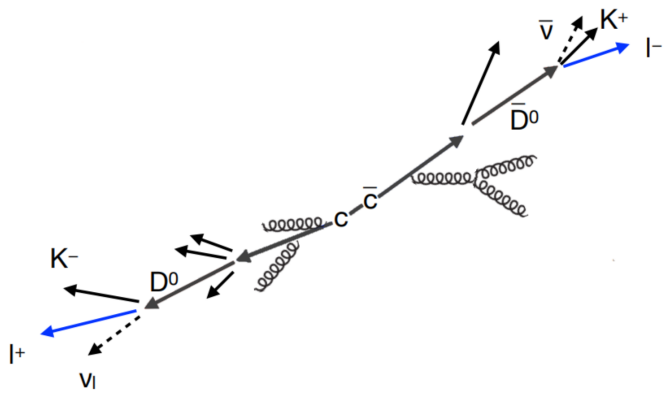

Figure 2.3.: Schematic view of a correlated dielectron originating from semileptonic heavy-flavour decays [49].

are called D mesons, mesons containing b quarks are referred to as B mesons. Open heavy-flavour baryons are called e.g. Λ_c^+ and Λ_b^0. The production mechanism of heavy-flavour quarks is not fully understood. Because of their large mass ($m_c \approx 1.3\,\mathrm{GeV}/c^2$ and $m_b \approx 4.2\,\mathrm{GeV}/c^2$), the leading-order process can be calculated with perturbative QCD but recent measurements indicate that next-to-leading order (NLO) or fixed-order-next-to-leading-order-log (FONLL) calculations improve the description of the charm production cross sections [50]. But these calculations suffer from weak constraints of the quark masses, the uncertainty of the parton distribution and fragmentation functions and therefore have large systematic uncertainties. Figure 2.2 shows the cross section of D^0 meson production as a function of the transverse momentum measured by the ALICE collaboration [48]. The comparison of the measurement to FONLL calculations shows that the measurement is at the upper limit of the uncertainty of the calculation.

The initial correlation of the quark-antiquark pair can be studied via the measurement of correlated dielectrons as the product of the semileptonic decay chains, e.g. $c \to D^0 \to K^- \nu_e e^+$ and $\bar{c} \to \bar{D}^0 \to K^+ \bar{\nu}_e e^-$. Figure 2.3 depicts a potential decay chain for the creation of a dielectron via a semileptonic heavy-flavour hadron decay. The dielectron channel allows a measurement of the charm cross section over the full transverse momentum range of the charm quark while at the same time being sensitive to angular correlations of the initial charm-anticharm pair.

2.5. Charmonium

A bound state of a charm-anticharm pair is called charmonium. Several charmonium resonances can decay directly into dielectrons like the J/ψ and its excited states $\psi(2S)$, $\psi(3S)$. In the presence of a QGP, the production of charmonia is

expected to be affected by colour-screening inside the medium [31]. This screening process is similar to Debye-screening in electromagnetic interactions where electric charges are screened by surrounding charges. The colour-screening radius r_D decreases when the density of color-charges increases which happens at higher collision energies and therefore larger temperatures of the produced medium. As soon as r_D becomes smaller than the binding radius of the charm-anticharm pair, the bound state can not be formed and dissociates into open-charm hadrons. This effect leads to an increasing suppression of the charmonium production at higher center-of-mass energies of the heavy-ion collision and therefore at higher temperatures of the QGP.

If the energy of the heavy-ion collision increases, the number of produced charm-anticharm pairs increases as well. Therefore, by chance, two charm-anticharm quarks from a different initial collision might bound. If the density of $c\bar{c}$ is high enough, this statistical process of so-called (re)combination increases the J/ψ production [32].

2.6. Direct Photons

Real and virtual photons, and therefore dielectrons, can be categorized into two sections. While one part of the photons originates from hadron decays as described in previous sections, the second part of photons stems from direct production processes. These direct photons can further be separated into thermal and non-thermal photons. Non-thermal photons are produced mostly independent from the produced QGP and can be created by bremsstrahlung, fragmentation processes or by hard scatterings in the initial stages of the collision. In elementary proton-proton collisions, these dielectrons from hard scatterings can be used to test perturbative QCD calculations. Another source of non-thermal photons can be found in photons produced in the preequilibrium phase before the the thermalization of the medium, a phase which is not well understood.

Thermal photons stem from annihilation and scatterings of quarks and gluons in the QGP, as well as from hadronic interactions in the hadron gas phase. These photons show a temperature dependence similar to black-body radiation $r_\gamma \propto T^4$. Photons produced in the QGP possess a harder transverse momentum spectrum compared to photons from the hadron gas phase, due to the higher temperature of the QGP in comparison to the hadron gas. This harder spectrum of photons produced in the QGP can analogously be translated into dielectrons at higher invariant mass helping to separate these two contributions. The invariant-mass distribution of virtual photons can be calculated with the Kroll-Wada formula 2.1, similar to the mass shape for dielectrons from hadron decays. The difference is that the assumption is made that direct photons originate from a point-like source and therefore the term including the electric form factor is set to unity: $S = 1$. This effect leads to a non-existing mass cut-off.

The measurement of real direct photons suffers from large systematic uncertainties originating from the subtraction of decay photons from the measured inclusive photon yield. The dominating background sources are decays of π^0 and η and these contributions can not be easily disentangled as function of transverse momentum. Virtual direct photons and therefore the dielectron measurement benefit from the additional kinematic observable: invariant mass. This observable allows to select the invariant mass range $m_{\mathrm{ee}} > m_{\pi^0}$ to study the direct photon contribution. With this analysis trick, the otherwise dominating π^0 contribution can be completely suppressed and therefore the systematic uncertainty of the subtraction of this contribution vanishes.

Another advantage, in addition to the smaller systematic uncertainty of the dielectron measurement in comparison the real photon measurement, is the Lorentz-invariance of the invariant mass distribution of the dielectron. This means that the temperature measurement as function of the invariant mass is not affected by the radial expansion of the medium which, in the case of the real photon measurement, leads to a blue-shift and therefore a modified measured temperature. Furthermore, the invariant mass spectrum acts like a chronometer. Dielectrons with higher invariant masses tend to be produced in earlier stages of a heavy-ion collision. A measurement of the direct photon contribution and its anisotropic flow in different invariant mass intervals can therefore directly disentangle the contributions from the QGP and the hadron gas phase. Hence, this measurement can help to solve the direct photon puzzle which is explained in more details in section 1.5.6.

2.7. Photon-induced Production

Relativistic charged projectiles, like heavy-ions in a collider, have a strong electromagnetic field arising from their Lorentz-contraction. These fields generate a high-density photon flux which is able to produce dielectron pairs at relatively small transverse momenta $p_{\mathrm{T,ee}} < 0.15\,\mathrm{GeV}/c$ [52]. This effect was initially investigated in the early 1930s by e.g. Landau and Lifshitz [53]. Two types of these photon-induced electromagnetic processes happen in heavy-ion collisions. The first process consists of a photon of one heavy ion which either interacts with the complete opposite heavy ion (coherent) or with single nucleons of this second heavy ion (incoherent), destroying this ion in the process [54]. This process is able to generate vector mesons, like the J/ψ, which themselves can decay into dielectron pairs. The coherent photoproduction of J/ψ is of particular interest since its cross section is expected to scale with the gluon distribution function in the ion which is hardly constrained experimentally [55]. This measurement allows for the study of the gluon shadowing effect at Bjorken-x values ranging from $\approx 10^{-5}$ to $\approx 10^{-2}$ [56]. The second electromagnetic process, leading to the production of dielectron pairs, is the interaction of a photon originating from one ion with a photon emitted from the other ion [57]. This

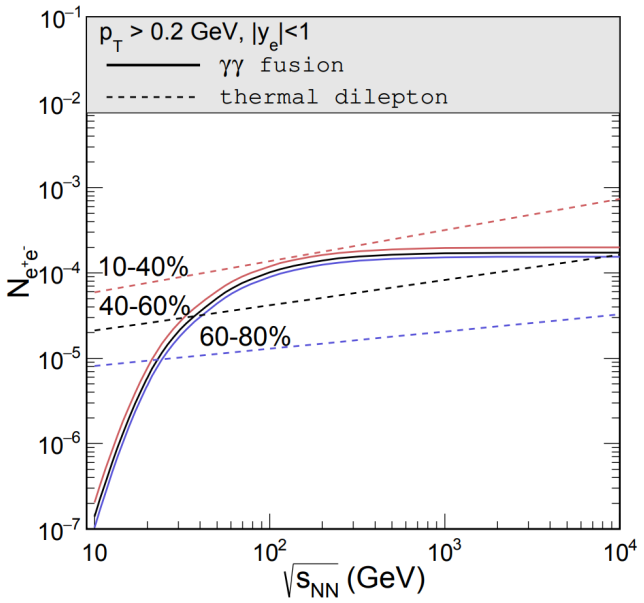

Figure 2.4.: Collision energy dependence of the photon fusion dielectron production and the thermal dielectron production in Au-Au collisions as a function of the collision energy $\sqrt{s_{\mathrm{NN}}}$ for different centrality intervals [51].

process $\gamma\gamma \rightarrow e^+e^-$ is typically referred to as photon fusion [51] or two-photon interaction [58, 59]. The dielectron production yield of this process is expected to be proportional to $Z_1^2 \cdot Z_2^2$ with $Z_{1,2}$ being the electric charge of the respective heavy ion. Therefore, the photon fusion process is expected to be much larger in heavy-ion collisions in comparison to the effect in proton-proton collisions. However, different theoretical models do not agree on the collision energy dependence of this contribution to the dielectron spectra. Figure 2.4 shows the collision energy dependence predicted by one model [51]. This model predicts an almost constant production yield for a center-of-mass-energy larger than $\sqrt{s_{\mathrm{NN}}} > 0.2\,\mathrm{TeV}$. A second model [58] predicts a strong rise as a function of the collision energy, contradicting the other model. Additionally, the pair transverse momentum spectrum of electrons originating from this electromagnetic process is sensitive to the magnetic field produced in heavy-ion collisions [59]. Photon-induced dielectrons are an ideal probe to measure this effect since they are produced early in the collision and experience the complete evolution of the magnetic fields while they do not interact strongly and are therefore mostly unaffected by the medium. Due to the different charge of electrons and positrons they are deflected in the magnetic field such that their pair transverse momentum $p_{\mathrm{T,ee}}$ increases.

3. Previous Dielectron Measurements

The following sections discuss selected previous dielectron and dimuon measurements in heavy-ion collisions at high energy accelerators like the Super Proton Synchrotron (SPS), the Relativistic Heavy-Ion Collider (RHIC) and the Large Hadron Collider (LHC).

3.1. SPS

The SPS was built in 1976 and serves several fixed-target experiments as accelerator. In present days it is used as pre-accelerator for the LHC. The fixed-target experiment CERES measured the dielectron production in several collision systems. While the invariant mass spectrum for proton-nucleus collisions (p-Be, p-Au [61]) could be explained by the estimated contributions from hadronic decays, the dielectron production in Pb-Au collisions showed an excess over the hadronic estimates [62, 63]. This dielectron spectrum as function of invariant mass in Pb-Au collisions at an energy of 158 GeV is shown in the left panel of figure 3.1 [60]. The solid line corresponds to the expected hadronic contribution. The data overshoots the hadronic estimate by a factor of 2.45 ± 0.71. The excess can be located predominantly in the mass range $0.2 < m_{\mathrm{ee}} < 0.6\,\mathrm{GeV}/c^2$. The right panel in figure 3.1 depicts two calculations for the contribution to the spectrum by the medium-modified ρ meson assuming a dropping ρ mass scenario [10, 64, 65] (dashed) and a spectral function broadening scenario (long-dashed) [66], respectively. While both calculations describe the mass spectrum at invariant masses $m_{\mathrm{ee}} < 0.7\,\mathrm{GeV}/c^2$ reasonably well, the mass range between the ω and the ϕ is better described by the ρ-broadening scenario [60].

To further disentangle the different contributions smaller statistical uncertainties and a higher mass resolution was required. While the latter could be achieved with the installation of a high-precision silicon vertex tracker, the former can be reached with measuring dimuons instead of dielectrons. The measurement of dimuons benefits from the usage of a trigger system and a higher purity due to muons being the only charged particles capable of traversing large absorber materials. The experi-

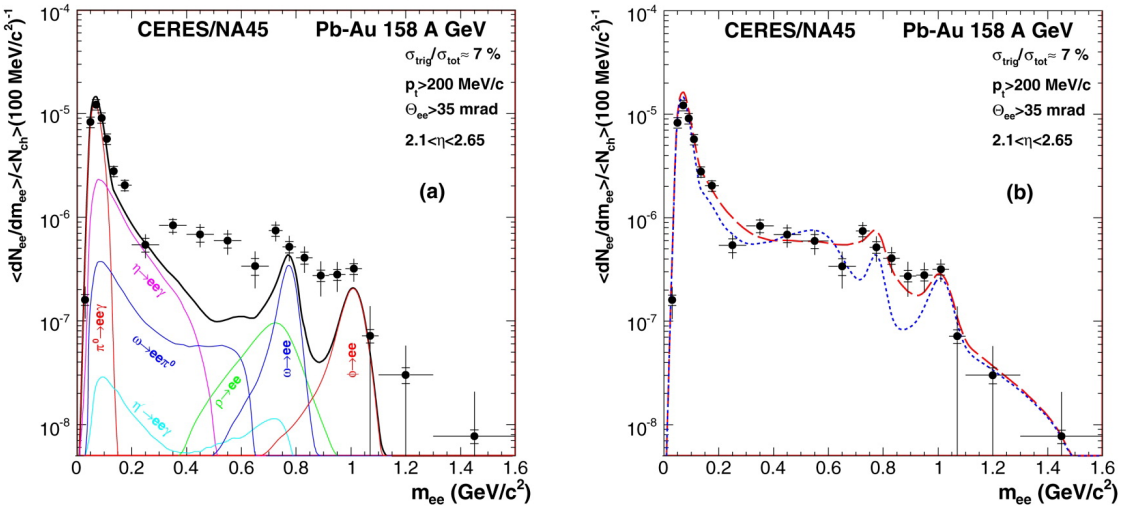

Figure 3.1.: The left panel shows the dielectron production as a function of invariant mass measured with CERES at the SPS [60]. It shows a clear excess of the data in comparison to the expected hadronic contributions. The right panel shows two hadronic expectations with calculations including the dropping ρ mass (dashed) and a spectral ρ broadening (long-dashed).

ment NA60 tried to utilize both methods to get a better insight into the dilepton production. The dimuon production was measured in 158 AGeV indium-indium collisions [67]. The left panel in figure 3.2 shows the dimuon spectrum as function of invariant mass with subtracted hadronic contribution except for the contribution from the ρ meson. The remaining excess spectrum is shown in the right panel together with two different calculations including the dropping ρ mass scenario (Brown/Rho) and the spectral-function broadening scenario (Rapp/Wambach). The data clearly favors the broadening scenario with no need for a mass dropping.

By fitting the excess m_{T} spectra in several mass intervals with an exponential function $\propto \exp\left(-m_{\mathrm{T}}/T_{\mathrm{eff}}\right)$ an effective temperature T_{eff} can be extracted. This effective temperature is shown in figure 3.3 as a function of the invariant mass for four different measurements. The green open circles indicate the temperature extracted from hadronic measurements while the red markers indicate the results from dimuon measurements which extracted with slightly different but comparable methods. The temperature dependence at small invariant muon masses M for muons and for hadrons rises almost linearly, consistent with expectations from radial flow induced by the expanding medium. Radial flow is typically developed at later stages of the collision process, indicating that these muons are also produced at later stages. However, dimuons at higher invariant mass $M > 1\,\mathrm{GeV}/c^2$ do not show this linear dependence indicating that they are produced in earlier partonic phases of the collision. Additionally, a fit in the invariant mass range $1.2 < M < 2.0\,\mathrm{GeV}/c^2$ yields a space-

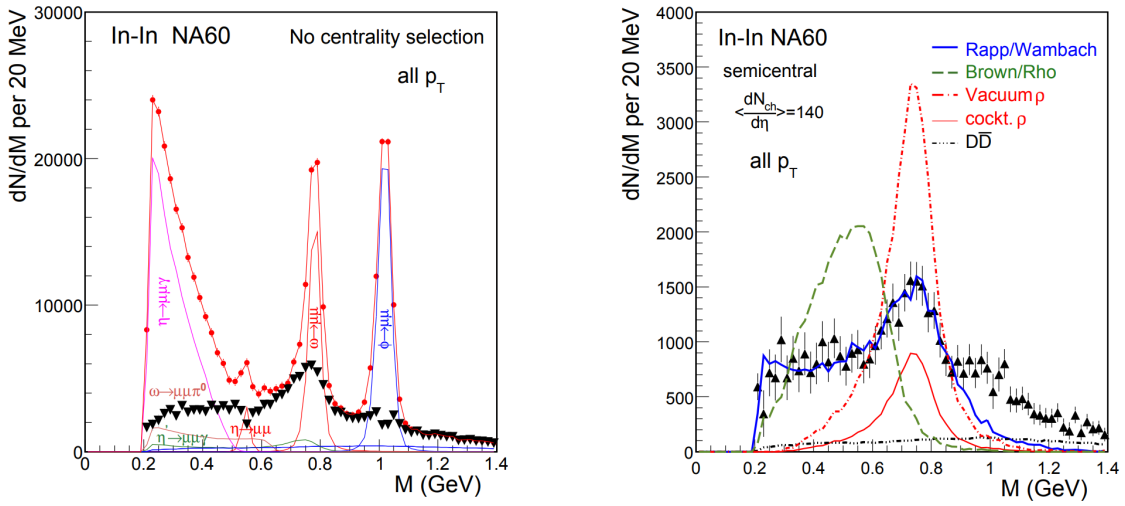

Figure 3.2.: Dimuon production as a function of the invariant mass measured by the NA60 collaboration [67]. The left panel shows the data with subtracted hadronic contributions. The right panel depicts the contribution of the ρ meson according to different theoretical calculations.

time averaged effective temperature $T_{\text{eff}} = (205 \pm 12)\,\text{MeV}$ which is higher than the predicted critical temperature $T_c \approx 155\,\text{MeV}$.

3.2. RHIC

The Relativistic Heavy Ion Collider (RHIC) with its two main experiments PHENIX and STAR was designed as a designated heavy-ion collider in Brookhaven, USA. RHIC can be used as a collider with a center-of-mass-energy of $\sqrt{s_{\text{NN}}} = 200\,\text{GeV}$ while the experiments at the SPS were all fixed-target. The PHENIX experiment measured dielectrons in elementary proton-proton, in deuteron-nucleus and nucleus-nucleus collisions. The measured dielectron yield in proton-proton collisions is compatible with the expectation from hadronic sources [69]. The result for deuteron-gold collisions shows a similar picture with no deviation from the hadronic expectations and therefore no significant modification by cold nuclear matter effects [70]. PHENIX was further able to extract total cross sections for charm and beauty production in both collision systems by simultaneously fitting the invariant mass and transverse momentum spectra. PHENIX also measured the dielectron production in Au-Au collisions at $\sqrt{s_{\text{NN}}} = 200\,\text{GeV}$. Similar to the SPS experiments they observed an enhancement of the dielectron production over the hadronic cocktail at lower invariant mass by a factor of $2.3 \pm 0.4(\text{stat.}) \pm 0.4(\text{syst.}) \pm 0.2(\text{model})$ [68]. The factor is extracted in comparison to the hadronic expectation which is based on measurements of the light-flavour meson decays and contribution from

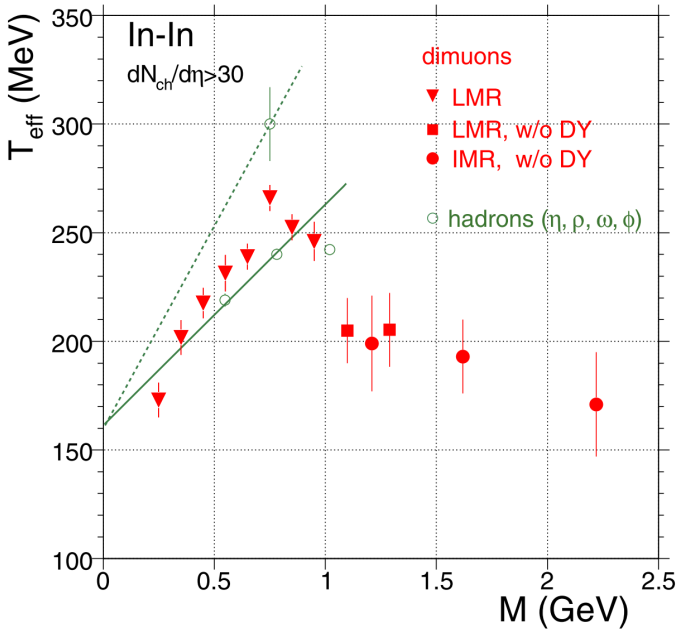

Figure 3.3.: Effective temperature as a function of invariant mass extracted from exponential fit to the m_{T} spectra in the according invariant mass range [67].

semileptonic open-charm hadron decays simulated with PYTHIA [71]. It is stated that the enhancement is distributed over the entire transverse momentum range $p_{\mathrm{T,ee}} < 5\,\mathrm{GeV}/c$. The left panel in figure 3.4 shows the invariant mass spectrum and the hadronic cocktail. PHENIX studied also the centrality dependence of the low-mass enhancement which can be found in the right panel of figure 3.4. As expected the enhancement rises with N_{part} and therefore with more central events, indicating that medium effects are important to describe the spectrum. It was further shown that similar theoretical calculations [72] which were able to describe SPS data, are also able to describe the enhancement at PHENIX. The data measured in the intermediate mass region $1.2 < m_{\mathrm{ee}} < 2.8\,\mathrm{GeV}/c^2$ which is dominated by semileptonic charm hadron decays deviates from the cocktail expectations by PYTHIA calculations by about 1 standard deviation from unity indicating no clear sign for cold- or hot-nuclear matter effects modifying the charm contribution.

The STAR collaboration measured also an enhancement of the data over the expected hadronic contributions in Au-Au collisions at $\sqrt{s_{\mathrm{NN}}} = 200\,\mathrm{GeV}$ [75]. The reported factor $1.77 \pm 0.11(\mathrm{stat.}) \pm 0.24(\mathrm{sys.}) \pm 0.33(\mathrm{cocktail})$ is compatible with recent PHENIX measurements at the same collision energy. The left panel in figure 3.5 shows the invariant mass spectrum and the ratio to the hadronic expectations. Besides the measurement at top RHIC energies, STAR also conducted dielectron measurements at smaller collision energies $\sqrt{s_{\mathrm{NN}}} = 19.6, 27, 39$ and $62.4\,\mathrm{GeV}$ [74]. The right panel on figure 3.5 shows that the data excess over the hadronic cocktail is

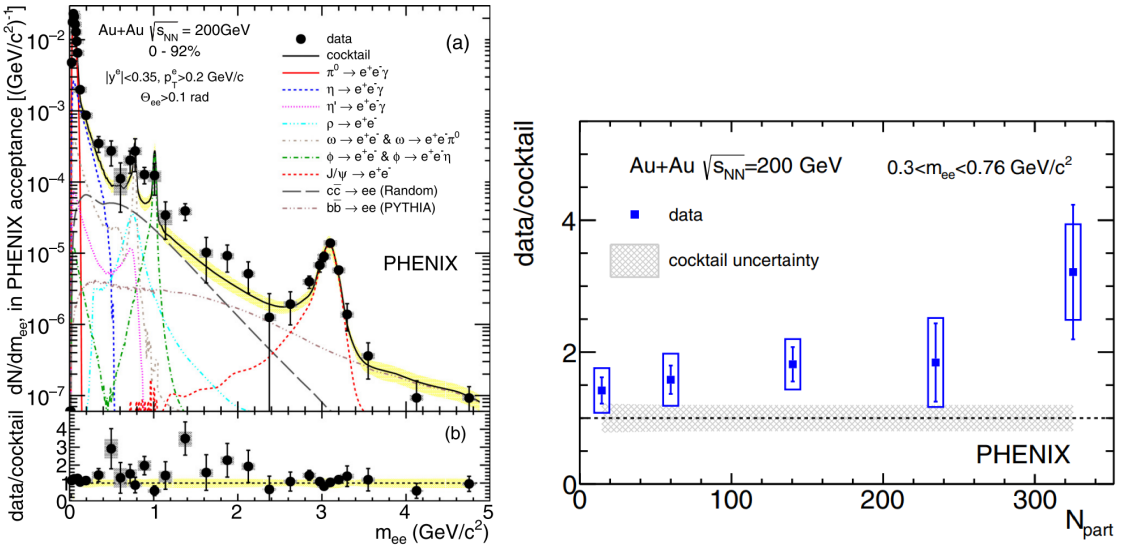

Figure 3.4.: Left panel depicts the dielectron invariant mass spectrum in Au-Au collisions compared to the cocktail of expected decays measured by PHENIX. The enhancement factor of data over hadronic cocktail as function of the number of participants in the collision is shown on the right. [68]

not dependent on the collision energy which is not expected because higher energies would lead to a larger and longer-living medium and therefore larger modification of the ρ meson. However, statistical uncertainties are large due to limited number of collisions and smaller dilepton production cross section at smaller energies.

The STAR collaboration studied the production of dielectrons with small transverse momentum $p_{\mathrm{T,ee}} < 0.15\,\mathrm{GeV}/c$ in Au-Au collision with a center-of-mass-energy $\sqrt{s_{\mathrm{NN}}} = 200\,\mathrm{GeV}$ in several centrality intervals [52]. The left plot in figure 3.6 shows the measured dielectron pair-transverse momentum $p_{\mathrm{T,ee}}$ distribution in comparison to the hadronic cocktail in the peripheral 60-80% centrality class. While the hadronic cocktail describes the data well for larger pair transverse momenta, the data exceeds the cocktail expectations at small $p_{\mathrm{T,ee}} < 0.15\,\mathrm{GeV}/c$. The right panel in figure 3.6 shows the measured invariant mass dependence of this excess in comparison to theoretical models [58, 59] including photon fusion, photonuclear production of the ρ meson and thermal dielectrons. The electromagnetic production mechanisms are introduced in section 2.7. Both applied models are able to describe the shape of the excess reasonably well over the complete invariant-mass distribution, while the STARlight model underestimates the total yield. This model [58, 76] uses a point-like charged heavy ion and prohibits the production of dielectron pairs within the boundaries of the nucleus. The model by Zha et al. [59] uses a Wood-Saxon-like charge distribution within the nucleus. Additionally, the latter model predicts that the p_{T}^2 distributions are sensitive to the extreme magnetic fields

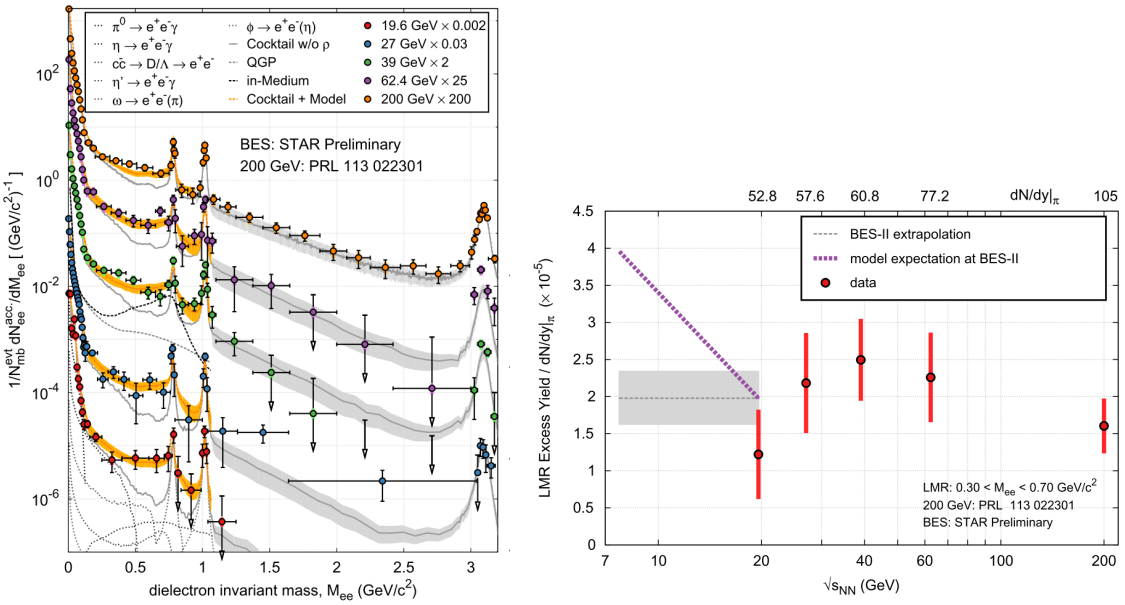

Figure 3.5.: Left panel depicts the dielectron invariant mass spectrum in Au-Au collisions compared to the cocktail of expected decays measured by STAR at different collision energies. [73] The enhancement factor of data over hadronic cocktail as function of the number of participants in the collision is shown on the right. [74]

produced in relativistic heavy-ion collisions. If the model includes this effect by the magnetic fields into the calculations, the agreement of the measured spectra and the models improves.

3.3. LHC

The nuclear research facility near Geneva, Switzerland, the Conseil Européen pour la Recherche Nucléaire, CERN, houses the worlds largest particle collider, the so-called Large Hadron Collider, LHC. The ALICE experiment, as one of the four major experiments at the LHC, published results on the dielectron production in pp-collisions at two energies $\sqrt{s} = 7$ and 13 TeV [44, 77] and Pb-Pb at a collision energy of $\sqrt{s_{\mathrm{NN}}} = 2.76$ TeV [78].

The invariant mass spectrum in comparison to the hadronic expectation in $\sqrt{s} = 7$ TeV collisions is illustrated in the left panel of figure 3.7. Expectations and measured spectrum agree within their uncertainties indicating that the dielectron production is understood in elementary collisions. Due to the good primary vertex resolution of the ALICE experiment, the pair distance-of-closest-approach $\mathrm{DCA_{ee}}$ can be utilized to separate prompt from non-prompt sources exploiting their different

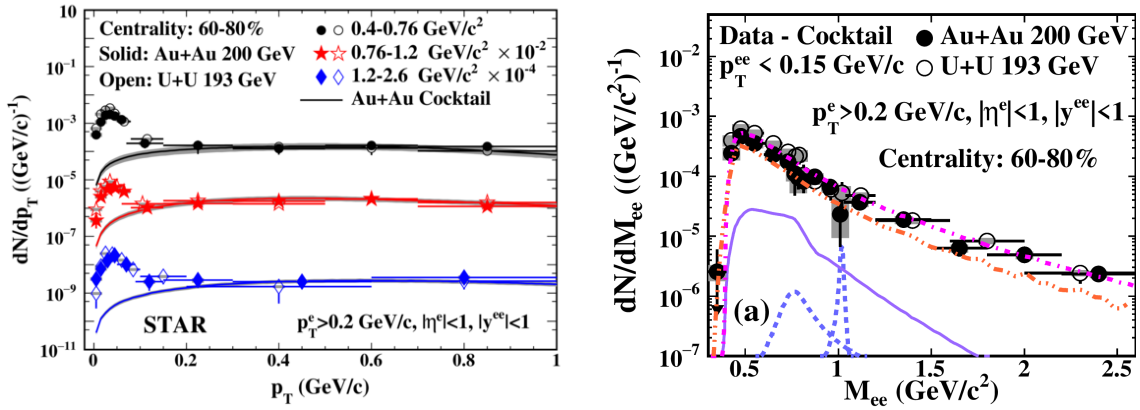

Figure 3.6.: Left panel shows the pair transverse momentum $p_{\mathrm{T,ee}}$ distribution of dielectron in several invariant mass m_{ee} intervals for peripheral collisions at $\sqrt{s_{\mathrm{NN}}} = 200\,\mathrm{GeV}$ in comparison to the hadronic cocktail [52]. The right panel shows the mass dependence of the excess over the cocktail as function of the invariant mass in comparison to theoretical models.

decay length. It is defined as the quadratic sum of the distance-of-closest-approach of the electron $\mathrm{DCA_{ele}}$ and positron $\mathrm{DCA_{pos}}$ to the primary vertex, each normalized to its respective resolution σ:

$$\mathrm{DCA_{ee}} = \sqrt{\left(\frac{\mathrm{DCA_{ele}}}{\sigma_{\mathrm{ele}}}\right)^2 + \left(\frac{\mathrm{DCA_{pos}}}{\sigma_{\mathrm{pos}}}\right)^2} \tag{3.1}$$

The $\mathrm{DCA_{ee}}$ distribution in the intermediate mass range $1.1 < m_{\mathrm{ee}} < 2.7\,\mathrm{GeV}/c^2$ is depicted in the right panel of figure 3.7 in comparison to the hadronic expectation. Data and expectations match indicating again that the production of dielectrons in proton-proton collisions is understood to the given level of precision. Especially indicating that there is no prompt contribution in this mass interval. A possible prompt contribution are dielectrons from thermal processes which are expected in heavy-ion collisions which produce a hot medium. Therefore, this measurement serves also as a feasibility study for these observables with the ALICE experiment for future high statistics data samples for heavy-ion collisions. However, in proton-proton collisions, this particular invariant mass range is sensitive to the contributions from semileptonic charm and beauty hadron decays. Due to the different shape of these contributions as function of m_{ee}, $p_{\mathrm{T,ee}}$ and $\mathrm{DCA_{ee}}$, it is possible to fit both heavy-flavour templates to the measured distributions and therefore measure their respective cross section. The shape of the respective heavy-flavour hadron contribution originates from two different models. On the one hand PYTHIA [71] which is a leading-order calculation and on the other hand Powheg which includes next-to-leading-order effects. The extracted cross sections for simultaneously fitting $(m_{\mathrm{ee}}, p_{\mathrm{T,ee}})$ and $\mathrm{DCA_{ee}}$ are shown in figure 3.8. While the left panel shows the results using the leading-order

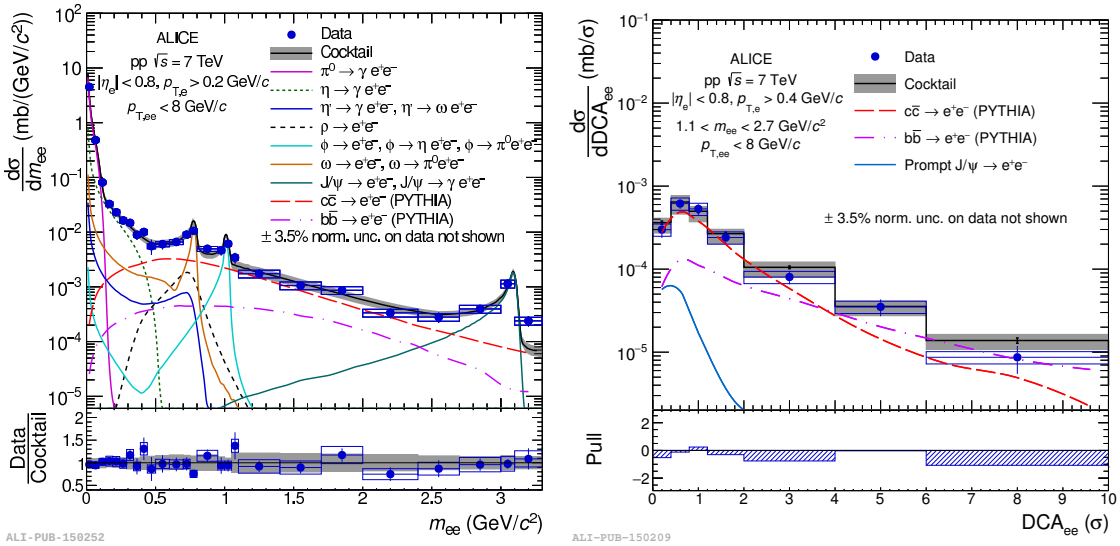

Figure 3.7.: Invariant mass m_{ee} measured in pp-collisions at $\sqrt{s} = 7\,\text{TeV}$ in comparison to the hadronic expectations (left) [44]. Pair distance-of-closest-approach DCA_{ee} spectra measured in the intermediate mass region $1.1 < m_{ee} < 2.7\,\text{GeV}/c^2$.

model PYTHIA, the right panel illustrates the results when using the POWHEG, which includes also next-to-leading-order calculations, as model for the respective heavy-flavour hadron contributions. All fit results match with the previous measurements, indicated by the vertical and horizontal lines, taking into account all uncertainties. However, the measurement indicates that the dielectron production is sensitive to the charm-quark production mechanism within the models.

The dielectron production measurement at $\sqrt{s} = 13\,\text{TeV}$ was performed taking into account inelastic and high-multiplicity events separately [77]. Figure 3.9 shows the invariant mass spectrum in comparison to the hadronic expectations (left) and the ratio of the dielectron spectra measured in high-multiplicity events to minimum bias events. Both spectra can be described with the hadronic expectations indicating no modifications of the dielectron production in high-multiplicity events apart from the already established modifications in the hadronic sector. Additionally, preliminary measurements with a reduced magnetic field in the ALICE central barrel were performed [80, 81]. The reduced magnetic field allows to reduce the minimal transverse momentum requirement to $p_{\text{T}} > 0.2 \rightarrow 0.075\,\text{GeV}/c$. This increases the dielectron acceptance and enables to measure very soft processes. This analysis serves also as a feasibility study for the upcoming high-statistics heavy-ion runs starting in 2021.

ALICE recently published measurements of the dielectron production in central Pb-Pb collisions at a center-of-mass energy $\sqrt{s_{\text{NN}}} = 2.76\,\text{TeV}$ recorded in 2011. The spectrum together with the ratio of data over hadronic expectation is shown in the top panel of figure 3.11. Data and expectations match taking into account large

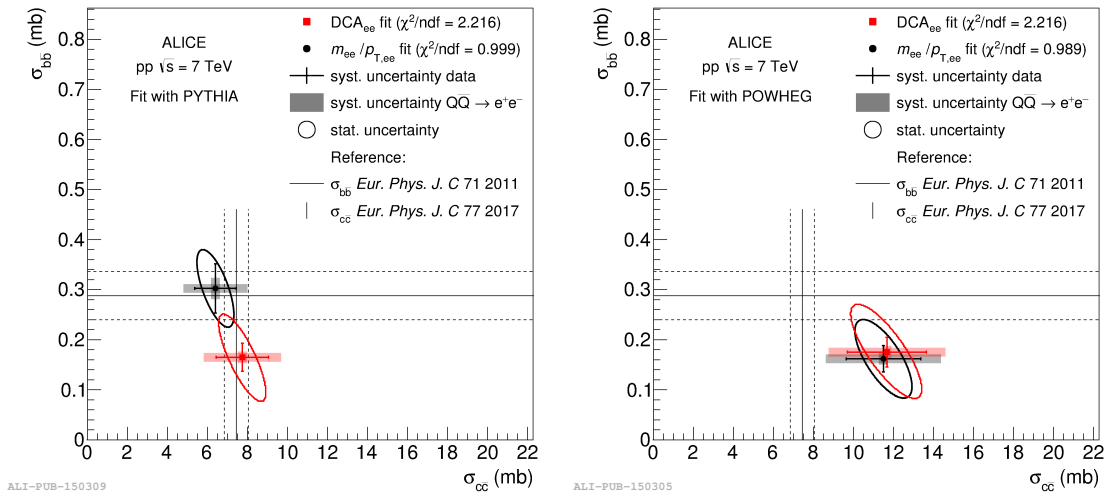

Figure 3.8.: Cross sections extracted by fitting templates of charm and beauty contribution to the m_{ee}, $p_{\mathrm{T,ee}}$ and $\mathrm{DCA}_{\mathrm{ee}}$ distributions [44]. While data points on the left are extracted using PYTHIA, the points on the right are retrieved by using Powheg simulations. Lines indicate the previously measured cross sections and their corresponding uncertainties. Error bars and boxes correspond to the systematic and statistical uncertainty on the data and uncertainties of the heavy-flavour hadron branching ratio, respectively.

statistical and systematic uncertainties of the data and the hadronic expectation. The bottom panel depicts the data in comparison to two calculations based on PHSD [82–84] and a fireball modell [72, 85]. With the given precision of the data both models are able to describe the spectrum in the low-mass region $0 < m_{\mathrm{ee}} < 1\,\mathrm{GeV}/c^2$. Additionally the direct photon yield was extracted and found to be consistent with PHENIX measurements and results from previous ALICE measurements based on electromagnetic calorimeters.

ALICE also presented a preliminary measurement of the very low-$p_{\mathrm{T,ee}}$ enhancement over the hadronic cocktail [79]. Figure 3.10 shows the dielectron yield as a function of the pair transverse momentum $p_{\mathrm{T,ee}}$ for peripheral Pb-Pb collisions at a center-of-mass-energy $\sqrt{s_{\mathrm{NN}}} = 5.02\,\mathrm{TeV}$ in comparison to the hadronic expectation with different assumptions regarding the effect of shadowing on the contribution by semileptonic open heavy-flavour decays. While the spectrum is reasonbly well described by the hadronic expectation for $p_{\mathrm{T,ee}} > 0.15\,\mathrm{GeV}/c$, the data exceed the expectation at small $p_{\mathrm{T,ee}}$. The shape of the excess is similar to the shape of the excess measured by the STAR collaboration which can be explained by photon-induced production of dielectrons and not by thermal dielectron production, see section 3.2 for more details on the STAR measurement.

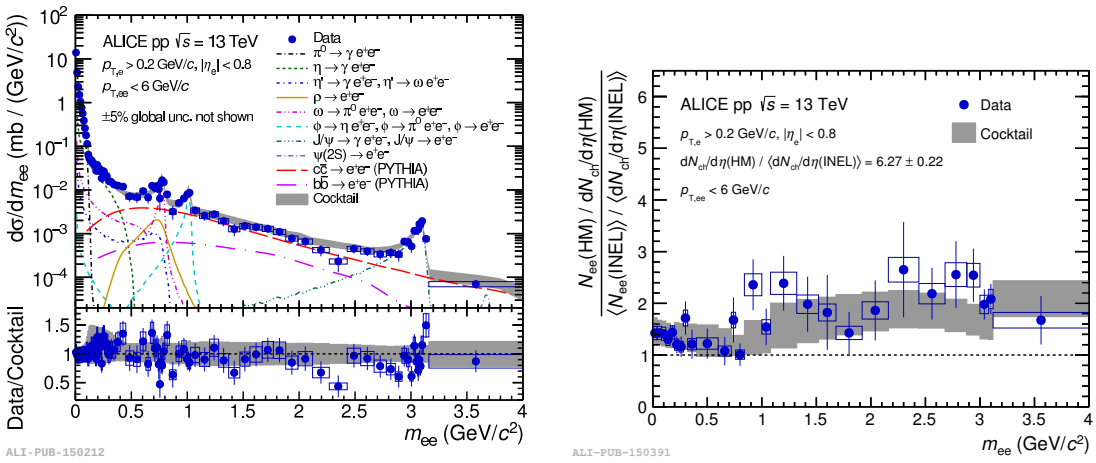

Figure 3.9.: Dielectron production as function of invariant mass in pp-collisions at $\sqrt{s} = 13\,\text{TeV}$ (left) [77]. Dielectron yield in high-multiplicity collisions relative to the yield extracted in minimum-bias collisions (right). Both are shown in comparison to the hadronic expectations.

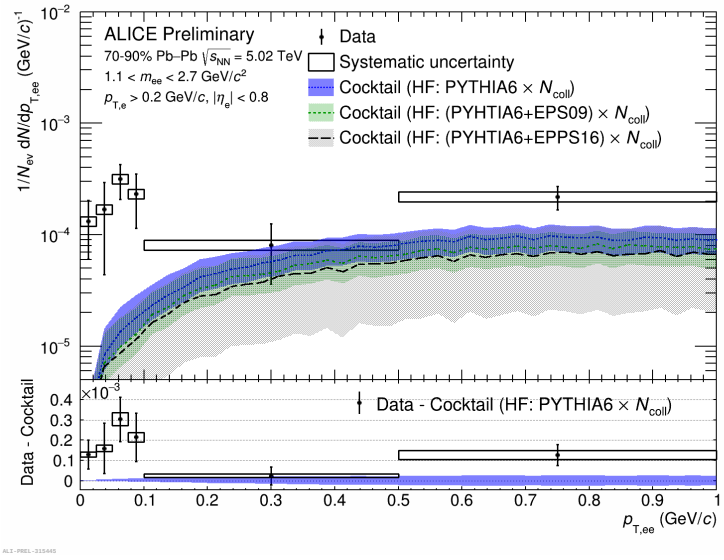

Figure 3.10.: Dielectron yield as a function of the pair transverse momentum $p_{\mathrm{T,ee}}$ for peripheral Pb-Pb collisions at a center-of-mass-energy $\sqrt{s_{\mathrm{NN}}} = 5.02\,\text{TeV}$ in comparison to the hadronic expectation with different assumptions regarding the effect of shadowing on the contribution by semileptonic open heavy-flavour decays [79].

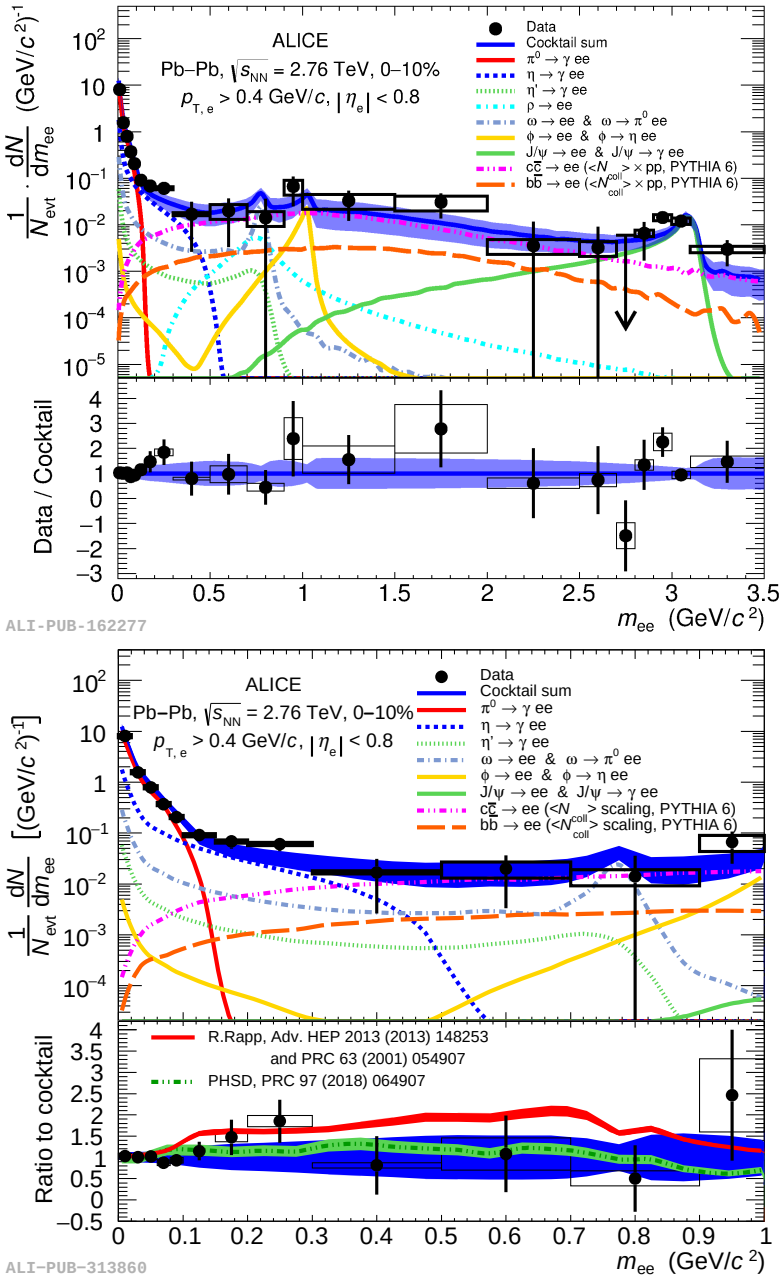

Figure 3.11.: Dielectron production as function of invariant mass in Pb-Pb collisions at $\sqrt{s_{\mathrm{NN}}} = 2.76\,\mathrm{TeV}$ in comparison to the hadronic expectation based on measurements (top) and two calculations from theory (bottom) [78].

4. LHC & ALICE

The Conseil européen pour la recherche nucléaire, CERN, was founded in 1954 in the vicinity of Geneva, Switzerland. Starting as a laboratory for studying atomic nuclei, over time it changed its primary research focus to high-energy physics and the understanding of subatomic interactions. Several scientific achievements have been made like the discovery of W- and Z-bosons as mediator of the weak interaction and the first production of a strongly interacting quark-gluon plasma both measured at the Super Proton Synchrotron (SPS). Another important discovery marks the detection of a particle which is consistent with the properties of the predicted Higgs boson at the largest particle accelerator ever built, the Large Hadron Collider (LHC). One of the four large experiments at the LHC is called ALICE (A Large Ion Collider Experiment). This experiment recorded the data which are analyzed in this thesis. LHC and ALICE are further introduced in the following sections.

4.1. LHC

The LHC [86] was built inside the tunnel of the Large Electron-Positron Collider, LEP, which was under operation from 1989 to 2000. The tunnel has a circumference of 26.659 km with a slope of 1.4 % in depths of $50-175$ m beneath the earth surface. During the first data-taking period between 2008 and 2013, which is called run-1, LHC was capable of accelerating protons up to a kinetic energy of $E_{\mathrm{proton}} = 4\,\mathrm{TeV}$ which leads to a center of mass energy of $\sqrt{s} = 8\,\mathrm{TeV}$. Lead ions could be accelerated to a center of mass energy per nucleon of $\sqrt{s_{\mathrm{NN}}} = 5.02\,\mathrm{TeV}$. The second period, run-2, started in 2015 and lasted until the end of 2018. During this data-taking, proton-proton collisions up to $\sqrt{s} = 13\,\mathrm{TeV}$ were recorded. Lead ions were accelerated up to $E_{\mathrm{Pb}} = 522.5\,\mathrm{TeV}$ which leads to a center of mass energy per nucleon of $\sqrt{s_{\mathrm{NN}}} = 5.02\,\mathrm{TeV}$.

To accelerate lead ions, an accelerator chain is required [87, 88]. It starts with pure lead being heated up to $\mathrm{T_{Pb}} \approx 550\,^{\circ}\mathrm{C}$. An electron beam is used to ionize the lead heated lead ions. Especially $^{208}\mathrm{Pb}^{29+}$ ions are selected and accelerated up to $\mathrm{E_{Pb}} = 4.2\,\mathrm{MeV/nucleon}$ inside of the linear accelerator Linac 3. The first stripper foil strips electrons from the lead ions leading to $^{208}\mathrm{Pb}^{54+}$ ions which are injected into the Low Energy Ion Ring, LEIR, and accelerated up to to $\mathrm{E_{Pb}} = 72.2\,\mathrm{MeV/nucleon}$.

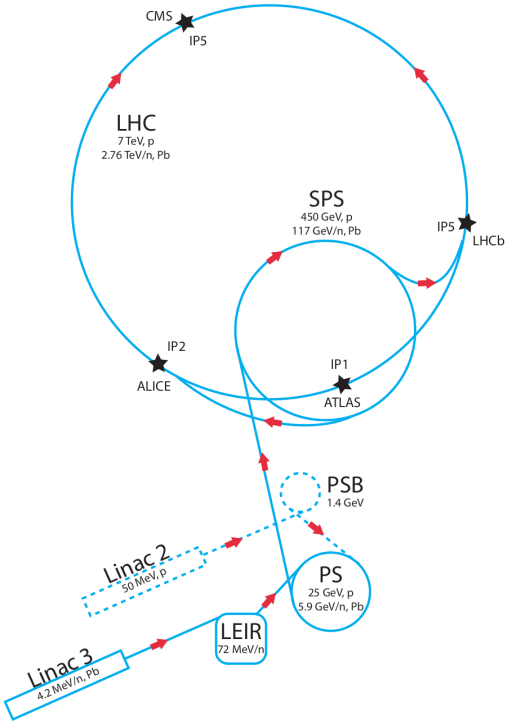

Figure 4.1.: LHC injector chain for lead ions and protons [14].

Those ions are further boosted up to $E_{Pb} = 5.9\,GeV/nucleon$ inside the Proton Synchrotron, PS. A second stripper foil is used to strip the remaining electrons. The fully ionized lead ions are fed into the Super Proton Synchrotron, SPS, where they are accelerated to $E_{Pb} = 177\,GeV/nucleon$. After the injection into the LHC they get boosted to the maximum center-of-mass energy of $\sqrt{s_{NN}} = 2.76\,TeV$ (run-1) or $\sqrt{s_{NN}} = 5.02\,TeV$ (run-2, this analysis). The acceleration procedure for protons is similar, starting at the Linac 2 and the Proton Synchrotron Booster PSB before entering the PS. A graphical representation of both injector chains can be found in figure 4.1.

LHC hosts two beam pipes directly next to each other, allowing particles to fly in opposite directions. The bunches are kept on track with 1232 large super-conducting dipole magnets which are cooled by liquid helium down to $T_{magnet} \approx 1.9\,K$ [89]. With an electric current of $I_{magnet} = 11\,850\,A$ the dipole magnets can reach magnetic fluxes of $B = 8.33\,T$. Additionally, 392 quadrupole magnets are used to focus the beams which disperse due to electrostatic forces between the positively charged ions.

The acceleration is done via radio-frequency cavities operating with an oscillation frequency of $f \approx 500\,MHz$ which presses the particles into so-called bunches. The time spacing between two bunches amounts to $t_{bunch} \approx 25\,ns$.

Bunches are continuously circling inside the two beam pipes and at four distinct

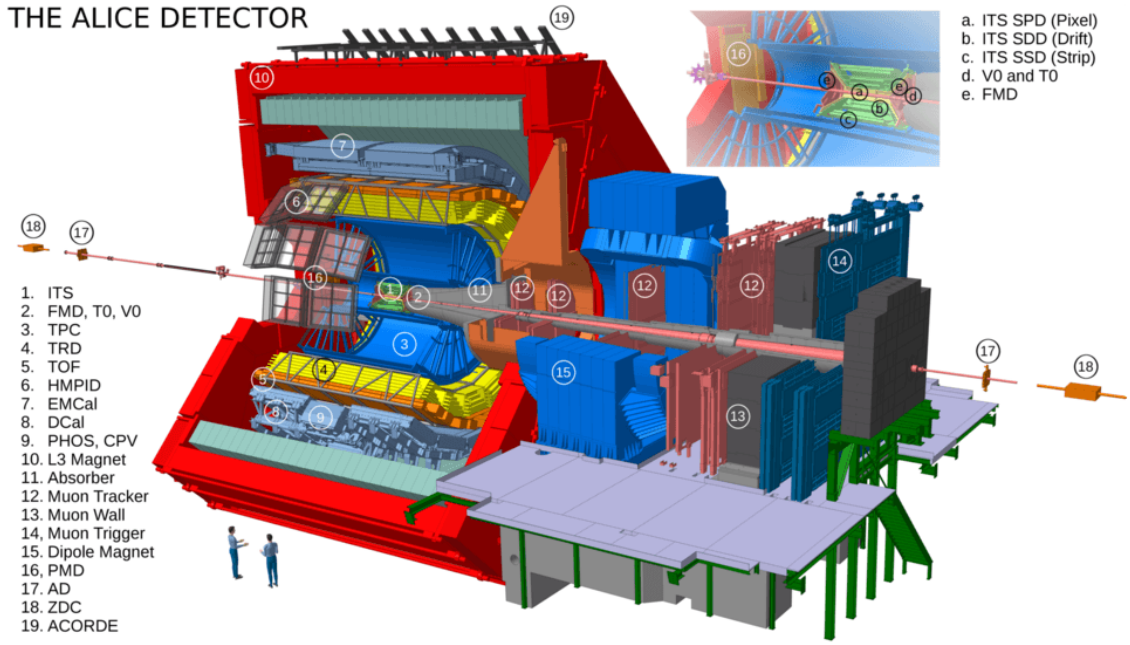

Figure 4.2.: ALICE with its subdetectors [91]. The overlay shows the part of the experiment which is closest to the primary vertex.

crossing points the particle beams are allowed to collide with the help of additional focusing higher-order magnets, like quadrupole magnet. At these collision points the four main experiments at the LHC are located: CMS (Compact Moun Solenoid), ATLAS (A Toroidal LHC ApparatuS), LHCb and ALICE [90]. While CMS and ATLAS are build as general purpose experiments and are famous for the discovery of a Higgs-like particle, LHCb is a forward detector focusing on beauty-quark physics.

4.2. ALICE

The ALICE experiment [3, 92–94] is designed for high-energy Pb-Pb collisions with high charged-particle multiplicities up to $N_{ch} \approx 30000$. The big strength of ALICE is the measurement of identified charged particles down to very low transverse momenta $p_{\mathrm{T}} > 150\,\mathrm{MeV/c}$ at mid-rapidity. This is possible because of the homogeneous solenoidal magnetic field of $B = 0.5\,\mathrm{T}$ in the central barrel provided by the L3-magnet. This magnetic field is relatively small compared to the other LHC experiments allowing unique measurements. In 2015, first pilot runs where recorded with an even more reduced magnetic field of $B = 0.2\,\mathrm{T}$. This field configuration allows for the measurement of even lower transverse momentum particles with $p_{\mathrm{T}} > 75\,\mathrm{MeV/c}$.

Figure 4.2 shows an overview of the ALICE experiment. It is built in several layers similar to an onion. Inside the large L3 magnet the so-called central barrel detectors,

i.e. Inner Tracking System (ITS), Time Projection Chamber (TPC), Ring Imaging Cherenkov Detector (HMPID), Transition Radiation Detector (TRD) and Time-Of-Flight Detector (TOF), are located together with the electromagnetical calorimeters EMCal, DCal and PHOS. Additionally, the smaller detectors T0, V0, ZDC and FMD are located close to the beam axis. In forward direction, azimuthal around the beam pipe, the muon arm with its several components, including a large dipole magnet, is located.
The next sections focus on the particle tracking and on the detectors which are used in this analysis: V0, ITS, TPC and TOF.

4.2.1. V0

The V0 detector [95] was mainly built to provide triggers for the event selection, for more details see section 6, and to separate beam-beam interactions from interactions of the beam with residual gas in the beam pipe. Additionally, the detector plays an important role in the centrality estimation of nucleus-nucleus collisions. The V0 detector consists of two cylindrical parts on each side of the interaction point along the beam line. The subdetector V0A is located 329 cm away from the nominal center of ALICE covering a pseudorapidity range of $2.8 < \eta < 5.1$ while V0C is placed 88 cm away on the other side of the experiment with respect to the nominal primary vertex with an acceptance of $-3.7 < \eta < -1.7$. It is built in concentric, segmented rings consisting of plastic scintillators connected to photo multipliers for read-out. In this analysis the V0 detector is used mainly for triggering and for the centrality selection.

4.2.2. Inner Tracking System

The major purpose of the Inner Tracking Systems [96, 97] is the reconstruction of the primary collision vertex and secondary vertices. Therefore, the ITS is placed closest to the nominal primary vertex. It is constructed in a cylindrical shape with six layers of silicon detectors with increasing radii. While the innermost layer has a radius $r = 3.9$ cm and thus is directly mounted behind the beam pipe, the outermost radius is $r = 42.8$ cm. Overall, the ITS covers a pseudorapidity range of $|\eta| < 0.9$ while the two most inner layers cover a range of $|\eta| < 1.75$. Figure 4.2.2 shows the detector setup during the data-taking period in 2015.

The two innermost layers are based on Silicon Pixel Detectors, SPD. A high granularity of the detector allows for a precise measurement of the distance-of-closest-approach to the primary vertex, DCA. Additionally, it incorporates fast digital read-out and good irradiation hardness allowing for the measurement of charged track densities up to 100 particles/cm^2. The middle two layers are made of Silicon Drift

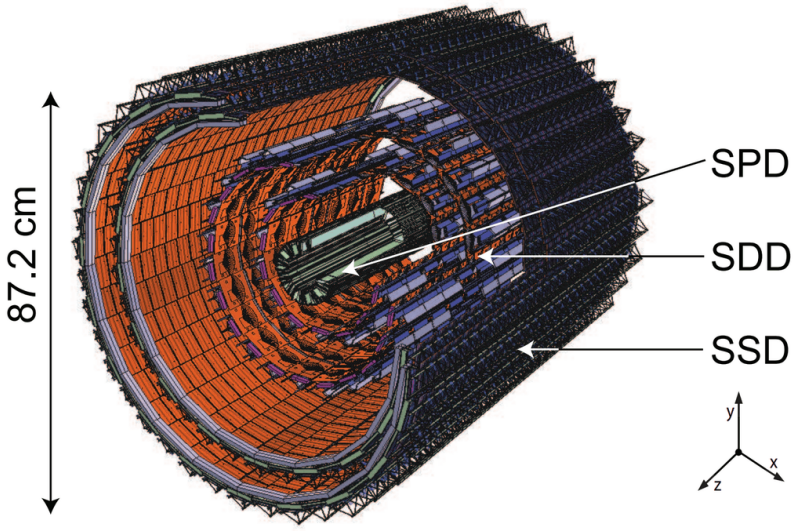

Figure 4.3.: Schematic view of the ITS [96].

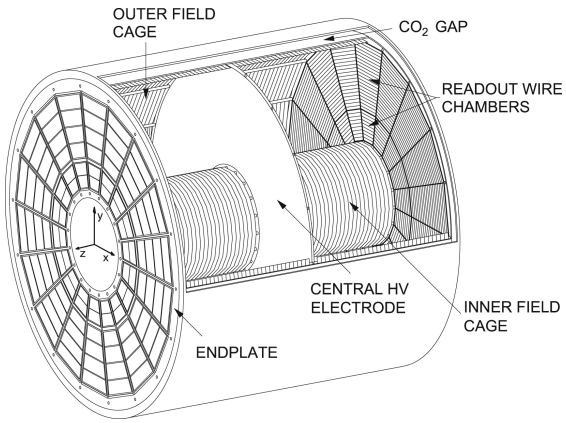

Figure 4.4.: Schematic layout of the TPC [98].

Detector, SDD, and the outermost two layers are built from double-sided Silicon micro-Strip Detectors, SSD. Those four layers have analogous read-out allowing for particle identification via measuring the energy loss by path length $\mathrm{d}E/\mathrm{d}x$, see section 7.2.1 for more details on the electron identification used in this analysis. The ITS is optimized for a small material budget with a radiation length of $X_0 = 1.1\,\%$. This leads to only few electrons coming from photon conversions in the detector material which is especially interesting in this analysis, see section 8.2 for a comprehensive overview of the impact of photon conversions.

4.2.3. Time Projection Chamber

The Time Projection Chamber [98] is the largest detector of ALICE. It allows for the reconstruction of charged particles and their identification via their specific energy loss per unit path length. Placed just behind the ITS with an inner radius of $r_{\text{in}} = 848\,\text{mm}$ and an outer radius of $r_{\text{out}} = 2446\,\text{mm}$ and a length of $l = 4994\,\text{mm}$, the TPC has an active volume of $V_{\text{active}} \approx 90\,\text{m}^3$. It covers a kinematic range of $|\eta| < 0.9$ with full azimuthal angle.

The TPC consists of a hollow cylinder divided by a central electrode perpendicular to the beam axis at the nominal vertex position of ALICE, see figure 4.2.3 for a sketch of the TPC. A homogeneous electric field between the central electrode and the readout chambers at the end plates of the TPC is applied. This electric field inside the field cage is set to $E_{\text{field}} = 400\,\text{V/m}$.

Charged particles traversing the TPC ionize the noble gas atoms along their trajectory. The created electrons drift towards the end caps of the detector due to the applied electric field. The end plates are divided into 18 equally large trapezoidal segments. The read-out electronics, which is mounted on these segments, are themselves separated into the Inner Read Out Chambers, IROC, closer to the vertex and Outer Read Out Chambers, OROC. The read out is based on Multi Wire Proportional Chambers, MWPC. The MWPCs amplify the incoming drifting electrons from the ionization process allowing for a precise measurement on the read out pad plane. The number of measured amplified electrons is proportional to the specific energy loss per unit path length of the particles traversing the TPC gas volume. This information can be used to identify electrons, which is further described in section 7.2.

The position of the arriving drift electrons on the read out plane carries the spatial information of the track in the r-ϕ plane. The TPC consists of 557568 readout pads organized in 159 rows providing a high granularity to allow for an excellent track separation to cope with the high number of charged tracks per event of $\mathrm{d}N_{\text{ch}}/\mathrm{d}\eta \approx 2000$ inside the central barrel. The track vector component parallel to the electric field is reconstructed via the drift time of those electrons given that the drift velocity inside the TPC is constant. Between two adjacent segments no active detector material is installed leading to dead areas in radial direction.

During data taking in 2015, the volume was filled with a mixture of argon and CO_2 with a relative composition of 88:12. In run-1 the TPC was filled with a neon-based gas mixture. In comparison to neon, argon allows for a more stable operation of the detector with the downside of being more sensitive to the accumulation of space-charge distortions. Space-charge distortions deteriorate the electric field inside the TPC and lead to a bad tracking resolution. The strength of this effect was unexpected and lead to the development of new correction algorithms which enhanced

the detector resolution compared to run-1 measurements.

4.2.4. Time-of-Flight

The Time-Of-Flight detector is mainly used for particle identification. It is divided into 18 equally large azimuthal segments in a distance of $r_{\mathrm{TOF}} = 3700\,\mathrm{mm}$ from the nominal vertex position and covers a pseudorapidity range of $|\eta| < 0.9$ with full azimuthal angle. It consists of multigap resistive plate chambers for fast read out.

The TOF measures the time of flight of particles starting from a time t_0 when the collision happens. This starting time t_0 can be estimated in different ways. It can be measured by the T0 detector close to the collision vertex, directly from the expected collision time given by the LHC or by correlating several TOF signals of the same event. The flight time of the particle is then calculated via $t_{\mathrm{particle}} = t_{\mathrm{hit}} - t_0$ with t_{hit} being the measured time of the hit in the TOF. The overall time resolution is estimated to be $\Delta t_{\mathrm{TOF}} = 80 - 100\,\mathrm{ps}$. This time can be used to estimate the velocity and therefore the mass of the particle combining this information with the measured momentum of the particle in the ITS and TPC. This leads to the good electron identification used in this analysis.

4.2.5. Tracking

The term tracking refers to an algorithm to find the track of a given particle inside a detector during the reconstruction process. Due to the magnetic field charged particle tracks are bent to a helix-like trajectory. The algorithm used is a so-called Kalman Filter. It is a recursive procedure which updates the initial estimate of the track with every added information.

The algorithm starts with combining two hits in the outer part of the TPC where the track density is small to get an initial TPC tracklet. This seed is further constrained to the primary vertex which was estimated by the two innermost layers of the ITS. More hits in the detector along the potential path within a predefined search window are examined to update the TPC tracklet parameters. At the outer ITS boundary the propagated tracklet is used as a seed for the ITS tracking. The combined information of the TPC and ITS tracklet is then used to reconstruct a so-called global track. This track is propagated to the outer detectors including the TOF to match with its corresponding hits. The last step of the tracking procedure includes a propagation of the track back again in inward direction. Those resulting tracks also determine the final position of the primary collision vertex.

5. Analysis Strategy

This thesis is focusing on the measurement of the dielectron production in Pb-Pb collisions at a center-of-mass energy of $\sqrt{s_{\mathrm{NN}}} = 5.02\,\mathrm{TeV}$. One of the goals of this analysis is the comparison of fully corrected invariant mass and transverse momentum spectra to a predicted hadronic cocktail based on previous ALICE measurements. The latter describes the expected dielectron yield from known hadronic sources without including thermal radiation of the medium or hot-matter effects regarding the heavy-quark contribution. Additionally, the contribution of virtual direct photons is estimated by a fit to the data with templates which are extracted from theoretical calculations. The analysis proofs to be relatively complex with several parts connected to each other, making this study challenging. A flow chart of the different analysis steps can be found in figure 5.1. The following chapter summarizes the analysis procedure and shows how the different parts work together. A more detailed description on the details on each step of the analysis can be found in the subsequent chapters of this thesis.

The dielectron analysis presented in this thesis is based on three major components:

- Raw data analysis (blue)
- Efficiency correction (orange)
- Hadronic cocktail (yellow)

The raw-data analysis focuses on the optimization of the event, track and pair selection criteria to extract the best possible information from the recorded data set. The first step of the analysis is the event selection. Only events coming from beam-beam interactions and which happen to be approximately in the center of the ALICE experiment are accepted. To pick high quality electron tracks, a track selection and electron identification procedure is performed. To improve the electron identification, a recalibration of the detectors with so-called V0 electrons is implemented. The next step is the pairing of the electron and positron candidates to form an unlike-sign and like-sign spectra. Due to effects originating from the particle acceptance of ALICE a correction with a so-called R-factor is needed. This R-factor is extracted with the mixed-event technique. From these three ingredients, a raw dielectron spectrum is extracted. This spectrum needs to be corrected for e.g. the impact from dielectrons originating from photon conversions and for effects coming from inefficiencies of the detectors.

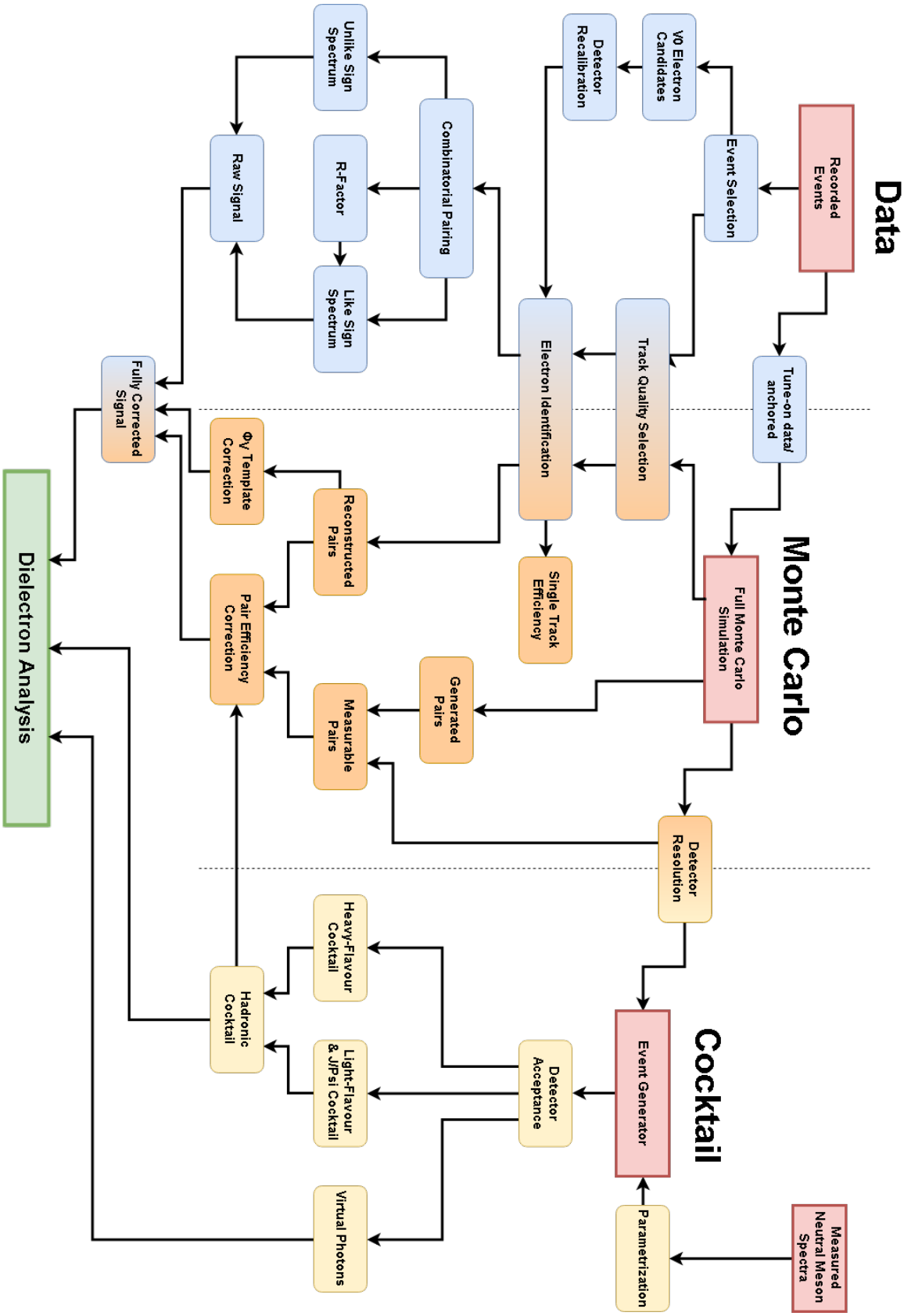

Figure 5.1.: Dielectron analysis strategy.

To correct for non-functioning parts of the experiment and for the track selection applied, a pair efficiency correction is needed which is based on a full Monte Carlo simulation. The same track selection and electron identification as in data is performed on simulated data. Tracks are paired to form correlated dielectron pairs. These resulting pairs can be counted before and after applying the track and pair selection to estimate the efficiency correction factor. Additionally a ϕ_V-template correction is performed to correct for the non-flat distribution of ϕ_V after all photon conversion selections. After application of all corrections the spectrum represents the fully corrected dielectron yield in the ALICE acceptance.

The third part of this analysis is about the generation of a so-called hadronic cocktail which the fully corrected dielectron spectrum is compared to. The hadronic cocktail is based on a measured charged pion transverse momentum spectrum, as an approximation of the neutral pion spectrum. Additionally, the hadronic cocktail includes a measurement of the J/Ψ transverse momentum spectrum. These measurements are parametrized and used as input, together with the detector resolution maps, for the event generator. The event generator produces the light-flavour and heavy-flavour part of the hadronic cocktail, respectively. A spectrum for the virtual direct photon yield is predicted by the generator which is used to measure the direct photon yield directly.

6. Data Set and Event Selection

6.1. Data set

The data set used in this analysis was recorded with ALICE during the heavy-ion data-taking period in the end of 2015. This data set includes Pb-Pb collisions with a center-of-mass energy of $\sqrt{s_{\mathrm{NN}}} = 5.02\,\mathrm{TeV}$. It is subdivided into three segments:

- LHC15o_pass3_lowIR
- LHC15o_pass1
- LHC15o_pass1_pidfix

Whereas the first segment consists of so-called runs with a low interaction rate of $\mathrm{IR} = 2 - 8\,\mathrm{Hz}$, the latter data subsets are recorded with an interaction rate of $\mathrm{IR} = 50 - 500\,\mathrm{Hz}$. The term run is defined by the ALICE collaboration as time period with stable detector settings and ranges typically around several minutes up to a few hours. The interaction rate describes the frequency of heavy-ion collisions in the experiment. During the reconstruction process of LHC15o_pass1 a software bug concerning the particle identification of heavy nuclei was found and fixed. The already reconstructed events were not reprocessed but the remaining events were reconstructed with the new algorithm leading to the period LHC15o_pass1_pidfix.

The data was recorded using the so-called minimum-bias trigger CINT7. This trigger does not select special events and therefore does not bias the analysis towards any rare processes. This trigger is implemented in such a way that it triggers data read-out only when signals in the SPD, V0A and V0C detectors are in coincidence with the time of a bunch crossing in ALICE as given by the LHC.

6.2. Differences between run-1 and run-2

The period analyzed in this thesis was the first heavy-ion period since 2011 and is the first during LHC run-2 after LHC run-1 (2008-2013) and the Long Shutdown 1 (LS1) between 2013 and 2015. During this shut-down many of the detectors inside

ALICE have been maintained, repaired and completed. Especially the ITS was suffering from many non-working units. The filters of the cooling systems of the ITS got clogged during run-1 operation which lead to insufficient cooling and raised the need to turn off parts of the detector to prevent further damage. During LS1 the cooling pipes were freed, restoring the detector almost completely.

During LS1 the gas in the TPC was changed from a neon-based to an argon-based mixture. Argon shows a more stable performance under high interaction rates but introduced space-charge distortions as further described in section 4.2.3. These distortions are corrected during the reconstruction procedure with the help of the fully installed TRD (Transition Radiation Detector), resulting in an improved tracking resolution compared to LHC run-1 data sets.

6.3. Monte-Carlo Simulation

For a complete understanding of the data a full detector simulation is essential. The ALICE collaboration produces and provides these simulations centrally. These simulations can be used to correct the data for detector inefficiencies and to estimate the detector resolution needed for the hadronic cocktail simulation, for more details see sections 11 on the hadronic cocktail and section 9.1 for the detector resolution. Because the full information of the underlying physics processes are available in simulations, they can be used to optimize track selection criteria to reject electrons from conversions and misidentified electrons and to estimate their residual contribution to the dielectron spectrum.

Two different simulations are used in this analysis: LHC16g1 and LHC18b5a. These data samples are *anchored* to the complete LHC15o period. This means that the exact detector configuration during those runs is used in the simulation including e.g. detector inefficiencies, dead pixels in the ITS, voltage settings in the TPC, noisy channels and timing information in the TOF. The detector simulation is performed with the GEANT3 software package [99].

The underlying physics simulation is performed with the HIJING [100] heavy-ion event generator. Pb-Pb collisions are simulated at a center-of-mass energy of $\sqrt{s_{\mathrm{NN}}} = 5.02\,\mathrm{TeV}$. LHC16g1 is a general purpose simulation meaning that it contains only minimum-bias Pb-Pb events and is used in this analysis for the template correction of the ϕ_V spectra as described in section 8.2. LHC18b5a, which is used for the determination of the detector resolution and the efficiency correction as described in section 9, is a dedicated dielectron simulation with added dielectron sources:

- one π^0, η, η', ρ, ω, ϕ and one J/ψ meson per event with a flat rapidity dis-

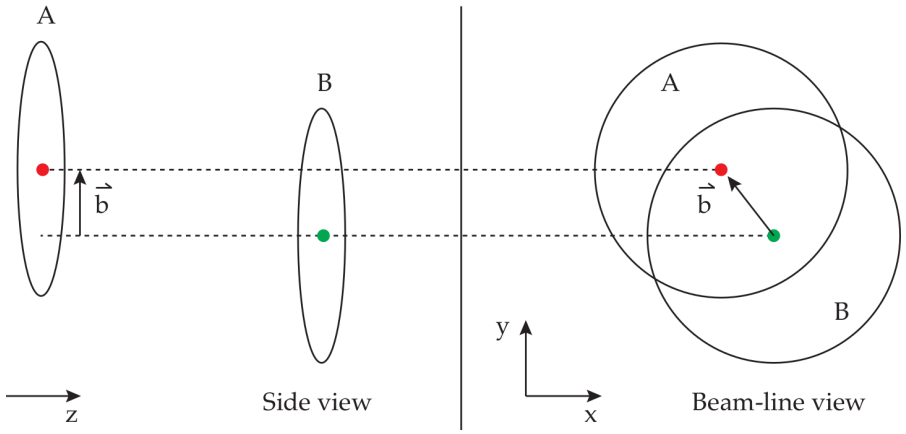

Figure 6.1.: Impact parameter b shown for two nuclei A and B. [14]

tribution within $|y| < 1.2$ and a flat transverse momentum distribution with $p_{\mathrm{T}} < 25\,\mathrm{GeV/c}$. The injected sources are forced to decay into dielectrons, meaning that the branching ratio BR(meson $\rightarrow e^+e^-X$) is set to 1.

- in 20% of the events: injected $c\bar{c}$ pairs produced with PYTHIA6 and forced to decay semileptonically via an open-charm hadron such that $c\bar{c} \rightarrow e^+e^- + X$. Events are only accepted if both electrons from the open-charm hadron decays are within the rapidity range $|y| < 1.2$.
- in 20% of the events: injected $b\bar{b}$ pairs produced with PYTHIA6 and forced to decay semileptonically via an open-beauty hadron such that $b\bar{b} \rightarrow e^+e^- + X$. Events are only accepted if both electrons from the open-beauty hadron decays are within the rapidity range $|y| < 1.2$.
- in 60% of the events: injected $b\bar{b}$ pairs produced with PYTHIA6 without any forced semileptonic decays. Events are accepted if at least one electron from $b \rightarrow e$ or $b \rightarrow c \rightarrow e$ lies within the rapidity range $|y| < 1.2$.

6.4. Centrality Estimation

When two nuclei collide the distance between the centers of the two nuclei is called impact parameter b. A sketch illustrating the impact parameter can be found in figure 6.1. This parameter b is not directly experimentally accessible. The so-called centrality is introduced which is related to the geometric overlap of the two colliding nuclei. The Glauber Monte Carlo model [101] is used to correlate the impact parameter and the centrality. In the ALICE collaboration the centrality is estimated with the measured multiplicity in both V0 detectors (V0M). See figure 6.2 for the number of events as a function of the V0M amplitude which corresponds

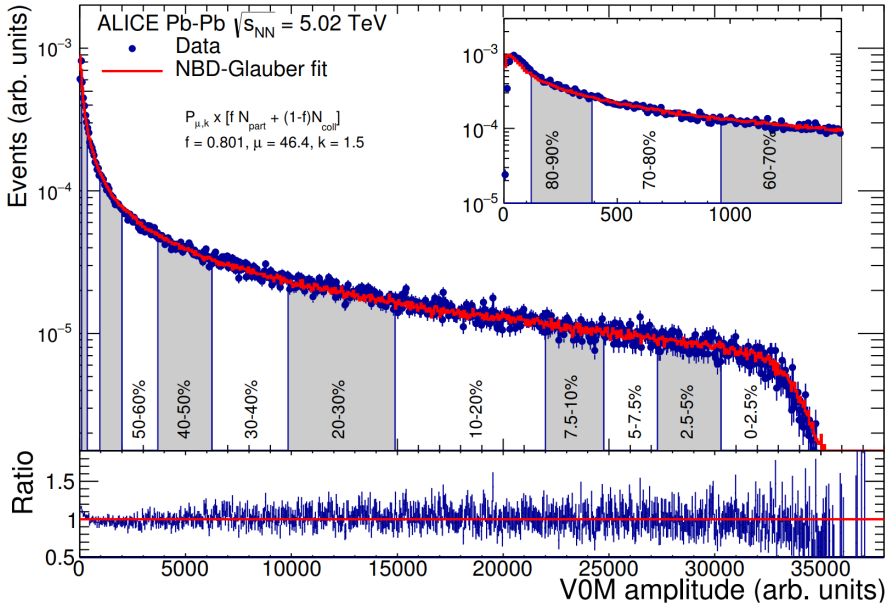

Figure 6.2.: V0M distribution measured in Pb-Pb collisions at $\sqrt{s_{\mathrm{NN}}} = 5.02\,\mathrm{TeV}$ subdivided into several centrality classes parametrized with a negative binomial distribution. The inlay focuses on the low multiplicity part of the distribution [102].

directly to the multiplicity in forward direction. This distribution can be fitted with a negative binomial distribution as input for the Glauber Monte Carlo simulations. Events with a high overlap of the two colliding nuclei show a high multiplicity in the V0 detectors. The top 5% of the distribution are defined as the 0-5% centrality class whereas the next lowest 5% correspond to the 5-10% class and so on.

In this analysis, only collisions with hadronic interaction are relevant but at LHC energies electromagnetic processes have a non-negligible cross section and contaminate the data. These electromagnetic processes produce only events with small multiplicities which consequently are present at the lower end of the V0 amplitude distribution. Additionally, events with beam-gas interaction also exhibit small multiplicities. These two effects are negligible in the centrality range of 0-90%. This can be studied by comparing the measured V0M data to the output of Glauber Monte Carlo simulations which are in good agreement with each other [102].

The Glauber Monte Carlo is then used to estimate the average number of participating nucleons N_{part} and the number of binary nucleon-nucleon collisions N_{coll}. The extracted values for the centrality classes used in this analysis can be found in table 6.1 [103]. The centrality classes for this analysis are chosen to have enough statistics while being compatible to other ALICE measurements. The centrality estimation, calculation of N_{part} and N_{coll} and their corresponding systematic uncertainties are centrally provided by a common framework in ALICE.

Centrality	$< N_{\text{part}} >$	syst.	$< N_{\text{coll}} >$	syst.
$0 - 20\,\%$	309.7	0.9	1273	14.1
$20 - 40\,\%$	159.4	1.32	468.2	6.92
$40 - 80\,\%$	47	0.8	83.3	2
$70 - 90\,\%$	11.3	0.12	10.9	0.2

Table 6.1.: Centrality classes used in this analysis with their corresponding $< N_{\text{part}} >$ and $< N_{\text{coll}} >$ and their systematic uncertainties.

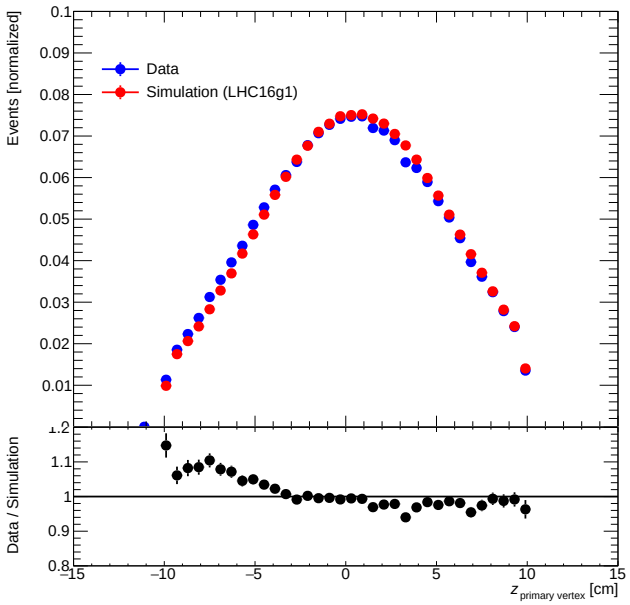

Figure 6.3.: The upper panel shows the $z_{\text{primary vertex}}$ distribution after selection. Blue indicates data while red indicates simulation. The lower panel shows the ratio data over simulation.

6.5. Event Selection

The centrally provided so-called offline event selection, which is used in this analysis, rejects events with beam induced background as well as events with only electromagnetic interactions. For this procedure the timing signal of V0A, V0C and the ZDC are correlated with the bunch crossing time given by the LHC.

The ALICE collaboration organizes several events in so-called runs. Within a given run the detector conditions typically remain stable. A complete list of runs, which are used in this analysis, can be found in section C. To achieve the best possible data quality, runs are selected in such a way that the detectors of ALICE relevant for this analysis, i.e. ITS, TPC, TRD, TOF, T0 and ZDC, have recorded data and

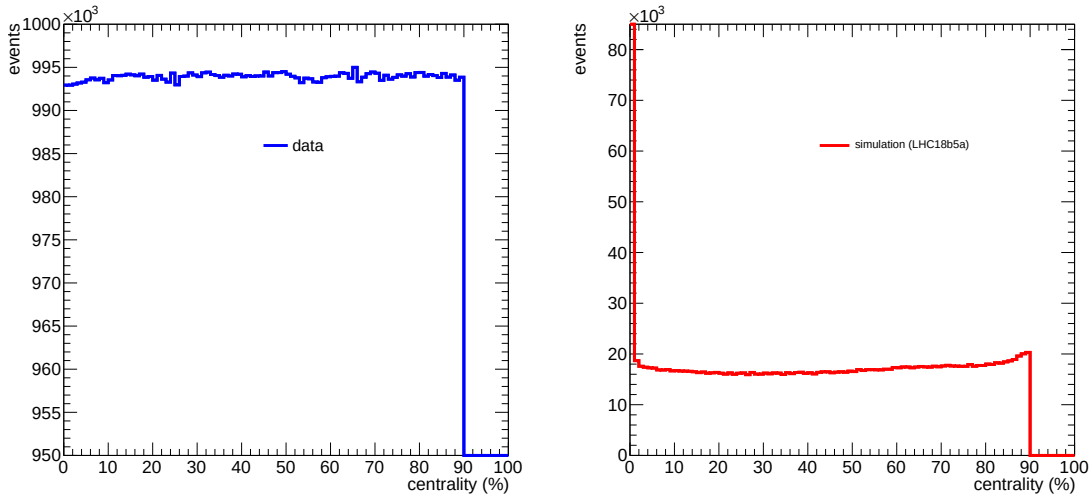

Figure 6.4.: Centrality distribution measured with the V0 detectors in data (left) and MC simulation (right). The dotted lines indicate the selected centrality classes.

have received positive quality-assurance feedback by the detector experts. All of these preselected runs are additionally tested to show a stable performance regarding specific observables crucial for this dielectron analysis like the mean number of electron candidates per event.

Events in this analyis are required to have at least one track pointing to the primary vertex. This selection assures that a reconstructed primary vertex was found in the given event. To further ensure uniform detector performance a heavy-ion collision needs to happen in the center of the experiment. Therefore the reconstructed primary vertex is required to be within 10 cm of the ALICE central barrel center in beam direction: $|z_{\text{primary vertex}}| < 10\,\text{cm}$ with $z_{\text{primary vertex}} = 0$ being at the center of the experiment. The upper panel of figure 6.3 shows the $z_{\text{primary vertex}}$ distribution in data and in the LHC16g1 simulation. The lower panel shows the ratio data over simulation which is in relatively good agreement to each other, except for small deviations at negative $z_{\text{primary vertex}} < 0$ positions.

As described in section 6.4 three centrality classes are chosen in this analysis: $0-20\,\%$, $20-40\,\%$, $40-80\,\%$ and $70-90\,\%$. These classes are selected to be compatible with other analyses, i.e. the $\pi^{\pm}$ and J/ψ transverse momentum measurement used as an input for the hadronic cocktail. In figure 6.4 the centrality distributions measured with the V0 detectors in data (left) and in MC simulation LHC16g1 (right) are shown. The dotted lines indicate the selected centrality classes in this analysis. While in data the distribution is flat, the simulation shows a peak at very small centralities and additionally a non-flat behaviour for larger centralities. This behaviour originates from the way centrality classes in simulations are defined

within the ALICE collaboration. The centrality classes are modeled in such a way that they reproduce the measured multiplicity in a given centrality bin. To resolve this issue the analysis is performed in small centrality classes and then later added together, i.e. 0-5%, 5-10% and 10-20% are analysed individually and then added together to receive the result for the most central 0-20%.

The same event selection is performed for data and simulation. The overall number of selected events after the complete event selection is about $\approx 90 \cdot 10^6$ events in recorded data within the $0 - 90\,\%$ centrality class. Accordingly LHC16g1 accounts for about $\approx 1.8 \cdot 10^6$ events while in LHC18b5a about $\approx 1.6 \cdot 10^6$ events were selected.

7. Single track analysis

Heavy-ion collisions produce a plethora of particles within the acceptance of the experiment. Most of these particles are hadrons and not of interest for the dielectron analysis presented in this thesis. Additionally, only tracks with a sufficient momentum and spatial resolution are suitable for this measurement. To ensure such a high-quality electron sample, a track selection together with an electron identification is performed. These selected electrons are required to be so-called primary tracks meaning that they do not originate from weak decays of strange hadrons without rejecting tracks from heavy-flavour mesons and baryons. Furthermore, electrons originating from photon conversions inside the detector material should be reduced to a minimum to reduce the background.

In the following section the selection criteria for a reference setting are presented. This reference setting is later used to calculate the resulting dielectron spectra. To estimate systematic effects originating from the track selection, all track requirements are varied. A more detailed discussion of this variation procedure can be found in section 10.1.

7.1. Track Selection

Charged particles are reconstructed from data recorded in the ITS and the TPC. This track reconstruction procedure is performed centrally by the ALICE collaboration. To meet the above mentioned requirements of this particular analysis, several selections are applied to the complete track sample. To ensure that tracks can be measured by the ALICE experiment with high precision a selection on the kinematic properties of the tracks is applied. This selection includes the transverse momentum range of $0.2 < p_T < 8\,\mathrm{GeV/c}$. The lower threshold is chosen to be slightly larger than the absolute acceptance minimum $p_\mathrm{T} > 0.15\,\mathrm{GeV}/c$ of the experiment in order to neglect edge effects. The maximum transverse momentum requirement is applied to set a well defined kinematic range for the generation of the hadronic cocktail and for the pair efficiency correction. Additionally, a pseudorapidity selection of $|\eta| < 0.8$ is applied to reduce potential edge effects of the detector.

In this analysis only primary tracks are considered. Primary tracks, following the

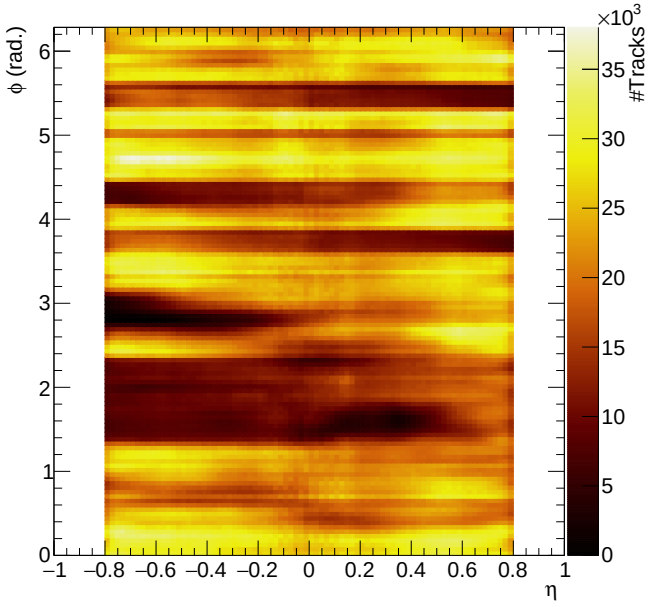

Figure 7.1.: Azimuthal angle φ and pseudorapidity η distribution of single electrons.

definition of ALICE [104], are tracks with a mean proper lifetime of $c\tau < 1\,\mathrm{cm}$ which are either produced directly in the collision or from decays of particles with $c\tau < 1\,\mathrm{cm}$ which originate from the interaction. This includes electrons originating from open charm and open beauty hadrons with decay lengths of $c\tau \approx 150\,\mu\mathrm{m}$ and $c\tau \approx 470\,\mu\mathrm{m}$, respectively. Secondary tracks are, by definition, not produced in the primary vertex and therefore do not point to it. This effect can be exploited to reject these secondary tracks with a selection on the distance of closest approach to the primary vertex in the xy- and z-plane: $|\mathrm{DCA}_{xy}| < 1\,\mathrm{cm}$ and $|\mathrm{DCA}_z| < 3\,\mathrm{cm}$. Secondary electrons from weak decays and from photon conversions in the detector material can thus be reduced. Nevertheless, the selection is rather loose to not reject tracks coming from the open-charm and open-beauty mesons mentioned above.

To accept only tracks with good momentum and spatial resolution, several selections on track properties related to the ITS and the TPC detector are made. Only global tracks with full tracking information of ITS and TPC combined (ITS and TPC refit tracks) are selected. Each track candidate is required to have a sufficient number of TPC clusters $n_{\mathrm{TPC}}^{\mathrm{cluster}}$ and crossed rows $n_{\mathrm{TPC}}^{\mathrm{cr.\ rows}}$. The latter is defined as the number of found clusters per reconstructed track and includes also found clusters on adjacent read-out rows if no cluster was found on the relevant row. This selection is directly related to the length of a track inside the TPC and is therefore strongly correlated to the transverse momentum resolution of this track. An additional selection is made on the ratio of crossed rows over findable clusters $n_{\mathrm{TPC}}^{\mathrm{cr.\ rows}}/n_{\mathrm{TPC}}^{\mathrm{findable}}$ where the latter is defined as the number of potential rows along the trajectory accounting for non-

Selection	Requirement
p_{T}	$0.2 - 8\,\mathrm{GeV/c}$
$\lvert\eta\rvert$	< 0.8
DCA_{xy}	$< 1\,\mathrm{cm}$
DCA_{z}	$< 3\,\mathrm{cm}$
TPC refit	true
ITS refit	true
Reject kink tracks	true
$n_{\mathrm{TPC}}^{\mathrm{cluster}}$	> 80
$n_{\mathrm{TPC}}^{\mathrm{cr.\ rows}}$	> 100
$n_{\mathrm{TPC}}^{\mathrm{cr.\ rows}}/n_{\mathrm{TPC}}^{\mathrm{findable}}$	$0.95 - 1.05$
$\chi^2_{\mathrm{TPC}}/n_{\mathrm{TPC}}^{\mathrm{cluster}}$	< 4
$n_{\mathrm{ITS}}^{\mathrm{cluster}}$	≥ 4
$\chi^2_{\mathrm{ITS}}/n_{\mathrm{ITS}}^{\mathrm{cluster}}$	< 3
Hit in SPD first layer	true
ITS shared cluster map	true

Table 7.1.: Requirements for reference selection.

functioning cluster readout and areas with no active detector material. To assure a high-quality reconstructed track the deviation of the cluster position in relation to the track position is evaluated. This observable $\chi^2_{\mathrm{TPC}}/n_{\mathrm{TPC}}^{\mathrm{cluster}}$ is defined as

$$\chi^2_{\mathrm{TPC}}/n_{\mathrm{TPC}}^{\mathrm{cluster}} = \frac{1}{n_{\mathrm{cluster}}^{\mathrm{TPC}}} \cdot \sum_{i=0}^{n_{\mathrm{cluster}}^{\mathrm{TPC}}} \frac{(xy)_{i,\mathrm{cluster}} - (xy)_{i,\mathrm{track}}}{\sigma^2_{i,xy}} + \frac{(z)_{i,\mathrm{cluster}} - (z)_{i,\mathrm{track}}}{\sigma^2_{i,z}} \quad (7.1)$$

with $n_{\mathrm{cluster}}^{\mathrm{TPC}}$ being the number of measured clusters, $(xy)_{i,\mathrm{cluster}}$ and $(xy)_{i,\mathrm{track}}$ being the position of the cluster or track in the xy-plane and $\sigma^2_{i,xy}$ the position resolution of the cluster, respectively for the z-component. Similar tracking requirements are applied for tracks in the ITS. The minimal number of clusters $n_{\mathrm{ITS}}^{\mathrm{cluster}} > 4$ is required to assure that at least two layers contribute to the particle identification. Similar to $\chi^2_{\mathrm{TPC}}/n_{\mathrm{TPC}}^{\mathrm{cluster}}$, for the ITS the observable $\chi^2_{\mathrm{ITS}}/n_{\mathrm{ITS}}^{\mathrm{cluster}}$ can be calculated. This requirement reduces the contamination coming from electrons from photon conversion. These tracks tend to have a broader $\chi^2_{\mathrm{ITS}}/n_{\mathrm{ITS}}^{\mathrm{cluster}}$ distribution compared to primary electrons.

Particles which decay into neutral particles like $\mathrm{K}^+ \to \pi^+ + \pi_0$ are reconstructed as continuous tracks with a so-called kink. The kink originates from the fact that the neutral decay daughter carries away energy without being measured by the ITS and the TPC which can only measure charged-particle tracks. These tracks get rejected with the help of the so-called kink-finder algorithm which is centrally provided by the collaboration.

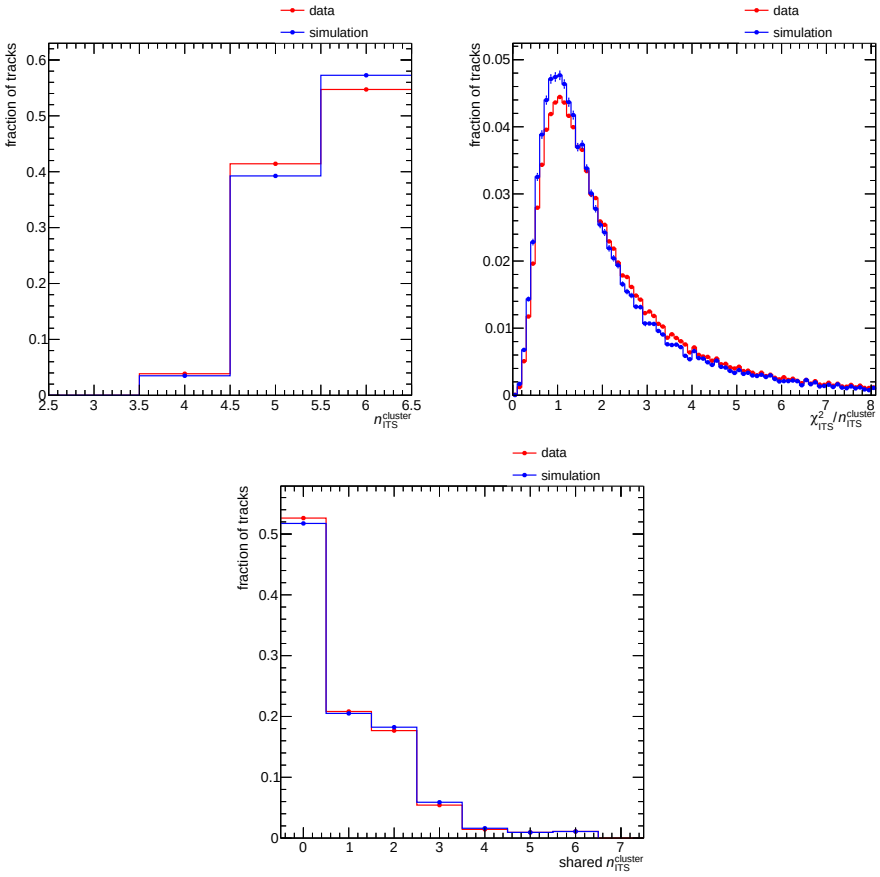

Figure 7.2.: Comparison of ITS tracking quality parameters between data and general purpose simulation LHC16g1a for electron candidates.

Two selections are made to further reduce the amount of electrons from photon conversions inside the detector material. Photons do not have mass and therefore dielectrons from photon conversions have a negligible opening angle. This leads to very close tracks within the ITS. This can be exploited via measuring the number of shared clusters per track in the ITS. More details on these specific selections and on the techniques to reduce the amount of conversion electrons can be found in section 8.2. All track selection criteria are summarized for the reference setting which is used in this analysis in table 7.1. Figure 7.1 shows the azimuthal angle φ and pseudorapidity η distribution of all selected electron candidates. The darker areas where the track density is significantly lower compared to the average result from non-active modules in the several layers of the ITS. Figure 7.2 shows the distribution of observables related to the ITS for data and simulation after all other selections except the selection on the observable which is shown in each plot, respectively. Simulation and data are in relatively good agreement with deviations up to $\approx 10\%$ for the number of clusters in the ITS $n_{\mathrm{ITS}}^{\mathrm{cluster}}$ which also effects the $\chi^2_{\mathrm{ITS}}/n_{\mathrm{ITS}}^{\mathrm{cluster}}$ distribution. Figure 7.3 shows the corresponding plots for the TPC related observables.

The overall agreement between data and simulation is not perfect. However, the relative number of selected tracks per selection criterion is fairly well reproduced in the simulation. The largest deviation of both is about $\approx 3\%$.

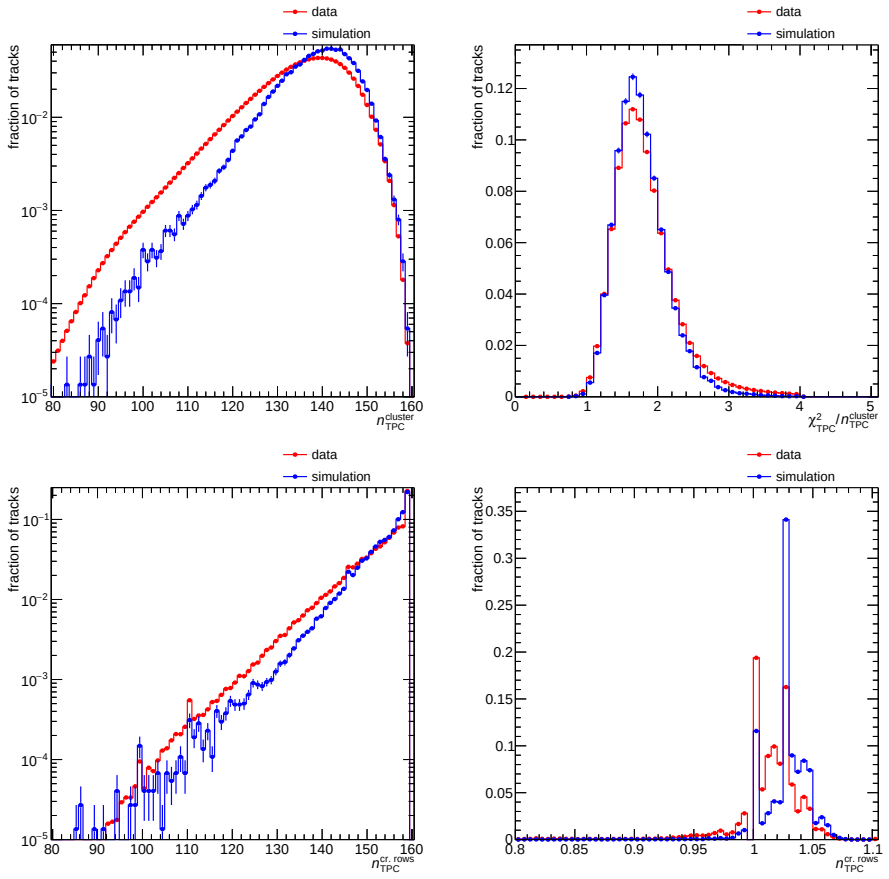

Figure 7.3.: Comparison of TPC tracking quality parameters between data and general purpose simulation LHC16g1a for electron candidates.

7.2. Electron Identification

A crucial step in the dielectron analysis is the identification of electrons, called eID. The selected sample of particles is called electron candidates and is typically contaminated by misidentified hadrons. The eID in this particular analysis uses information of the ITS, TPC and TOF detectors to maximize the number of correctly identified electrons while simultaneously minimizing the number of misidentified particles. The following sections introduce the underlying physics to separate different particle species with the different detectors, the relevant observable $n_{\sigma,\mathrm{p}}^{\mathrm{det}\cdot}$, the recalibration process which is required to get a uniform detector response and the actual selections

which are made to achieve the final electron candidate sample.

7.2.1. Particle Identification in TPC and ITS

Charged particles traversing a medium suffer from energy loss depending on their momentum. Figure 7.4 shows the the energy loss of a muon traversing copper as a function of the muon momentum as an example for the loss mechanisms. For relativistic particles the energy-loss is described by the Bethe-Bloch formula. In a given material and in the range $1 \lesssim \beta\gamma \lesssim 1000$ the energy loss is logarithmic to $\beta\gamma$. Particles with a fixed momentum $p = m\beta\gamma$ but different mass show a distinguishable specific energy loss per path length. These particles can thus be identified by simultaneously measuring their specific energy loss in the TPC or ITS and their momentum. The latter can then be compared to the expected values for a given particle species, like electrons in this analysis. Figure 7.5 shows the specific energy loss as function of the particle rigidity p/z in the TPC (left) with z being the electric charge of the particle, and the specific energy loss as function of the particle momentum p measured in the ITS (right). The solid lines indicate the nominal value per particle species calculated with the Bethe-Bloch formula. Within a large momentum range $0.2 \lesssim p \lesssim 4\,\mathrm{GeV}/c$ the TPC is capable of separating electrons and pions. However in the momentum regions where the kaon and proton bands cross the electron band, information from additional detectors is needed. In these regions a measurement with the ITS can help to reject kaons and protons.

7.2.2. Particle Identification with TOF

As described in section 4.2.4 the TOF correlates the start time of an event with the time-of-flight t_{TOF} of the particle hitting the TOF detector and its reconstructed momentum:

$$\beta = \frac{1}{t_{\mathrm{TOF}} \cdot c} \tag{7.2}$$

$$m = \frac{p}{\beta\gamma} = \frac{p}{c} \cdot \sqrt{\frac{c^2 t_{\mathrm{TOF}}^2}{l^2} - 1} \tag{7.3}$$

with c being the speed of light, p the particle momentum and l the length of the trajectory from the reconstructed primary vertex to the TOF. Due to the deflection of charged particles by the magnetic field only particles with a minimum transverse momentum of $p_{\mathrm{T}} \gtrsim 0.3\,\mathrm{GeV}/c$ can reach the TOF detector. For very small momenta $p \lesssim 0.5\,\mathrm{GeV}/c$ the TOF is able to separate pions and electrons. While kaons can be distinguished from electrons up to $p \lesssim 1.5\,\mathrm{GeV}/c$, protons can be rejected up to $p \lesssim 3.5\,\mathrm{GeV}/c$. The measured TOF β as a function of the particle momentum is

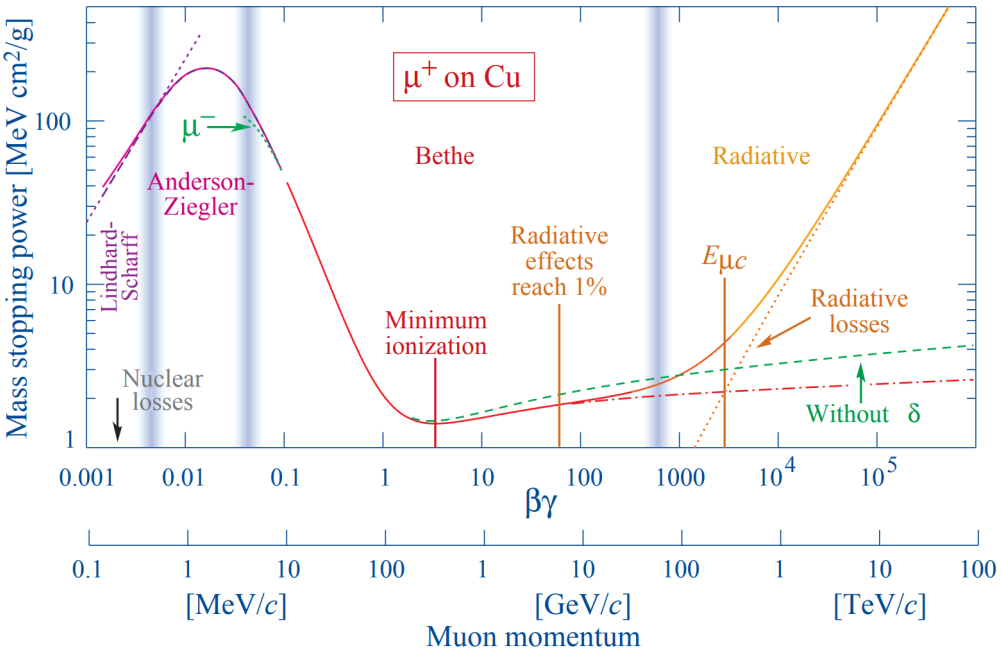

Figure 7.4.: Energy loss of muons traversing copper [105].

shown in figure 7.6.

7.2.3. Calibration

The relevant observables for the electron identification, which are provided centrally within the ALICE analysis framework and which are used in this analysis, are expressed in terms of so-called number of sigmas measured in a detector $\mathrm{n}_{\sigma,\mathrm{p}}^{det.}$:

$$n_{\sigma,\mathrm{p}}^{\mathrm{det.}} = \frac{\mathrm{sig}_{\mathrm{meas.,\ p}}^{\mathrm{det.}} - \mathrm{sig}_{\mathrm{exp.,\ p}}^{\mathrm{det.}}}{\sigma_{e,\mathrm{p}}} \tag{7.4}$$

with $\mathrm{sig}_{\mathrm{meas.,\ p}}^{\mathrm{det.}}$ as the measured detector specific signal, $\mathrm{sig}_{\mathrm{exp.,\ p}}^{\mathrm{det.}}$ as the expected signal and $\sigma_{e,p}$ as the detector resolution in units of the standard deviation, all in respect to a particle species p. This definition leads to a normal distribution around the nominal position of the particle ensuring that i.e. with a $|n_{\sigma,\mathrm{electron}}^{\mathrm{det.}}| < 3$ selection 99.7% of all electrons are selected.

The detector response $\mathrm{n}_{\sigma,\mathrm{e}}^{det.}$ after calibration is expected to be of Gaussian shape with mean $\mu = 0$ and width $\sigma = 1$. This property is especially important for the efficiency correction. Only if the recorded data and the simulated data are equally calibrated a meaningful efficiency correction is possible. The calibration which is centrally provided is already relatively good but it also dependents on the event and track

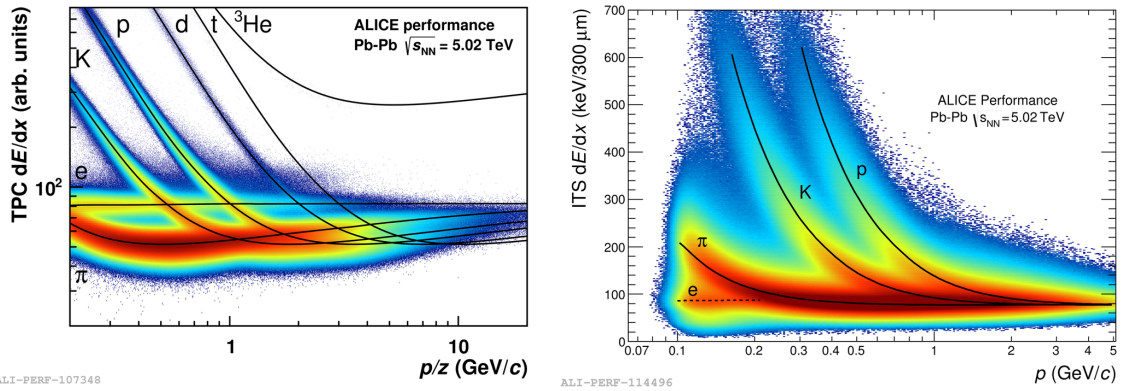

Figure 7.5.: Specific energy loss per unit path length as function of the particle rigidity p/z measured with the ALICE TPC on the left and as function of the particle momentum p in the ALICE ITS on the right. The lines indicate the nominal values per particle species calculated with the Bethe-Bloch formula [106].

selections made in this specific analysis. The calibration with the analysis-specific selections is not perfect as shown later. To assure that data and simulation are correctly calibrated a calibration map is extracted and later used to recalibrate the eID information from the eID detectors. This recalibration is performed in intervals of the pseudorapidity η, the momentum p and the multiplicity measured in the TPC $N_{\mathrm{Trk}}^{\mathrm{TPC}}$.

The recalibration process is performed for the signals measured with the ITS, TPC and TOF both in data and in simulation. Except for the simulated signal of the TPC which is not recalibrated because of the flag *tuneOnData* which can be set in the analysis process to assure a perfect calibration. The procedure is very similar for the different detectors and will be presented for the correction of the TPC signal measured in data. For the recalibration procedure a clean electron sample is required. This clean electron sample is selected by not using the standard selections in this dielectron analysis but using a specific sample of electrons originating from photon conversions $\gamma \to e^+ + e^-$ in the detector material which is excluded in the normal analysis. These conversion electrons can be selected without using any TPC eID information by using so-called V0 topological selections and the information from the TOF detector. This electron selection without the TPC is crucial to be able to use these electrons to recalibrate the TPC signal. Additional track quality selection criteria, similar to those used in the dielectron analysis, are applied to minimize a possible bias between the electrons used in the dielectron analysis and the electrons used in the recalibration procedure. As an example, the non-recalibrated TPC specific energy-loss in units of sigma for electrons $n_{\sigma,\mathrm{ele}}^{\mathrm{TPC}}$ in a given momentum $0.2 < p < 0.3\,\mathrm{GeV}/c$, pseudorapidity $-0.3 < \eta < -0.2$ and multiplicity $500 < N_{\mathrm{Trk}}^{\mathrm{TPC}} < 1000$ interval is shown in figure 7.7. The line indicates a

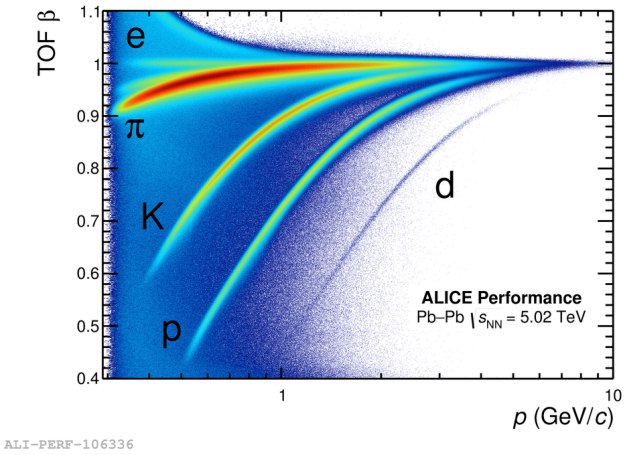

Figure 7.6.: Particle velocity β as function of the particle momentum [107].

Gaussian fit with mean $\mu = -0.44$ and width $\sigma = 0.92$ to the data points. This fit should not be affected by residual contamination and therefore the fit range is limited to $-1.5 < n_{\sigma,\mathrm{ele}}^{\mathrm{TPC}} < 2$. This fitting procedure can be repeated in all momentum, pseudorapidity and multiplicity bins leading to a three-dimensional calibration map. Figure 7.8 illustrates the mean μ (left) and the width σ (right) of the calibration map as function of momentum and pseudorapidity in a multiplicity interval $500 < N_{\mathrm{Trk}}^{\mathrm{TPC}} < 1000$. The bins are chosen in a way that the statistical uncertainty of the Gaussian fit is reasonably small while simultaneously having a fine granularity. Especially for small transverse momenta the mean μ deviates from its nominal value $\mu = 0$ while the distribution of the width σ of the distribution is almost uniform. Not shown is the dependence on the measured multiplicity $N_{\mathrm{Trk}}^{\mathrm{TPC}}$. For larger multiplicities, the width of the distribution gets broader hinting to a loss of TPC clusters as described in [108].

This three-dimensional calibration map can be used as a correction map for the actual electrons used in the dielectron analysis. This correction map is then applied on a track-by-track basis on the measured $n_{\sigma,\mathrm{e}}^{\mathrm{TPC}}$ as a function of the pseudorapidity η, the momentum p and the multiplicity measured in the TPC $N_{\mathrm{Trk}}^{\mathrm{TPC}}$.:

$$n_{\sigma,\mathrm{e}}^{\mathrm{TPC,\ calibrated}}(p_{\mathrm{T}},\eta,N_{\mathrm{Trk}}^{\mathrm{TPC}}) = \frac{n_{\sigma,\mathrm{e}}^{\mathrm{TPC,\ measured}}(p_{\mathrm{T}},\eta,N_{\mathrm{Trk}}^{\mathrm{TPC}}) - \mu^{\mathrm{corr.\ map}}(p_{\mathrm{T}},\eta,N_{\mathrm{Trk}}^{\mathrm{TPC}})}{\sigma^{\mathrm{corr.\ map}}(p_{\mathrm{T}},\eta,N_{\mathrm{Trk}}^{\mathrm{TPC}})} \tag{7.5}$$

with $\mu(p_{\mathrm{T}},\eta,N_{\mathrm{Trk}}^{\mathrm{TPC}})$ and $\sigma(p_{\mathrm{T}},\eta,N_{\mathrm{Trk}}^{\mathrm{TPC}})$ extracted from the respective correction map.

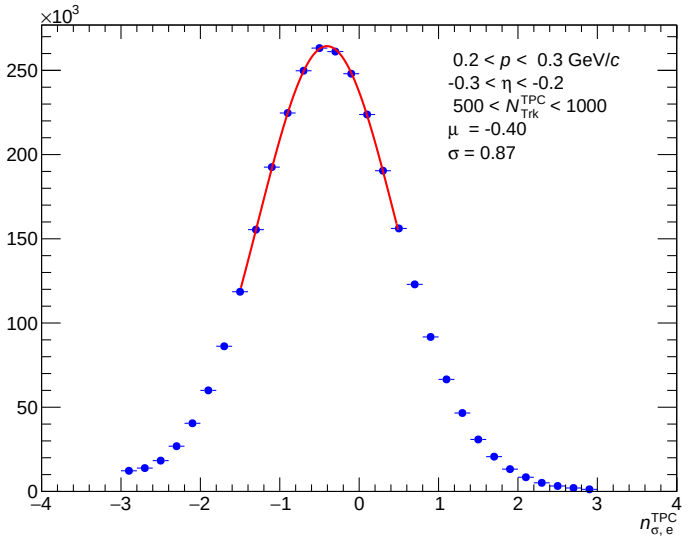

Figure 7.7.: TPC specific energy loss in units of σ, see equation 7.4, in the interval $0.2 < p_{\mathrm{T}} < 0.3\,\mathrm{GeV}/c$, $-0.3 < \eta < -0.2$ and $500 < N_{\mathrm{Trk}}^{\mathrm{TPC}} < 1000$. A Gaussian fit to the data is shown.

7.2.4. Electron selection based identification

This section introduces two different sets of selection criteria summarized into so-called selection schemes. They differ in the explicit usage of the eID information measured with the TOF detector. A third scheme which is used for systematic studies is based on rejecting hadrons explicitely and is introduced in the next chapter.

Both electron selection schemes are based on a simultaneous selection of electrons in ITS, TPC and TOF while rejecting pions in the TPC. The TPC, as can be seen in figure 7.5, is able to separate charged pions and electrons over a large momentum range $0.2 \lesssim p \lesssim 4\,\mathrm{GeV}/c$ which is fully exploited in these schemes. Furthermore, the kaon and proton bands are crossing the electron band in the TPC at different momenta. To reject these hadrons the ITS and the TOF is utilized. The TOF is especially strong in rejecting kaons and protons but exhibits a relatively small efficiency. Additionally, due to the deflection of electrons in the magnetic field, electrons are required to have transverse momenta larger than $p_{\mathrm{T}} > 0.4\,\mathrm{GeV}/c$. Therefore, these two different electron identification schemes are used: *TOFif* and *TOFreq*. Both use the same ITS and TPC selections but the TOF information is used slightly different. The selection interval of electrons is the same for both schemes but for *TOFif* the TOF information is only used when a TOF hit is associated to the track. Compared to *TOFreq* where a signal in the TOF is required for all electron candidates, *TOFif* has a higher efficiency but lower purity. Due to the reduced acceptance of the TOF for low momenta the scheme TOFreq uses the TOF

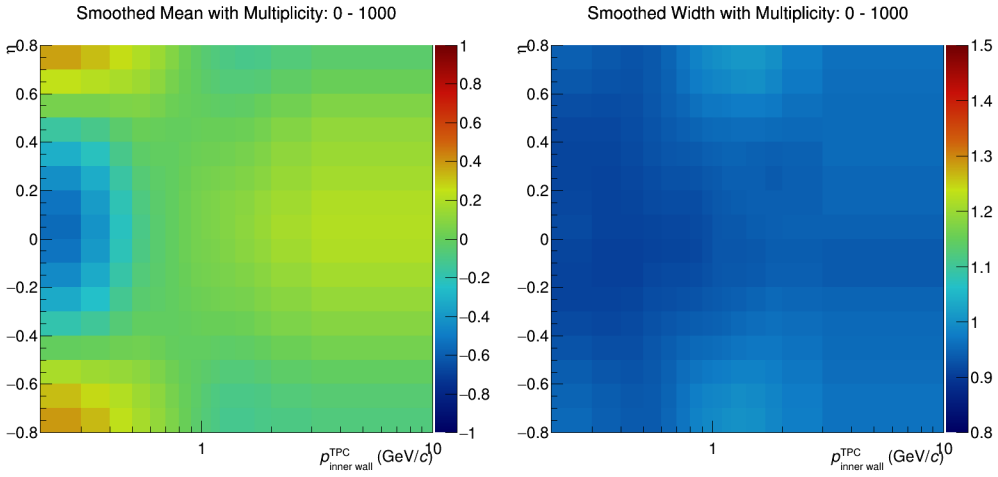

Figure 7.8.: TPC recalibration correction map for the multiplicity interval $0 < N^{\mathrm{TPC}}_{\mathrm{Trk}} < 1000$. The left panel shows the mean and the right panel the width of the Gaussian fit to the data.

Selection	Requirement
$n^{\mathrm{ITS}}_{\sigma_e}$ inclusion	[-3.5, 1.5]
$n^{\mathrm{TPC}}_{\sigma_e}$ inclusion	[-2, 3]
$n^{\mathrm{TPC}}_{\sigma_\pi}$ exclusion	> 4.5
$n^{\mathrm{TOF}}_{\sigma_e}$ inclusion	[-2, 3] if available
$n^{\mathrm{TPC}}_{\sigma_e}$ inclusion	[-2, 3]

Table 7.2.: Electron selection criteria for the reference electron identification which is based on a TOFif scheme.

information only for electron candidates with a transverse momentum larger than $p_{\mathrm{T}} > 0.4\,\mathrm{GeV}/c$.

The reference electron selection is based on a *TOFif* approach while the *TOFreq* scheme is used to investigate systematic effects of the electron selection. The $n^{\mathrm{TPC}}_{\sigma_e}$ distribution is shown in figure 7.9 for electron candidates selected by the reference selection. The specific selection criteria can be found in table 7.2. The residual kaons and protons cross the electron band causing a hadron-contaminated electron sample. Additionally for larger momenta p the pion exclusion rejects tracks with small $n^{\mathrm{TPC}}_{\sigma_e}$.

A high electron purity n_{purity} is essential for the next steps in the analysis especially for the combinatorial pairing, see section 8. Purity is defined as the relative number of all correctly identified electrons over all electron candidates. The higher the electron purity in the selected electron sample without reducing the detection efficiency the smaller the statistical uncertainties on the resulting dielectron spectra. Resid-

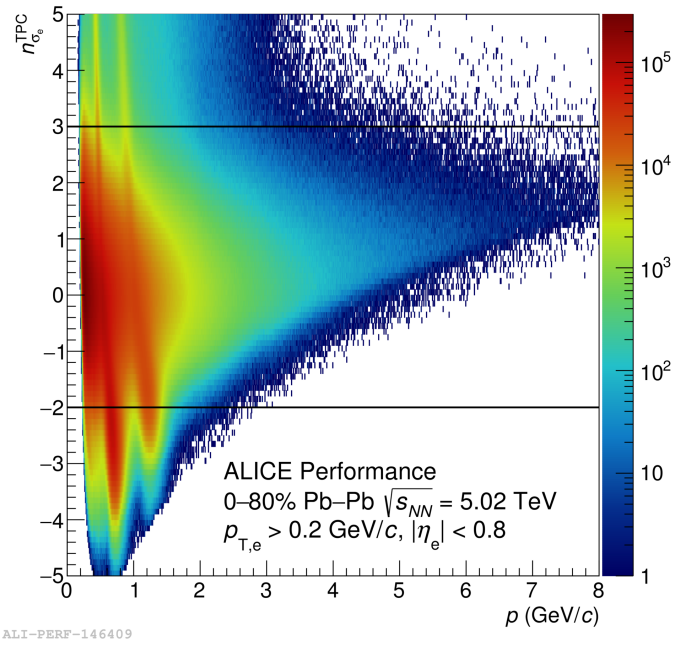

Figure 7.9.: $n_{\sigma_e}^{\mathrm{TPC}}$ as function of momentum p after applying the ITS and TOFif electron selection requirements of the reference selection. The horizontal lines indicate the selection which is applied to the tracks.

ual hadronic contamination can lead to correlated hadronic yield in the dielectron spectrum which can not be subtracted with the used like-sign method. Therefore, this contamination increases the systematic uncertainty of the measurement.

The purity is estimated with two slightly different methods depending on the momentum of the electron. The first method is used for relatively small momenta $0.2 < p < 1.5\,\mathrm{GeV}/c$ where the pion contribution is well separated from the electrons. The second method is used for higher electron momenta. To estimate the purity at small momenta as a function of the electron momentum p, the $n_{\sigma_e}^{\mathrm{TPC}}$ distribution is extracted in momentum intervals of $\Delta p = 50\,\mathrm{MeV}/c$ without applying the TPC electron inclusion requirement to be also able to analyse the tails of the distribution. The resulting $n_{\sigma_e}^{\mathrm{TPC}}$ distributions are fitted with a three component function consisting of a sum of three templates, one for electrons, one for kaons and one for protons. All three templates are parametrized with a skewed Gaussian distribution with four parameters: absolute normalization N, mean μ, width σ and skewness ξ. To constrain the fitting process, start parameters of these templates are extracted from pure samples of each particle species. The electron templates are derived from electrons from photon conversion selected with topological requirements as described in section 7.2.3. The kaon and proton templates are constructed with the same track requirements as described in table 7.1 with an additional strict selection in the TOF to increase the purity of the respective sample. The track selection

is required to ensure that the shapes of the extracted particle templates are similar to the parametrized $n_{\sigma,\mathrm{e}}^{\mathrm{TPC}}$ distribution. For the final fit the parameters μ, σ and ξ are constrained to vary within $\pm 10\%$ around their starting value while the absolute normalization N is not constrained. In the left panel of figure 7.10 the $n_{\sigma,\mathrm{e}}^{\mathrm{TPC}}$ distribution in the momentum interval $0.65 < p < 0.7\,\mathrm{MeV}/c$ is shown together with the resulting parametrization including the templates for electrons (blue), kaons (red) and protons (green). In this momentum range the relative proton contribution is negligible. The black vertical lines correspond to the $n_{\sigma,\mathrm{e}}^{\mathrm{TPC}}$ selection for the analysis electron candidates. The yield per particle species n_{particle} can be calculated by integrating between these vertical lines for all 3 components individually. The purity in every momentum interval can then be estimated with:

$$n_{\mathrm{purity}} = \frac{n_{\mathrm{electrons}}}{n_{\mathrm{electrons}} + n_{\mathrm{kaons}} + n_{\mathrm{protons}}} \tag{7.6}$$

The purity for higher momenta $p > 1.5\,\mathrm{GeV}/c$ is affected only by contamination with charged pions. It is extracted with a fit of two skewed Gaussian distributions to the $n_{\sigma,\pi}^{\mathrm{TPC}}$ distribution without applying the TPC pion rejection requirement. Because of decreasing statistics, larger momentum intervals of $\Delta p = 0.25\,\mathrm{GeV}/c$ are chosen and the upper limit of the purity estimation is set to $p = 3\,\mathrm{GeV}/c$. In the right panel in figure 7.10 the $n_{\sigma,\pi}^{\mathrm{TPC}}$ distribution is shown in the momentum interval of $1.75 < p < 2\,\mathrm{GeV}/c$ with fitted templates of electrons (blue) and pions (red). The mean value of the pion distribution is not located at $\mu = 0$ because of the electron inclusion selection in the TPC. The poor accordance of the fit to the data around $n_{\sigma_\pi}^{\mathrm{TPC}} \approx 0.5$ originates from proton contamination and is not affecting the purity of the electron sample. The vertical line indicates the upper limit of the pion rejection. Similar as in the method for small momenta the templates are integrated within the selected region $n_{\sigma_\pi}^{\mathrm{TPC}} > 4$:

$$n_{\mathrm{purity}} = \frac{n_{\mathrm{electrons}}}{n_{\mathrm{electrons}} + n_{\mathrm{pions}}} \tag{7.7}$$

The extracted purity n_{purity} as function of the measured particle momentum is shown in figure 7.11. The momentum regions where kaons and protons are not separable from electrons in the TPC show smaller purity. Not shown is the purity estimation for the *TOFreq* scenario which results in a higher purity of almost 100%. This high level of purity would ensure that no unwanted residual electron-hadron correlation contaminated the dielectron spectrum. However, the strict selections which are required to achieve these levels of purity reduce the number of electrons in the sample. This leads to a higher statistical uncertainty in the resulting dielectron spectrum. The effect of the purity on the resulting spectrum is further discussed in 10.1.

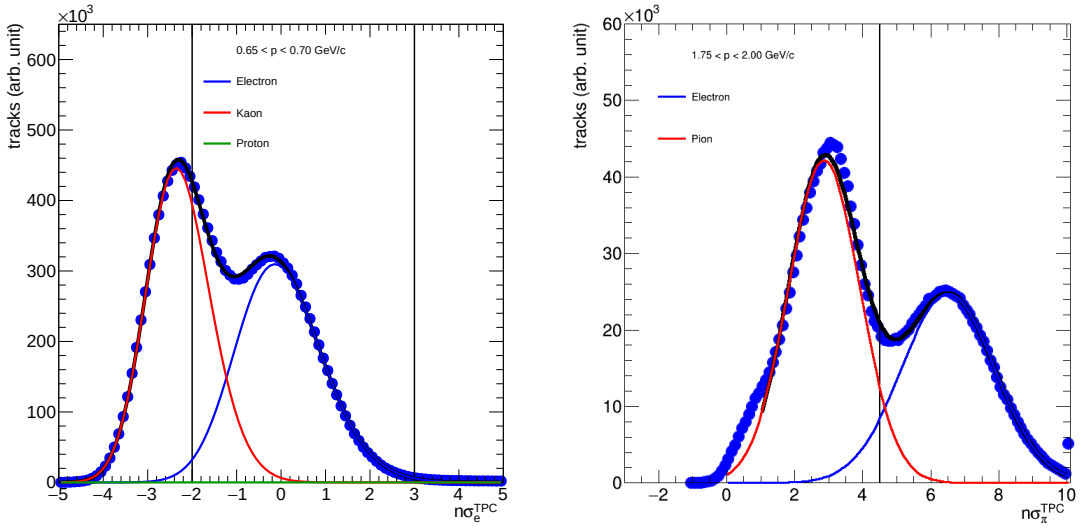

Figure 7.10.: $n_{\sigma,\mathrm{e}}^{\mathrm{TPC}}$ distribution in the interval $0.65 < p < 0.7\,\mathrm{MeV}/c$ (left) and $n_{\sigma,\pi}^{\mathrm{TPC}}$ distribution in the interval $1.75 < p < 2\,\mathrm{GeV}/c$ (right). Colored lines indicate the fitted templates for electrons, kaons, protons and pions. Vertical lines in the left panel indicate the final selection criteria. Vertical line in the right panel shows the lower limit of the selection.

7.2.5. Hadron rejection based identification

The electron identification schemes presented in section 7.2.4 is based on subsequently checking the detector response of TPC and TOF. This process can lead to rejection of electrons which were clearly identified in one detector but happen to be ambiguous in another detector. Therefore, a third way of electron identification is analyzed as a systematic cross check to the two previously introduced schemes. This third electron selection scheme is based on the rejection of pions, kaons and protons with the TPC [81]. Additionally to this sample of electrons, clearly identified with the TPC, another sample of electron candidates, which are clearly identified with the TOF information, is selected. Both samples are combined via a logical OR to take care of potential double counting of electron candidates. The selection criteria for a specific set of selection according to this hadron-rejection scheme are summarized in table 7.3. The selection excludes pions, kaons and protons with the TPC and includes electrons identified with the TOF detector. The $n_{\sigma,\mathrm{e}}^{\mathrm{TPC}}$ distribution is shown in figure 7.12 for electron candidates selected with the TPC only (TPC sample), the TPC and TOF sample (TOF sample) and the final selection criteria (logical OR between the two). The missing hadron bands are clearly visible in the TPC sample. Furthermore, the selection of electrons with the TOF shows residual contamination of kaons and protons. The quantification of the purity as performed in section 7.2.4 is complex and difficult. The method used earlier, which is based on fitting the Gaussian distributions of $n_{\sigma_e}^{\mathrm{TPC}}$, is not applicable because the electron distribution

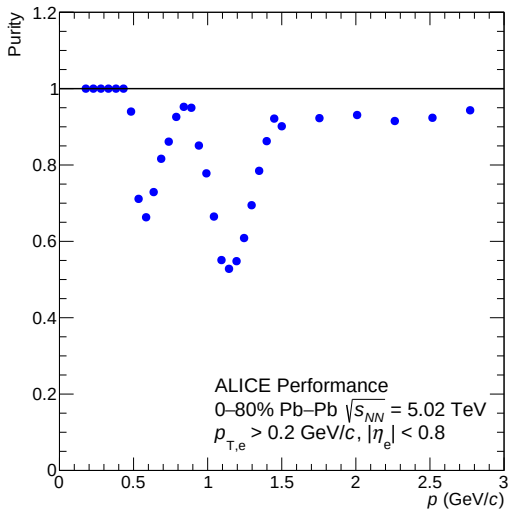

Figure 7.11.: Purity as a function of momentum p for the reference electron identification based on an *TOFif* scheme.

in the vicinity of the rejected hadron bands is no longer Gaussian. The purity is nevertheless expected to be higher than the one in the *TOFif* scheme. However, this electron selection requires a very careful evaluation of the matching of the relevant eID information in data and simulation because of the complex band structure of the hadron bands within the TPC. This electron identification scheme was used in the latest dielectron analysis in proton-proton collisions at a center-of-mass energy $\sqrt{s} = 13\,\text{TeV}$ [77].

7.2.6. TOF Matching Efficiency

All three general electron identification schemes TOFif, TOFreq and HadrRej rely on the performance of the Time-of-Flight detector. A crucial part of its performance is the so-called track matching between tracks measured in the inner detectors ITS and TPC and so-called associated hits in the TOF. A mismatch could lead to a decrease of the efficiency and/or purity of the electron sample. Most of the charged particles produced in a heavy-ion collision are either pions, kaons or protons and only a small fractions are electrons. If an electron track gets wrongly assigned to a hit triggered by an e.g. kaon, the electron track is misidentified by the TOF as a kaon. Since the electron identification selection is tuned to reject kaons and protons, the misidentified electron track is discarded by the TOF, leading to a smaller detection efficiency of electrons. Another type of mismatch is the mismatch of a pion cluster to a e.g. kaon track. Due to the low mass of a charged pion $m_{\pi^\pm} \approx 0.14\,\text{GeV}/c^2$ and therefore similar times-of-flight at a given particle momentum compared to electrons, the TOF can not separate electrons from charged pions for small momenta

	Selection	Requirement
TPC sample	$n_{\sigma_e}^{\mathrm{TPC}}$ inclusion	[-3, 3]
	$n_{\sigma,\pi}^{\mathrm{TPC}}$ exclusion	> 4.5
	$n_{\sigma,\mathrm{K}}^{\mathrm{TPC}}$ exclusion	[-3, 3]
	$n_{\sigma,\mathrm{p}}^{\mathrm{TPC}}$ exclusion	[-3, 3]
TOF sample	$n_{\sigma_e}^{\mathrm{TOF}}$ inclusion	[-3, 3]
	$n_{\sigma_\pi}^{\mathrm{TPC}}$ exclusion	> 4.5

Table 7.3.: Electron selection criteria for the hadron-rejection based electron identification. Both samples are added together for the resulting sample of electron candidates.

$p < 0.5\,\mathrm{GeV}/c$, see figure 7.6 for comparison. If neither ITS nor TPC reject the kaon, this kaon track could be matched in the TOF with a hit which was triggered by a pion. The "slow" kaon is associated with a "fast" pion, which itself is not separable from an electron in the TOF, and therefore is not rejected by the TOF. This effect would lead to a contamination of the electron sample. The first effect influences the single electron efficiency and can be corrected with the help of simulations. A detailed discussion of the efficiency correction can be found in section 9. To achieve a reliable efficiency correction the mismatch probability in measured data and in the according simulation have to be in agreement.

To extract the TOF matching efficiency a so-called clean electron sample is required, similar to the clean sample consisting of V0 electrons obtained in section 7.2.3. The transverse momentum p_{T} of these electrons is then compared to the p_{T} distribution of electrons with the additional requirement that the track should have triggered a hit in the TOF. The same procedure is repeated in the general purpose Monte-Carlo simulation LHC16g1. Here, the complete information of the simulation can be used to identify electrons and to ensure that the electron sample is pure. The upper panels in the upper plots in figure 7.13 show the respective p_{T} distributions for electrons without (red) and with (blue) associated TOF hit for data (left) and simulation (right). The respective ratios in the lower panels show the extracted TOF matching efficiency. Due to the curvature of charged tracks caused by the magnetic field of the detector, tracks are required to have a transverse momentum larger than $p_{\mathrm{T}} > 0.4\,\mathrm{GeV}/c$ to reach the TOF which limits the comparison for low-p_{T} particles. At high transverse momentum the distribution is limited by vanishing statistics for V0 electrons in data. Overall the matching efficiency increases as function of p_{T}. Tracks with larger transverse momentum p_{T} are less bend and therefore traverse less material. The lower plot shows the ratio of both extracted TOF matching

efficiencies. The largest deviation of $\approx 5\%$ is located at a transverse momentum $p_{\mathrm{T}} \approx 0.7\,\mathrm{GeV}/c$. Therefore, the TOF is reasonably well described in the simulation. The residual deviation will be reflected in the pair efficiency correction and therefore also in the systematic uncertainty of the resulting dielectron spectrum, see section 10 for a detailed discussion of the systematic uncertainty.

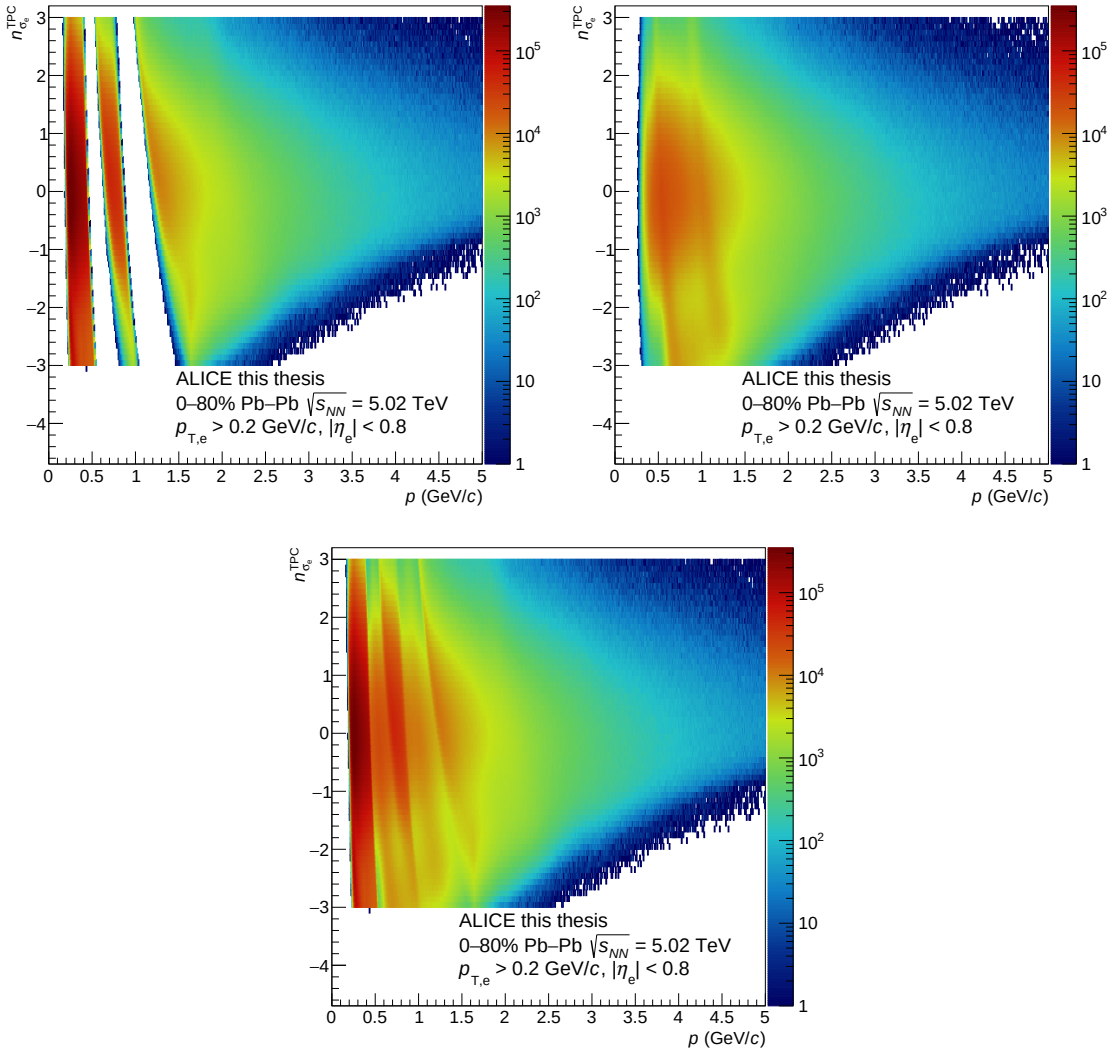

Figure 7.12.: TPC (upper left) and TOF (upper right) sample of hadron-rejection based electron identification. The electron selection is shown in the lower panel.

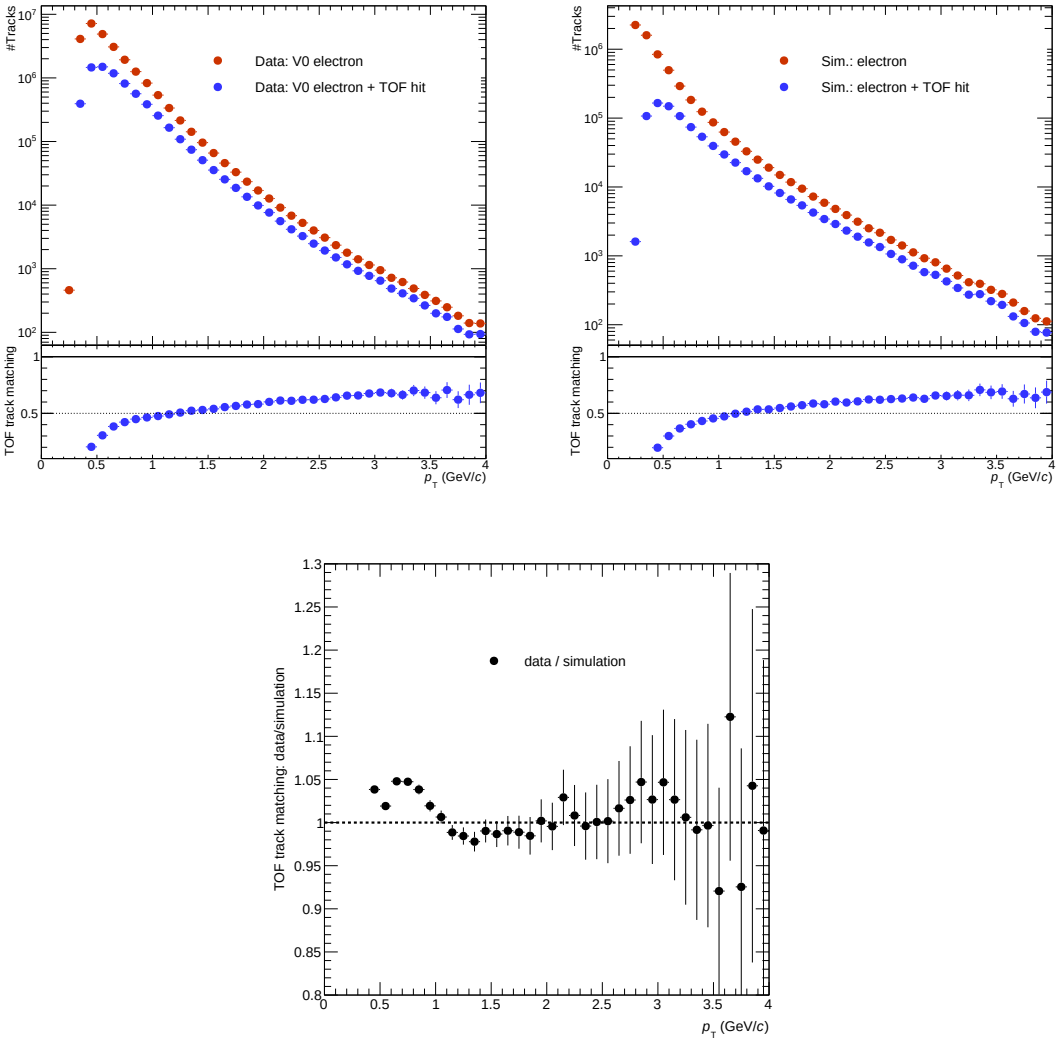

Figure 7.13.: The upper plots show the distributions of clean electron samples without (blue) and with (red) associated hit in the TOF as function of the transverse momentum p_T for data (left) and simulation (right). The lower panels show the ratio of both distributions and corresponds to the TOF matching efficiency. The lower panel shows the ratio of both TOF matching efficiency distributions.

8. Pair Analysis

The dielectron distribution as a function of the invariant mass m_{ee} and the pair transverse momentum $p_{\mathrm{T,ee}}$ consists of pairs of correlated electrons and positrons originating from a decay of a particle, from correlated heavy-flavour hadron decays or other sources as described in more detail in section 2. The information of the origin of each electron and positron is not accessible experimentally. For this reason, it is not possible to clearly assign an electron to its correlated positron. A statistical method based on the so-called unlike-sign, *ULS*, and like-sign, *LS*, spectra is used to separate the dielectron signal S from combinatorial dielectron pairs while taking simultaneously into account correlated background sources. In order to overcome detector acceptance effects the like-sign spectrum is corrected with the so-called R-factor:

$$S = ULS - LS \cdot R \tag{8.1}$$

The following sections introduce the procedure to obtain the required ingredients ULS, LS and R to extract the dielectron signal S.

8.1. Signal Extraction

The ULS spectrum is extracted by combining all electron candidates with all positron candidates selected within one event after applying the selection criteria, see section 7.1 for more details on the track selection and electron identification. This procedure ensures that all correlated dielectron pairs are taken into account. However, with this method also unwanted correlated and uncorrelated background pairs are included. Correlated background can consist of electron-hadron pairs where one electron is paired with a correlated and misidentified hadron. Other sources of correlated background are discussed in more detail in section 8.1.1. Uncorrelated background consists of random, combinatorial pairs of electrons and positrons which are not correlated. The LS spectrum is used to estimate the non-physical combinatorial pairs and the correlated background pairs. It is built from a combination of two spectra as function of the invariant mass m_{ee} and the pair transverse momenta $p_{\mathrm{T,ee}}$ from pairs of electrons with electrons (N_{--}) and from pairs of positrons with positrons (N_{++}) which are created in the same event. Both spectra (N_{++} and N_{--}) suffer from small statistics in a given invariant mass and pair transverse momentum

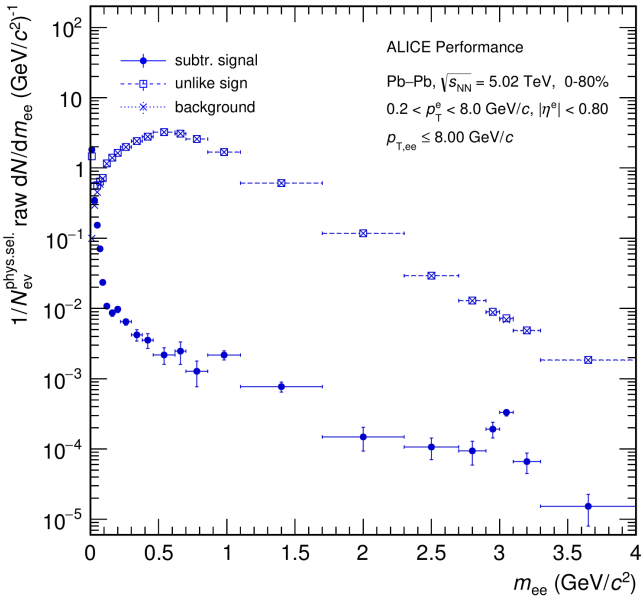

Figure 8.1.: ULS LS S.

range. Additionally the detector has a slightly different efficiency for positrons in comparison to electrons. To minimize the bias introduced by these two effects the so-called hybrid method is used to combine both spectra to the LS spectrum. The hybrid method is a combination of the arithmetic and the geometric mean:

$$LS = \begin{cases} 2 \cdot \sqrt{N_{++} \cdot N_{--}}, & N_{++} \neq 0 \wedge N_{--} \neq 0 \\ \frac{N_{++}+N_{--}}{2}, & \text{else} \end{cases} \tag{8.2}$$

The geometric mean is used to combine both spectra if both, N_{++} and N_{--}, have non-zero content in the given mass and pair transverse momentum interval. If the content would be zero the resulting like-sign spectrum would also be zero. Using only the geometric mean would therefore underestimate the background. The advantage of the geometric mean is, that it is more robust to charge-asymmetries as shown in [68]. The arithmetic mean is used to cope with the effect of underestimation, since it does not result in zero if only one of both spectra evaluates to zero.

Figure 8.1 shows the invariant-mass m_{ee} distribution of the subtracted signal, the unlike-sign and the background for 0-80% most central Pb-Pb collisions integrated over the pair transverse momentum $p_{\mathrm{T,ee}}$. The strong rise at small invariant masses due to the Dalitz decays of the light-flavour mesons and the contribution from the J/ψ meson at $m_{\mathrm{ee}} \approx 3\,\mathrm{GeV}/c^2$ are clearly visible. A detailed discussion of the signal in relation to the background can be found in section 8.3.

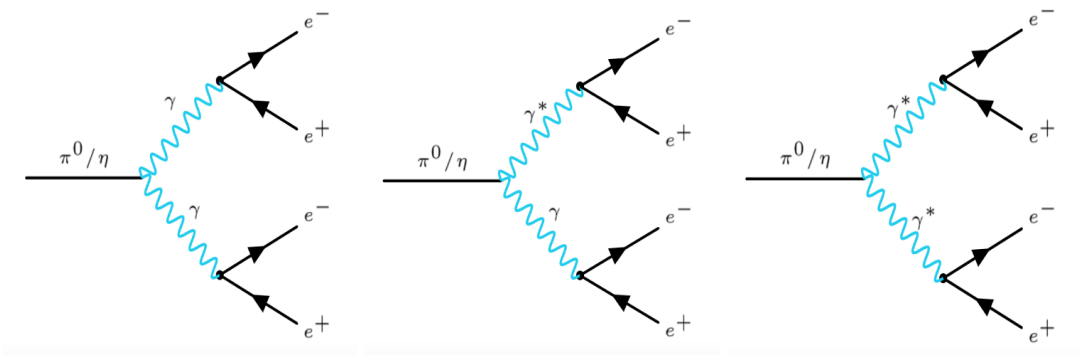

Figure 8.2.: Processes that generate cross pairs from a neutral meson decay: double photon conversion (left), Dalitz decay & photon conversion (middle) and double Dalitz decay (right).

8.1.1. Correlated Background

The ULS spectrum includes correlated pairs which are considered as background in this analysis. One source of this background stems from correlated dielectrons from mesons originating from the same jet or from back-to-back jets. Another source of these correlated background pairs are so-called cross pairs. In this process the electron (positron) coming from one (virtual) photon is correlated with the positron (electron) from the other (virtual) photon via their common neutral meson m^0 ancestor. Three slightly different types of cross-pairs are shown in figure 8.2 and can be described as:

- Double conversions where a neutral meson decays into two photons which themselves convert into dielectrons inside the detector material: $m^0 \rightarrow \gamma\gamma \rightarrow e^+e^-e^+e^-$
- Dalitz decay of a neutral meson together with a conversion of the photon
- Double Dalitz decay of a neutral meson directly into a 4-lepton state

The invariant mass of such correlated background pairs is limited by the mass of the neutral meson. Most of these mesons are π^0, resulting in a contribution to the dielectron spectrum only at low mass.

All of the above mentioned processes, including the correlation via jets, are charge-symmetric, meaning that their contribution to the ULS and LS spectra are expected to be identical [44]. This allows the usage of the LS spectrum to subtract these correlated contributions from the ULS distribution. Correlated contributions from misidentified hadrons are included in the systematic uncertainty of the resulting spectrum, see 10.1 for a detailed explanation.

z-vertex	centrality	event plane
-10, -5, 0, 5, 10	0, 5, 10, 20, 30, 50, 80	$-\pi/2$, $-\pi/4$, 0, $\pi/4$, $\pi/2$

Table 8.1.: Mixing classes for the R-factor calculation.

8.1.2. R-Factor

Unlike- and like-sign pairs have a slightly different acceptance in the detector. In contrast to unlike-sign pairs, like-sign pairs are deflected by the magnetic field in a similar direction due to their common electric charge. Therefore dielectrons with the same charge are more likely to fly into the same inactive detector regions compared to unlike-sign pairs. Since this effect is purely acceptance-related, it can be estimated with a mixed-event technique. The technique combines particles from different events to ensure that there is no correlation between these two and therefore this method is able to purely reproduce acceptance effects. The quantity describing this acceptance correction factor is called R-factor and is defined as

$$R = \frac{M^{+-}}{2 \cdot \sqrt{M^{++} \cdot M^{--}}} \tag{8.3}$$

with M^{+-}, M^{++} and M^{--} being the unlike- and like-sign spectra extracted from the mixed-event technique. Only events with similar z-vertex position, centrality and event-plane orientation are mixed to ensure uniform performance of the detector. As an example, events with high multiplicity typically include particles with higher average momenta compared to events with smaller multiplicities and therefore have a different invariant mass and pair transverse momentum distribution. These properties are categorized in mixing classes. The intervals of the centrality, event plane angle and reconstructed z-vertex position that define the mixing classes are summarized in table 8.1.

The R-factor correction is applied as a function of the invariant mass m_{ee} and the pair transverse momentum $p_{\mathrm{T,ee}}$. The R-factor for the reference selection criteria is shown in figure 8.3 as function of m_{ee} in several $p_{\mathrm{T,ee}}$ intervals. The distribution deviates only at small invariant mass significantly from unity, indicating that only pairs with small opening angle are affected by this acceptance effect. Additionally, the correction factor deviates more from unity with increasing pair transverse momentum which can also be lead back to the smaller opening angle at higher pair momenta.

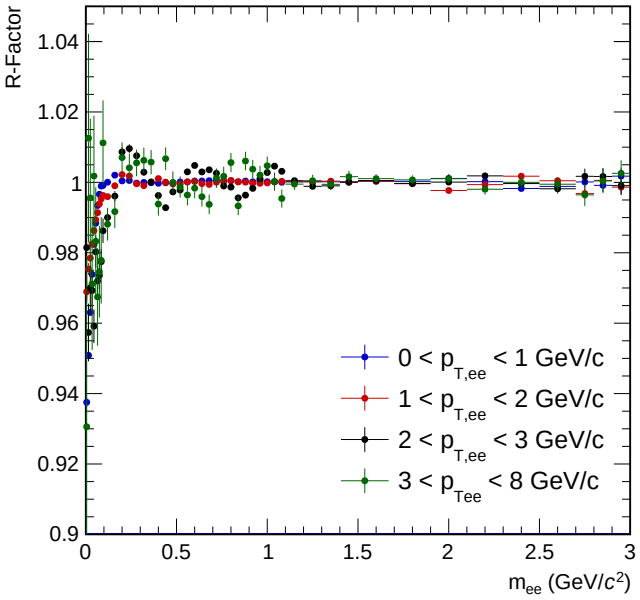

Figure 8.3.: R-factor as a function of the invariant mass m_{ee} in several intervals of pair transverse momentum $p_{\mathrm{T,ee}}$ for the reference selection scheme.

8.2. Photon Conversion Rejection

Electrons and positrons from real photon conversions are the major contribution to the dielectron combinatorial background [44, 109]. Reducing this background is a crucial part of this analysis and can be done via single track selections and pair selections. Using single track criteria has the advantage of rejecting background electrons and positrons before the pairing step and thereby effectively reducing the amount of combinatorial pairs and consequentially enhancing the significance of the measurement. The combinatorial background in this analysis is approximately proportional to the number of selected charged particles squared N_{ch}^2 while the signal increases only linearly which motivates a careful rejection of all possible background tracks.

Most of the real photon conversions happen in the beam pipe and in the six layers of the ITS. To reject electrons from so-called late conversions in outer parts of the detector, tracks are required to have an associated cluster in the innermost layer of the ITS SPD, see figure 8.4. This selection provides the advantage that only one of the two leptons ($\gamma \rightarrow e^+e^-$) has to be within the detector acceptance. However, compared to proton-proton collisions, the particle multiplicity and therefore particle density in the ITS is significantly larger in Pb-Pb collisions. This behaviour can lead to reconstructed tracks with incorrectly associated clusters in the first ITS layers and therefore smaller background rejection power for late conversions. This *fake*

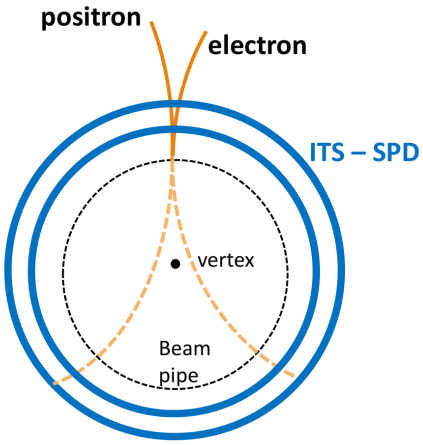

Figure 8.4.: Sketch of a dielectron pair coming from a real photon conversion. Tracks are required to have a cluster in the first ITS layer. Additionally, positron and electron are close to each other, sharing a cluster in the innermost layer of the ITS.

matching is suppressed with requiring a minimum of 4 ITS clusters per track and $\chi^2/n_{\text{cluster}}^{\text{ITS}} < 3$.

Real photons do not have an intrinsic rest mass. Therefore electrons and positrons coming from photon conversions inside the detector material show no opening angle at their production vertex. This property leads to so-called *close pairs* and produces shared detector clusters inside the ITS. The left panel of figure 8.5 shows the number of shared clusters within the ITS for electrons from signal, i.e. light- and heavy-flavour primary hadron decays (red) and conversion (blue) pairs extracted from simulated Pb-Pb collisions of the general purpose simulation LHC16g1. While the signal peaks at zero shared clusters the distribution for conversion pairs is broader and peaks at two shared clusters. The requirement of having exactly zero shared ITS clusters rejects most of the electrons from conversions while keeping most of the signal pairs.

However, a better separation power can be obtained by monitoring the position of the ITS layer where a shared cluster occurs. The right panel in figure 8.5 shows the shared cluster position with one being the innermost and six being the outermost layer of the ITS for electrons having exactly one ITS shared cluster associated to the reconstructed track. If a track has one shared cluster in the first ITS layer it has a high probability of being a track belonging to a signal pair. Requiring all tracks to have zero shared clusters would reject all those tracks. Therefore, the following single track requirement is introduced: tracks with no shared cluster in the ITS or one single ITS shared cluster found in the innermost layer of the ITS SPD are kept in the analysis. After applying this selection criteria, signal electrons originating from light meson decays are still rejected by mistake due to their small opening angle. The

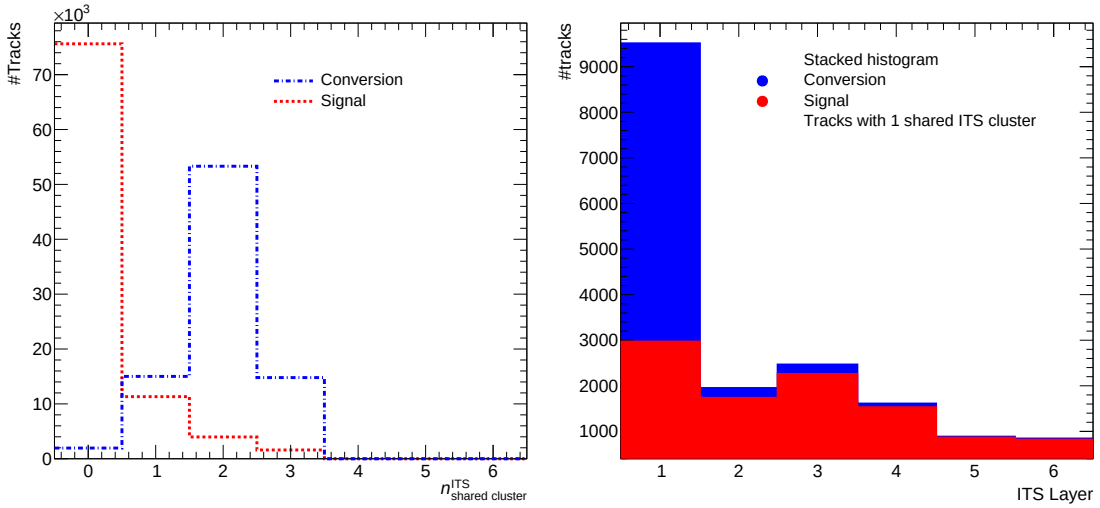

Figure 8.5.: (left) Distribution of electrons coming from signal pairs (red) and from photon conversion pairs (blue) passing all other track requirements as a function of the number of shared cluster per track in simulated Pb-Pb collisions. Most of the signal tracks share zero ITS cluster while electrons coming from conversions tend to have a larger number of shared cluster. (Right) Shared cluster position of tracks with exactly one measured shared ITS cluster with one being the innermost and six being the outermost ITS layer.

effects on the number of signal pairs and real photon conversion pairs of the different selection criteria, on single tracks are summarized in table 8.2. With the application of both requirements, a hit in the first ITS layer and the given configuration for ITS shared clusters, conversion pairs can be significantly reduced to about 1.4 % of all conversion pairs passing the other selection criteria while only losing about 40 % of all signal pairs. Despite a large fraction of rejected signal electrons, these selections increase the signal to background ratio by a factor of about 2 while simultaneously improving the significance by a factor of about $\sqrt{2}$ implying that mostly background was removed.

The remaining dielectron pairs from photon conversions can be estimated via their relative orientation to the magnetic field ϕ_V. Electrons from photon conversion originate from a displaced, secondary vertex. The extrapolation of displaced conversion electron tracks to the collision point results nevertheless in a non-vanishing opening angle, caused by the deflection of the tracks in the magnetic field. This leads to a small but finite reconstructed invariant mass of the photon conversion. The further the dielectron pairs originate from the primary vertex, the higher is the reconstructed invariant mass. This artificial opening angle of the electron-positron pair is only determined by the magnetic field and preferentially in the plane perpen-

Conversion rejection selections	Signal pairs	Conversion pairs
No selection	100 %	100 %
SPD first layer	$\approx 77\,\%$	$\approx 41\,\%$
Shared ITS cluster	$\approx 80\,\%$	$\approx 20\,\%$
Both	$\approx 60\,\%$	$\approx 1.4\,\%$

Table 8.2.: Effect of single track selection on pairs from signal and real photon conversions pairs. The numbers indicate how many pairs remain after applying the respective selection criterion.

dicular to the magnetic field direction which can be used to filter such conversion pairs. The observable ϕ_{V} describes the angle between the normal vector of the opening angle plane of the pair with the magnetic field direction which is along the z-axis of the experiment:

$$\begin{aligned}
\vec{u} &= \frac{\vec{p_1} + \vec{p_2}}{|\vec{p_1} + \vec{p_2}|} \\
\vec{v} &= \frac{\vec{p_1} \times \vec{p_2}}{|\vec{p_1} + \vec{p_2}|} \\
\vec{w} &= \vec{u} \times \vec{v} \\
\vec{u_a} &= \frac{\vec{u} \times \vec{z}}{|\vec{u} \times \vec{z}|} \\
\phi_{\mathrm{V}} &= \arccos\left(\frac{\vec{w} \cdot \vec{u_a}}{|\vec{w}| \cdot |\vec{u_a}|}\right)
\end{aligned}$$

with $\vec{p_1}$ being the 3-momentum vector of the electron and $\vec{p_2}$ being the 3-momentum vector of the positron. The ϕ_{V} distribution for dielectron pairs from photon conversions is expected to peak around $\phi_{\mathrm{V}} = \pi$ while the distribution for signal dielectrons is uniform. Therefore, remaining contribution from conversions can be disentangled from signal pairs by a peak at high ϕ_{V} sticking out a flat signal distribution. Figure 8.6 shows the ϕ_{V} distribution for dielectron pairs coming from hadronic decays (red) and from photon conversions (blue) in the general purpose simulation LHC16g1 in the 0-80% most central events. The left plot shows the distributions without a selection on ITS shared cluster. As expected, the contribution from photon conversions is located dominantly at large $\phi_{\mathrm{V}} > 2$. Applying a selection on ITS shared cluster suppresses this contribution significantly by a factor ≈ 1.5. The standard approach [44] to suppress residual photon conversion pairs consists of rejecting dielectron pairs with $\phi_{\mathrm{V}} > 2$ and then correcting the spectrum with a flat interpolation according to the average of the remaining pairs. Due to the introduction of the selection on tracks with shared ITS cluster the ϕ_{V} distribution of signal pairs is not uniform in the complete phase space and therefore the correction is not viable anymore. This

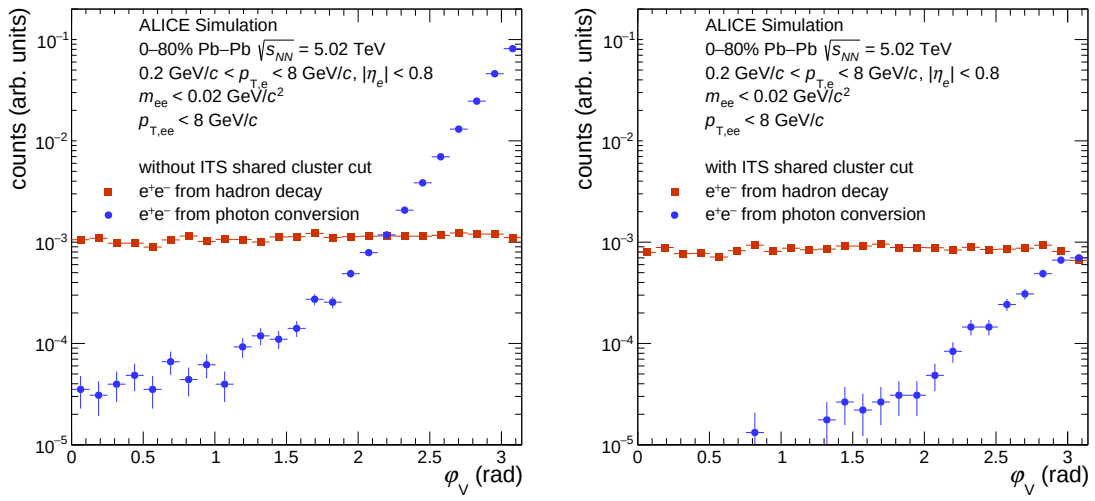

Figure 8.6.: ϕ_{V} distributions for dielectron pairs coming from hadronic decays (red) and from photon conversions (blue) in the general purpose simulation LHC16g1 in the 0-80% most central events. Left side without applying the selection on ITS shared cluster, right with this selection in place.

lead to the development of a new technique to correct the spectrum which was implemented in the Frankfurt dielectron group [81, 110]. This new approach, which is used in this analysis, consists of correcting the residual conversion dielectrons with a template fit procedure. ϕ_{V} templates for the dielectron signal S and for conversion dielectrons B as a function of the invariant mass and the pair transverse momentum are extracted from simulations. The weighted sum

$$f^{m_{\mathrm{ee}},p_{\mathrm{T,ee}}}(\phi_{\mathrm{V}}) = a_1^{m_{\mathrm{ee}},p_{\mathrm{T,ee}}} \cdot S^{m_{\mathrm{ee}},p_{\mathrm{T,ee}}}(\phi_{\mathrm{V}}) + a_2^{m_{\mathrm{ee}},p_{\mathrm{T,ee}}} \cdot B^{m_{\mathrm{ee}},p_{\mathrm{T,ee}}}(\phi_{\mathrm{V}}) \tag{8.4}$$

is fitted to the measured ϕ_V dielectron spectrum extracted from data with a_i as normalization parameters. Figure 8.7 shows the ϕ_{V} distribution in a particular invariant mass and pair transverse momentum interval after application of the single track requirements. The dielectron spectrum extracted from data displays its maximum at high ϕ_{V} and can be described by a fit of the weighted sum of a signal and conversion template extracted from simulations. The maximum deviation of the fitted weighted sum of both templates to the data is in the order of 20%. The scaled signal (magenta) template is used as the corrected dielectron yield in this phase space interval. This procedure is repeated for small invariant masses $m_{\mathrm{ee}} < 80\,\mathrm{MeV}/c^2$ and all pair transverse momenta $p_{\mathrm{T,ee}} < 8\,\mathrm{GeV}/c^2$.

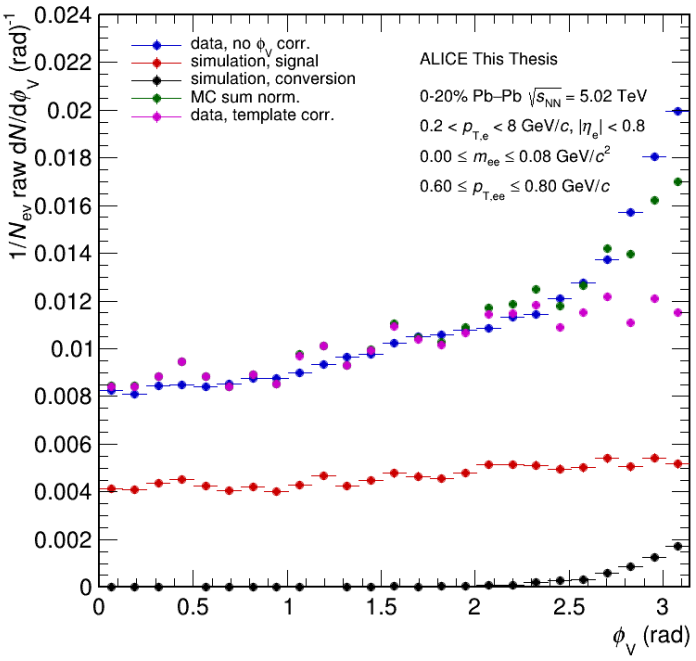

Figure 8.7.: ϕ_V distribution for $m_{ee} \leq 0.8\,\mathrm{GeV}/c^2$ and $0.6 < p_{T,ee} \leq 0.8\,\mathrm{GeV}/c^2$. The conversion template (black) shows a peak at high ϕ_V while the signal template (red) has a flatter distribution. The uncorrected data (blue) is fitted with a weighted sum of both templates (green). The resulting corrected spectra consists of the fitted signal template (magenta).

8.2.1. Acceptance Gain with $p_T > 0.2\,\mathrm{GeV}/c$

The first published ALICE results on the production of dielectrons in heavy-ion collisions is based on a minimum transverse momentum selection of $p_T > 0.4\,\mathrm{GeV}/c$ for the single electron [78]. The analysis which is discussed in this thesis uses a minimum transverse momentum selection of $p_T > 0.2\,\mathrm{GeV}/c$ increasing the acceptance and phase space enormously. For the first time in heavy-ion collisions at LHC energies, this selection allows for the study of the production of low-momentum and low-mass dielectron pairs which was not feasible in the previous analysis. Thermal radiation by the QGP and the hadron gas phase contribute to this kinematic region, making the access to this particular phase space particularly interesting. However, the amount of electrons and positrons from photon conversion in the material and therefore the background increases also dramatically. To suppress the background and make this analysis feasible, the introduction of the photon conversion rejection methods discussed in section 8.2 are crucial.

Figure 8.8 shows the relative acceptance gain for dielectron pairs when lowering the

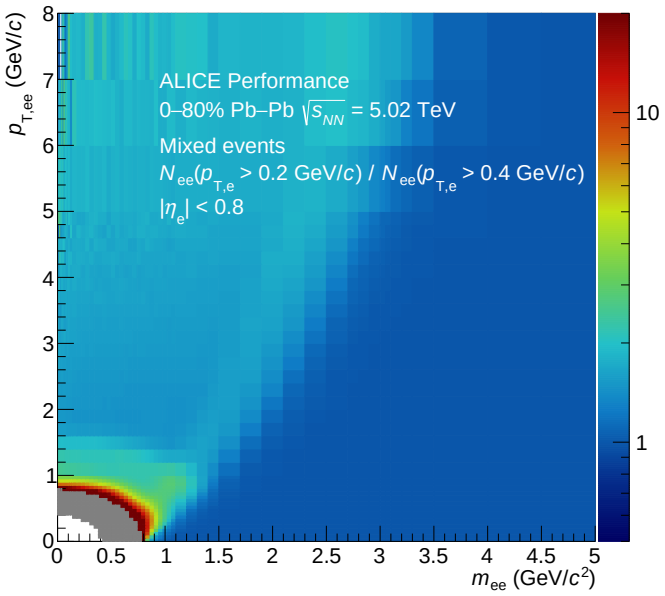

Figure 8.8.: Relative acceptance gain for dielectron pairs when lowering the minimum transverse momentum selection for single electrons from $p_{\mathrm{T}} > 0.4\,\mathrm{GeV}/c$ to $p_{\mathrm{T}} > 0.2\,\mathrm{GeV}/c$, shown for uncorrelated dielectron pairs calculated with the mixed-event technique.

minimum transverse momentum selection for single electrons from $p_{\mathrm{T}} > 0.4\,\mathrm{GeV}/c$ to $p_{\mathrm{T}} > 0.2\,\mathrm{GeV}/c$. Shown are uncorrelated dielectrons obtained with the mixed-event technique. The mixed-event method is discussed in more detail in section 8.1.2. These uncorrelated dielectrons show directly the increase in phase-space at small invariant masses and small pair transverse momenta indicated with the grey region where the gain is infinitely large. A gain in acceptance directly corresponds to a larger amount of measurable dielectron pairs in a given phase-space interval. The acceptance increases close to the acceptance hole by a factor of ≈ 20. Even at higher pair transverse momenta the acceptance increases by a factor of ≈ 2.

8.3. Raw Signal, S/B, Significance

The resulting dielectron yield in Pb-Pb collisions with a center-of-mass energy $\sqrt{s_{\mathrm{NN}}} = 5.02\,\mathrm{TeV}$ in the 20% most central events as a function of the invariant mass and the pair transverse momentum $\mathrm{d}N^{\mathrm{raw}}/\mathrm{d}m_{\mathrm{ee}}\mathrm{d}p_{\mathrm{T,ee}}$ is shown in figure 8.9. The invariant mass projections of this two-dimensional spectrum can be seen in figure 8.10. They show the typical shape of dielectron mass spectra like the steep descend at small masses, the distinct J/ψ peak around $m_{\mathrm{ee}} \approx 3.1\,\mathrm{GeV}/c^2$ and the

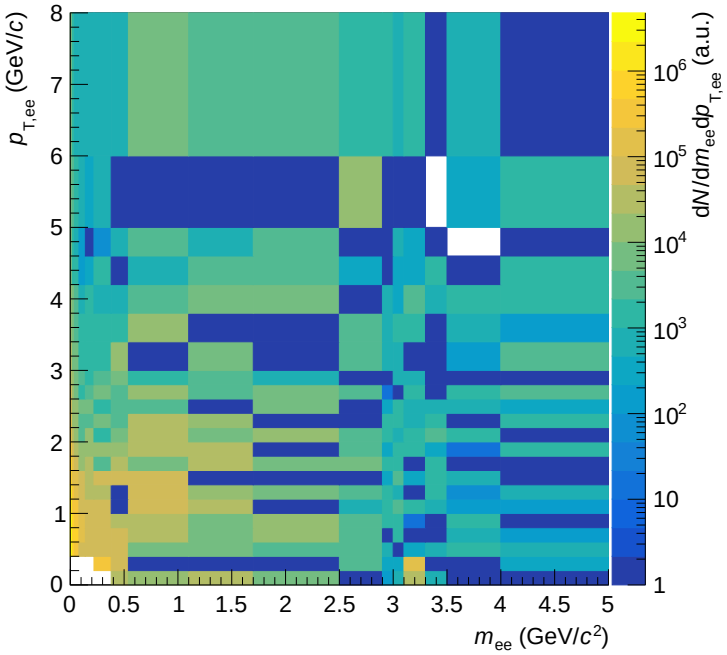

Figure 8.9.: Raw dielectron yield as a function of invariant mass m_{ee} and pair transverse momentum $p_{T,ee}$ in the most 0-20% central Pb-Pb collisions at $\sqrt{s_{NN}} = 5.02\,\text{TeV}$.

fall of the continuum produced by semi-leptonic decays of $c\bar{c}$ and $b\bar{b}$. Figure 8.11 shows the pair transverse momentum spectra in several mass bins. The dielectron spectra for the centrality classes 20-40% and 40-80% can be found in annex D.

The signal to background ratio S/B is shown in the left panel of figure 8.12 as a function of m_{ee} for three centrality classes. This distribution illustrates greatly the difficulty to measure the dielectron signal in nucleus-nucleus collisions because a small signal is extracted which is sitting on top of an enormous background. At smaller invariant mass $m_{ee} < 0.14\,\text{GeV}/c^2$ the spectrum is dominated from the signal of the π^0 decay with almost no combinatorial background. In the minimum around $m_{ee} = 0.5\,\text{GeV}/c^2 \approx m_\eta$ the signal to background ratio decreases to $\approx 1/3000$. In first order, the number of signal pairs is proportional to the number of charged particle in a given event $S \propto N_{ch}$. However, the number of background pairs scales quadratically with the multiplicity $B \propto N_{ch}^2$. Therefore, the S/B is significantly smaller over the complete mass range for more central events, which typically have a high multiplicity, compared to more peripheral collisions with small multiplicities.

The S/B is not the only figure to judge the quality of a selection scheme. The statistical significance s is also important and is directly linked to the statistical uncertainty ΔS of the resulting dielectron signal S: $s = S/\Delta S$. Taking into ac-

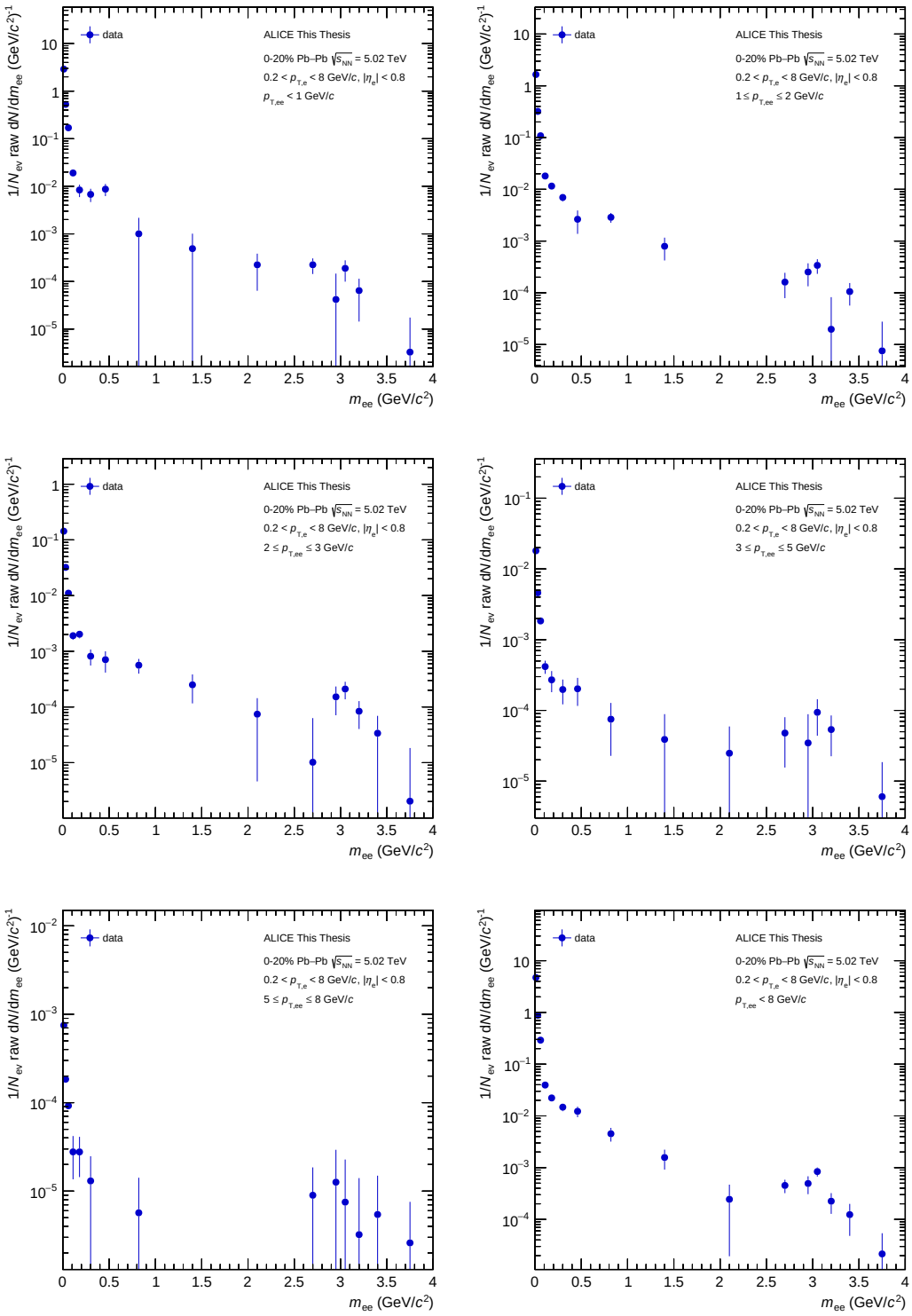

Figure 8.10.: Raw dielectron yield as a function of the invariant mass m_{ee} in several pair transverse momentum $p_{\mathrm{T,ee}}$ bins in the most 0-20% central Pb-Pb collisions at $\sqrt{s_{\mathrm{NN}}} = 5.02\,\mathrm{TeV}$.

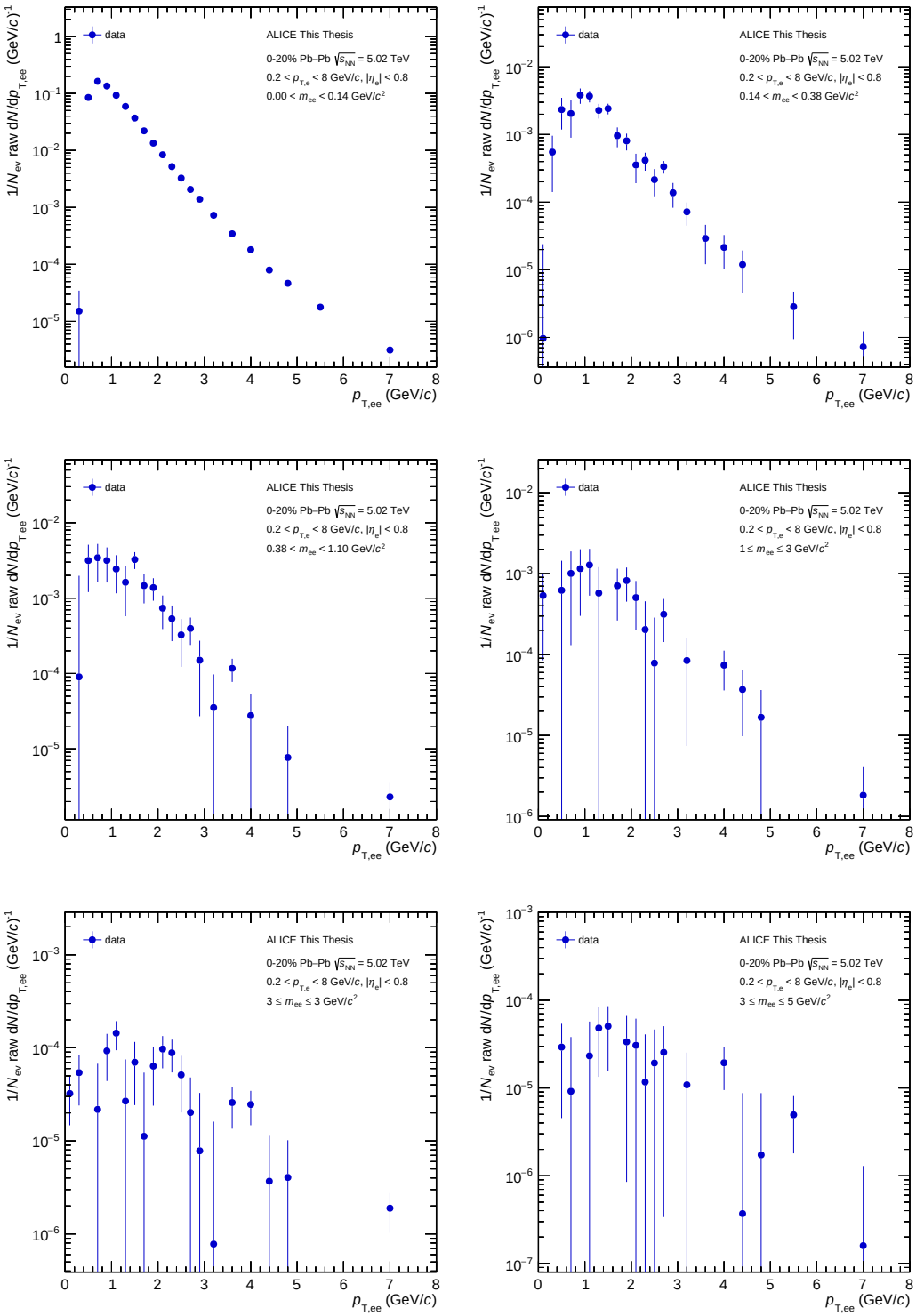

Figure 8.11.: Raw dielectron yield as a function of the pair transverse momentum $p_{\mathrm{T,ee}}$ in several pair invariant mass m_{ee} bins in the most 0-20% central Pb-Pb collisions at $\sqrt{s_{\mathrm{NN}}} = 5.02\,\mathrm{TeV}$.

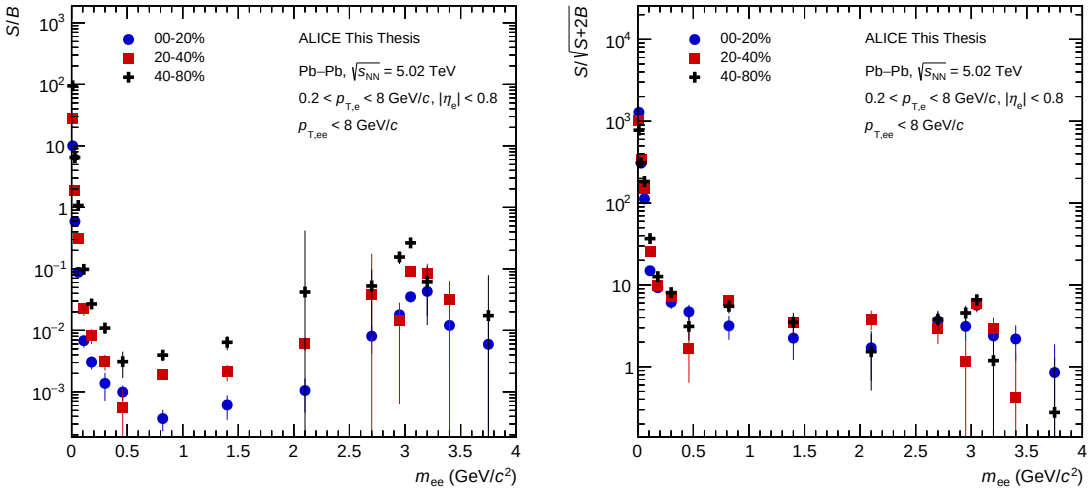

Figure 8.12.: Comparison of the signal to background ratio (left) and significance (right) as a function of the invariant mass m_{ee} in the centrality range of 0-20%, 20-40% and 40-80% most central events.

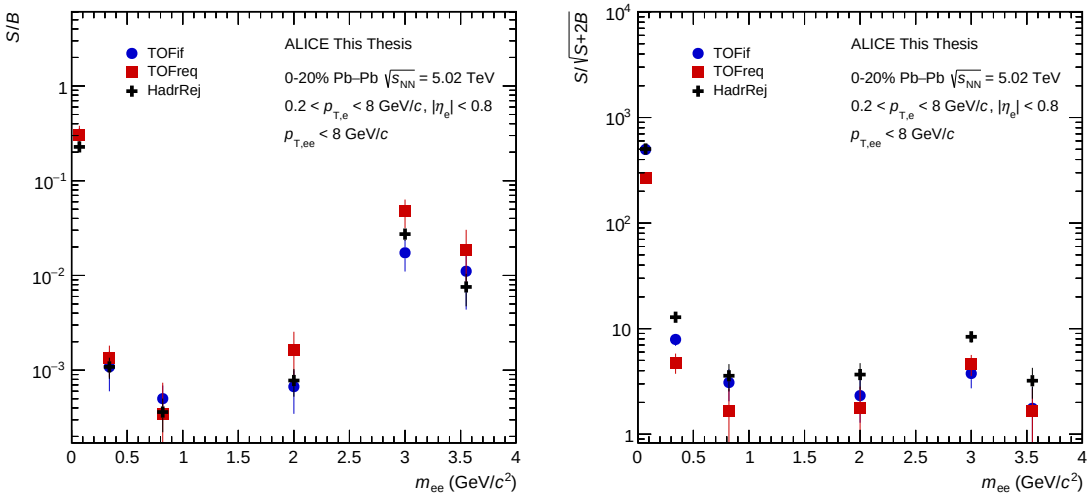

Figure 8.13.: Comparison of the signal to background ratio (left) and significance (right) as a function of the invariant mass m_{ee} of three different selections in the centrality range of 0-20% most central events.

count that the background B is estimated with the like-sign method, the statistical significance [109] of the dielectron signal, is defined as:

$$s = \frac{S}{\sqrt{S + 2B}} \tag{8.5}$$

The statistical significance is shown in the right panel of figure 8.12 as a function of the invariant mass for the three centrality classes 0-20%, 20-40% and 40-80%. The statistical significance as a direct measure for the statistical uncertainty is used to establish the binning of the dielectron signal histogram. The binning is chosen in a way that the significance of the dielectron signal above $m_{\mathrm{ee}} > 0.5\,\mathrm{GeV}/c^2$ are compatible bin-by-bin. In this analysis, the binning was chosen in a way that the statistical significance is ≈ 3 for higher invariant masses.

The left panel on figure 8.13 shows the signal to background ratio S/B for the three different electron identification selections TOFif, TOFreq and HadrRej. See section 7.2 for a detailed discussion of the electron identification procedure. The figure shows that the S/B depends on the electron identification scheme and therefore on the residual amount of hadronic contamination inside the electron candidate sample. These misidentified hadrons add to the uncorrelated combinatorial background and therefore decrease the S/B. The TOFreq identification scheme results in the highest purity leading to only small background originating from hadronic contamination while simultaneously not being to strict to not reject the complete signal. TOFif and HadrRej have a comparable signal to background ratio. The right plot on figure 8.13 shows the statistical significance as a function of the invariant mass for three different electron identification selection TOFif, TOFreq and HadrRej. Despite the high signal over background ratio of the TOFreq identification scheme, the statistical significance of this spectrum is smaller compared to the TOFif and HadrRej identification scheme. The strict electron identification and therefore the high purity of the electron sample do not compensate the rejection of dielectron signal pairs by the strict selection.

9. Efficiency Studies

The measured raw spectra in section 8.3 are affected by detector specific effects. These effects have to be corrected for, to allow for a comparison to theory calculations. The following chapter summarizes the steps which are required for this detector correction.

9.1. Detector Resolution

Charged particles traversing the experiment are affected by several detector specific effects deteriorating the accuracy of their resonstructed momentum. Charged particles and especially electrons emit synchrotron-like radiation (bremsstrahlung) when they are deflected by the magnetic field. No correction for this effect is applied during the reconstruction step. Additionally, charged particles interact with the detector material via multiple coulomb-like scatterings which also leads to a modification of their momentum. Finally, tracks measured with the detectors and reconstructed with the tracking algorithm have only a finite spatial resolution. These effects, particularly bremsstrahlung, lead to a reconstructed transverse momentum which is typically smaller than the *true* transverse momentum of the particles determined by the underlying physical processes of the collision: $p_{\mathrm{T}}^{\mathrm{rec}} \lessapprox p_{\mathrm{T}}^{\mathrm{gen}}$. This momentum shift can further be translated into a reconstructed invariant mass smaller than the generated one.

A multidimensional unfolding procedure based on full detector simulations is very complex and does not give stable and trustful results around resonance peaks. Alternatively, dielectron spectra are usually shown as a function of the measurable, i.e. reconstructed, observables like the reconstructed invariant mass m_{ee} and pair transverse momentum $p_{\mathrm{T,ee}}$. To perform a fair comparison with theory calculations, these calculations have to be smeared according to the resolution of the detector. In this analysis the dielectron spectrum will be compared to a hadronic cocktail which contains an estimate of known sources decaying into dielectrons. Therefore, the hadronic cocktail is *smeared* according to the detector resolution to ensure a consistent comparison with the data.

Additional to the smearing of the cocktail is the smearing within the efficiency cal-

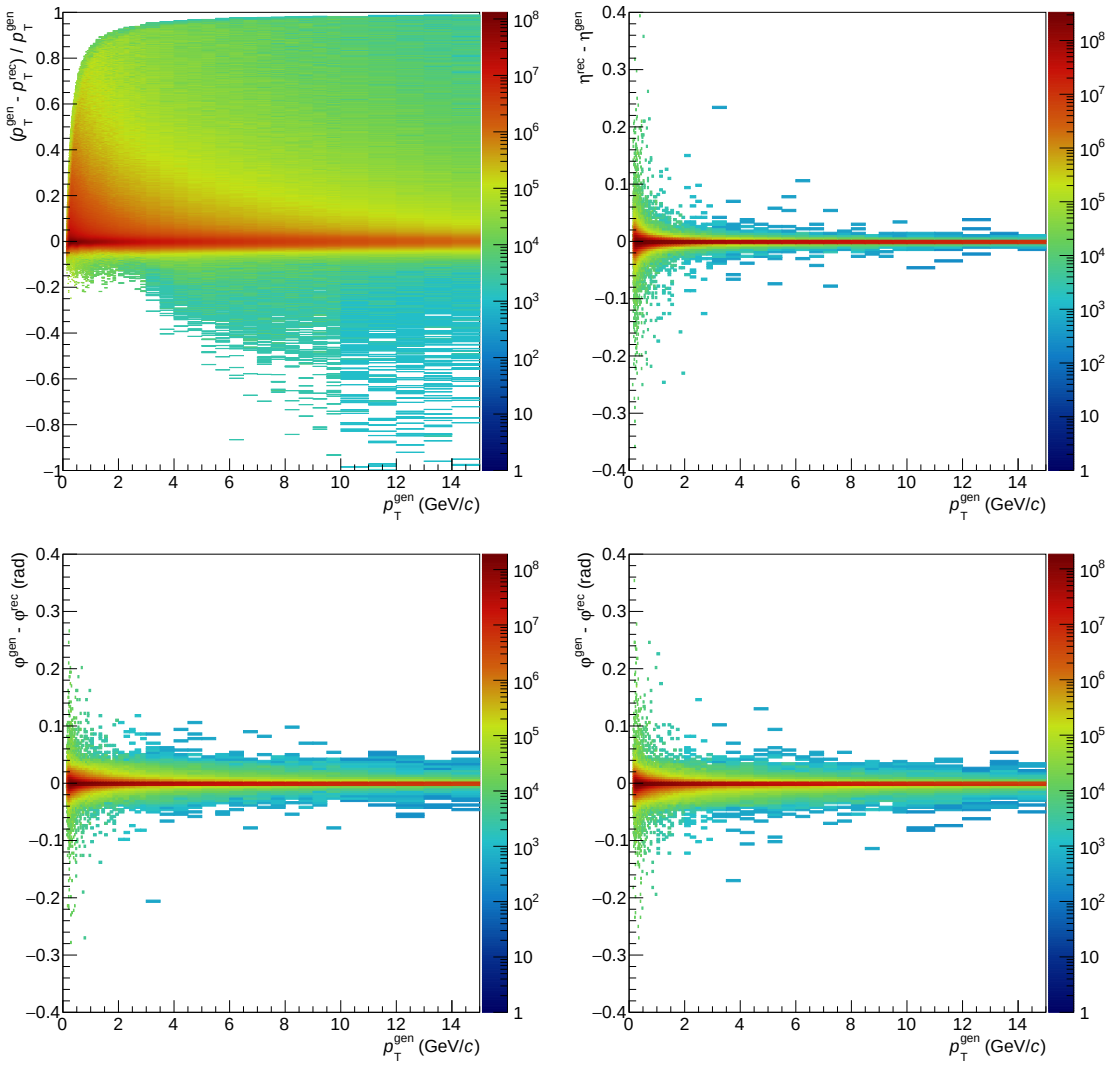

Figure 9.1.: Transverse momentum (top left) and pseudorapidity (top right) resolution matrices as a function of the generated transverse momentum of electrons and positrons. Azimuthal angle resolution matrices as a function of the generated transverse momentum of positrons (bottom left) and electrons (bottom right).

culations. These efficiency calculations are based on the probability of measuring a track or pair with given generated kinematics. Since this generated momentum cannot be extracted in the measurement, the generated values have to be transformed in *measurable* observables taking into account the above mentioned detector effects, i.e. the detector resolution: e.g. $p_{\mathrm{T}}^{\mathrm{gen}} \rightarrow p_{\mathrm{T}}^{\mathrm{meas}}$. This leads to an efficiency correction based on the measured and not the generated values:

$$\epsilon^{\mathrm{pair}}(m_{\mathrm{ee}}^{\mathrm{meas}}, p_{\mathrm{T,ee}}^{\mathrm{meas}}) = \frac{N^{\mathrm{rec}}(m_{\mathrm{ee}}^{\mathrm{rec}}, p_{\mathrm{T,ee}}^{\mathrm{rec}})}{N^{\mathrm{meas}}(m_{\mathrm{ee}}^{\mathrm{meas}}, p_{\mathrm{T,ee}}^{\mathrm{meas}})} \tag{9.1}$$

with ϵ^{pair} being the efficiency, N^{rec} the number of reconstructed pairs in a given $(m_{\mathrm{ee}}, p_{\mathrm{T,ee}})$ interval and N^{meas} the number of generated pairs in the same interval after smearing of the generated momentum.

To obtain *measurable* values the following transformation is performed:

$$\begin{aligned} p_{\mathrm{T}}^{\mathrm{meas}} &= p_{\mathrm{T}}^{\mathrm{gen}} + \Delta p_{\mathrm{T}} \\ \eta^{\mathrm{meas}} &= \eta^{\mathrm{gen}} + \Delta\eta \\ \varphi^{\mathrm{meas}} &= \varphi^{\mathrm{gen}} + \Delta\varphi \end{aligned}$$

with the smearing values Δp_{T}, $\Delta\eta$ and $\Delta\varphi$ obtained from detector response matrices. These response matrices are extracted from full detector simulations as $(p_{\mathrm{T}}^{\mathrm{gen}} - p_{\mathrm{T}}^{\mathrm{rec}})/p_{\mathrm{T}}^{\mathrm{gen}}$, $\eta^{\mathrm{rec}} - \eta^{\mathrm{gen}}$ and $\varphi^{\mathrm{gen}} - \varphi^{\mathrm{rec}}$ distributions as a function of the generated transverse momentum $p_{\mathrm{T}}^{\mathrm{gen}}$. The respective distributions are shown in figure 9.1.

To extract Δp_{T}, $\Delta\eta$ and $\Delta\varphi$ for a given generated momentum $p_{\mathrm{T}}^{\mathrm{gen}}$, the detector response matrices are projected on $(p_{\mathrm{T}}^{\mathrm{gen}} - p_{\mathrm{T}}^{\mathrm{rec}})/p_{\mathrm{T}}^{\mathrm{gen}}$, $\eta^{\mathrm{rec}} - \eta^{\mathrm{gen}}$ and $\varphi^{\mathrm{gen}} - \varphi^{\mathrm{rec}}$ in a given $p_{\mathrm{T}}^{\mathrm{gen}}$ slice around the $p_{\mathrm{T}}^{\mathrm{gen}}$ value. Random values are drawn according to the corresponding projected distribution for each of the three variables. An example for a projection is shown in figure 9.2 in $0.82 < p_{\mathrm{T}}^{\mathrm{gen}} < 0.88\,\mathrm{GeV}/c$ for the observable $(p_{\mathrm{T}}^{\mathrm{gen}} - p_{\mathrm{T}}^{\mathrm{rec}})/p_{\mathrm{T}}^{\mathrm{gen}}$. With these drawn values the respective Δp_{T}, $\Delta\eta$ and $\delta\varphi$ can be calculated straightforwardly. The dependence of the transverse momentum or azimuthal angle on the pseudorapidity was found to be negligible which allows an independent smearing of the three observables.

9.2. Single electron efficiency

In this analysis the single electron efficiency is used only to illustrate detector and selection effects. The pair efficiency used for correcting the raw dielectron spectrum is extracted in section 9.3.

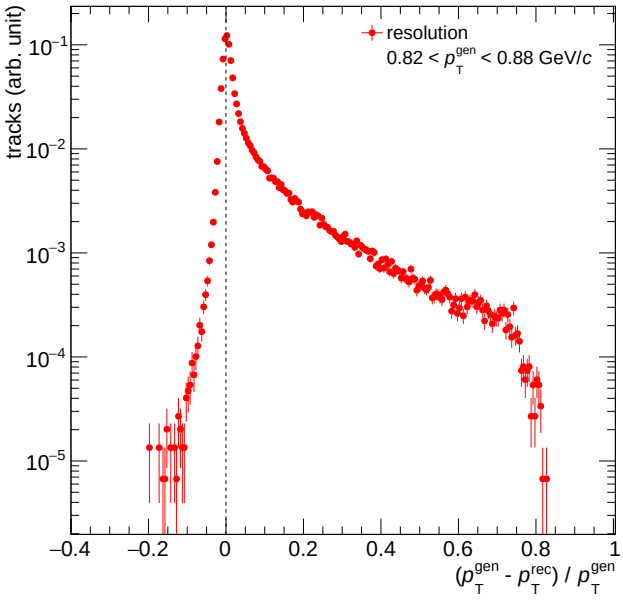

Figure 9.2.: $(p_{\mathrm{T}}^{\mathrm{gen}} - p_{\mathrm{T}}^{\mathrm{rec}})/p_{\mathrm{T}}^{\mathrm{gen}}$ distribution in the generated transverse momentum slice $0.82 < p_{\mathrm{T}}^{\mathrm{gen}} < 0.88\,\mathrm{GeV}/c$. The tail on the right side originates from energy loss of electrons.

The single electron reconstruction efficiency $\epsilon_{\mathrm{track}}$ is defined as the number of reconstructed electrons after all selection criteria over the number of generated electrons as a function of the kinematic observables p_{T}, η and φ. The efficiency is extracted from the dedicated dielectron full Monte-Carlo simulation LHC18b5a. The detector resolution matrices are applied on the generated particles as described in section 9.1:

$$\epsilon^{\mathrm{track}}(p_{\mathrm{T}}^{\mathrm{meas}}, \eta^{\mathrm{meas}}, \varphi^{\mathrm{meas}}) = \frac{N^{\mathrm{rec}}(p_{\mathrm{T}}^{\mathrm{rec}}, \eta^{\mathrm{rec}}, \varphi^{\mathrm{rec}})}{N^{\mathrm{meas}}(p_{\mathrm{T}}^{\mathrm{meas}}, \eta^{\mathrm{meas}}, \varphi^{\mathrm{meas}})} \tag{9.2}$$

Figure 9.3 shows the single electron reconstruction efficiency as a function of p_{T} (left), η (middle) and φ (right), each integrated over the other two observables, for three electron identification schemes TOFif (top), TOFreq (middle) and HadrRej (bottom).

For the efficiency calculation only electrons from physical primary processes are selected. Secondary electrons like electrons from real photon conversions in the detector material, which show a different efficiency, are not considered and mostly removed in the analysis.

The reconstruction efficiency is directly related to the track and electron selection together with the detector performance. The efficiency decreases at high momenta due to the hard pion rejection in the electron identification process, as can be seen

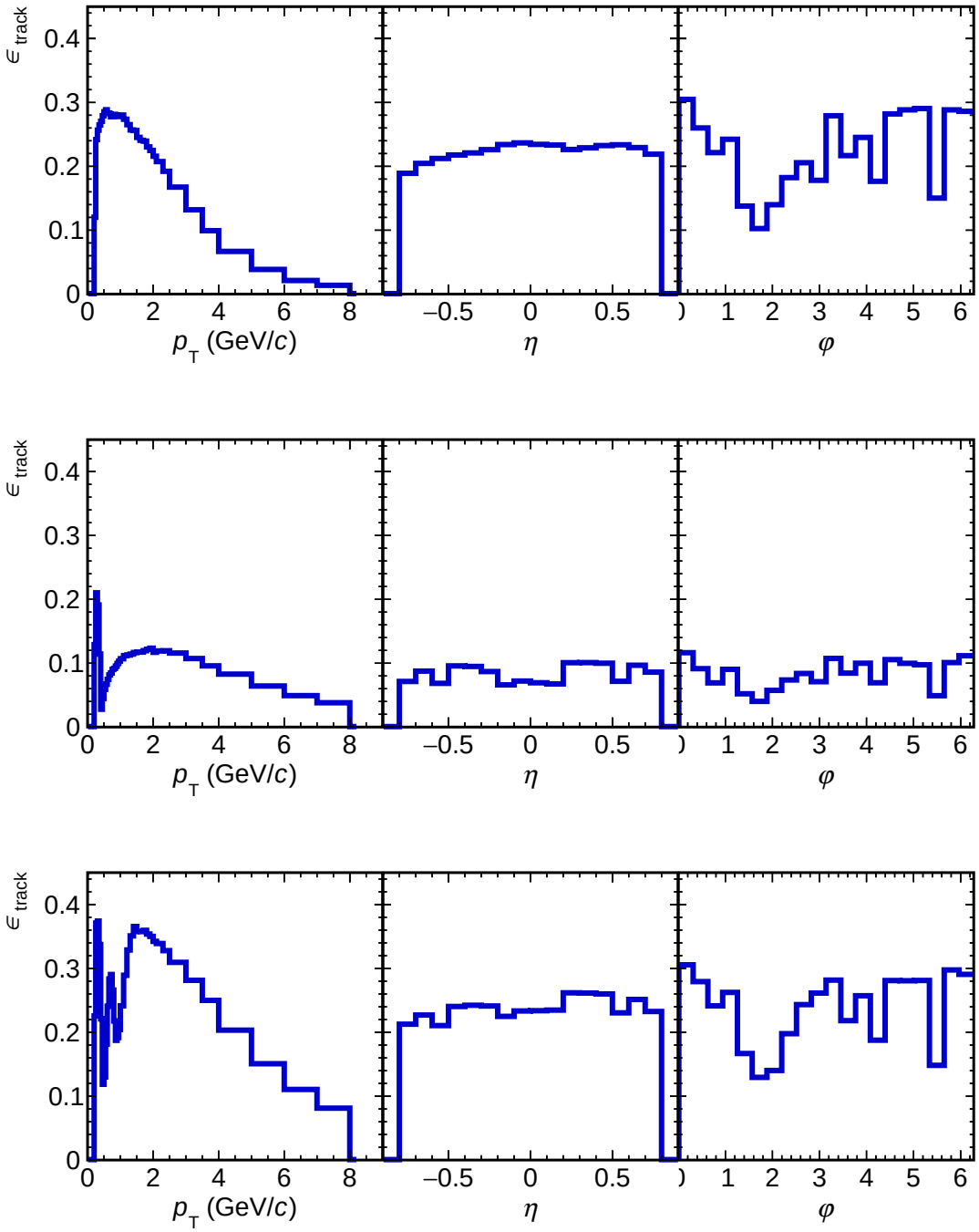

Figure 9.3.: Single electron efficiency after application of all selection criteria for the 0-20% most central collisions as a function of p_{T}, η and φ. The top plot is based on a TOFif, middle on a TOFreq and bottom on a HadrRej identification scheme, respectively.

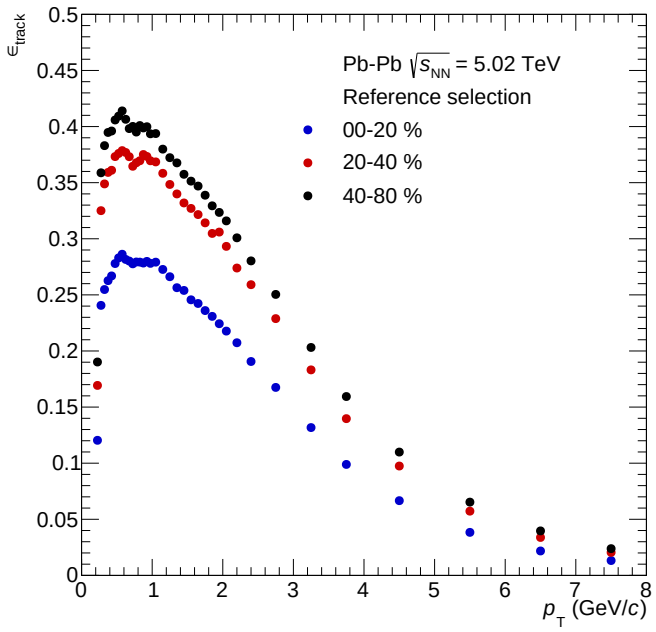

Figure 9.4.: Single electron efficiency after application of all selection criteria as a function of p_T for the three centrality classes $0-20\%$, $20-40\%$ and $40-80\%$ of the most central events.

figure 7.9. In addition, particles with large momenta are only slightly bend in the magnetic field, leading to a higher probability for those particles to fly exactly along the radial support structure of the TPC. At small particle transverse momenta the strength of the magnetic field and the corresponding fraction of electrons not reaching the outer part of the TPC limits the efficiency. The efficiency as function of φ is characterized by non-functioning areas in the ITS SPD while it is rather flat as a function of η.

The three different electron identification schemes lead to different efficiencies. While TOFreq and TOFif share a similar shape at higher momenta $p_T > 0.4\,\mathrm{GeV/c}$ the overall efficiency of TOFreq is lower because of the TOF acceptance together with the TPC-TOF track matching efficiency. The TOFreq identification does not use the information of the TOF at transverse momenta $p_T < 0.4\,\mathrm{GeV/c}$ leading to a comparable efficiency in this kinematic region. The electron identification scheme based on the hadron rejection HadrRej has a similar efficiency as TOFif with a characteristic structure around $p_T \approx 0.6\,\mathrm{GeV/c}$ and $p_T \approx 1\,\mathrm{GeV/c}$ where the kaon and proton bands are rejected in the TPC, respectively.

Figure 9.4 shows the centrality dependence of the single electron efficiency. This dependence can predominantly be attributed to the ITS shared cluster selection. This selection rejects spatially close tracks the first two layers of the ITS. These tracks have a higher probability to occur in more central events where the track

density is simply higher compared to peripheral events.

9.3. Dielectron Pair Efficiency

The probability that the ALICE experiment measures a dielectron pair coming from the collision process in the fiducial acceptance of the detector ($p_{\mathrm{T}} > 0.2\,\mathrm{GeV}/c$ and $|\eta| < 0.8$) after applying all selection criteria is called dielectron pair efficiency. The detector resolution matrices are applied to all generated electrons and positrons, similar to the method used for the smearing of the generated single electrons in section 9.2. The pair efficiency ϵ^{pair} is calculated as a function of the invariant mass m_{ee} and the pair transverse momentum $p_{\mathrm{T,ee}}$:

$$\epsilon^{\mathrm{pair}}(m_{\mathrm{ee}}^{\mathrm{meas}}, p_{\mathrm{T,ee}}^{\mathrm{meas}}) = \frac{N^{\mathrm{rec}}(m_{\mathrm{ee}}^{\mathrm{rec}}, p_{\mathrm{T,ee}}^{\mathrm{rec}})}{N^{\mathrm{meas}}(m_{\mathrm{ee}}^{\mathrm{meas}}, p_{\mathrm{T,ee}}^{\mathrm{meas}})} \tag{9.3}$$

It is used to correct the uncorrected spectra $\frac{\mathrm{d}N_{\mathrm{ee}}^{\mathrm{raw}}}{\mathrm{d}m_{\mathrm{ee}}\mathrm{d}p_{\mathrm{T,ee}}}$ from section 8.3 to obtain the final dielectron spectrum:

$$\frac{\mathrm{d}N}{\mathrm{d}m_{\mathrm{ee}}\mathrm{d}p_{\mathrm{T,ee}}} = \frac{\mathrm{d}N_{\mathrm{ee}}^{\mathrm{raw}}(m_{\mathrm{ee}}, p_{\mathrm{T,ee}})}{\mathrm{d}m_{\mathrm{ee}}\mathrm{d}p_{\mathrm{T,ee}}} \cdot \frac{1}{\epsilon^{\mathrm{pair}}(m_{\mathrm{ee}}, p_{\mathrm{T,ee}})} \tag{9.4}$$

The dielectron pair efficiency is extracted from the full Monte-Carlo simulation LHC18b5a which is a dedicated dielectron simulation, see section 6.3 for more details on this specific simulation. In this simulation, HIJING was used to simulate the underlying Pb-Pb collisions while additional light- and heavy-flavour sources were added. Light flavour mesons, like $\pi^0 \to e^+e^-\gamma$, are distributed uniformly in transverse momentum to get smaller statistical uncertainties at higher momenta. The p_{T} of the meson and their corresponding decay electrons is then reweighted such that it reproduces the expected p_{T} distributions used as input for the hadronic cocktail calculation which are exponentially falling. Without the reweighting procedure, averaging over larger momentum intervals, which is required due to small statistics in data, results in wrong pair efficiencies. The dielectron spectrum in the simulation as a function of the invariant mass is already similar to the hadronic cocktail and therefore does not require reweighting. This unweighted invariant mass distribution is shown in figure 9.5. Figure 9.6 shows the unweighted (left) and reweighted (right) dielectron spectrum of all light-flavour hadron sources as a function of the pair transverse momentum. The rise of the π^0 contribution at $p_{\mathrm{T,ee}} \approx 1\,\mathrm{GeV}/c$ originates from feed-down of heavier hadrons. The strong fall at $p_{\mathrm{T,ee}} \approx 0.4\,\mathrm{GeV}/c$ can be explained by the fiducial selection of $p_{\mathrm{T}}^{\mathrm{e}} > 0.2\,\mathrm{GeV}/c$.

The pair efficiency is calculated for correlated dielectrons from same-mother decays,

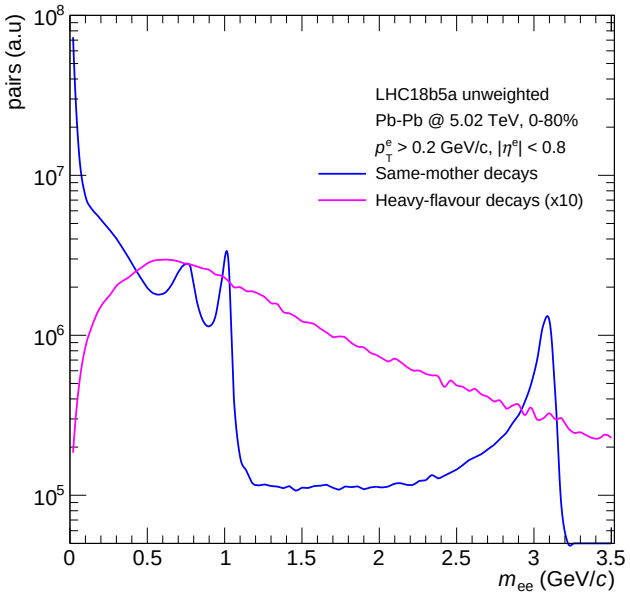

Figure 9.5.: Dielectron spectrum originating from so-called same-mother and heavy-flavour hadron decays as a function of invariant mass m_{ee} extracted from dedicated dielectron simulation LHC18b5a.

like $\pi^0 \to e^+e^-\gamma$ and $J/\psi \to e^+e^-$, and semileptonic heavy-flavour hadron decays, like $c\bar{c} \to D + X \to e + Y$, separately because of different methods used. Correlated background dielectrons coming from real photon conversions are not considered. Dielectrons from light-flavour hadron sources and from J/ψ are correlated via the momentum conservation of their mother in the decay. In simulations it can easily be checked if an electron-positron pair originates from the same mother. The pair efficiency of correlated dielectrons coming from semileptonic heavy-flavour hadron decays can not be extracted by studying the decay history of their hadronic mother but have to be traced all the way back to the heavy $Q\bar{Q}$ pair. In Pb-Pb simulations, the decay history of correlated heavy-flavour dielectrons becomes complex and ambiguous, especially when several $Q\bar{Q}$ pairs per event are involved and therefore renders the extraction of the pair efficiency of correlated heavy-flavour pairs difficult and not reliable. Studies with only one $Q\bar{Q}$ pair within a proton-proton collision [111] showed that pair efficiencies extracted from correlated, and from combinatorial pairs of electrons and positrons coming from heavy-flavour hadron decays, are equal. This allows for the usage of the pair efficiency of unlike-sign pairs calculated from electrons and positrons from heavy-flavour hadron decays as a replacement of the pair efficiency of correlated pairs originating from $c\bar{c}$ and $b\bar{b}$ quarks. Due to limited statistics in the simulation the pair efficiency of $c\bar{c} \to e^+e^-$ and $b\bar{b} \to e^+e^-$ is not calculated separately.

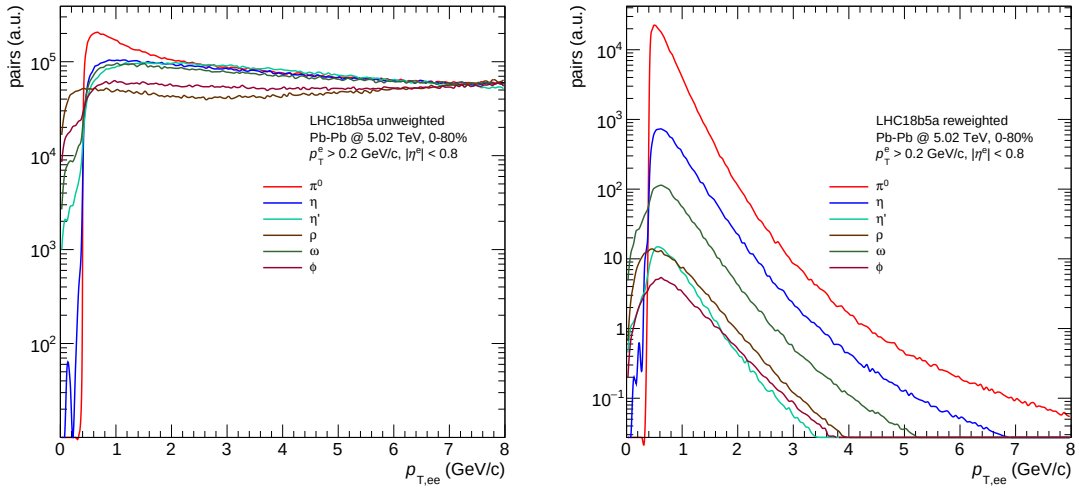

Figure 9.6.: Unweighted (left) and reweighted (right) dielectron spectrum of dedicated dielectron simulation LHC18b5a separated into different sources.

Figure 9.7 shows the pair efficiency for dielectrons from same-mother decays (blue) and for dielectron from semileptonic heavy-flavour hadron decays (magenta). Overall both efficiencies agree with each other within their statistical uncertainties. However, a quantitative study of any systematic deviation of both is limited by the statistics present in the simulation. The relatively large decay length of the heavy-flavour hadrons $c\tau > 200\,\mu\text{m}$ can cause a difference in the pair efficiency in comparison to the pair efficiency from same-mother decays. Electrons from heavy-flavour hadrons might not originate in the primary vertex of the collision and therefore traverse the detector geometry slightly different. Additionally, the electron and positron are potentially closer to each other at the most inner layers of the ITS because the magnetic field could not bend them apart as if they would have originated in the primary vertex. This effect leads to a higher rejection propability by the selection on the number of ITS shared cluster. Furthermore, the invariant mass and pair transverse momentum distribution inside of a given bin can be slightly different for both pair efficiencies. This effect on the pair efficiency is minimized by choosing as small bins as possible but is limited by the given statistic.

Several detector related effects lead to a deterioration of the pair efficiency for more central events due to the higher track density inside the detector. Especially the ITS shared cluster selection enhances the centrality dependence of the pair efficiency. With increasing density of charged particles in central Pb-Pb collisions, the probability for an electron candidate to share an ITS cluster with a neighboring uncorrelated track increases. Figure 9.8 shows this dependence for several $p_{\text{T,ee}}$ intervals. For all five selected intervals the pair efficiency is reduced by a factor of ≈ 2 going from peripheral events to central events. To take this effect into account, the pair efficiency correction has to be applied in small centrality intervals. These intervals are

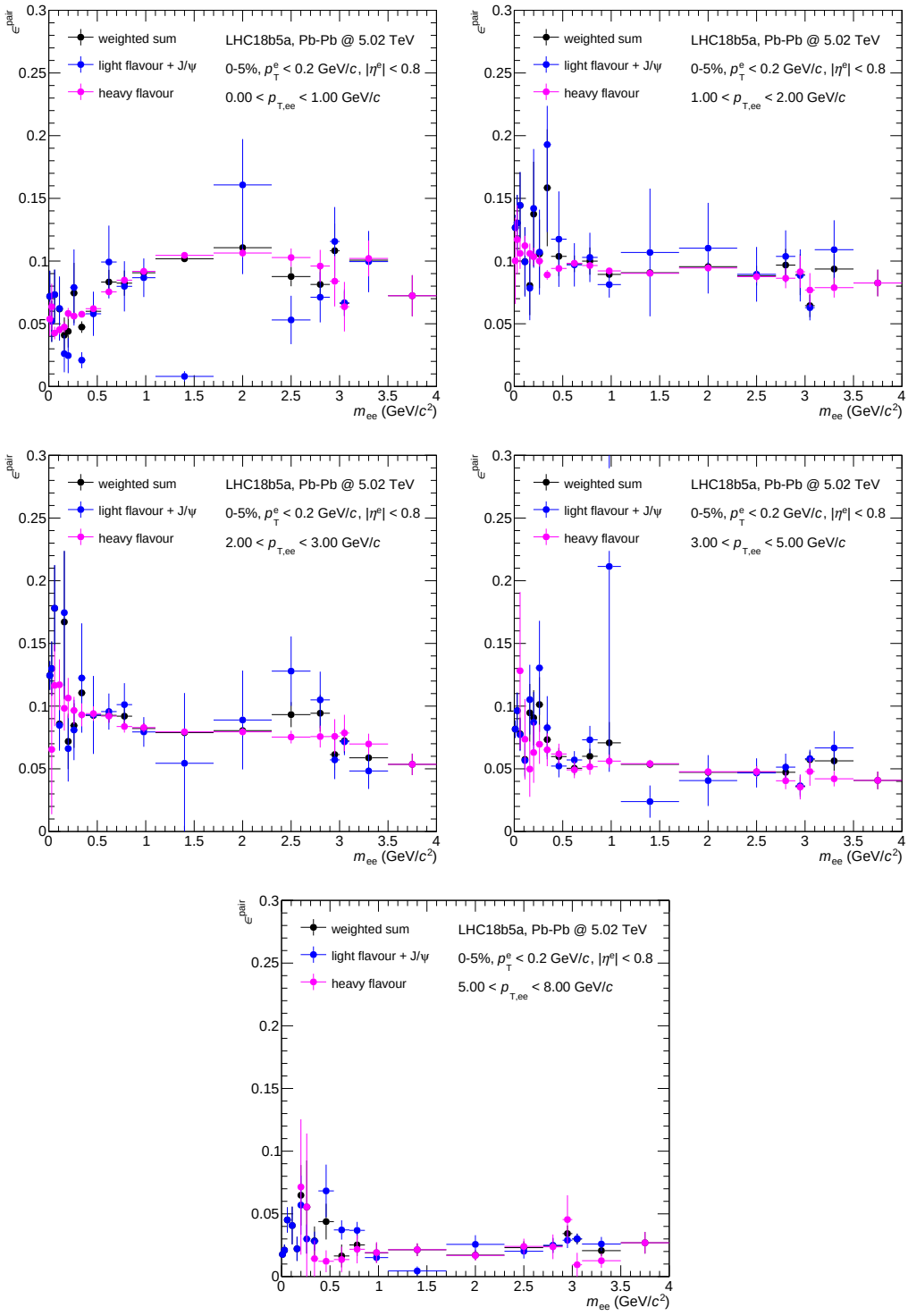

Figure 9.7.: Dielectron pair efficiency as a function of m_{ee} in several $p_{T,ee}$ ranges separated into the efficiency of correlated light-flavour meson with J/ψ decays, unlike-sign efficiency of electrons coming from heavy flavour and cocktail-weighted sum of both.

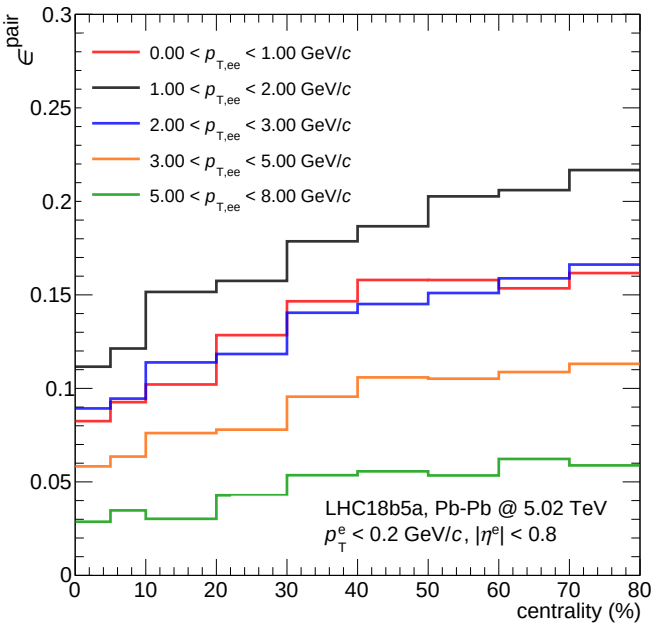

Figure 9.8.: Pair efficiency originating from light-flavour mesons and the J/ψ as a function of centrality for different $p_{\mathrm{T,ee}}$ intervals.

constraint to have reasonable statistical fluctuations. The chosen centrality classes for the pair efficiency correction are: 0-5%, 5-10%, 10-20%, 20-40%, 40-60%, 60-80% and 70-90%.

To apply the pair efficiency on the raw dielectron spectrum, both extracted, and potentially different, pair efficiencies have to be combined to a single pair efficiency because it is not possible to distinguish dielectron originating from same-mother decays or from decays of heavy-quark hadron decays. To combine both, they are added with weights according to the relative contribution in the hadronic cocktail in a given invariant mass m_{ee} and pair transverse momentum $p_{\mathrm{T,ee}}$ interval:

$$\epsilon^{pair}(m_{\mathrm{ee}}, p_{\mathrm{T,ee}}) = \frac{N^{LF+J/\psi}}{N^{sum}} \cdot \epsilon^{LF+J/\psi}(m_{\mathrm{ee}}, p_{\mathrm{T,ee}}) + \frac{N^{\mathrm{HF}}}{N^{sum}} \cdot \epsilon^{\mathrm{HF}}(m_{\mathrm{ee}}, p_{\mathrm{T,ee}}) \qquad (9.5)$$

with $\epsilon^{LF+J/\psi}$, ϵ^{HF} being the pair efficiency for dielectrons from light-flavour meson and J/ψ decay and from heavy-flavour hadron decay, respectively. $N^{LF+J/\psi}$, N^{HF} and N^{sum} are the expected yields and the sum extracted from the hadronic cocktail.

Figure 9.7 shows the projected pair efficiencies $\epsilon^{LF+J/\psi}$ (blue), ϵ^{HF} (magenta) and the weighted sum of both ϵ^{pair} (black) as a function of m_{ee} in several $p_{\mathrm{T,ee}}$ intervals. The weighted sum is then used to correct the raw dielectron signal. The pair efficiency is around $\epsilon^{pair} \approx 10\%$ for small transverse momenta $p_{\mathrm{T,ee}} < 2\,\mathrm{GeV}/c$ and decreases to $\epsilon^{pair} \approx 3\%$ for large $p_{\mathrm{T,ee}}$.

10. Systematic Uncertainty

Every measurement comes with an intrinsic, so-called systematic uncertainty. Several sources for systematic uncertainties have to be identified and considered to estimate the total systematic uncertainty of the measurement. In this analysis, the track and electron identification requirements, the tracking performance, the contamination of the primary electron sample with hadrons and electrons from photon conversions contribute to the systematic uncertainty as well as the description of the background with the like-sign method. The following sections describe the procedure used to extract simultaneously the systematic uncertainty from all sources and one additional systematic uncertainty only related to the background estimation. Both are added in quadrature to obtain the final systematic uncertainty.

10.1. Selection Criteria Variation

To estimate the systematic uncertainty from the tracking, electron identification, hadron contamination and photon conversions in the material all electron selection criteria are varied simultaneously. These variations leads to various tracking efficiencies and to different levels of hadronic contamination of the electron candidate sample. The resulting uncorrected spectra have to be corrected with the according pair efficiency correction as described in section 9.3. With this approach a large range of signal to background ratios and significances are probed as shown in figure 8.13. Therefore, this method does not only allow for the systematic study of possible effects due to the tracking and electron identification but also provides a test of the background estimates.

The following track selection requirements are varied: $n^{\text{ITS}}_{\text{Cl.,min}}$, $\chi^2_{\text{max}}/n^{\text{ITS}}_{\text{Cl.}}$, $n^{\text{TPC}}_{\text{Cl.,min}}$, $n^{\text{TPC}}_{\text{cr. rows,min}}$, $\chi^2/n^{\text{TPC}}_{\text{Cl.,max}}$ and the ITS shared cluster scheme. With this variation the tracking resolution and the number of electrons from real photon conversions alters by significant amounts. The electron identification is based on three different identification schemes as described in section 7.2: *TOFif*, *TOFreq* and *HadrRej*. For all three schemes ten selection sets are chosen resulting in a total of 30 different selections. While for *TOFif* and *TOFreq* the n_σ-intervals are varied, the variation of the *HadrRej* approach consists of shifting the rejected kaon and proton bands individually by ± 0.5. All applied variations are listed in appendix F.

m_{ee} / $p_{T,ee}$	$0 < p_{T,ee} < 1\,GeV/c$	$1 < p_{T,ee} < 8\,GeV/c$	$p_{T,ee}$-integrated
$0 < m_{ee} < 0.14\,GeV/c^2$	0.38	0.11	0.32
$0.14 < m_{ee} < 5\,GeV/c^2$	0.35	0.13	0.27

Table 10.1.: Relative systematic uncertainties in several kinematic regions. Sel. 1-10, 11-20, 21-30 correspond to a scenario based on TOFif, TOFreq and HadrRej, respectively.

After the signal extraction and pair-efficiency correction statistical fluctuations are dominating any possible systematic deviations. To reduce statistical fluctuations and to quantify systematic uncertainties a coarse binning as a function of the invariant mass with only two bins ranging from $0 < m_{ee} < 0.14\,GeV/c^2$ and from $0.14 < m_{ee} < 5\,GeV/c^2$ was chosen. Additionally three pair transverse momentum ranges were chosen: $0 < p_{T,ee} < 1\,GeV/c$, $1 < p_{T,ee} < 8\,GeV/c$ and $p_{T,ee}$-integrated. Figure 10.1 shows the corrected yield in the two first mentioned kinematic regions. Track and electron selection 19 showed huge statistical fluctuations. Therefore, it deviated from the average value and was rejected beforehand. The dotted blue line indicates the average yield while the solid red line shows the statistics-weighted average. Selections 1-10 are based on the *TOFif*, while 11-20 are based on the *TOFreq* and 21-30 on the *HadrRej* selection schemes. At small invariant mass $m_{ee} < 0.14\,GeV/c^2$ schemes 1-20 and 21-30 appear to form two groups with systematically different yield. At higher masses $m_{ee} > 0.14\,GeV/c^2$ those groups vanish but overall fluctuations seem to dominate. Selection 5 was chosen as the reference selection because it is close to the weighted average.

The systematic uncertainty is then evaluated as the root-mean-square (RMS) of the distribution of all corrected yields weighted with their respective statistical uncertainty in a the coarse bins with respect to the average value and can be found in table 10.1. The systematic uncertainty at small momenta is larger compared to higher momenta where no further dependence on the momentum was seen.

10.2. R-Factor Variation

The different acceptance of like-sign and unlike-sign dielectron pairs is accounted for with the R-factor. A detailed explanation of the R-factor can be found in section 8.1.2. To estimate the systematic uncertainty of this correction the mixing-classes are varied according to table 10.2.

Figure 10.2 shows the effect on the corrected yield as function of the invariant mass for the 0-20% most central Pb-Pb events. All the 5 different distributions are compatible within their statistical uncertainties. Therefore, no systematic uncertainty regarding the R-factor is applied.

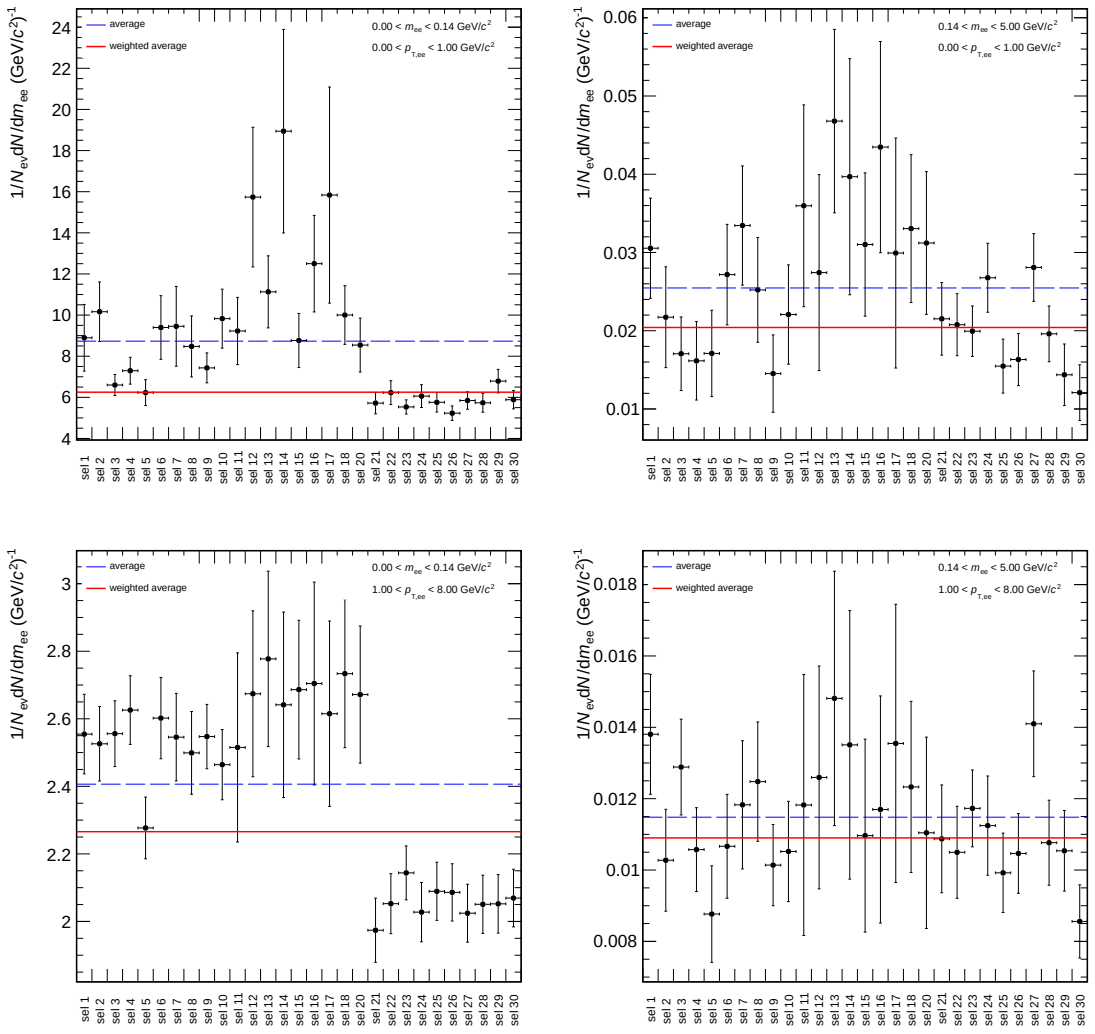

Figure 10.1.: Corrected yield for different track and electron selection schemes in different kinematic regions. The dotted blue line indicates the average yield while the solid red line shows the statistics-weighted average.

variation	z-vertex	centrality	event plane
1	-10, -5, 0, 5, 10	0, 5, 10, 20, 30, 50, 80	$-\pi/2$, $-\pi/4$, 0, $\pi/4$, $\pi/2$
2	-10, 0, 10	0, 5, 10, 20, 30, 50, 80	$-\pi/2$, $-\pi/4$, 0, $\pi/4$, $\pi/2$
3	-10, 5, 0, 5, 10	0, 5, 10, 20, 30, 50, 80	$-\pi/2$, $\pi/2$
4	-10, -5, 0, 5, 10	0, 10, 20, 30, 50, 80	$-\pi/2$, $-\pi/4$, 0, $\pi/4$, $\pi/2$
5	-10, -5, 0, 5, 10	0, 5, 10, 20, 30, 50, 80	$-\pi/2$, $\pi/2$ in 12 steps

Table 10.2.: Mixing classes to estimate systematic uncertainty of R-factor.

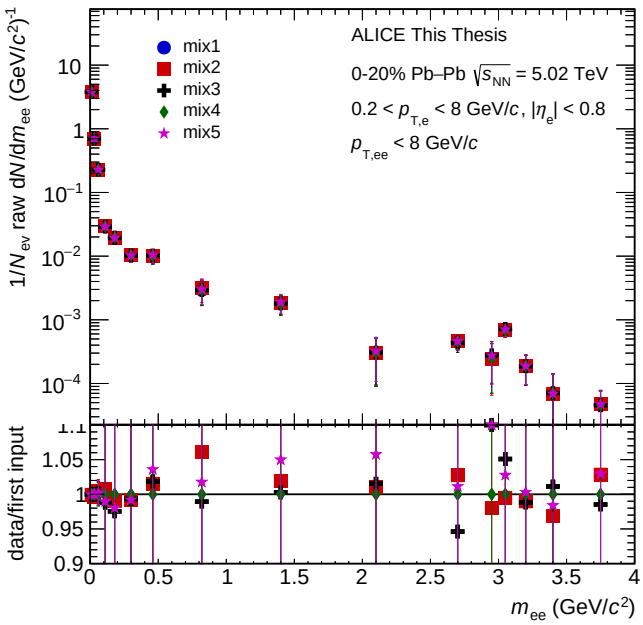

Figure 10.2.: Relative deviation of the different spectra obtained with varying mixing-classes in comparison to the standard selection.

11. Hadronic Cocktail

The extracted dielectron signal is compared to a so-called hadronic cocktail containing all known hadronic dielectron sources. Figure 11.1 shows the complete hadronic cocktail. All ingredients will be discussed in the following sections.

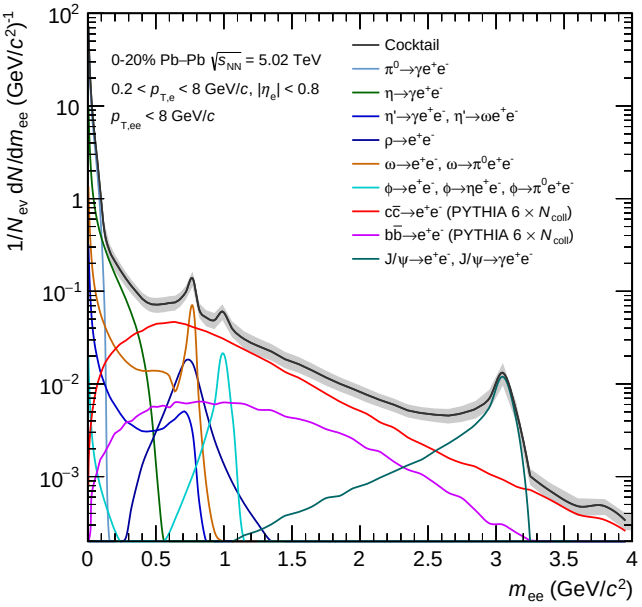

Figure 11.1.: Hadronic cocktail as described in sections 11.1, 11.2 and 11.3 for a minimum transverse momentum $p_T > 0.2\,\mathrm{GeV/c}$ and $|\eta| < 0.8$ in the 0-20% most central Pb-Pb collisions.

11.1. Light Flavour

The so-called light-flavour cocktail consists of dielectrons coming from the decay of light-flavour hadrons which are listed in table 11.1. The contributions of these particles to the dielectron spectrum are estimated with a simulation. The simulation is based on the event generator PYTHIA [71] together with the external decayer

Particle	decay	BR (%)
π^0	γe^+e^-	(1.174 ± 0.035)
η	γe^+e^-	$(6.9 \pm 0.4) \cdot 10^{-3}$
ρ	e^+e^-	$(4.72 \pm 0.05) \cdot 10^{-5}$
ω	e^+e^-	$(7.28 \pm 0.14) \cdot 10^{-5}$
	$\pi^0e^+e^-$	$(7.7 \pm 0.6) \cdot 10^{-4}$
η'	γe^+e^-	$< 9 \cdot 10^{-4}$
	ωe^+e^-	$(2.0 \pm 0.4) \cdot 10^{-4}$
ϕ	e^+e^-	$(2.954 \pm 0.030) \cdot 10^{-4}$
	ηe^+e^-	$(1.15 \pm 0.10) \cdot 10^{-4}$
	$\pi^0e^+e^-$	$(1.12 \pm 0.28) \cdot 10^{-5}$

Table 11.1.: Particles and their decays with according branching ratio contributing to the light-flavour cocktail [4].

EXODUS [112] and generates the respective particles according to the parametrisation of input spectra extracted from previous measurements. *EXODUS* simulates the two- and three-body decays of these generated particles into dielectrons. It is assumed that all mesons are produced unpolarized and with a flat rapidity distribution at mid-rapidity $|y| < 1.2$. The 3-body Dalitz decays are assumed to follow the Kroll-Wada equation, which can be found in equation 2.1. The shape is multiplied with electromagnetic form-factors measured by the NA60 collaboration [46]. While the mass shape of 2-body decays of ω and ϕ mesons follows the Gounaris-Sakurai formula [113], the mass shape of the $\rho \to e^+e^-$ decay was measured by the NA60 collaboration in proton-nucleus collisions at 400 GeV. The parametrisation of their result, which requires a Boltzmann-like term beyond the standard resonance peak description, is used in this analysis.

The input parametrizations of the decaying mesons are based on the measured preliminary $\pi^\pm$ spectrum [114] as a function of transverse momentum, which is presented in the left plot of figure 11.2. The π^0 spectrum is not measured at this time at small transverse momenta $p_\mathrm{T} \approx 0.2\,\mathrm{GeV}/c^2$ which is especially relevant for comparisons to the dielectron spectrum. Additionally, the statistical fluctuations and systematic uncertainties are much larger compared to the charged pion spectrum. At larger momenta the neutral and charged pions agree within their uncertainties as shown in figure 11.3 [115].

The $\pi^\pm$ spectra are summarized according to the centrality intervals which are used in this analysis 0-20%, 20-40% and 40-80%. To parametrize the distributions a ALICE-wide cocktail fitting framework is used. This framework includes predefined fitting functions and facilitates the whole fitting procedure. The $\pi^\pm$ spectra are

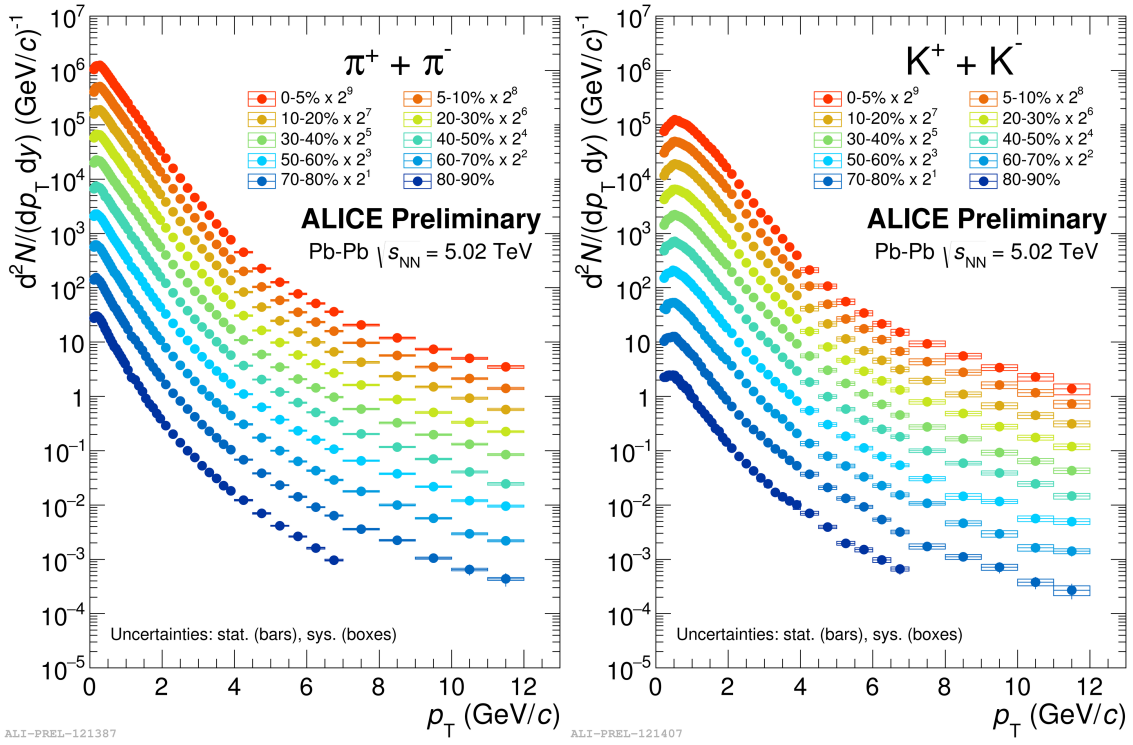

Figure 11.2.: $\pi^{\pm}$ and $K^{\pm}$ spectrum as a function of transverse momentum in several centrality classes in Pb-Pb collisions at $\sqrt{s_{\mathrm{NN}}} = 5.02\,\mathrm{TeV}$ [114].

parameterized with the following function which is named modified k-function:

$$\frac{a \cdot (\sqrt{p_{\mathrm{T}}^2 + m^2} - b \cdot p_{\mathrm{T}})}{\sqrt{1-b^2}} \cdot \exp^{\frac{b \cdot p_{\mathrm{T}} - \sqrt{p_{\mathrm{T}}^2 + m^2}}{c \cdot \sqrt{1-b^2}}} + \frac{d}{(\frac{1+p_{\mathrm{T}}}{e})^f} + \frac{g}{(\frac{1+p_{\mathrm{T}}}{h})^i} \tag{11.1}$$

with $a, b, c, d, e, f, g, h, i$ being parameters of the fit, p_{T} and m being the transverse momentum and mass of the given particle. Figure 11.4 shows the measured data and the parametrization of the charged pion spectrum in 0-20% most central Pb-Pb collisions at $\sqrt{s_{\mathrm{NN}}} = 5.02\,\mathrm{TeV}$. The deviation of the parameterisation to the measured spectrum was found to be smaller than 5% in all given centrality classes with a $\chi^2/\mathrm{ndf} = 48.35$. Additionally, the central values of the points were shifted according to their upper and lower systematic uncertainty, resulting in an upper and lower parametrization.

The measured $K^{\pm}$ is used as an approximation for the non-measured η spectrum. This approximation seems valid because the η meson and the kaon share similar rest masses. Figure 11.5 shows the parametrization of the $K^{\pm}/\pi^{\pm}$ ratio as function of the transverse momentum p_{T} with a maximum deviation at $p_{\mathrm{T}} = 11 - 12\,\mathrm{GeV}/c$ of $\approx 20\%$. The input spectra of all other light mesons ω, ρ, η' and ϕ are based of m_{T}-scaling of the $\pi^{\pm}$ spectrum. The concept of m_{T}-scaling [116] was introduced in 1965

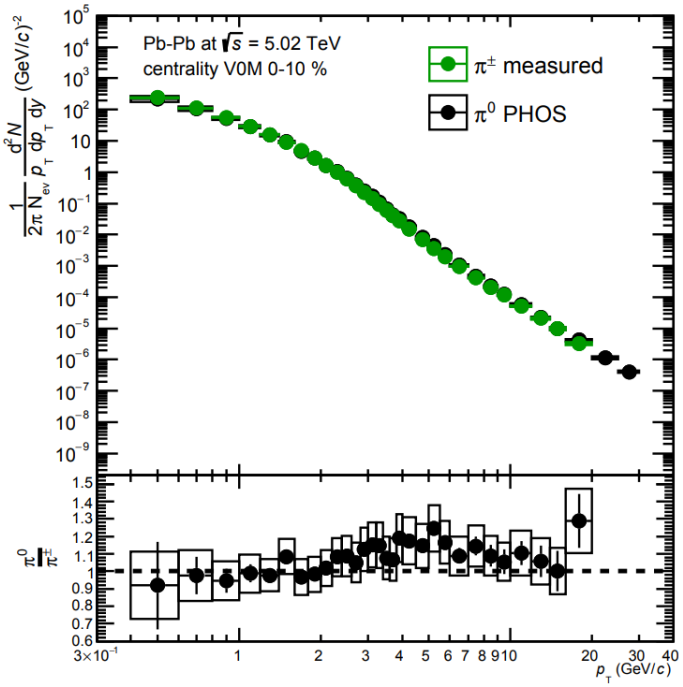

Figure 11.3.: $\pi^{\pm}$ and π^{0} spectra as a function of transverse momentum in 0-10% most central Pb-Pb collisions at $\sqrt{s_{\mathrm{NN}}} = 5.02\,\mathrm{TeV}$ [115].

by Hagedorn to describe hadron production in proton-proton collisions. It states that the transverse mass $m_{\mathrm{T}} = \sqrt{m^2_{\mathrm{meson}} - m^2_{\pi^0} + p^2_{\mathrm{T}}}$ spectrum of all produced hadrons should follow an exponential tail with the same slope parameter. A scaling factor for each meson is extracted from the ratio to the $\pi^{\pm}$ spectrum at high transverse momentum. The following extracted values where used:

- ρ m_{T}-scaling factor $= 1. \pm 0.2$ [117]
- ω m_{T}-scaling factor $= 0.85 \pm 0.17$ [118]
- η' m_{T}-scaling factor $= 0.4 \pm 0.08$ (extracted from PYTHIA 6 simulation [44])
- ϕ m_{T}-scaling factor $= 0.13 \pm 0.026$ [119]

The detector response matrices are applied to p_{T}, η and φ of all created electrons and positrons as described in section 9.1. Subsequently, the required acceptance cuts in p_{T} and η are applied on every single electron.

11.2. Heavy Flavour

$c\bar{c}$ and $b\bar{b}$ pairs are produced in hard processes at the beginning of the heavy-ion collision at a time-scale of $t = \frac{1}{2m_{\mathrm{Q}}} = 0.1\,\mathrm{fm}/c$ and $0.02\,\mathrm{fm}/c$ for charm and beauty

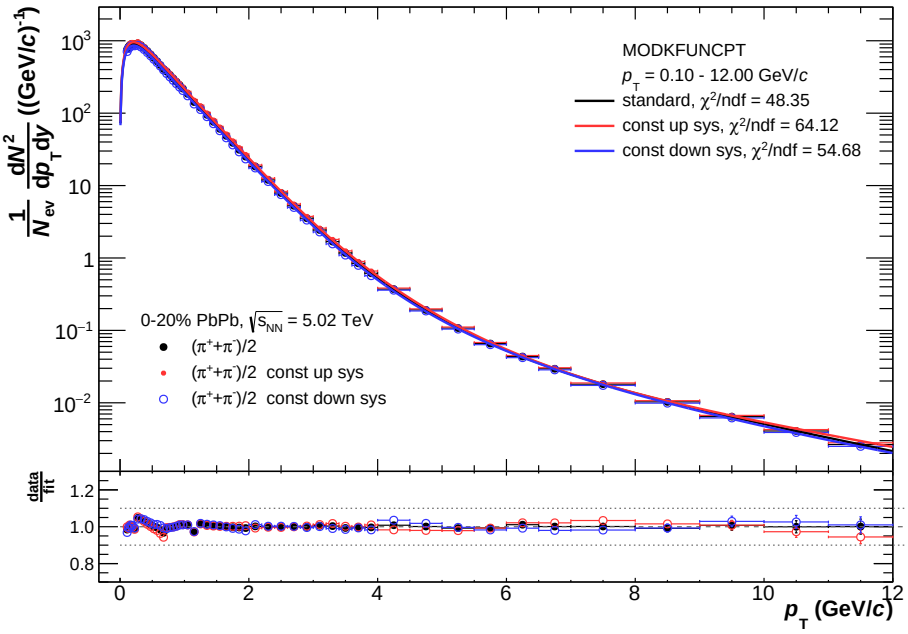

Figure 11.4.: Parametrization of $\pi^{\pm}$ spectrum as function of transverse momentum p_{T} in 0-20% most central Pb-Pb collisions at $\sqrt{s_{\mathrm{NN}}} = 5.02\,\mathrm{TeV}$ extracted with the common cocktail fitting framework. Black data points show the central value of the measured $\pi^{\pm}$ yield, red and blue points represent the upper and lower systematic, respectively.

quarks, respectively. They contribute also to the dielectron spectrum via the semileptonic decay of their fragmentation products, i.e. open-charm and open-beauty hadrons. The dielectron production of heavy-flavour hadron decays is estimated using the PYTHIA6 event generator with the Perugia2011 tune [120]. The results are normalized to the $c\bar{c}$ and $b\bar{b}$ production cross sections measured in pp collisions at $\sqrt{s} = 7\,\mathrm{TeV}$ scaled with the number of binary collisions $\langle N_{\mathrm{coll}} \rangle$ extracted from Glauber simulations. The scaling factors $\langle N_{\mathrm{coll}} \rangle$ can be found in section 6.4. The $c\bar{c}$ cross section is measured at mid-rapidity $\mathrm{d}\sigma^{c\bar{c}}_{\sqrt{s}=7\,\mathrm{TeV}}/\mathrm{d}y|_{y=0} = (0.954 \pm 0.119)\,\mathrm{mb}$ [48]. The total $b\bar{b}$ cross section is measured to be $\sigma^{b\bar{b}}_{\sqrt{s}=7\,\mathrm{TeV}} = (0.288 \pm 0.048)\,\mathrm{mb}$ [121]. To accommodate for the different collision energy, a pQCD-driven downscaling based on the so-called fixed-order next-to-leading logarithmic calculations (FONLL) [122, 123] was executed [124]. This FONLL model claims to describe the heavy-flavour production over a large range of transverse momenta. The resulting scaling factors are $0.83(+11.6\%, -2.4\%)$ for $\mathrm{d}\sigma^{c\bar{c}}_{\sqrt{s}=7\,\mathrm{TeV}}/\mathrm{d}y|_{y=0}$ and 0.71 $(+3.3\%, -1.8\%)$ for $\sigma^{b\bar{b}}_{\sqrt{s}=7\,\mathrm{TeV}}$. The systematic uncertainties of this procedure are dominated by the uncertainty of the factorisation scale, the renormalization scale and the bare quark masses used in the FONLL calculations [125, 126].

To safe computing time, the simulation of the contribution of $c\bar{c} \to e^+e^-$ requires at least one $c\bar{c}$-quark per event which is then forced to decay semileptonically into

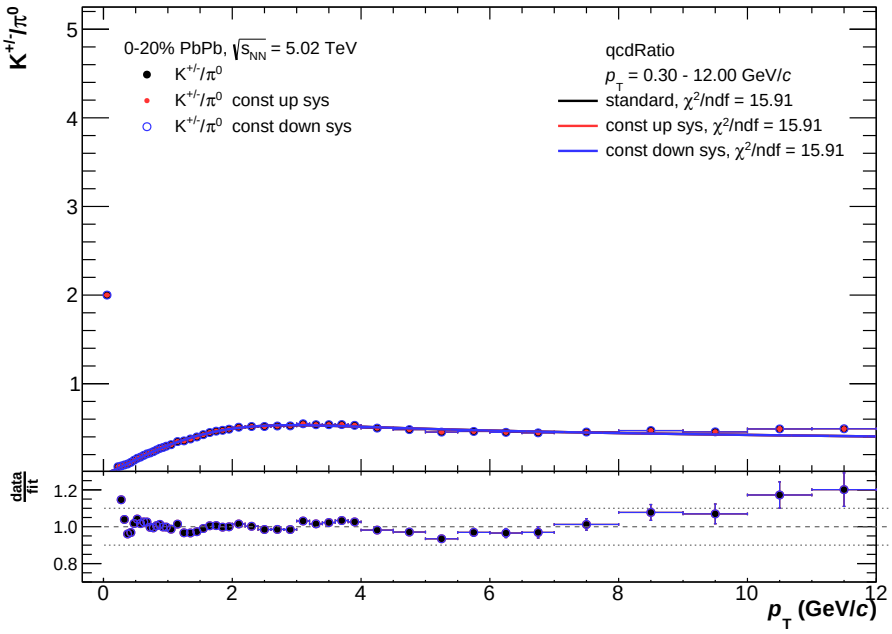

Figure 11.5.: Parametrization of $\pi^{\pm}/K^{\pm}$ ratio as function of transverse momentum p_{T} in 0-20% most central Pb-Pb collisions at $\sqrt{s_{\mathrm{NN}}} = 5.02\,\mathrm{TeV}$ extracted with the common cocktail fitting framework. Black data points show the central value of the measured $\pi^{\pm}$ yield, red and blue points represent the upper and lower systematic, respectively.

dielectrons. To normalize this contribution, it is scaled by the branching ratio of charmed hadron decays to electrons of $\mathrm{BR}_{c\to e} = 0.096 \pm 0.004$ [4]. An uncertainty of ± 0.009 to the branching ratio is added in quadrature to take into account differences between the Λ_c/D^0-ratio measured by ALICE [127] and the value measured by the LEP experiments [128]. These uncertainties add up to a total systematic uncertainty of the dielectron pair of $\pm 24\%$ estimated for proton-proton collisions. Due to different production cross sections in Pb-Pb collisions the branching ratio might still deviate from these results. The aforementioned time-saving procedure is not applicable for the contribution of $b\bar{b} \to e^+e^-$ because of the plethora of different decays and fragmentation processes which have to be taken into account correctly. The contribution of $b\bar{b} \to e^+e^-$ includes processes with an intermediate charmed hadron like $b \to B \to D \to e^-$. The branching ratios are directly taken from PYTHIA and agree within uncertainties with the PDG values [4].

The detector response matrix is applied as a function of p_{T}, η and φ to all created electrons and positrons. Afterwards the acceptance selections as a function of p_{T} and η are applied to every single electron. From those smeared electrons and positrons unlike-pairs and like-pairs are formed. To be consistent with data analysis the final spectrum is obtained by subtracting the like-sign from the unlike-sign spectrum.

So far, this approach neglects any hot- or cold-nuclear matter effects which can affect the heavy-flavour production in heavy-ion collisions. To estimate the impact of cold-nuclear matter effects, like shadowing, on the contribution coming from $c\bar{c}$ a weighting method based on the nuclear modification factor R_{AA} of charm quarks [129] is introduced. The nuclear modification factor is typically defined as the yield measured in Pb-Pb collisions $N_{\mathrm{Pb\text{-}Pb}}$ over the yield measured in proton-proton collisions N_{pp} scaled by the number of binary collisions N_{coll}:

$$R_{\mathrm{AA}} = \frac{N_{\mathrm{Pb\text{-}Pb}}}{N_{\mathrm{coll}} \cdot N_{\mathrm{pp}}} \tag{11.2}$$

Two different calculations including the nuclear modification factor R_{AA} of charm quarks have been performed. The first calculation was done using CTEQ10 parton distribution functions (PDF) [130] and EPPS16 [131] nuclear modification. The resulting R_{AA} distribution is shown in figure 11.6. The second calculation is based on CTEQ6M PDFs [132] and EPS09NLO [133]. Both CTEQ PDFs are constructed via a global fit on measured data from deep-inelastic scattering experiments like HERA-1 and ZEUS. Additionally, the more recent CTEQ10 parametrization includes improved measurements from the experiments CDF and DØ. EPPS16 and EPS09NLO are nuclear PDFs describing the modifications of the parton distribution when these partons are within a nucleus, like in the Pb nucleus. The uncertainty of the more recent EPPS16 calculation is larger because of the authors choice to add more degrees of freedom to the calculation which have only minimal constraints from data. Nevertheless, the measurements of D-meson production in p-Pb collisions in ALICE [134] and LHCb [135] are in agreement with the EPS09 calculations and therefore also with EPPS16. The weight of a dielectron is then calculated as the average R_{AA} of both initial charm quarks assuming that the charm production is fully correlated:

$$\omega(\mathrm{e^+e^-}) = \frac{1}{2} \cdot (R_{\mathrm{AA}}(p_{\mathrm{T},c}) + R_{\mathrm{AA}}(p_{\mathrm{T},\bar{c}})) \tag{11.3}$$

Applying the according weight to every dielectron originating from a $c\bar{c}$-pair results in a suppression of the $c\bar{c} \to e^+e^-$ contribution. The left plot in figure 11.7 shows the contributions of semileptonic open-charm hadron decays modified with both presented methods in violet (EPPS16) and blue (EPS09). The uncertainty band corresponds to the uncertainty of the nPDFs. Cold-nuclear matter effects are expected to have a smaller impact on the beauty contribution which is why no modifications of the spectrum are considered.

A second method to further understand possible medium modifications of the charm contribution is based on the measured nuclear modification factor R_{AA} of single electrons coming from semileptonic heavy-flavour hadron decays (HFE R_{AA}): $c, b \to$

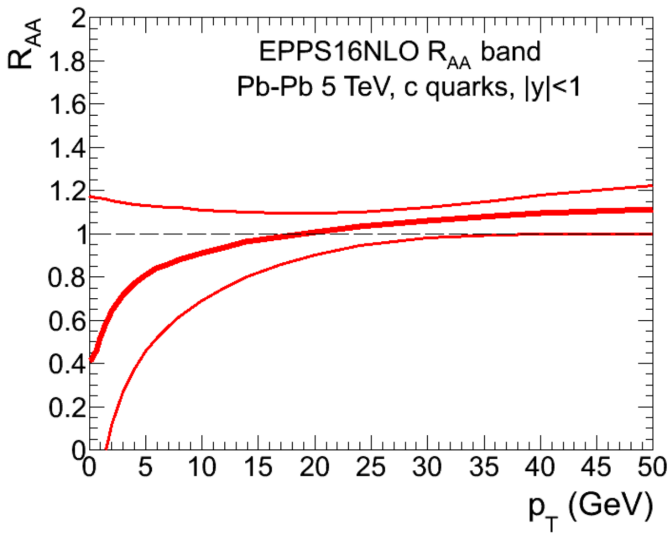

Figure 11.6.: Nuclear modification factor of charm quarks at mid-rapidity using calculations with CTEQ10 PDFs and EPPS16 nuclear modification. The uncertainty band corresponds to the EPPS16 uncertainty.

e. This approach does not only include cold-nuclear matter effects but also hot-nuclear matter effects like energy loss of heavy quarks in the medium and collectivity effects. In figure 11.8, the measured R_{AA} as a function of p_{T} is shown for three centrality classes [136]. The measurement is performed with a minimum transverse momentum of the electron of $p_{\mathrm{T}} > 0.5\,\mathrm{GeV}/c$. An extrapolation with a constant fitted to the data points in $0.5 < p_{\mathrm{T}} < 1\,\mathrm{GeV}/c$ is done to estimate values to lower momenta. An unexpected ordering of the data points at small transverse momenta as a function of the centrality can be observed. The data points for the 30-50% most central Pb-Pb collisions are below the other centrality classes. However, taking into account the systematic uncertainties of all three measurements this unexpected effect is not significant. The systematic uncertainties of the R_{AA} measurement are propagated into the final results.

The weight estimation is performed assuming two different extreme scenarios: In one scenario it is assumed that the suppression of the electron and positron are fully correlated like it is the case for cold-nuclear matter effects. Therefore, the mean of the R_{AA} of both electrons is used. In the other scenario, the suppression of the electrons and positrons are considered to be fully uncorrelated leading to the usage of the product:

$$\omega_{\mathrm{correlated}}(\mathrm{e^+e^-}) = \frac{1}{2}(R_{\mathrm{AA}}(p_{\mathrm{T,\,e^+}}) + R_{\mathrm{AA}}(p_{\mathrm{T,\,e^-}}))$$
$$\omega_{\mathrm{uncorrelated}}(\mathrm{e^+e^-}) = R_{\mathrm{AA}}(p_{\mathrm{T,\,e^+}}) \cdot R_{\mathrm{AA}}(p_{\mathrm{T,\,e^-}})$$

The modification is applied separately in the measured centrality classes. The effect

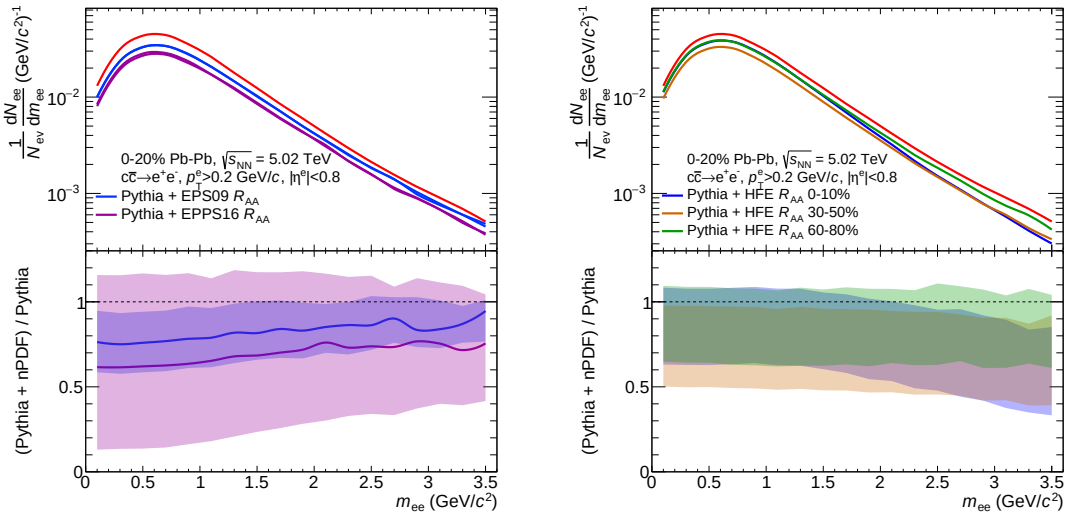

Figure 11.7.: Dielectron yield from semi-leptonic open-charm hadron decays. The vacuum contribution is compared to modified contributions calculated with two different methods. The left panel shows the effect of applying EPPS16 and EPS09 nPDFs. The uncertainty band corresponds to the systematic uncertainty of the according nPDF. In the right panel the effect of the weighting according to the nuclear modification factor of single electrons from heavy-flavour hadron decays is shown. The uncertainty bands indicate the limits assuming full correlation or no correlation between the resulting electrons.

of the HFE R_{AA} is summarized in the right plot of figure 11.7 as a function of invariant mass m_{ee} integrated over pair transverse momentum $p_{\mathrm{T,ee}}$. In contrast to the modification with EPPS16 and EPS09 which shows an almost constant suppression of the yield as a function of invariant mass, the effect of the HFE R_{AA} at the most central events indicates a mass-dependency in comparison to the vacuum expectation. Especially at higher masses, $m_{\mathrm{ee}} > 1.5\,\mathrm{GeV}/c^2$, the suppression increases for more central events. These dielectrons with large invariant mass originate predominantly from high-p_{T} D mesons and have large electron transverse momentum. Their yield is shifted towards lower electron transverse momenta and invariant mass due to the energy-loss mechanism of charm quarks in the QGP. A caveat of this method is the usage of single heavy-flavour electrons, including the beauty contribution, in comparison to electrons originating from open-charm hadrons only. However, at small transverse momentum $p_{\mathrm{T,ee}} < 3\,\mathrm{GeV}/c$ the charm contribution is expected to dominate the heavy-flavour contribution.

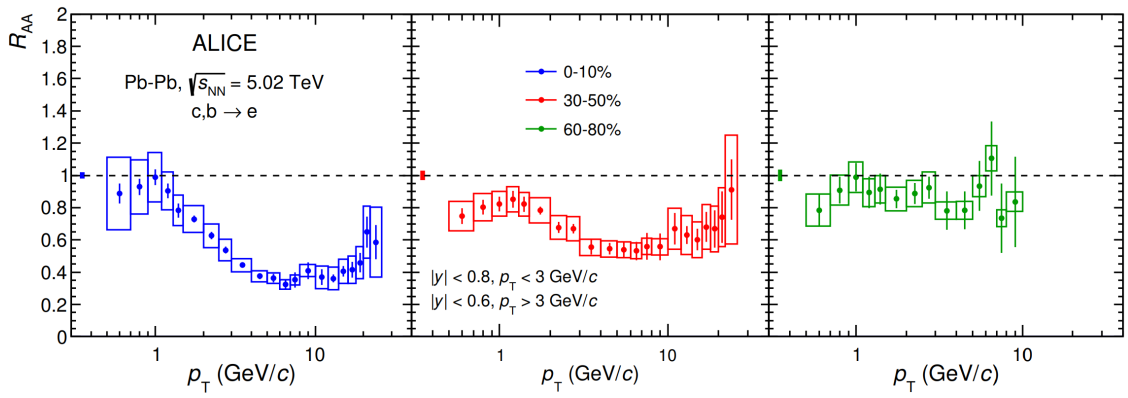

Figure 11.8.: Nuclear modification factor R_{AA} as a function of transverse momentum p_{T} for single electrons coming from heavy-flavour decays for three centrality classes in Pb-Pb collisions $\sqrt{s_{\mathrm{NN}}} = 5.02\,\mathrm{TeV}$ [136].

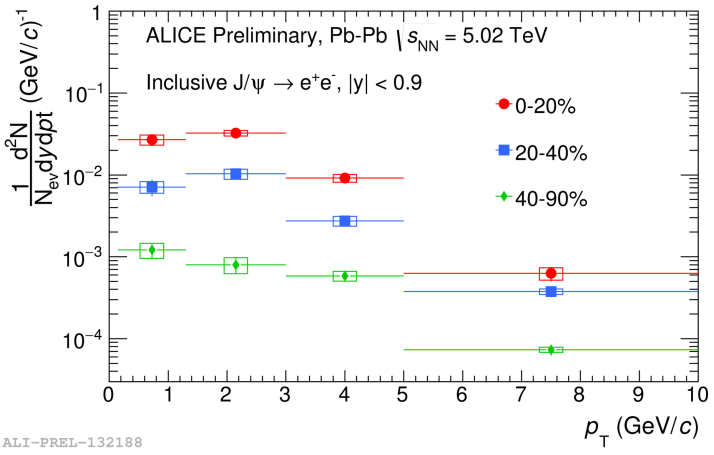

Figure 11.9.: J/ψ yield as a function of transverse momentum for three centrality classes in Pb-Pb collisions at $\sqrt{s_{\mathrm{NN}}} = 5.02\,\mathrm{TeV}$ [137].

11.3. J/ψ

The J/ψ contribution to the hadronic cocktail originates from the measured transverse momentum spectrum of the J/ψ meson. The according spectrum can be seen in figure 11.9 [137]. The spectra are parametrized with the function

$$N(p_{\mathrm{T}}) = a \cdot p_{\mathrm{T}} \cdot (\exp^{-b \cdot p_{\mathrm{T}} - |c| \cdot p_{\mathrm{T}}^2} + \frac{p_{\mathrm{T}}}{c})^{-d} \tag{11.4}$$

where a, b c and d are free parameters. To obtain the J/ψ contribution a fast simulation is performed. This fast simulation generates J/ψ according to the parametrized J/ψ transverse momentum spectrum and decays those particles into dielectrons taking into account radiative processes and the application of the detector response

Particle	BR	m_{T}	N_{coll}	cross section	fit	FONLL scaling
π^0	2.98	0	0	0	0	0
η	5.8	-15, +10	0	0	0	0
η'	6.38	20	0	0	0	0
ρ	1.11	20	0	0	0	0
ω	1.92	20	0	0	0	0
ϕ	1.02	30	0	0	0	0
J/ψ	0.54	0	0	0	30	0
$c\bar{c}$	24	0	2	10.2	0	+11.6, -2.4
$b\bar{b}$	10	0	2	30.4	0	+3.3, -1.8

Table 11.2.: Mass-independent relative systematic hadronic cocktail uncertainties in percent. These uncertainties are applied to their corresponding particle by adding them quadratically.

matrix as well as the kinematic selections on single electrons.

The contribution from ψ(2S) decays is not considered due to the lack of measured cross sections at mid-rapidity and missing sensitivity in this dielectron analysis.

11.4. Cocktail Uncertainties

Every cocktail contribution in this analysis has different sources of systematic uncertainties, like the uncertainty on the branching ratio (BR), m_{T}-scaling factors, number of binary collisions from Glauber simulations, measured cross sections, J/ψ-fit parameters and FONLL scaling factors of heavy-flavour cross sections. To estimate the total systematic uncertainty all uncertainties per contribution are added in quadrature. The relativ uncertainties are summarized in table 11.2.

The measured $K^{\pm}$ spectrum serves as an approximation for the η input spectrum. The η contribution to the cocktail can also be calculated via m_{T}-scaling as done for the other light mesons. The upper panel of figure 11.10 shows the dielectron cocktail contribution as a function of the pair transverse momentum $p_{\mathrm{T,ee}}$ of the η meson assuming the $K^{\pm}/\pi\pm$ ratio (red) and m_{T}-scaling as input. The lower panel shows the ratio of both. The difference of both resulting cocktail spectra is accounted for with an additional mass-independent uncertainty of -15% and +10%.

To estimate the systematic uncertainty of the parametrization of the π^0, the input spectra are fitted to the upper and lower edge of the systematic uncertainty of the charged pion p_{T} spectrum. These two parametrizations are used as the base-

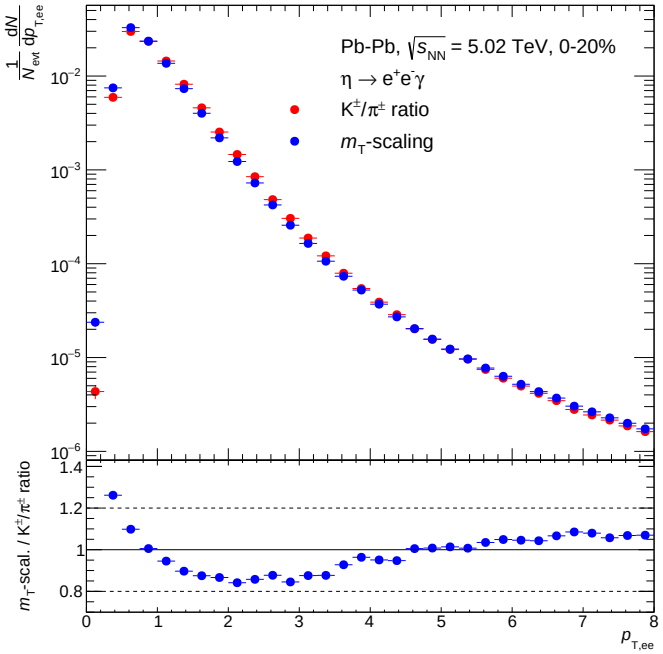

Figure 11.10.: Dielectron pair transverse momentum $p_{\mathrm{T,ee}}$ spectrum of the simulated η meson Dalitz decay for the hadronic cocktail. Red data points illustrate the result using the $K^{\pm}/\pi\pm$ ratio as input, blue data points show the yield assuming m_{T}-scaling.

line of two new dielectron cocktail calculations and act as the upper and lower systematic uncertainty of the parametrization of the light-flavour hadronic cocktail. Additionally, to account for the difference of neutral pions and charged pions a mass-independent uncertainty of 20% is assumed. The uncertainty of the parametrization of the J/ψ is estimated to be 30%.

To get a precise measurement of the thermal contribution of the QGP in the intermediate mass range $1.1 < m_{\mathrm{ee}} < 2.9\,\mathrm{GeV}/c^2$ the systematic uncertainty of the charm and beauty contribution have to be reduced. Especially the uncertainty of the branching ratio of $c\bar{c} \rightarrow e^+e^-$, which is dominated by the uncertainty of the Λ_c cross section measurement, has to be better understood.

The uncertainties on the neutral pion parametrization, the m_{T}-scaling factors, the branching ratio and the uncertainty on the heavy-flavour cross sections are shown together with the sum of all uncertainties as a function of invariant mass m_{ee} in figure 11.11.

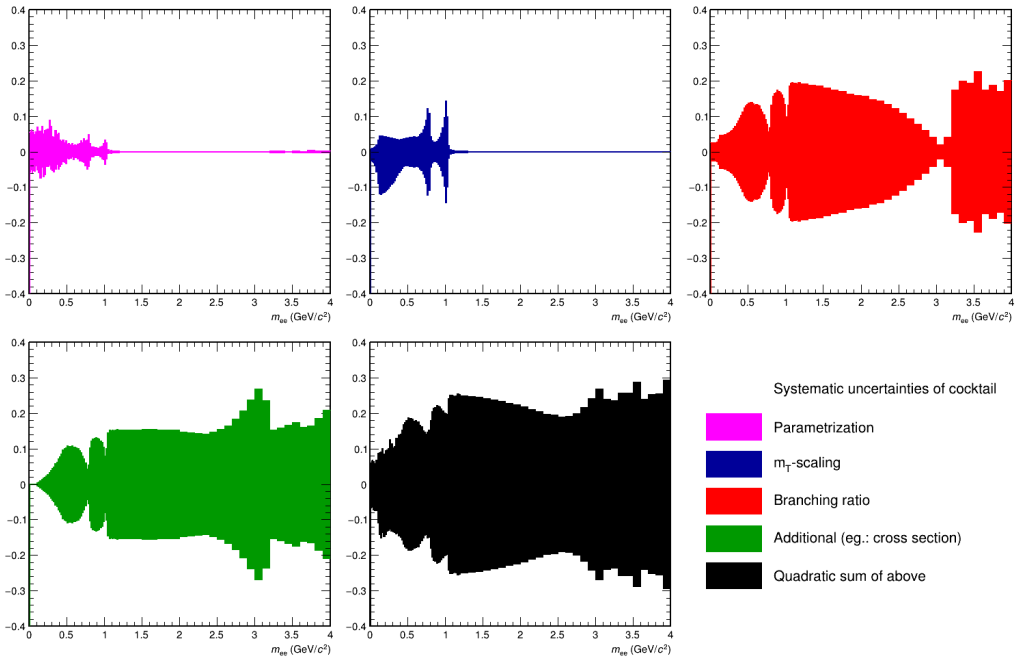

Figure 11.11.: Total relative hadronic cocktail uncertainty as a function of the invariant mass together with several selected uncertainties.

12. Results

In this chapter the results of this analysis are presented. Fully corrected dielectron spectra are compared to the hadronic cocktail based on ALICE measurements and additionally to two theoretical predictions including in-medium modifications of the ρ meson. Furthermore, the direct virtual photon yield as a function of transverse momentum is extracted and compared to previous measurements in Pb-Pb collisions at a center-of-mass energy of $\sqrt{s_{\mathrm{NN}}} = 2.76\,\mathrm{TeV}$.

12.1. Dielectron Spectra

In this section, the first dielectron measurements in Pb-Pb collisions at a center-of-mass energy of $\sqrt{s_{\mathrm{NN}}} = 5.02\,\mathrm{TeV}$ for several centrality classes are presented. These dielectron yields are illustrated as fully-corrected spectra within the acceptance requirements $p_{\mathrm{T}} > 0.2\,\mathrm{GeV}/c$ and $|\eta| < 0.8$ for the decay electrons. This analysis is the first dielectron measurement in nucleus-nucleus collisions at the LHC with a single electron momentum of $p_{\mathrm{T}} > 0.2\,\mathrm{GeV}/c$. This allows for the first time to study dielectrons with both small invariant masses and small transverse momenta. This analysis also serves as a feasibility study for future high-precision and high-statistics measurements at LHC run 3 starting in 2021.

Figure 12.1 shows the fully corrected dielectron spectrum as a function of the invariant mass m_{ee} integrated over the pair transverse momentum $p_{\mathrm{T,ee}}$ in Pb-Pb collisions at $\sqrt{s_{\mathrm{NN}}} = 5.02\,\mathrm{TeV}$ for several centrality intervals in the ALICE acceptance. The data are compared to the hadronic cocktail expectations without medium modifications of the charm and beauty contribution and without thermal radiation. While the error bars describe statistical uncertainties, the boxes show systematic uncertainties. The grey band around the total cocktail expectation represents systematic uncertainties of the cocktail. The lower panel shows the ratio between data and cocktail. More corrected spectra in several centrality classes in different kinematic regions are presented in appendix G.

Throughout all centrality classes the hadronic cocktail expectations and data are in good agreement in the region $2.9 < m_{\mathrm{ee}} < 3.3\,\mathrm{GeV}/c^2$ around the J/ψ and in the very low-mass region $m_{\mathrm{ee}} < 0.14\,\mathrm{GeV}/c^2$ which is dominated by the Dalitz decay

Centrality (%)	data over cocktail	stat.	syst.	cocktail	significance
0-20	1.42	± 0.23	± 0.22	± 0.09	1.23σ
20-40	1.31	± 0.24	± 0.23	± 0.08	0.91σ
40-80	0.89	± 0.15	± 0.16	± 0.06	0.48σ

Table 12.1.: Data-over-cocktail ratio in the invariant mass region $0.14 < m_{\mathrm{ee}} < 0.54\,\mathrm{GeV}/c^2$ for different centrality classes in Pb-Pb collisions at $\sqrt{s_{\mathrm{NN}}} = 5.02\,\mathrm{TeV}$.

of the neutral pion. This behaviour is expected because both, the π^0 and the J/ψ contribution estimated in the hadronic cocktail are based on ALICE measurements at the same collision energy and centrality class. Figure 12.2 shows the dielectron spectrum as a function of the pair transverse momentum in several invariant mass intervals. These spectra show a good agreement of the dielectron yield measured in the J/ψ region over the complete $p_{\mathrm{T,ee}}$ range while the dielectron measurement in the π^0 region seems to overshoot the cocktail estimation at higher momentum. This small deviation is also partially seen in other dielectron measurements at different energies and collision systems within ALICE and is not well understood but might be related to direct photon production [44, 77]. For invariant masses larger than $m_{\mathrm{ee}} > 3.5\,\mathrm{GeV}/c^2$ fluctuations in the measured unlike-sign and like-sign spectra dominate, resulting in large statistical uncertainties which currently limits the analysis at high invariant masses.

In the mass range directly above the pion mass which is dominated by the η contribution and by correlated semileptonic heavy-flavour hadron decays the data points are slightly above the cocktail expectation. This phenomenon is typically attributed to a contribution of thermal radiation of the produced QGP and hadron gas. Table 12.1 shows the enhancement of the data over the hadronic cocktail in three centrality classes. As expected, this effect is most pronounced in central collisions compared to peripheral events where the thermal contribution is predicted to be the largest. This enhancement in terms of direct photon contribution will be further discussed in section 12.3. Section 12.4 shows this enhancement in comparison with theory prediction.

In the mass range which is dominated by the contribution of dielectrons from semileptonic heavy-flavour hadron decays $0.54 < m_{\mathrm{ee}} < 2.5\,\mathrm{GeV}/c^2$ the hadronic cocktail overestimates the data. This observation is discussed in the following section 12.2.

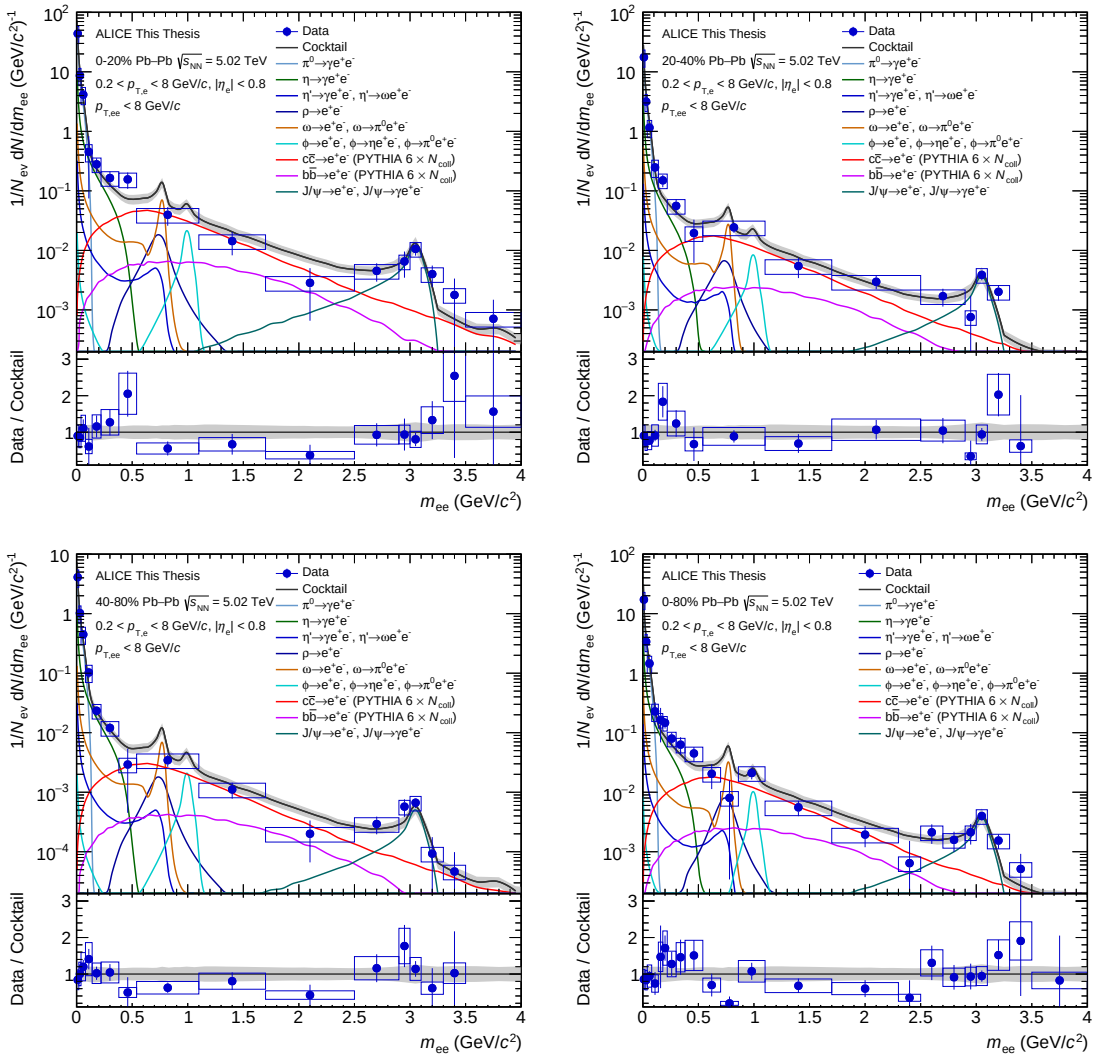

Figure 12.1.: Fully corrected dielectron yield as a function of the invariant mass m_{ee} integrated over pair transverse momentum $p_{T,ee}$ in Pb-Pb collisions in several centrality intervals at $\sqrt{s_{NN}} = 5.02\,\text{TeV}$ in the ALICE acceptance compared to the hadronic cocktail expectations without any medium effects. While error bars describe statistical uncertainties, boxes depict systematic uncertainties. The grey band around the total cocktail expectation represents systematic uncertainties of the cocktail. The lower panel shows the ratio between data and cocktail.

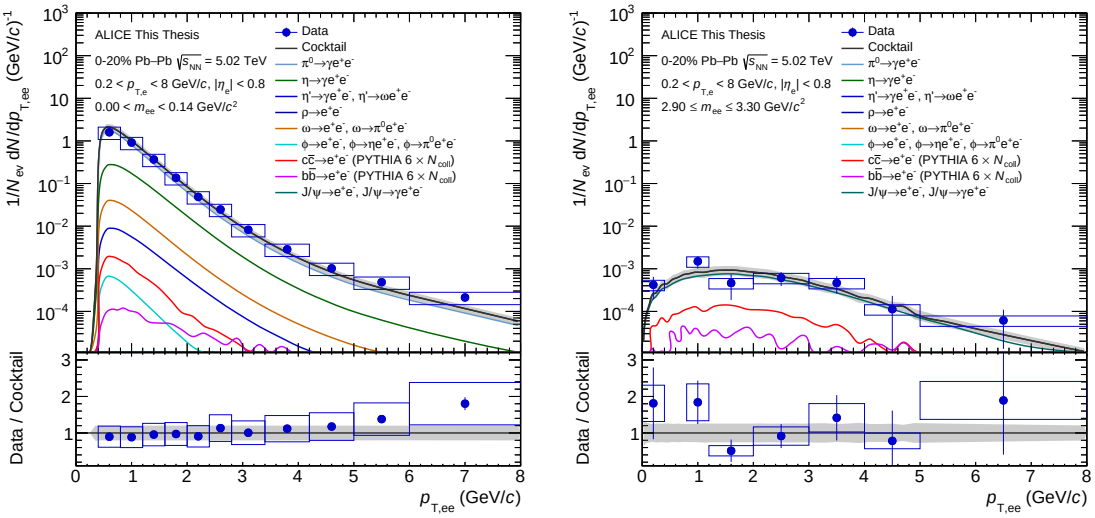

Figure 12.2.: Fully corrected dielectron yield as a function of the pair transverse momentum $p_{\mathrm{T,ee}}$ in the invariant mass interval $0 < m_{\mathrm{ee}} < 0.14\,\mathrm{GeV}/c^2$ (left) and $2.9 < m_{\mathrm{ee}} < 3.3\,\mathrm{GeV}/c^2$ (right) in the 0-20% most central Pb-Pb collisions at $\sqrt{s_{\mathrm{NN}}} = 5.02\,\mathrm{TeV}$ in the ALICE acceptance compared to the hadronic cocktail expectations.

12.2. Heavy-flavour Modification

The semileptonic heavy-flavour hadron decay contribution to the hadronic cocktail dominates over a wide range of invariant masses, $0.54 < m_{\mathrm{ee}} < 2.5\,\mathrm{GeV}/c^2$. While for smaller pair transverse momentum, $p_{\mathrm{T,ee}} \lesssim 3\,\mathrm{GeV}/c$, the dominating contribution originates from semileptonic open $c\bar{c}$ meson decays, for higher momenta the contribution from semileptonic open $b\bar{b}$ meson decays outweighs all other components. A comparison of the measured data to the hadronic cocktail in the aforementioned invariant mass interval shows that the data are systematically below the hadronic cocktail, as can be seen in figure 12.1. The contribution by semileptonic open-charm hadron decays, which is shown here, is not modified by cold- or hot-nuclear matter effects. To quantify this effect, the measured dielectron yield and the hadronic cocktail are integrated in this particular invariant mass range are compared to each other. Figure 12.3 shows the data-over-cocktail ratio in several centrality classes. The uncertainty of the cocktail calculation is shown with a gray band. The suppression factors extracted from data are summarized in table 12.2.

To estimate a combined suppression factor, the assumption is made that the modification of the charm and beauty contribution at low pair transverse momenta $p_{\mathrm{T,ee}}$ and invariant mass m_{ee} has a weak centrality dependence which can be neglected. Under this assumption a constant is fitted to the data-over-cocktail ratio in the centrality classes 0-20%, 20-40% and 40-80%. The result of the fit is indicated by the

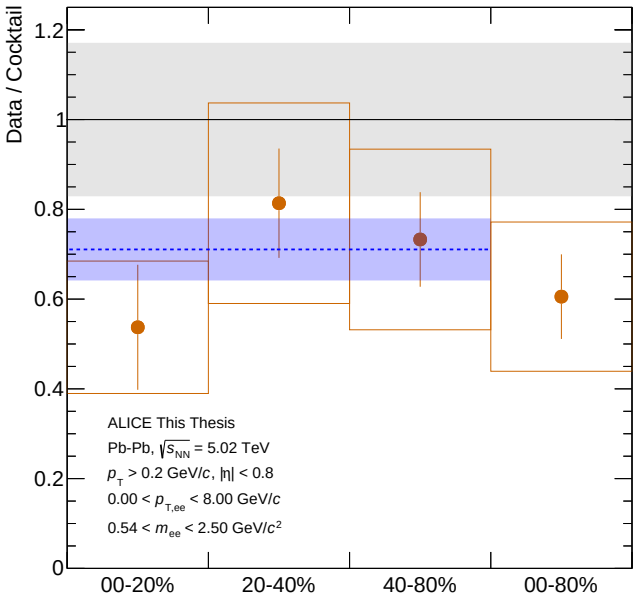

Figure 12.3.: Ratio of measured dielectron yield over expected hadronic cocktail in the mass range where the contribution of dielectron from semileptonic heavy-flavour hadron decays dominates the cocktail. While the dotted line indicates a constant value fitted to the data points, the blue band indicates the uncertainty of the fit. The gray band represents the hadronic cocktail uncertainties.

blue dotted line with the statistical uncertainty depicted by the blue band. This combined suppression factor is also shown in table 12.2. Considering only statistical uncertainties the suppression of the data in comparison to the hadronic cocktail has a significance of about 4.2σ while taking into account also the systematic uncertainty of the measurement and of the hadronic cocktail the significance drops to 1.2σ.

The assumption that medium effects are centrality-independent neglects the fact that hot-medium effects show a centrality dependence: i.e. the total energy loss of heavy-flavour quarks traversing the medium is dependent on the quark-gluon plasma size and therefore is also dependent on the centrality. This energy loss mechanism leads to a momentum shift of the heavy-flavour hadrons towards lower momenta and therefore to softer decay electrons. Consequently the invariant mass shape of dielectrons from heavy-flavour hadron decays is modified in Pb-Pb collisions compared to the vacuum expectation. Therefore, hot-nuclear matter effects should lead to a larger suppression of the data in comparison to the vacuum hadronic cocktail in central Pb-Pb collisions in this intermediate invariant mass range.

In chapter 11.2 two methods were introduced to modify the charm contribution with respect to medium effects. The first method is based on theoretical inputs

Centrality (%)	data over cocktail	stat.	syst.	cocktail	significance
0-20	0.53	± 0.14	± 0.15	± 0.09	2.1σ
20-40	0.81	± 0.12	± 0.22	± 0.14	0.7σ
40-80	0.73	± 0.11	± 0.20	± 0.12	1.0σ
0-80	0.61	± 0.09	± 0.16	± 0.10	1.9σ
combined	0.71	± 0.07	± 0.20	± 0.12	1.2σ

Table 12.2.: Data-over-cocktail ratio in the invariant mass region $0.54 < m_{\mathrm{ee}} < 2.5\,\mathrm{GeV}/c^2$ for different centrality classes in Pb-Pb collisions at $\sqrt{s_{\mathrm{NN}}} = 5.02\,\mathrm{TeV}$ and a combined fit over the different centrality classes.

regarding the modification of the parton distribution function taking into account only cold-nuclear matter effects like shadowing (EPPS16 and EPS09) and no hot-nuclear matter effects. The second method is based on the ALICE measurement of the nuclear modification factor R_{AA} of single electrons originating from heavy-flavour hadron decays in the same collision system Pb-Pb at $\sqrt{s_{\mathrm{NN}}} = 5.02\,\mathrm{TeV}$. These heavy-flavour hadrons and therefore also the measured electrons are affected by cold- and hot-nuclear matter effects. The resulting modified contributions to the hadronic cocktail from $c\bar{c}$ decays are compatible with the extracted suppression factors. In figure 12.4 the result of the charm modification on the hadronic cocktail is presented in comparison to the measured dielectron yield in the 0-20% centrality class. An improved description of the data is achieved. However, the statistical and systematic uncertainties of the dielectron data, and the systematic uncertainty of the nuclear modification factors do not allow for a quantitative investigation of the impact of cold- and hot-nuclear matter effects regarding the contribution of dielectrons from heavy-flavour hadron decay.

The contribution of correlated semileptonic $b\bar{b}$ decays is also expected to be modified by cold- and hot-nuclear matter effects. However, due to the dominance of the contribution from charmed hadron decays, this effect is negligible for the integrated invariant mass spectra.

12.3. Direct Photon Extraction

The dielectron spectrum measured in nucleus-nucleus collisions is expected to include an additional contribution from virtual direct photons which is not included in the hadronic cocktail presented in chapter 11. This contribution is twofold: At small transverse momenta $p_{\mathrm{T,ee}}$, thermal production of virtual photons is expected to dominate. At higher $p_{\mathrm{T,ee}}$ virtual direct photons produced in hard processes become more relevant. Virtual direct photons are directly correlated to real direct photons. The latter can be measured via electromagnetic calorimeters or the photon

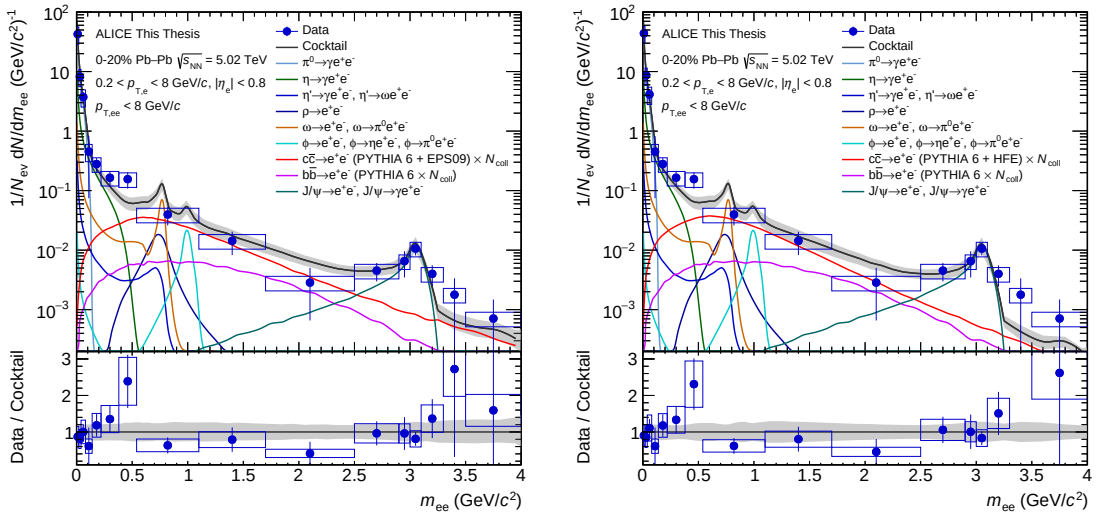

Figure 12.4.: Fully corrected dielectron spectrum in comparison to two hadronic cocktails including EPS09-modified (left) and heavy-flavour electron R_{AA}-modified (right) contributions from semileptonic $c\bar{c}$ hadron decays.

conversion method [138, 139]. These measurements usually have large systematic uncertainties at $p_T < 5\,\mathrm{GeV}/c$ due to the large background from decay photons. The measurement of virtual direct photons via dielectrons has the advantage that by selecting an invariant mass range $m_{ee} > m_{\pi^0}$ the photon contribution from π^0 decays can be suppressed and therefore systematic uncertainties are reduced. The drawback of this approach is the small internal conversion probability $\mathcal{O}(10^{-2})$ and the rapidly decreasing cross section as a function of the invariant mass [44]. The virtual photon production is connected to the real photon production by the Kroll-Wada equation [45] which can be simplified in the limit $p_{T,ee} \gg m_{ee}$.

In this analysis the virtual photon spectrum is simulated according to the Kroll-Wada equation as a function of the invariant mass and the pair transverse momentum. This spectrum is smeared according to the detector resolution as described in section 9.1. The acceptance requirements $p_T > 0.2\,\mathrm{GeV}/c$ and $|\eta| < 0.8$ are applied. The resulting spectrum is used as a template f_{dir} to estimate the virtual direct photon contribution. The measured invariant mass distributions are fitted in several transverse momentum ranges with a three-component function:

$$\frac{\mathrm{d}N}{\mathrm{d}m_{ee}} = f(m_{ee}, r) = r \cdot f_{dir}(m_{ee}) + (1 - r) \cdot f_{LF}(m_{ee}) + f_{HF}(m_{ee}) \tag{12.1}$$

with f_{LF}, f_{HF} and r being the invariant mass parametrization of the light-flavour contribution to the hadronic cocktail, the absolute normalized contribution from semileptonic heavy-flavour hadron decays and the fit parameter, respectively. The

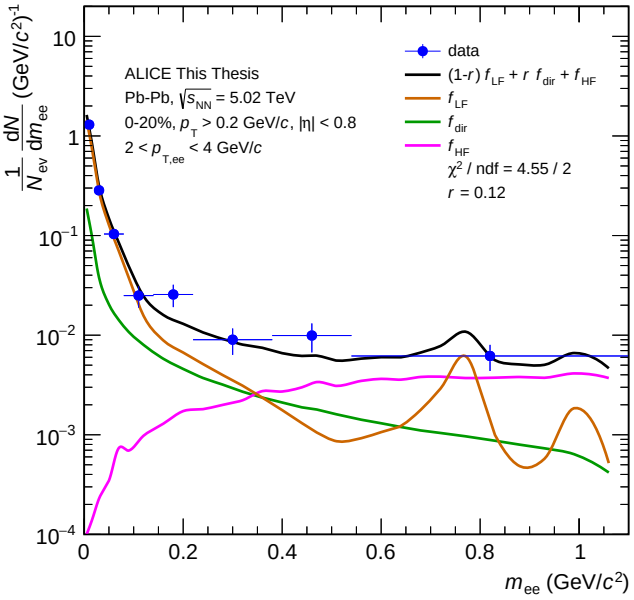

Figure 12.5.: Invariant mass spectrum in the pair transverse momentum range $2 < p_{\mathrm{T,ee}} < 4\,\mathrm{GeV}/c^2$. Data points are compared to the hadronic cocktail including the direct photon contribution.

parametrizations of f_{dir} and f_{LF} are normalized to the measured yield in the invariant mass region $m_{\mathrm{ee}} < 0.04\,\mathrm{GeV}/c^2$ where both templates have nearly identical shape. The fit is performed in the invariant mass range $0.08 < m_{\mathrm{ee}} < 0.38\,\mathrm{GeV}/c^2$ to ensure that $p_{\mathrm{T,ee}} \gg m_{\mathrm{ee}}$ holds true, that the π^0 contribution is suppressed and that the statistical uncertainties are reasonably small. In figure 12.5 the result of the fitting procedure in the pair transverse momentum range $2 < p_{\mathrm{T,ee}} < 4\,\mathrm{GeV}/c^2$ is shown together with the resulting direct photon yield and the light- and heavy-flavour hadron contribution in the 0-20% most central Pb-Pb collisions. To estimate systematic uncertainties on the extracted r, three sources of uncertainty are considered: the fitting interval, the η/π^0 ratio and the contribution from heavy-flavour hadrons. The lower end of the fitting region is shifted to $m_{\mathrm{ee}} = 0.14\,\mathrm{GeV}/c^2$ which only resulted in a small systematic uncertainty. The upper end is not shifted to higher values due to the condition $p_{\mathrm{T,ee}} \gg m_{\mathrm{ee}}$ which should be fulfilled. A shift to lower invariant masses would decrease the statistical uncertainty but would increase systematic uncertainties drastically and is therefore rejected. The η/π^0 ratio is the dominant factor in the systematic uncertainty evaluation. The ratio is shifted according to the uncertainty of the η measurement and the fit procedure is repeated. The hadronic cocktail contribution from heavy-flavour hadron decays is varied within their own systematic uncertainty and the fitting procedure is repeated.

The fit parameter r can be interpreted as the number of direct virtual photons over

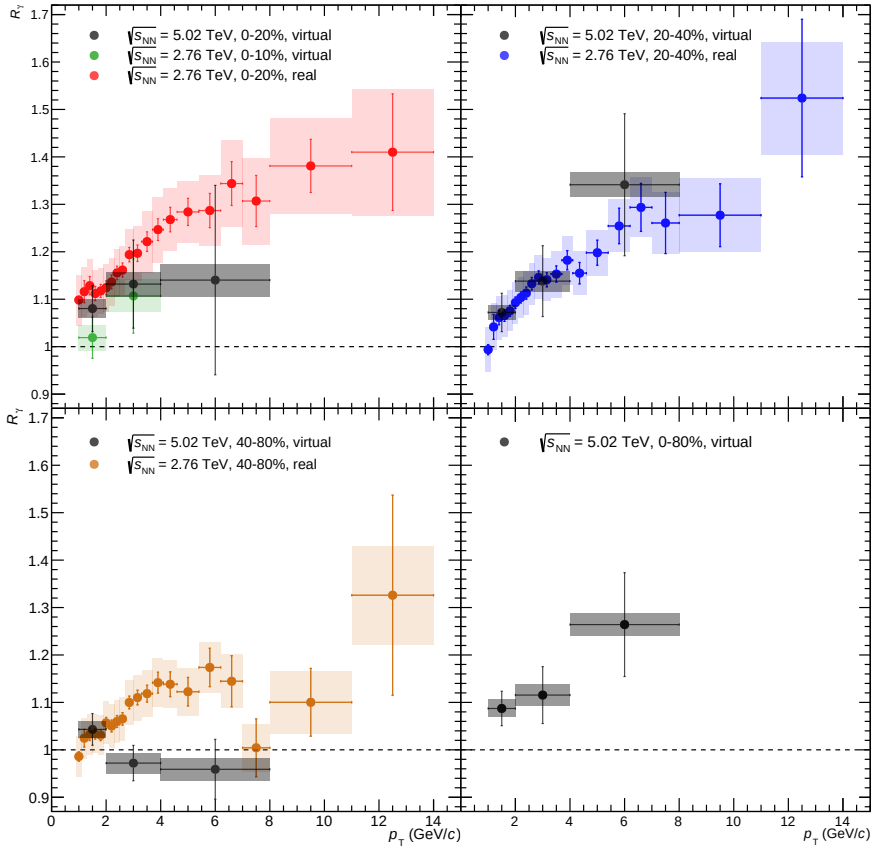

Figure 12.6.: R_γ distribution as a function of the transverse momentum in different centrality classes compared to previous ALICE direct photon measurements [78, 139]. While error bars correspond to statistical uncertainties, boxes depict systematic uncertainties.

the number of inclusive photons at $m_{ee} = 0$ where the contribution from heavy-flavour hadron decays is negligible:

$$r = \frac{f_{dir}}{f_{dir} + f_{LF}} = \frac{\gamma_{dir}}{\gamma_{dir} + \gamma_{decay}} = \frac{\gamma_{dir}}{\gamma_{inclusive}} \tag{12.2}$$

R_γ is traditionally used to illustrate the direct photon yield in comparison to decay photons:

$$R_\gamma = \frac{1}{1 - r} = \frac{\gamma_{inclusive}}{\gamma_{decay}} \tag{12.3}$$

Figure 12.6 shows the extracted R_γ distribution in different centrality classes in comparison to previous ALICE measurements based on real [139] and virtual photon [78] measurements at a different center-of-mass energy per nucleon pair of $\sqrt{s_{NN}} = 2.76\,\text{TeV}$. The direct photon cross section of initial hard parton-parton scatterings is

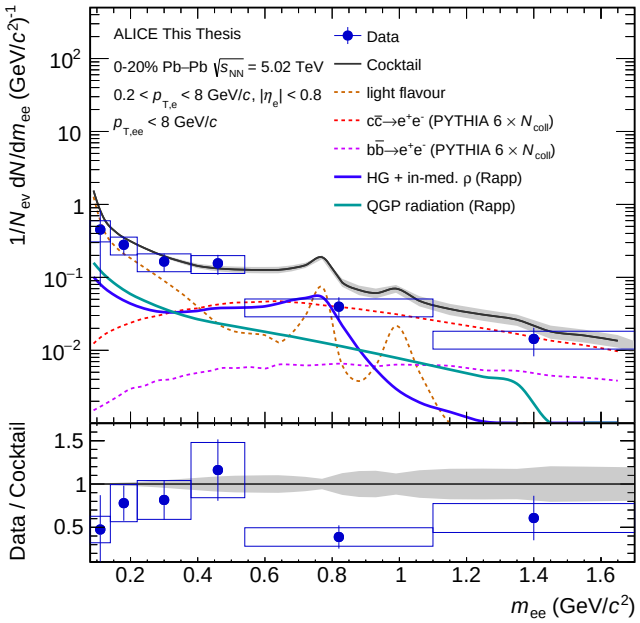

Figure 12.7.: Dielectron yield in comparison to the hadronic cocktail including thermal contributions from a fireball model [72, 85] in 0-20% most central Pb-Pb collisions at $\sqrt{s_{\mathrm{NN}}} = 5.02\,\mathrm{TeV}$.

expected to be increasing slower with collision energy [140] as the hadron production [141]. This effect would lead to smaller extracted R_γ at high transverse momentum $p_{\mathrm{T}} > 3\,\mathrm{GeV}/c$. However, the production of thermal photons at higher energies is expected to be larger due to the higher initial temperature, size and life time of the produced QGP [78]. Within uncertainties the measurement in the centrality classes 0-20% and 20-40% are compatible with the measurements at slightly lower $\sqrt{s_{\mathrm{NN}}}$. In these collision systems a non-zero direct photon yield can be extracted which rises as a function of transverse momentum. However, at small transverse momenta a finite yield hints to the production of thermal photons. The virtual photon measurement in peripheral collisions shows a smaller yield of direct photons which is compatible with the absence of direct photons. While systematic uncertainties of the virtual photon measurement are smaller compared to the real photon analysis, statistical uncertainties are fairly larger, as expected. This direct photon measurement in the dielectron channel is able to confirm the previous ALICE measurement at a smaller collision energy. Therefore, it serves as valuable input to resolve the direct photon puzzle.

12.4. Comparison to Theory

The measured dielectron spectrum in 0-20% most central collisions is compared to two theoretical models including thermal dielectrons from partonic and hadronic phases. Both models include the acceptance requirements $p_{\mathrm{T}} > 0.2\,\mathrm{GeV}/c$ and $|\eta| < 0.8$ for single electrons but do not incorporate detector resolution effects. The first model is based on an expanding thermal fireball and provides only the contribution from thermal radiation from the QGP and hadron gas [72, 85]. The other contributions are taken from the hadronic cocktail as described before. The model uses an equation of state of the QGP which is extracted by lattice-QCD calculations with a critical temperature of $T_{\mathrm{c}} = 0.17\,\mathrm{GeV}$. It applies medium modifications to the ρ meson which are obtained from a many-body theory. The latter predicts a broadening of the electromagnetic spectral functions of vector mesons. This broadening is an effect of the partial restoration of chiral symmetry at the phase boundary [78]. The same model was used to successfully describe the dielectron measurements at lower energies (SPS and RHIC). The second model [84] originates from the Parton-Hadron-String Dynamics (PHSD) transport model and provides the full dielectron yield including all different contributions except for the contribution from J/ψ. Under the assumption that the degrees of freedom in the QGP are massive off-shell particles the thermal dielectron contribution from the partonic phase is calculated. The dielectron production in the hadronic phase is calculated using in-medium modified electromagnetic spectral functions of low-mass vector mesons. The broadening is assumed to originate from elastic collisions in the hadron gas phase [78]. This model also includes the contribution from semileptonic open heavy-flavour hadron decays using the Dynamical Quasi-Particle Model [142].

In figure 12.7 the measured spectrum in the 0-20% most central Pb-Pb collisions at $\sqrt{s_{\mathrm{NN}}} = 5.02\,\mathrm{TeV}$ is compared to the hadronic cocktail as described in section 11 including thermal contributions from the hadron gas and the QGP predicted by the thermal fireball model. The spectrum is shown in the invariant mass range $0.08 < m_{\mathrm{ee}} < 1.7\,\mathrm{GeV}/c^2$. For smaller invariant masses the input format is not compatible with the measurement. Additionally, the theory model predicts contributions only up to $m_{\mathrm{ee}} < 1.5\,\mathrm{GeV}/c^2$. The thermal fireball model is able to describe the enhancement of the data over the purely hadronic cocktail estimate in the mass range $0.14 < m_{\mathrm{ee}} < 0.54\,\mathrm{GeV}/c^2$. The yield in the mass interval $0.54 < m_{\mathrm{ee}} < 1.1\,\mathrm{GeV}/c^2$ is overestimated without thermal dielectron contributions and is even further overshot by the cocktail including the contributions by the thermal fireball model. In this cocktail, the $c\bar{c}$ and $b\bar{b}$ contributions are calculated without any cold- or hot-nuclear matter effects.

In figure 12.8 the prediction by the PHSD model is presented in comparison to the measured data. The model does not provide the contribution from J/ψ meson decays. For this reason the J/ψ contribution based on the ALICE measurement, as

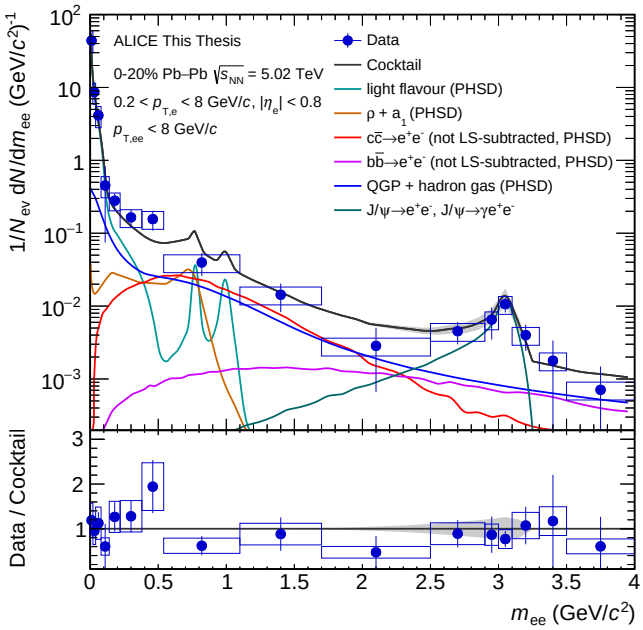

Figure 12.8.: Dielectron yield in comparison to the hadronic cocktail including thermal contributions from the model by PHSD.

described in section 11.3, is used. The low-mass region $0.14 < m_{ee} < 0.54\,\mathrm{GeV}/c^2$ is fairly well described by the model while the invariant mass range dominated by the contribution from $c\bar{c}$ hadron decays is slightly overestimated. However the complete mass spectrum can be described by the model within statistical and systematic uncertainties of the data, while the theoretical model itself does not include systematic uncertainties.

12.5. Excess at Small Transverse Momentum

The left panel of figure 12.9 shows the measured dielectron yield as function of the pair transverse momentum $p_{T,ee}$ in the invariant-mass interval $1.1 < m_{ee} < 2.9\,\mathrm{GeV}/c^2$ in comparison to the hadronic expectations for the 70-90% most central Pb-Pb collisions at a center-of-mass energy of $\sqrt{s_{NN}} = 5.02\,\mathrm{TeV}$. The data exceeds the hadronic expectations at small transverse momenta $p_{T,ee} < 0.15\,\mathrm{GeV}/c$ by a factor of $9.31 \pm 2.85(\mathrm{stat.}) \pm 1.52(\mathrm{syst.}) \pm 1.34(\mathrm{cockt.})$ while at higher $p_{T,ee} > 0.4\,\mathrm{GeV}/c$ data and hadronic cocktail match reasonably well. The measured yield in the interval $0.2 < p_{T,ee} < 0.4\,\mathrm{GeV}/c$ is negative due to a statistical fluctuation of the background. The right panel of figure 12.9 shows the excess over the cocktail as "data − cocktail" spectrum in comparison to preliminary results which were extracted in an independent analysis of the same data set. See section 3.3 for a detailed discussion of this

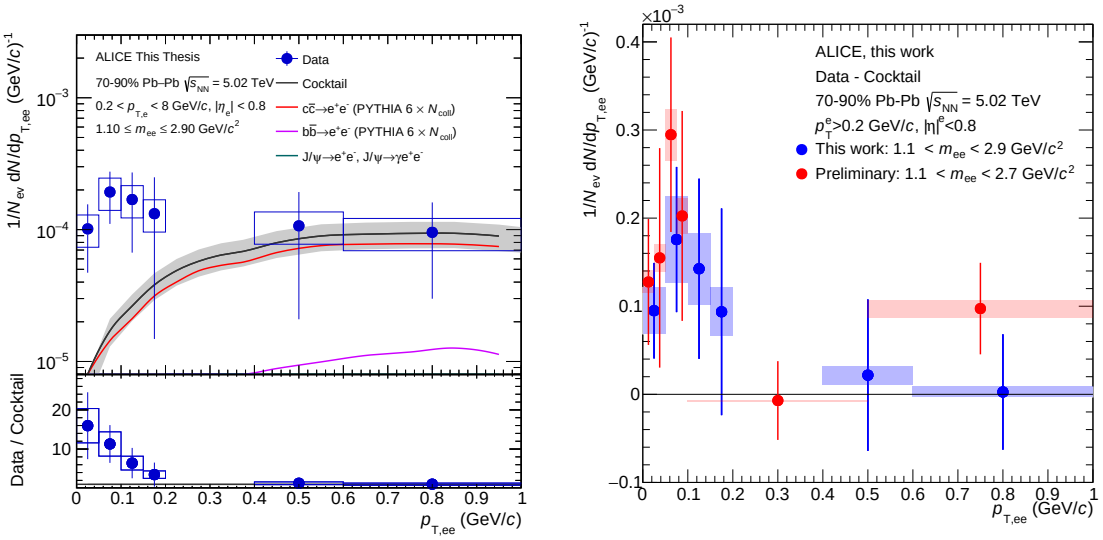

Figure 12.9.: Dielectron yield as function of the pair transverse momentum $p_{\mathrm{T,ee}}$ in the invariant-mass interval $1.1 < m_{\mathrm{ee}} < 2.9\,\mathrm{GeV}/c^2$ in comparison to the hadronic expectations for the 70-90% most central Pb-Pb collisions at a center-of-mass energy of $\sqrt{s_{\mathrm{NN}}} = 5.02\,\mathrm{TeV}$ (left). Excess over the hadronic cocktail in comparison to a preliminary analysis of the same data set (right).

m_{ee} (GeV/c^2)	data over cocktail	stat.	syst.	cocktail	significance
0.38 - 1.1	21.91	± 5.52	± 3.77	± 3.53	2.77σ
1.1 - 2.9	9.31	± 2.85	± 1.52	± 1.34	2.37σ
2.9 - 3.3	24.69	± 7.82	± 4.41	± 4.50	2.36σ

Table 12.3.: Data-over-cocktail ratio in the pair transverse momentum interval $0 < p_{\mathrm{T,ee}} < 0.15\,\mathrm{GeV}/c$ in three invariant-mass intervals for 70-90% most central Pb-Pb collisions at $\sqrt{s_{\mathrm{NN}}} = 5.02\,\mathrm{TeV}$.

result. Statistical uncertainties are represented with error bars, systematic uncertainties are indicated with colored boxes. Within the uncertainties the preliminary measurement can be confirmed by the analysis discussed in this thesis.

This measurement is also performed in two additional invariant-mass intervals to extract the invariant-mass dependence of this excess contribution. The invariant-mass intervals were chosen to be compatible with the binning of the invariant-mass spectra shown in section 12.1. Table 12.3 shows the data-over-cocktail ratio for $p_{\mathrm{T,ee}} < 0.15\,\mathrm{GeV}/c$ in three invariant-mass intervals, the corresponding uncertainties and the significance of this enhancement which is $> 2\sigma$ for every invariant-mass interval indicating that there is a contribution to the dielectron spectrum which is not included in the hadronic cocktail. Figure 12.10 shows the invariant-mass dependence of this excess in comparison to two other measurements. These two

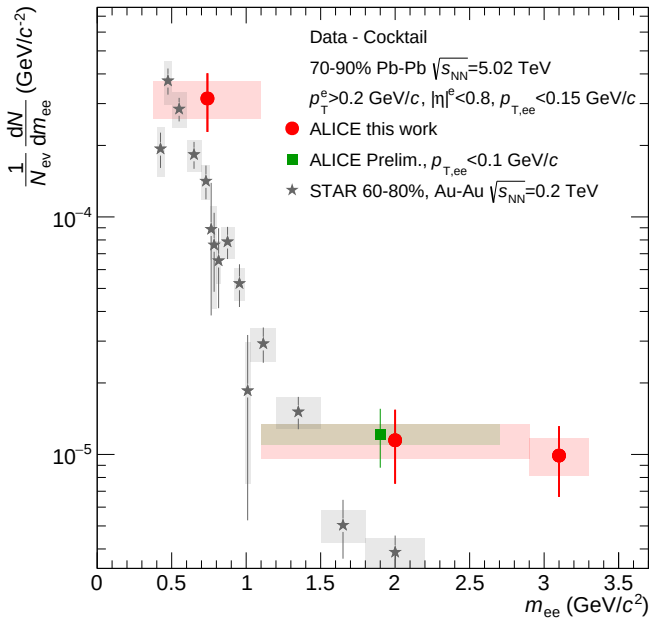

Figure 12.10.: Excess over the hadronic cocktail in the pair transverse momentum interval $0 < p_{\mathrm{T,ee}} < 0.15\,\mathrm{GeV}/c$ in comparison to the preliminary ALICE analysis and a measurement by the STAR collaboration [52].

measurements are discussed in more detail in section 3. The measurement shows a compatible shape as a function of invariant mass in comparison to the results by STAR at a center-of-mass-energy $\sqrt{s_{\mathrm{NN}}} = 0.2\,\mathrm{TeV}$ [52]. However, the overall yield is higher by a factor of $1.98 \pm 0.28(\mathrm{stat.}) \pm 0.19(\mathrm{syst.})$ in the invariant mass range $0.38 < m_{\mathrm{ee}} < 1.1\,\mathrm{GeV}/c^2$ and $1.3 \pm 0.35(\mathrm{stat.}) \pm 0.19(\mathrm{syst.})$ in the higher invariant mass range $1.1 < m_{\mathrm{ee}} < 2.9\,\mathrm{GeV}/c^2$.

The left panel in figure 12.11 shows the $p^2_{\mathrm{T,ee}}$ spectrum in comparison to the results at $\sqrt{s_{\mathrm{NN}}} = 0.2\,\mathrm{TeV}$. The shape of the excess in a given invariant mass interval is compatible to the shape reported by the STAR collaboration. Additionally, the width of the pair transverse momentum distribution reported as $\sqrt{\langle p^2_{\mathrm{T,ee}} \rangle}$ is shown in the right panel of figure 12.11 and also compatible within the uncertainties indicating that the source of the excess is the same in both measurements. The excess over the hadronic cocktail was also investigated in more central centrality classes. However, due to the extremely fast rising background in more central events, the statistical significance of the data is not sufficient to quantify an enhancement over the hadronic cocktail.

Up to now, no theoretical models for the collision energy $\sqrt{s_{\mathrm{NN}}} = 5.02\,\mathrm{TeV}$ and for electrons within the ALICE acceptance selection $p^e_{\mathrm{T}} = 0.2\,\mathrm{GeV}/c$ and $|\eta^e| < 0.8$ are available. Therefore, the results presented in this thesis are interpreted with

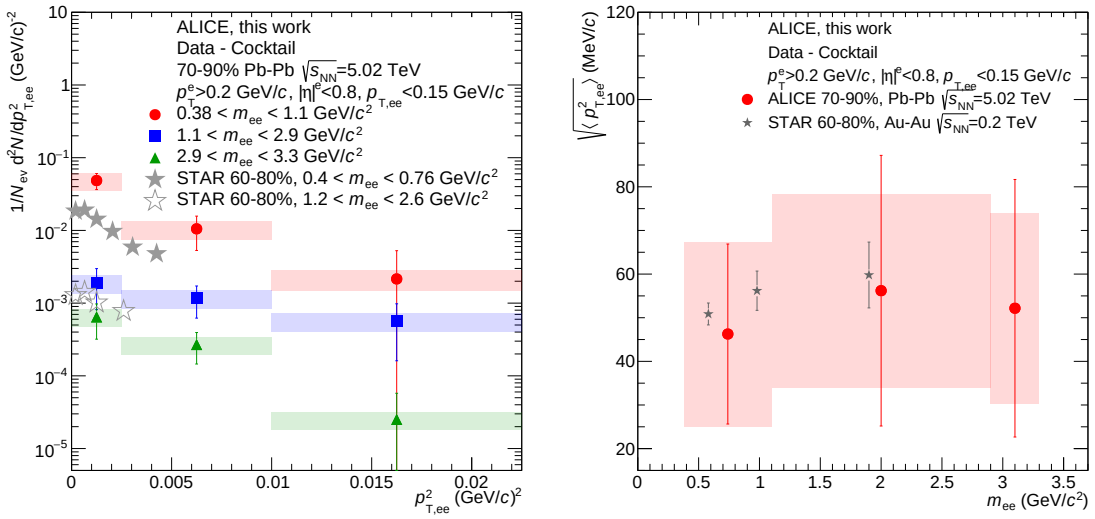

Figure 12.11.: Squared pair transverse momentum $p^2_{\mathrm{T,ee}}$ in three invariant mass intervals in comparison to STAR results [52] (left). Standard deviation $\sqrt{\langle p^2_{\mathrm{T,ee}} \rangle}$ as a function of the invariant mass m_{ee} (right).

respect to the compatibility of the results with the corresponding measurement of the STAR collaboration. Theoretical models are able to describe the measured excess spectrum of this measurement with a combination of thermally and photon-induced dielectron pairs [58, 59]. The main contribution to the excess originates from the two-photon interaction process $\gamma\gamma \rightarrow e^+e^-$ coming from the photon flux produced by the contracted magnetic field of the ultrarelativistic heavy ions. One of these models, by Zha et al. [52], is able to describe the invariant mass m_{ee} and the squared pair-transverse momentum $p^2_{\mathrm{T,ee}}$ spectra relatively good. A second model, STARlight [58], is able to describe the overall shapes of the distributions but underestimate the total produced yield. The former model by Zha et al. assumes a Wood-Saxon-like charge distribution within the incoming nuclei instead of a point like source which ignores the dielectron production within the nucleus in the STARlight model. Additionally, the model by Zha et al. is also shown with an applied magnetic field originating from the heavy-ion collision. It is assumed that the electron and positron traverse this magnetic field for the distance of 1 fm and the magnetic field is constant with $B = 10^{14}$ T. With this assumption, the agreement of the model with all aforementioned distributions improves. This indicates that the photon-induced production of dielectrons is sensitive to the magnetic fields which occur during the collision. Because of the qualitative agreement of the results reported by STAR and the results in this thesis, one can conclude that the measured excess originates from photon-induced processes.

A third model [51] of the photon-induced dielectron production predicts an almost constant production cross section as a function of the collision energy $\sqrt{s_{\mathrm{NN}}}$ start-

ing from $\sqrt{s_{\mathrm{NN}}} > 0.2\,\mathrm{TeV}$ as shown in figure 2.4. The yield of photon-induced dielectrons at $\sqrt{s_{\mathrm{NN}}} = 5.02\,\mathrm{TeV}$ measured in this thesis is higher compared to the results obtained at $\sqrt{s_{\mathrm{NN}}} = 0.2\,\mathrm{TeV}$. This would indicate that the model predicts the energy dependence not correctly. However, the significance of this measurement is not sufficient to rule out this scenario, assuming that the collision energy dependence is negligible, the Z^4 dependence of the photon flux and taking into account the difference of the electric charge of the heavy ion ($Z_{\mathrm{Au}} = 79e$, $Z_{\mathrm{Pb}} = 82e$). The measured effect amounts to a significance of $\approx 1.24\sigma$ in the lower invariant mass range $0.38 < m_{\mathrm{ee}} < 1.1\,\mathrm{GeV}/c^2$ and $\approx 0.48\sigma$ in the higher invariant mass range $1.1 < m_{\mathrm{ee}} < 2.9\,\mathrm{GeV}/c^2$, with the caveat that the respective invariant-mass intervals are not exactly equivalent.

13. Summary and Outlook

Dielectrons are one of the most interesting probes to investigate the properties of the QGP. This thesis discusses the first dielectron analysis of Pb-Pb collisions at a center-of-mass energy of $\sqrt{s_{\mathrm{NN}}} = 5.02\,\mathrm{TeV}$. It is the first centrality-dependent dielectron analysis of heavy-ion collisions at one of the LHC experiments and additionally the first dielectron analysis with a minimum transverse momentum requirement for single electrons of $p_{\mathrm{T}} > 0.2\,\mathrm{GeV}/c$. This requirement allows for the first time for the study of soft processes in the dielectron channel.

The measured spectra are compared to the expected contributions by hadrons like π^0, η, η', ρ, ω, ϕ and J/ψ together with the contribution from semileptonic decays of open heavy-flavour hadrons. The hadronic cocktail and the data agree within uncertainties at small masses and at the J/ψ as expected due to previous measurements serving as input for the contribution of the π^0 and the J/ψ in the hadronic cocktail. The region dominated by the other light-flavour mesons $0.14 < m_{\mathrm{ee}} < 1.1\,\mathrm{GeV}/c^2$ is not described well by the hadronic cocktail hinting to hot-medium-related effects like the modification of the ρ meson or the presence of thermal and prompt virtual direct photons. Two theoretical models are able to describe the data within statistical and systematic uncertainties. Under the assumption that the difference between data and expectations stems only from the contribution of virtual direct photons, this contribution is extracted for pair transverse momenta $p_{\mathrm{T,ee}} > 1\,\mathrm{GeV}/c$. These extracted spectra are compared to previous measurement from ALICE at a different center-of-mass energy. The spectra agree within their statistical and systematic uncertainties. Due to the large statistical uncertainties of the dielectron spectra, this measurement can not put an additionally constraint on theoretical models but can confirm previous measurements by ALICE. However, the measurement can confirm the previously published results. The measured dielectron spectrum in the invariant mass range $0.54 < m_{\mathrm{ee}} < 2.5\,\mathrm{GeV}/c^2$ shows a suppression compared to the expectations by PYTHIA which are scaled with the number of binary collisions and normalized to the measured cross section in proton-proton collisions. This suppression can be described by modifying the contribution from open charm hadrons with hot- and cold-matter effects. However, a precise quantification is not possible due to large statistical and systematic uncertainty on the data and on the expectation. The systematic uncertainty on the expectations suffers from a poorly measured cross sections of charmed hadrons like the Λ_c. Additionally, a excess of the data over the expectations of the hadronic cocktail is found in the pair transverse momentum

region $0 < p_{\mathrm{T,ee}} < 0.15\,\mathrm{GeV}/c$. The shape of this excess is similar to the shape reported by the STAR collaboration but the total yield is higher. This excess can be contributed to photon-induced production of dielectron pairs originating from the strong electromagnetic fields by the incoming lead nuclei.

In 2018 ALICE recorded a new data set including Pb-Pb collisions at different centralities. This data set accumulated about ≈ 5 times more statistics, dependent on the centrality. It allows for a more differential analysis and might give the possibility to further reduce the systematic uncertainty which is at the moment also limited by statistical fluctuations. Additionally, a new observable $\mathrm{DCA_{ee}}$ was tested in proton-proton collisions at a center-of-mass energy of $\sqrt{s} = 7\,\mathrm{TeV}$. This observable exploits the different decay lengths of hadrons, allowing for the distinction between dielectrons from open charm, open beauty and prompt decays. This observable will help to further pin down the contribution of heavy-flavour hadrons in the mass range $0.54 < m_{\mathrm{ee}} < 2.5\,\mathrm{GeV}/c^2$ allowing for the measurement of the thermal contribution of the QGP.

During the Long-Term Shutdown 2 which started in 2018 and ends in 2021 the TPC and the ITS are upgraded [97, 143]. These upgrades allow for an improved tracking and vertex resolution, enhancing the effectiveness of the $\mathrm{DCA_{ee}}$ observable significantly. Additionally the data-taking rate of ALICE will increase by a factor of about ≈ 50 due to continuous read-out of the TPC, resulting in dramatically increased number of recorded collisions. Additionally, it is foreseen to lower the magnetic field of the experiment to $B = 0.2\,\mathrm{T}$. This will allow for a reduction of the minimum electron transverse momentum requirement to $p_{\mathrm{T}} > 0.075\,\mathrm{GeV}/c$ increasing the sensitivity to measure soft processes. A pilot data-taking period and dielectron analysis was already performed for proton-proton collisions with a center-of-mass-energy $\sqrt{s} = 13\,\mathrm{TeV}$ [81]. With these improvements a precise quantification of the contribution of the thermal QGP radiation and more differential results on the photon-induced production of dielectron are foreseen.

A. Observables

ALICE Coordinate System

The nominal collision vertex inside ALICE serves as the origin of the Cartesian coordinate system. The main coordinates are defined as [144]:

- **z** is defined as being parallel to the beam direction. The muon arm is located at negative z values at the so-called c-side. The opposite direction is often referred to as c-side.
- **x** is perpendicular to the beam axis. Positive values point to the center of the LHC.
- **y** is perpendicular to x and y. Positive values point upwards.
- φ is the azimuthal angle in the x-y-plane. It increases clockwise looking from the collision vertex to the muon arm.
- θ is the polar angle which increases from positive z ($\theta = 0$) to negative z ($\theta = \pi$).

Kinematic Observables

The 3-momentum vector can be split into a longitudinal p_{L} and a transverse component p_{T}. While the longitudinal component corresponds to the momentum in z direction $p_{\mathrm{L}} = p_{\mathrm{z}}$, the transverse momentum is defined as the momentum transverse to the beam axis:

$$p_{\mathrm{T}} = \sqrt{p_{\mathrm{x}}^2 + p_{\mathrm{y}}^2} \tag{A.1}$$

with p_{x} and p_{y} as the momentum in x and y direction, respectively. The transverse momentum and the transverse mass $m_{\mathrm{T}} = \sqrt{m^2 + p_{\mathrm{T}}^2}$ are Lorentz-invariant under longitudinal transformations. A measure along the beam direction is called rapidity:

$$y = \frac{1}{2} \ln(\frac{E + p_{\mathrm{L}}}{E - + p_{\mathrm{L}}}) \tag{A.2}$$

with E being the energy of the particle. This energy is difficult to measure experimentally because it requires the measurement of the particles mass. The pseu-

dorapidity η is closely related to y and defined in relation to the polar angle θ:

$$\eta = -\ln(\tan(\frac{\theta}{2})) \tag{A.3}$$

For massless particles or approximately for particles with $p \gg m_{\text{rest}}$ the rapidity and pseudorapidity are equal $\eta = y$.

In collider experiments the Lorentz-invariant Mandelstam variable s can be expressed as:

$$s = (P_1 + P_2)^2 = (E_{1,\text{beam}} + E_{2,\text{beam}})^2 \tag{A.4}$$

with P_1 and P_2 being the 4-momentum of Particle 1 and 2, respectively.

The invariant mass of a particle decaying into two decay products can be calculated:

$$m_{\text{ee}} = \sqrt{m_1^2 + m_2^2 + 2E_1E_2 - 2\vec{p_1} \cdot \vec{p_2}} \tag{A.5}$$

m_1 and m_2 are the rest masses of the respective decay products while E_1, E_2, $\vec{p_1}$ and $\vec{p_2}$ are their corresponding energy and momentum. The pair transverse momentum of a particle can be calculated as:

$$p_{\text{T,ee}} = \sqrt{(p_{\text{x},1} + p_{\text{x},2})^2 + (p_{\text{y},1} + p_{\text{y},2})^2} \tag{A.6}$$

B. Computing Setup

The coding environment *ALIROOT* which is used in this analysis is based on the software framework *ROOT* [145]. *ROOT* contains many software tools to facilitate data analysis like I/O operations, statistical tools and APIs to simulate particle collisions. *ALIROOT* implements additional tools and contains detector specific information to allow data reconstruction and analysis within the ALICE experiment. Additionally, *ALIROOT* enables analyzers to use the LHC Grid, a world-wide pool of servers, to distribute computing load.

Over the years ALICE collected a huge amount of data which was reconstructed and distributed to the servers of the LHC Grid. To analyze this data an efficient way of processing was implemented: LEGO trains. Trains which carry the software the analyzer wants to be executed on the data are sent to the different storage and computing servers. The results of those computations are conveniently collected and merged into one final file.

For this analysis the mainly used software package is called *dielectron framework*. This framework was developed to unify the efforts of many developers. It features a high flexibility for the analyzer while featuring high-quality code.

The following versions of ALICE software was used for the extraction of the dielectron spectra from recorded data and for the pair efficiency from simulations:

- ROOT::v5-34-30-alice10-14
- ALIROOT::v5-09-36-1
- ALIPHYSICS::vAN-20180830-1

This analysis is based on the AOD production 194 of LHC15o data.

C. Run List

The analyzed runs from pass3_lowIR are: 244975, 244980, 244982, 244983, 245061, 245064, 245066, 245068, 246390, 246391, 246392

The analyzed runs from pass1 are: 246994, 246991, 246989, 246984, 246982, 246980, 246948, 246945, 246928, 246851, 246847, 246846, 246845, 246844, 246810, 246809, 246808, 246807, 246805, 246804, 246766, 246765, 246763, 246760, 246759, 246758, 246757, 246751, 246750, 246495, 246493, 246488, 246487, 246434, 246431, 246428, 246424, 246276, 246275, 246272, 246271, 246225, 246222, 246217, 246185, 246182, 246181, 246180, 246178, 246153, 246152, 246151, 246148, 246115, 246113, 246089, 246087, 246053, 246052, 246049, 246048, 246042, 246037, 246036, 246012, 246003, 246001, 245963, 245954, 245952, 245949, 245923, 245833, 245831, 245829, 245705, 245702, 245700, 245692, 245683

The analyzed runs from pass1_pidfix are: 245554, 245545, 245544, 245543, 245542, 245540, 245535, 245507, 245505, 245504, 245501, 245497, 245496, 245454, 245452, 245450, 245446, 245441, 245439, 245411, 245409, 245407, 245401, 245397, 245396, 245353, 245349, 245347, 245346, 245345, 245343, 245259, 245232, 245231, 245152, 245151, 245146, 245145

D. Additional Raw Spectra

While figure D.1 and D.3 show the invariant mass spectrum in several pair transverse momentum ranges, figure D.2 and D.4 shows transverse momentum spectra in several mass ranges. The spectra are shown for the 20-40% and 40-80% most central events, respectively.

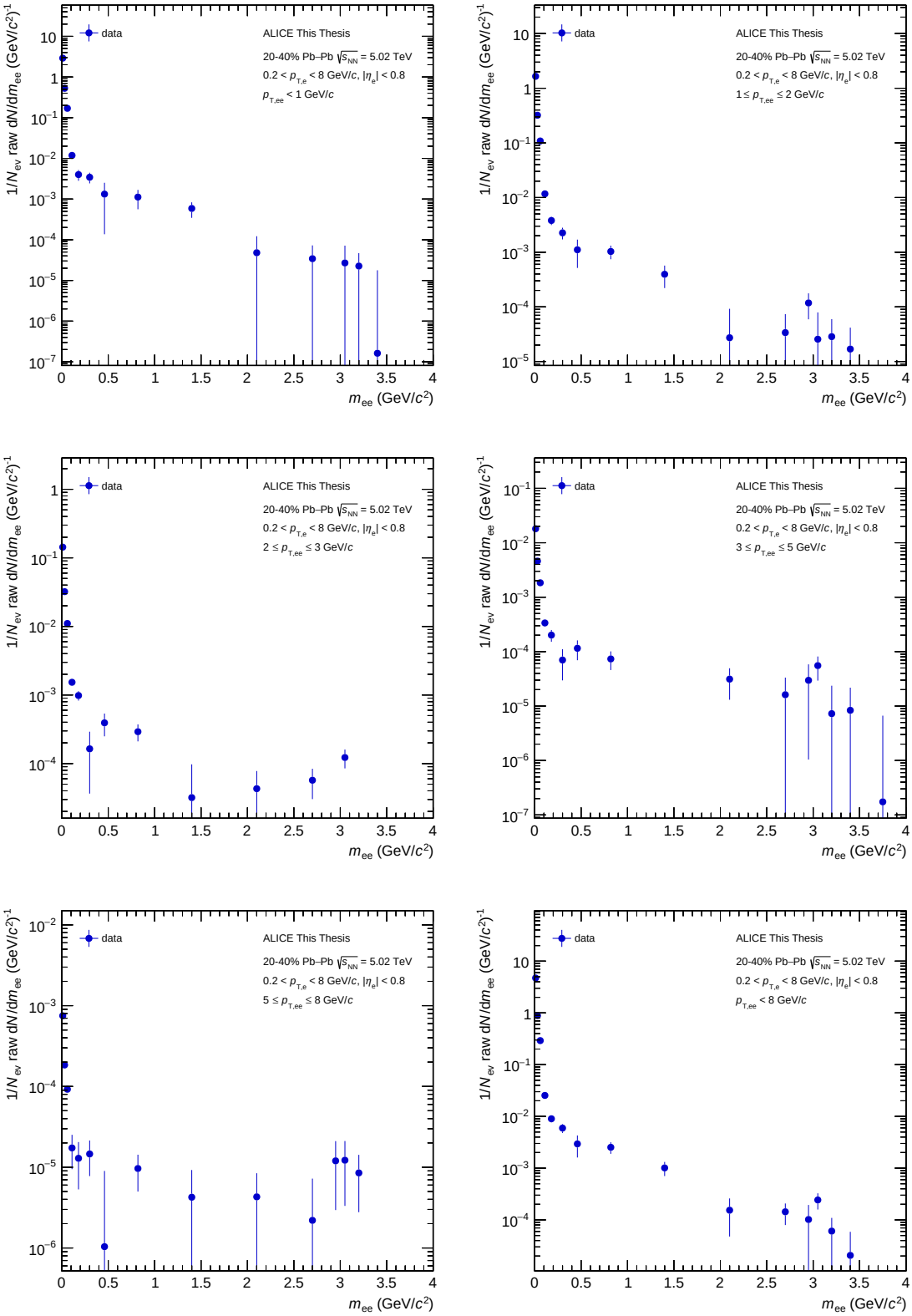

Figure D.1.: Raw dielectron yield as a function of invariant mass m_{ee} in several pair transverse momentum $p_{T,ee}$ bins in the most 20-40% central Pb-Pb collisions at $\sqrt{s_{NN}} = 5.02\,\text{TeV}$.

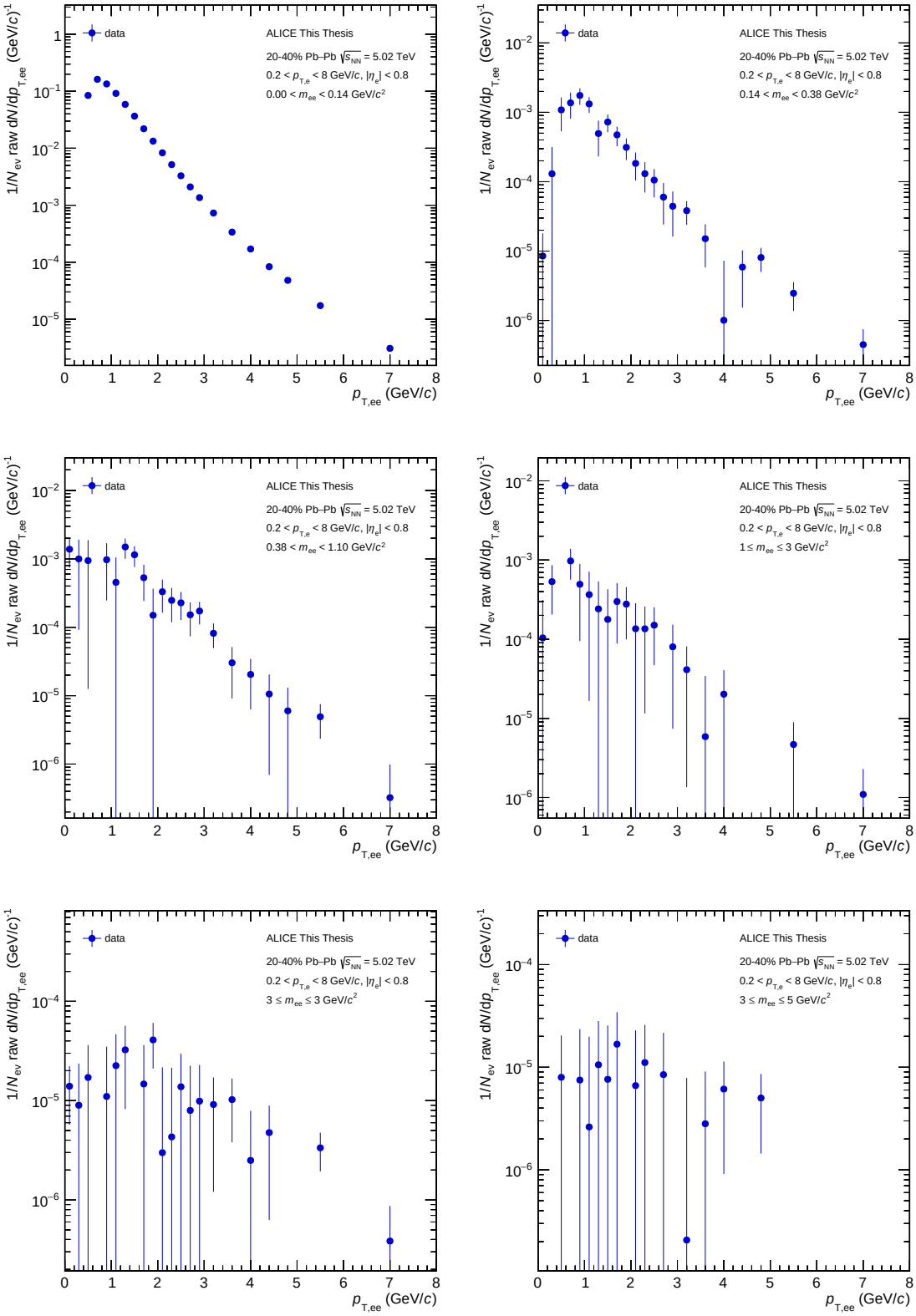

Figure D.2.: Raw dielectron yield as a function of pair transverse momentum $p_{\mathrm{T,ee}}$ in several pair invariant mass m_{ee} bins in the most 20-40% central Pb-Pb collisions at $\sqrt{s_{\mathrm{NN}}} = 5.02\,\mathrm{TeV}$.

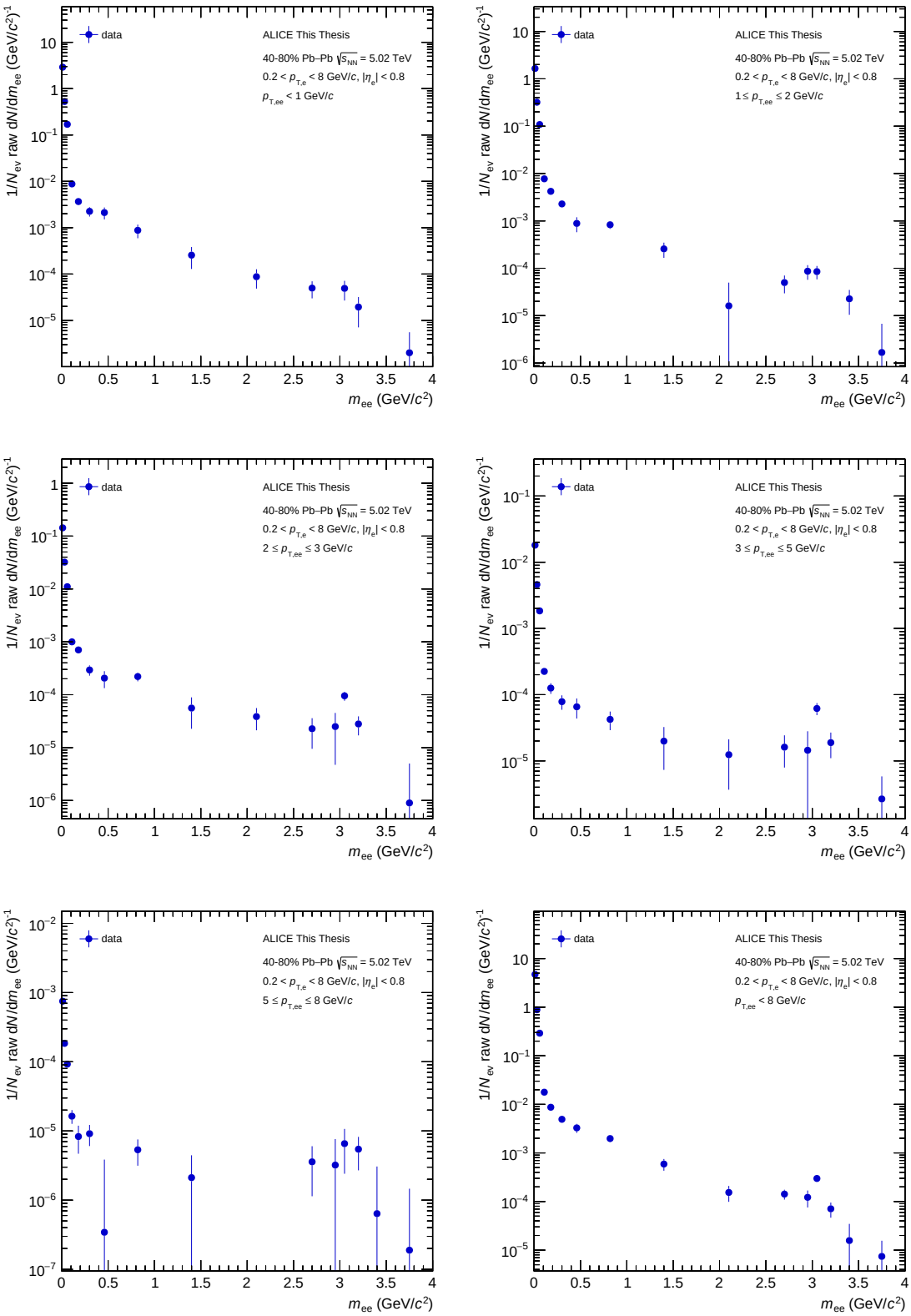

Figure D.3.: Raw dielectron yield as a function of invariant mass m_{ee} in several pair transverse momentum $p_{T,ee}$ bins in the most 40-80% central Pb-Pb collisions at $\sqrt{s_{NN}} = 5.02\,\text{TeV}$.

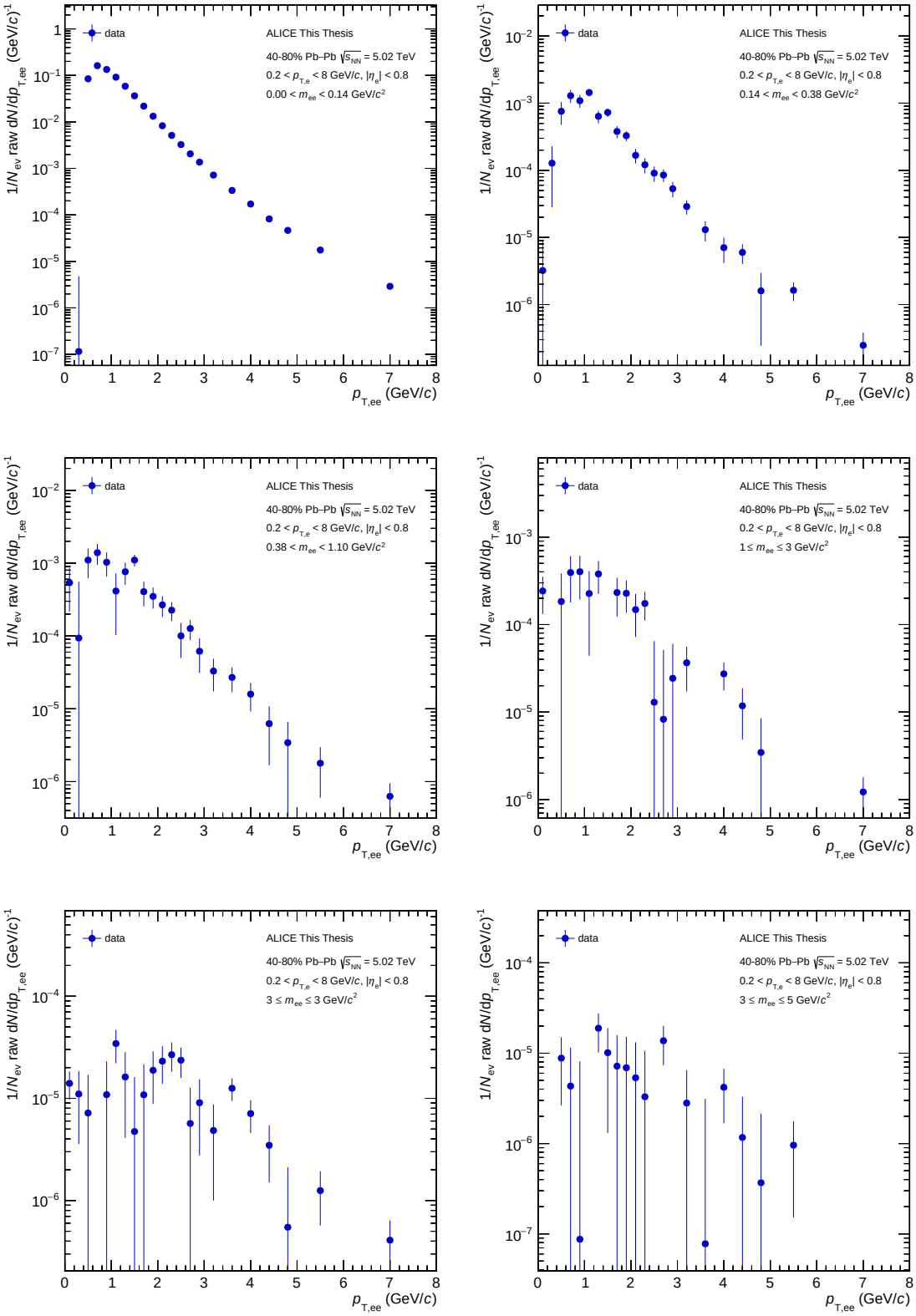

Figure D.4.: Raw dielectron yield as a function of pair transverse momentum $p_{\mathrm{T,ee}}$ in several pair invariant mass m_{ee} bins in the most 40-80% central Pb-Pb collisions at $\sqrt{s_{\mathrm{NN}}} = 5.02\,\mathrm{TeV}$.

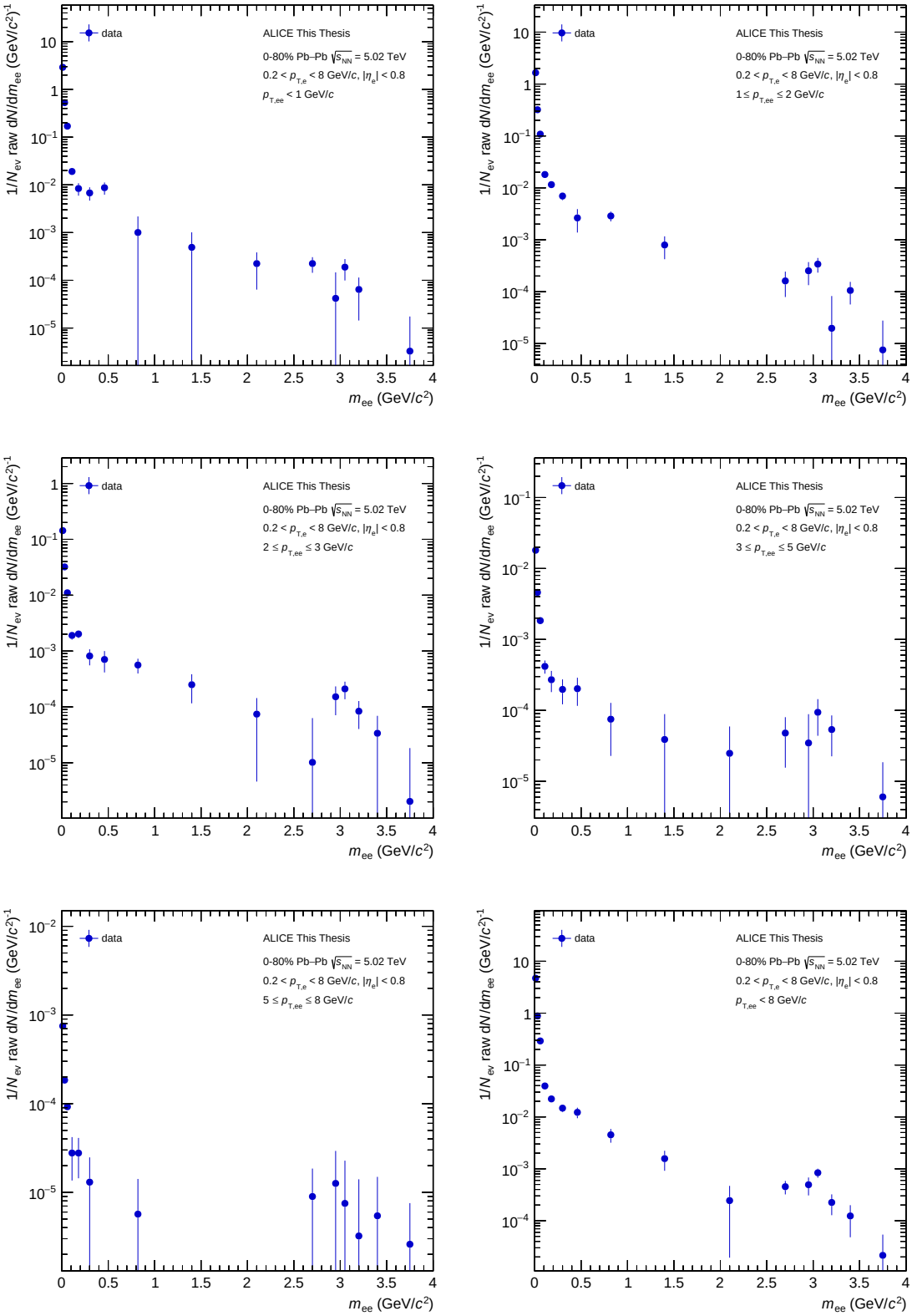

Figure D.5.: Raw dielectron yield as a function of invariant mass m_{ee} in several pair transverse momentum $p_{T,ee}$ bins in the most 00-80% central Pb-Pb collisions at $\sqrt{s_{NN}} = 5.02\,\text{TeV}$.

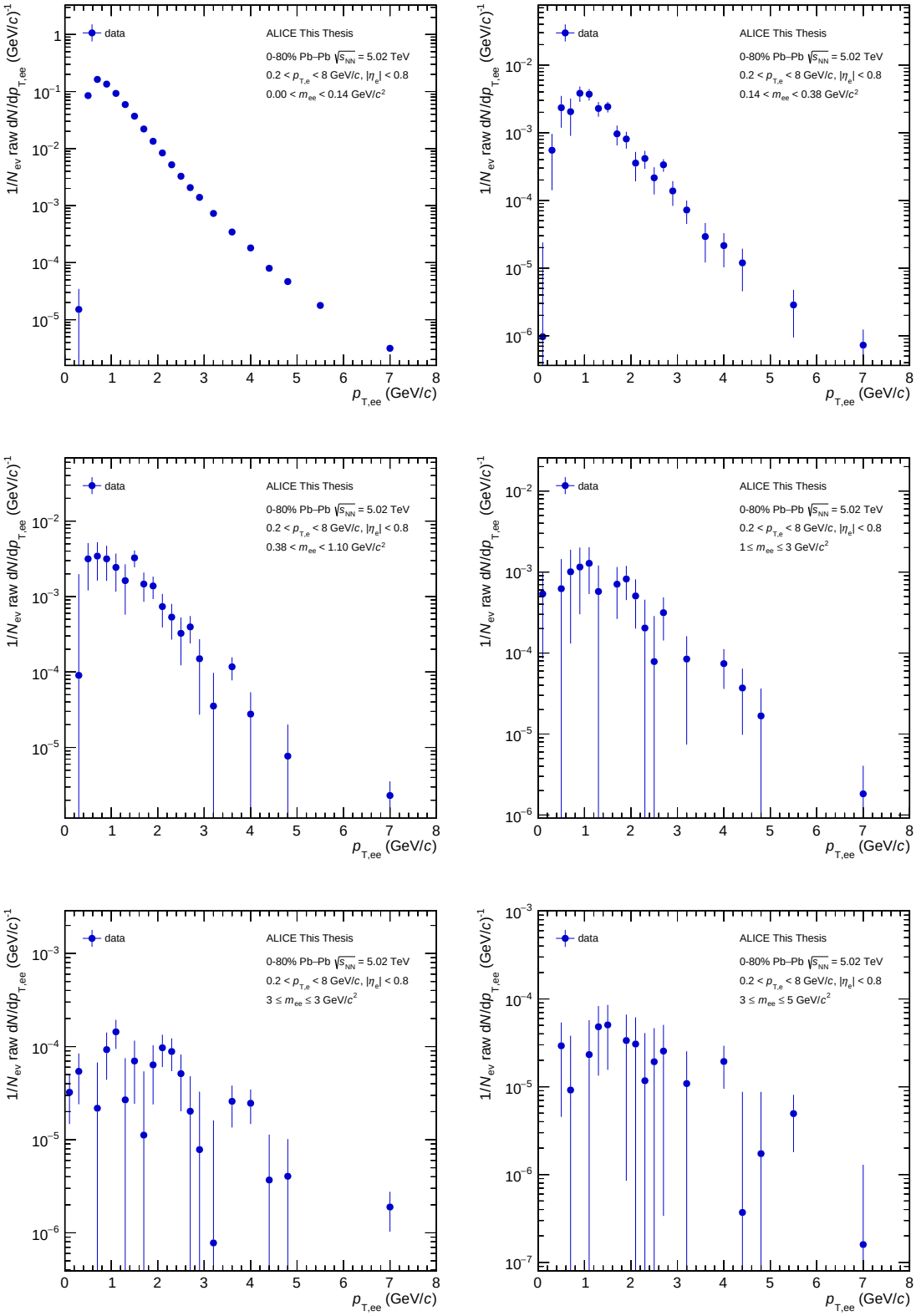

Figure D.6.: Raw dielectron yield as a function of pair transverse momentum $p_{\mathrm{T,ee}}$ in several pair invariant mass m_{ee} bins in the most 00-80% central Pb-Pb collisions at $\sqrt{s_{\mathrm{NN}}} = 5.02\,\mathrm{TeV}$.

E. Bug in Dielectron Simulation

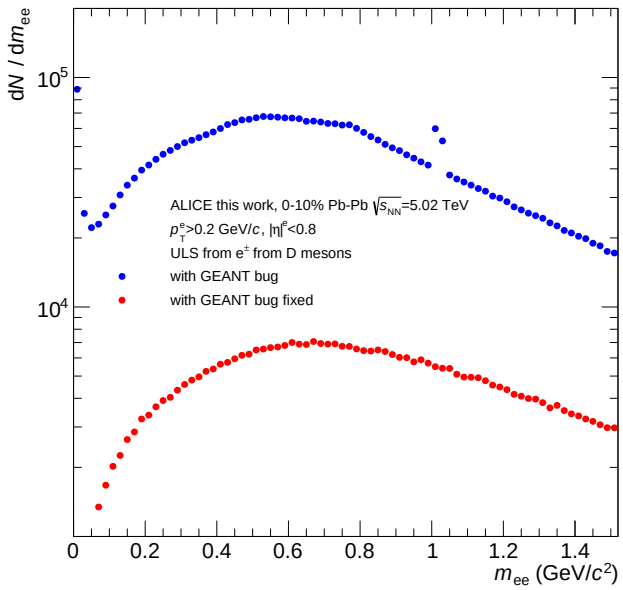

Figure E.1.: Unlike-sign spectra of electrons originating from D meson decays in the dedicated dielectron simulation LHC18b5a in the 0-10% most central collisions.

The several injected signals of the dedicated dielectron simulation LHC18g5a are discussed in more detail in section 6.3. The underlying Pb-Pb event is simulated with the HIJING model. All generated tracks are propagated through a simulation of the ALICE detector via the GEANT package. This dedicated dielectron simulation includes a bug concerning the decay into electrons of hadrons carrying a charm quark. The blue data points in figure E.1 show the unlike-sign distribution ULS for electrons originating from charmed hadron decays as a function of the invariant mass m_{ee}. The distribution is expected to be similar to the contribution calculated for the hadronic cocktail, see 11.2 for more details on the generation of the heavy-flavour hadronic cocktail. However, at very small invariant masses and around $m_{\mathrm{ee}} \approx 1\,\mathrm{GeV}/c^2$ unexpected structures emerge, hinting to a Dalitz decay or a resonance decay, respectively. The reason for this behavior is a wrong configuration of HIJING. In this particular simulation charmed hadrons are declared stable. These

hadrons are propagated to GEANT which itself decays these hadrons with its own decayer leading to decays of the form: $D \to \pi^0 X \to e^+e^-\gamma$ or $D \to \phi X \to e^+e^-\gamma$. GEANT does not add the intermediate decay particle (π^0 and ϕ) to the decay history of the electron. Therefore, the decay history states that the electrons originate directly from the charmed hadron, although they stem from the decay of the π^0 or ϕ, respectively. This bug can be avoided if an additional check is included to make sure that the charmed hadron does not decay into two leptons. The red points in figure E.1 show the unlike-sign spectrum of electrons from charmed meson decays with the workaround in place. The unexpected structures vanish and, as expected, the number of pairs decreases.

F. Systematic Variation

In this sector the different selection schemes are listed for the estimation of the systematic uncertainty. While table F.1 contains the various settings for the track selection, tables F.2 and F.3 contain the variation of the electron identification.

sel.	$n^{\text{ITS}}_{\text{Cl.,min}}$	$\chi^2_{\text{max}}/n^{\text{ITS}}_{\text{Cl.}}$	$n^{\text{TPC}}_{\text{Cl.,min}}$	$n^{\text{TPC}}_{\text{cr. rows,min}}$	$\chi^2/n^{\text{TPC}}_{\text{Cl.,max}}$	ITS sh. cl. map
1	4	4	80	80	4	true
2	3	4	80	80	4	false
3	4	3	100	100	5	true
4	4	5	80	80	4	true
5	4	3	80	100	4	true
6	4	4	100	100	5	true
7	4	4	80	80	3	false
8	4	3	100	100	5	true
9	4	5	100	100	3	true
10	3	4	100	100	5	false
11	4	3	80	80	5	true
12	4	4	100	80	3	false
13	4	5	100	80	45	true
14	4	5	80	100	4	false
15	4	5	80	100	5	true
16	3	3	100	80	5	true
17	4	5	80	100	4	false
18	4	5	100	80	3	true
19	4	3	100	100	5	false
20	3	5	80	80	4	true
21	4	5	80	80	5	true
22	4	4	100	80	3	false
23	3	5	100	100	4	true
24	4	4	80	100	5	false
25	4	3	80	100	4	true
26	3	3	100	100	4	true
27	4	5	80	100	5	false
28	4	3	100	100	3	true
29	4	5	100	80	3	false
30	3	3	80	80	6	true

Table F.1.: Requirements for systematic track variation.

sel.	$n\sigma_{\mathrm{ele}}^{\mathrm{ITS}}$	$n\sigma_{\mathrm{ele}}^{\mathrm{TPC}}$	$n\sigma_{\mathrm{ele}}^{\mathrm{TOF}}$	$n\sigma_{\mathrm{pion}}^{\mathrm{TPC}}$	TOF mode
1	-3.5, 0.5	-2, 3.5	-2.5, 3	3.5	available
2	-3.5, 1	-1.5, 3.5	-2.5, 3	3.5	available
3	-3, 1	-2, 3	-3, 2.5	3.5	available
4	-3, 1	-1.5, 3	-2.5, 3	4.5	available
5	-3.5, 1.5	-2, 3	-3, 3	4.5	available
6	-3.5, 0.5	-2, 3	-3, 3	4.5	available
7	-3.5, 0.5	-2, 3	-2.5, 3	3.5	available
8	-3.5, 0.5	-2, 3.5	-3, 3	3.5	available
9	-3.5, 1	-2, 3	-2.5, 3	4.5	available
10	-3, 1	-2, 3	-3, 2.5	4.5	available
11	-3.5, 0.5	-2, 3.5	-2.5, 2.5	3.5	required
12	-3.5, 1	-1.5, 3	-3, 2.5	3.5	required
13	-3.5, 0.5	-2, 3	-2.5, 3	4.5	required
14	-3, 0.5	-2, 3.5	-2.5, 3	4.5	required
15	-3, 1	-2, 3.5	-2.5, 2.5	3.5	required
16	-3, 0.5	-1.5, 3.5	-3, 2.5	4.5	required
17	-3.5, 0.5	-2, 3.5	-2.5, 3	3.5	required
18	-3.5, 1	-1.5, 3	-3, 2.5	4.5	required
19	-3, 0.5	-1.5, 3	-3, 3	3.5	required
20	-3.5, 1	-2, 3.5	-2.5, 2.5	3.5	required

Table F.2.: Requirements for systematic electron identification variation for selections similar to *TOFif* and *TOFreq*.

sel.	$n\sigma_{\mathrm{kaon}}^{\mathrm{TPC}}$ variation	$n\sigma_{\mathrm{proton}}^{\mathrm{TPC}}$ variation	$n\sigma_{\mathrm{pion}}^{\mathrm{TPC}}$
21	+0.5	0	4
22	+0.5	0	4.5
23	-0.5	-0.5	4
24	+0.5	+0.5	3.5
25	0	+0.5	4
26	-0.5	0.5	4
27	-0.5	-0.5	3.5
28	0	0	3.5
29	0.5	0.5	4.5
30	0.5	0	4.5

Table F.3.: Requirements for systematic electron identification variation similar to the *HadrRej* aproach.

G. Fully Corrected Spectra

This chapter shows the fully corrected dielectron spectra in the 0-20%, 20-40%, 40-80% and 0-80% most central Pb-Pb collisions at a center-of-mass energy $\sqrt{s_{\mathrm{NN}}} = 5.02\,\mathrm{TeV}$. These spectra are shown in different kinematic ranges as a function of invariant mass m_{ee} and pair transverse momentum $p_{\mathrm{T,ee}}$.

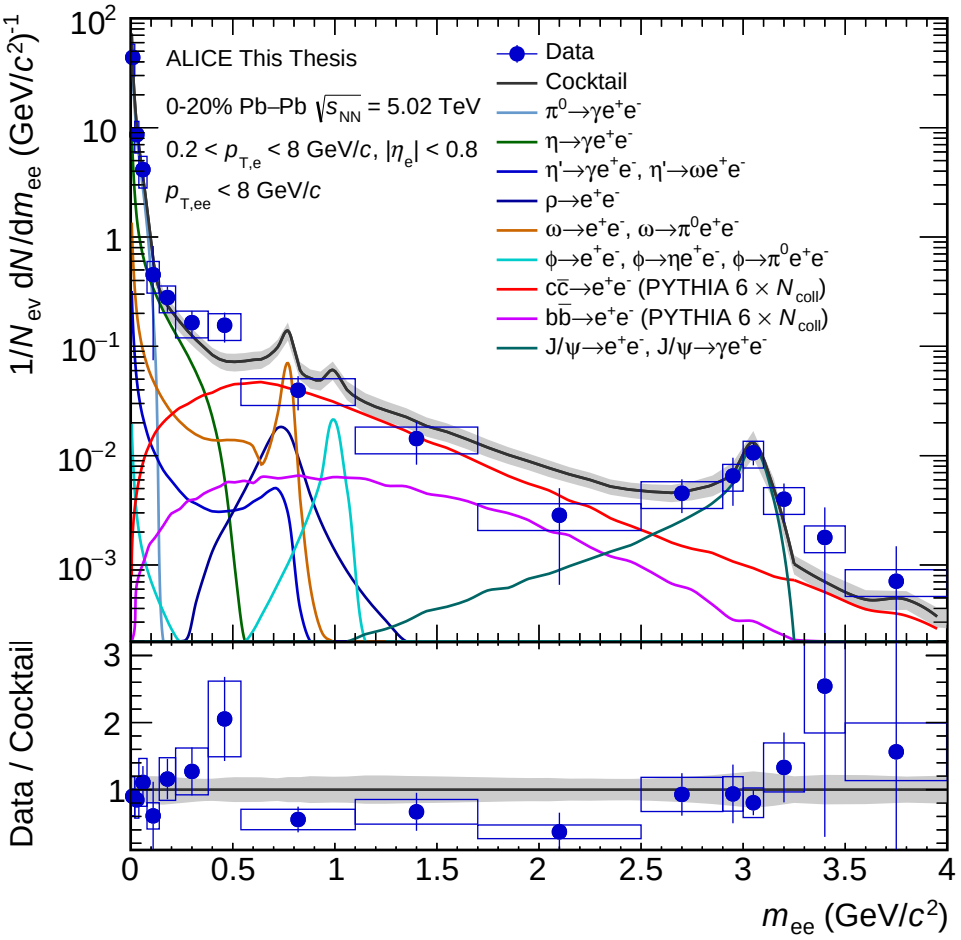

Figure G.1.: Fully corrected dielectron yield as a function of invariant mass m_{ee} integrated over pair transverse momentum $p_{T,ee}$ in the most 0-20% central Pb-Pb collisions at $\sqrt{s_{NN}} = 5.02\,\text{TeV}$ in the ALICE acceptance compared to the hadronic cocktail expectations. While error bars describe statistical uncertainties, boxes depict systematic uncertainties. The grey band around the total cocktail expectation represents systematic uncertainties of the cocktail. The lower panel shows the ratio between data and cocktail.

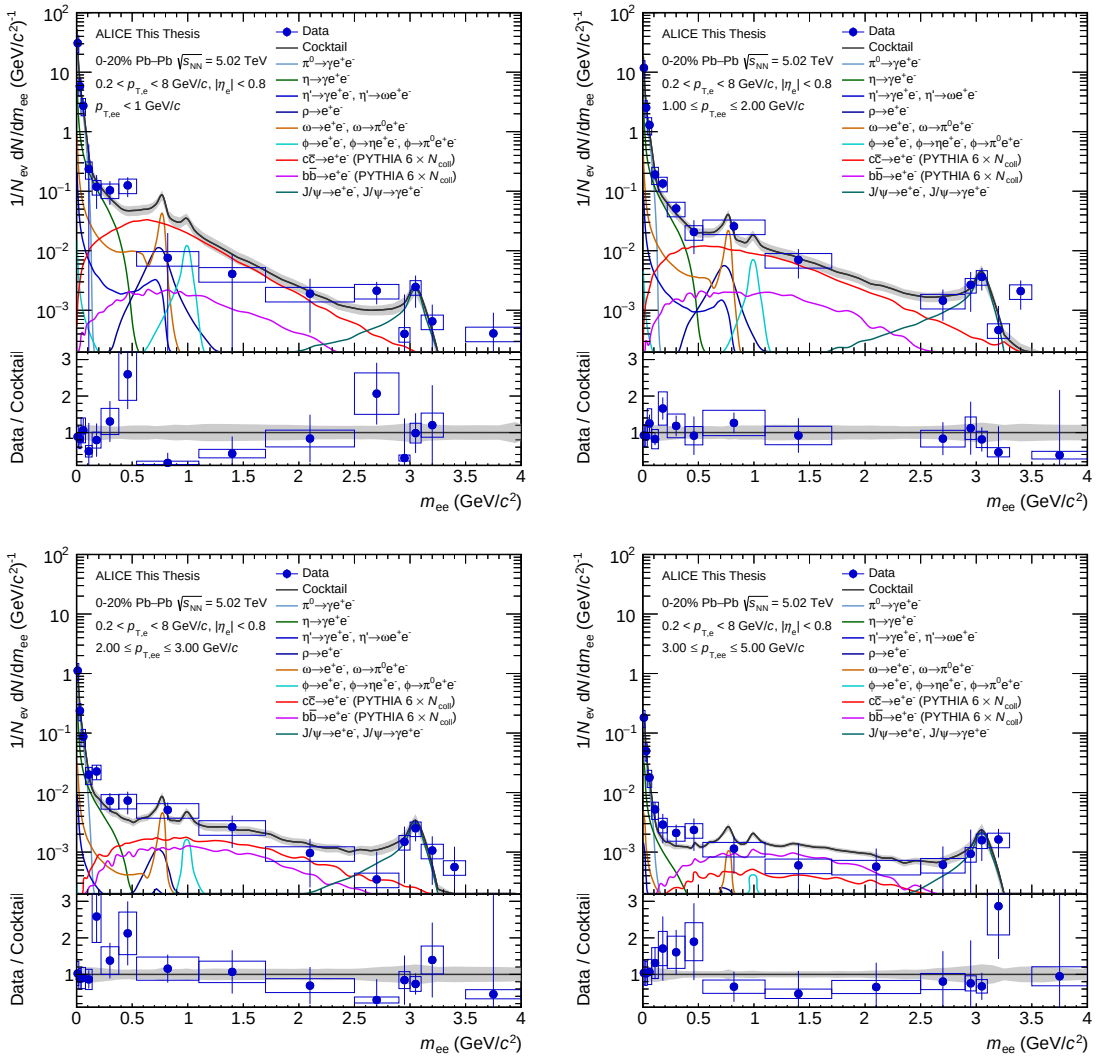

Figure G.2.: Fully corrected dielectron yield as a function of invariant mass m_{ee} in several pair transverse momentum $p_{T,ee}$ ranges in the most 0-20% central Pb-Pb collisions, similar to figure G.1.

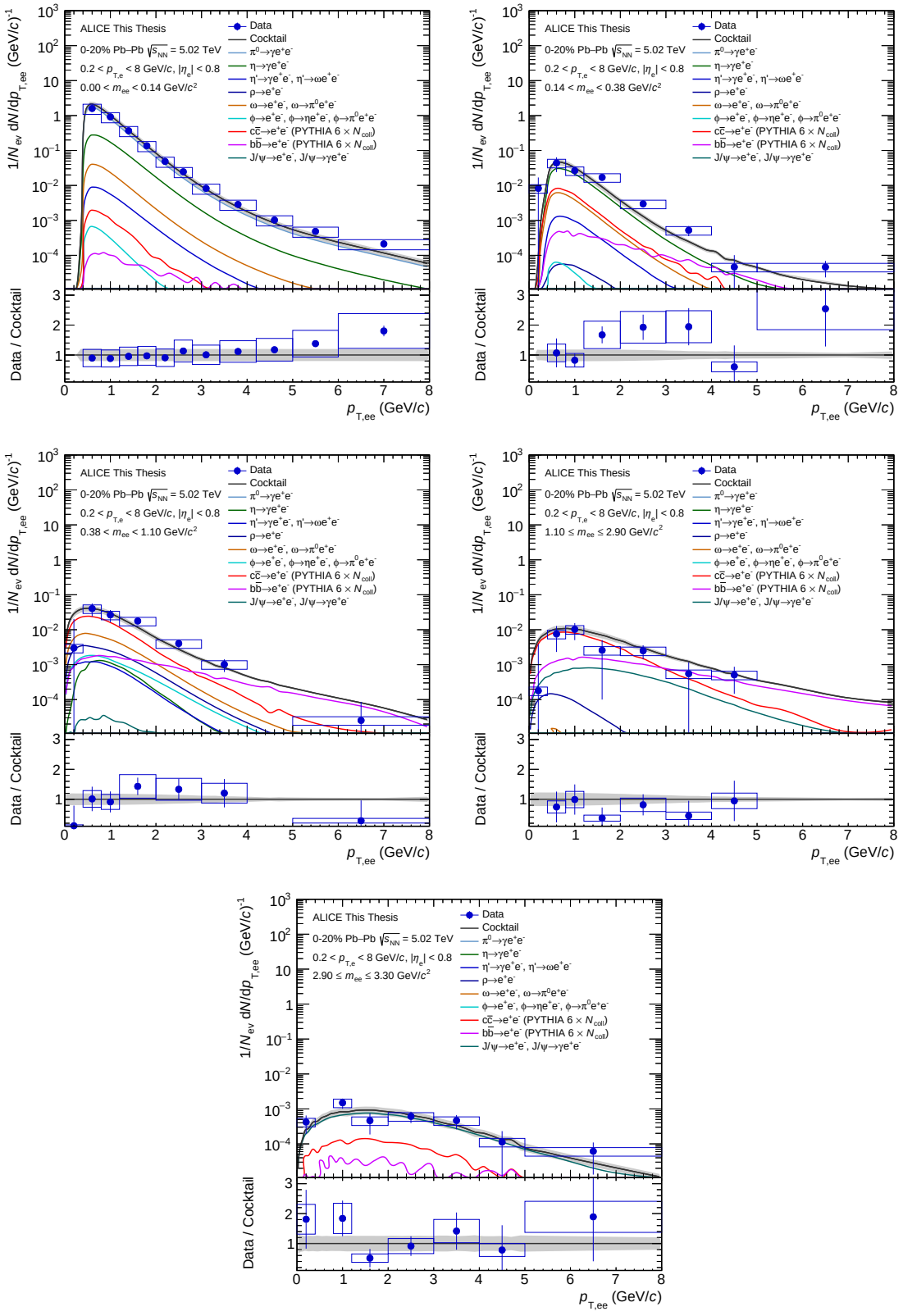

Figure G.3.: Fully corrected dielectron yield as a function of pair transverse momentum $p_{\mathrm{T,ee}}$ in several invariant mass m_{ee} ranges in the most 0-20% central Pb-Pb collisions, similar to figure G.1.

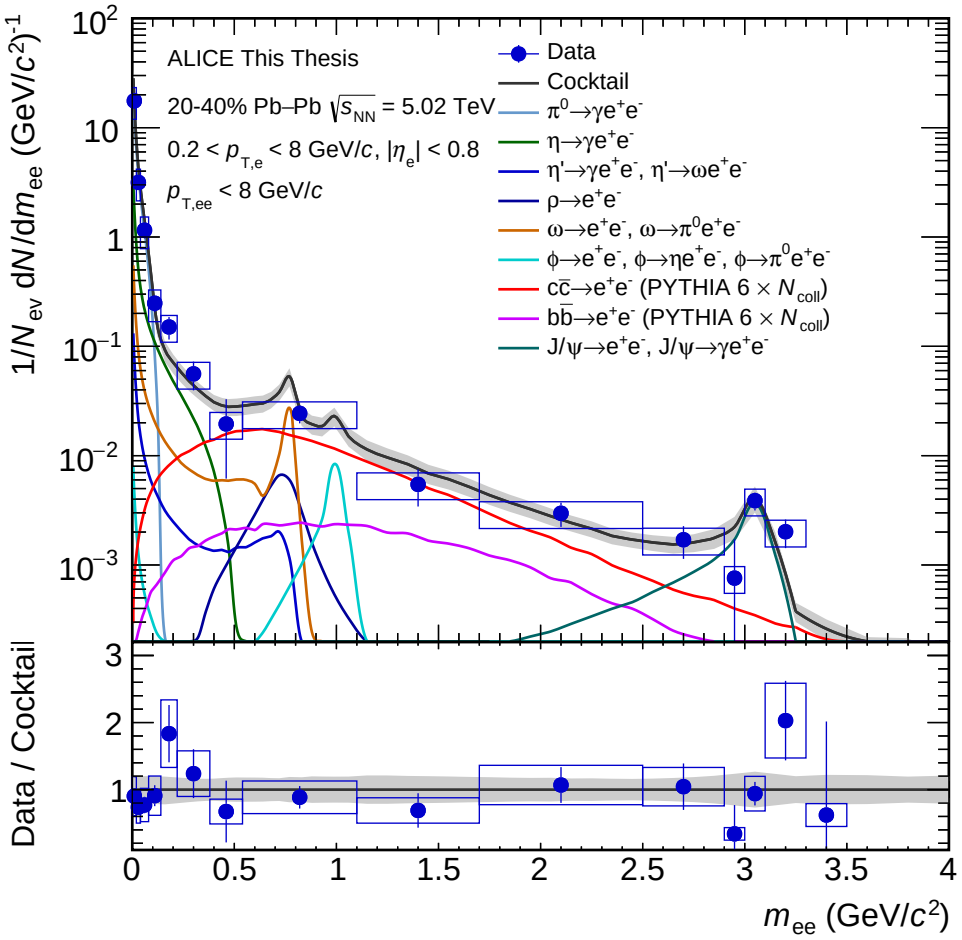

Figure G.4.: Fully corrected dielectron yield as a function of invariant mass m_{ee} integrated over pair transverse momentum $p_{T,ee}$ in the most 20-40% central Pb-Pb collisions at $\sqrt{s_{NN}} = 5.02\,\text{TeV}$ in the ALICE acceptance compared to the hadronic cocktail expectations. While error bars describe statistical uncertainties, boxes depict systematic uncertainties. The grey band around the total cocktail expectation represents systematic uncertainties of the cocktail. The lower panel shows the ratio between data and cocktail.

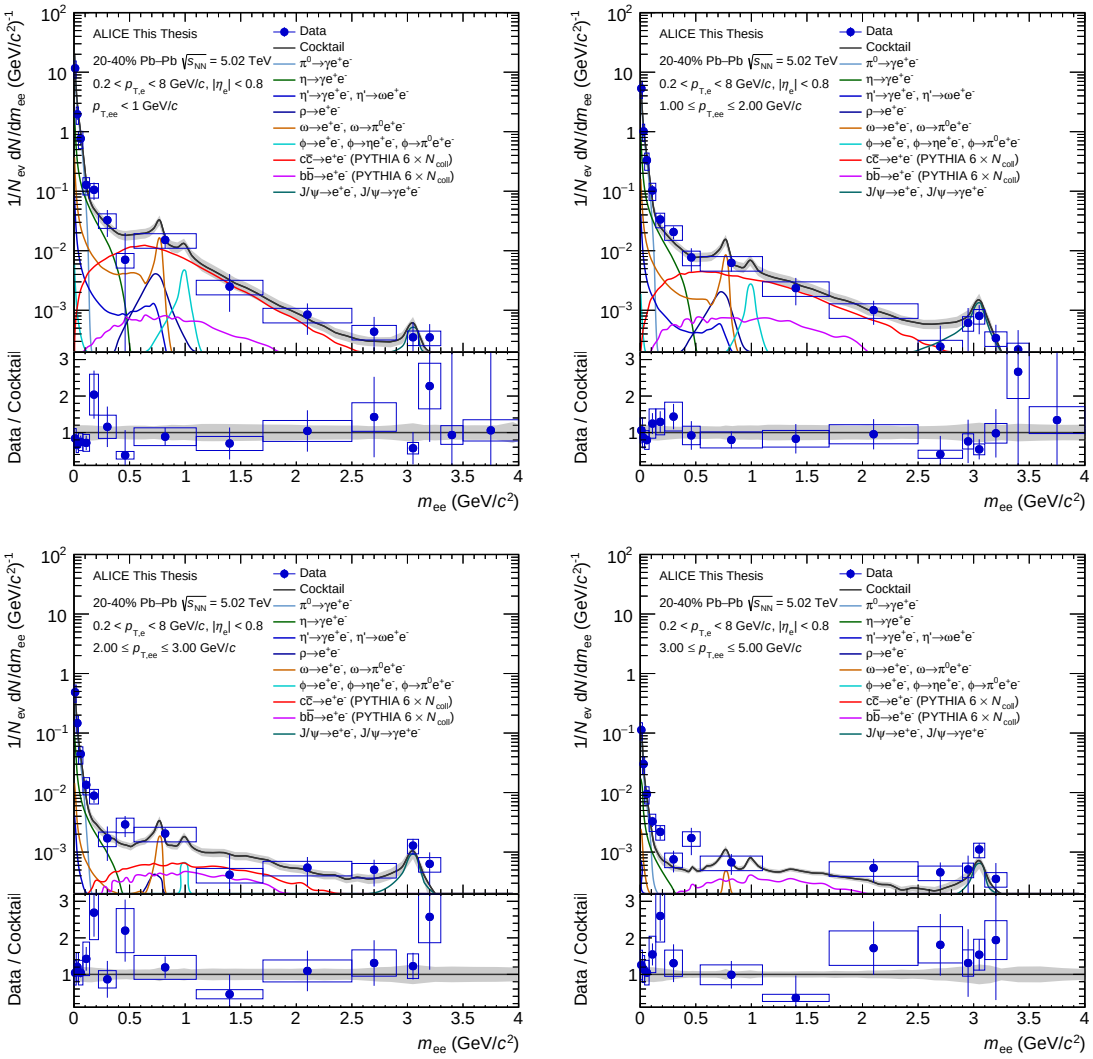

Figure G.5.: Fully corrected dielectron yield as a function of invariant mass m_{ee} in several pair transverse momentum $p_{T,ee}$ ranges in the most 20-40% central Pb-Pb collisions, similar to figure G.1.

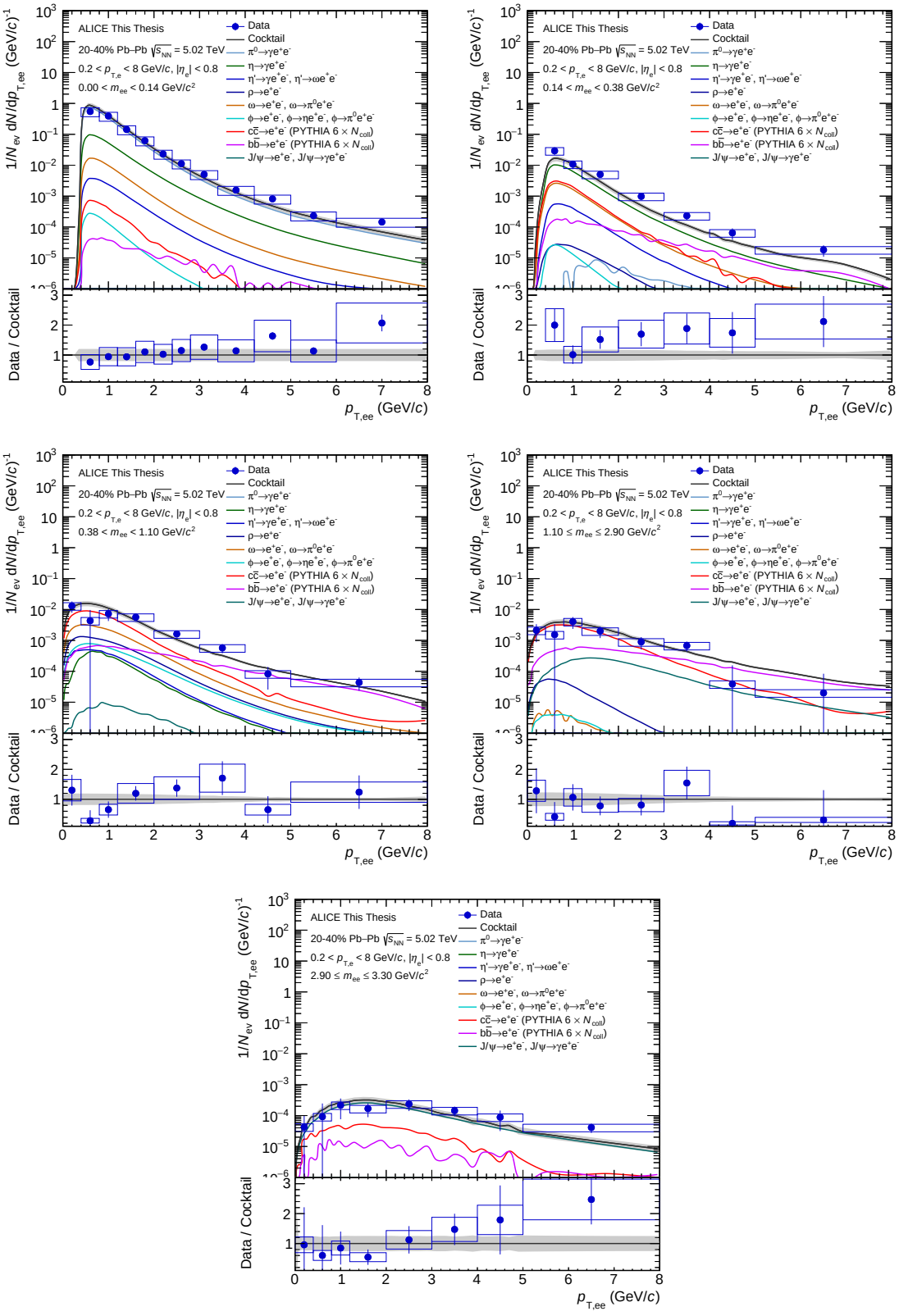

Figure G.6.: Fully corrected dielectron yield as a function of pair transverse momentum $p_{\mathrm{T,ee}}$ in several invariant mass m_{ee} ranges in the most 20-40% central Pb-Pb collisions, similar to figure G.1.

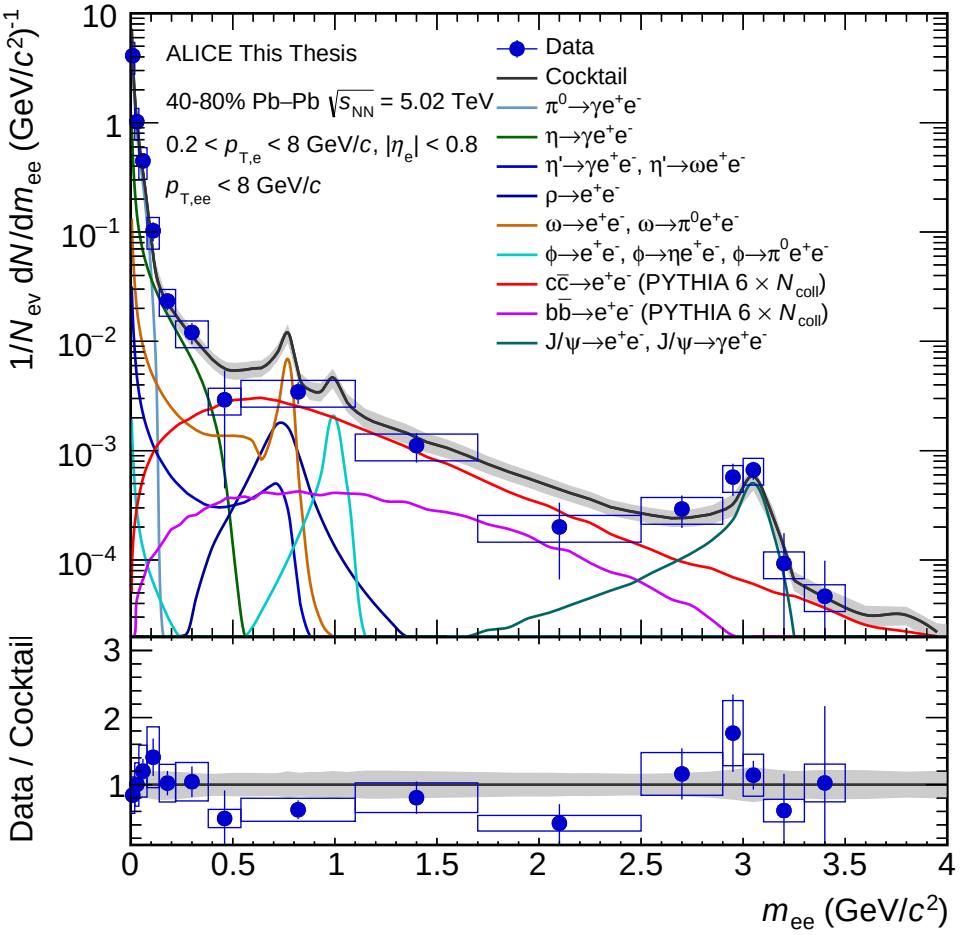

Figure G.7.: Fully corrected dielectron yield as a function of invariant mass m_{ee} integrated over pair transverse momentum $p_{T,ee}$ in the most 40-80% central Pb-Pb collisions at $\sqrt{s_{NN}} = 5.02\,\text{TeV}$ in the ALICE acceptance compared to the hadronic cocktail expectations. While error bars describe statistical uncertainties, boxes depict systematic uncertainties. The grey band around the total cocktail expectation represents systematic uncertainties of the cocktail. The lower panel shows the ratio between data and cocktail.

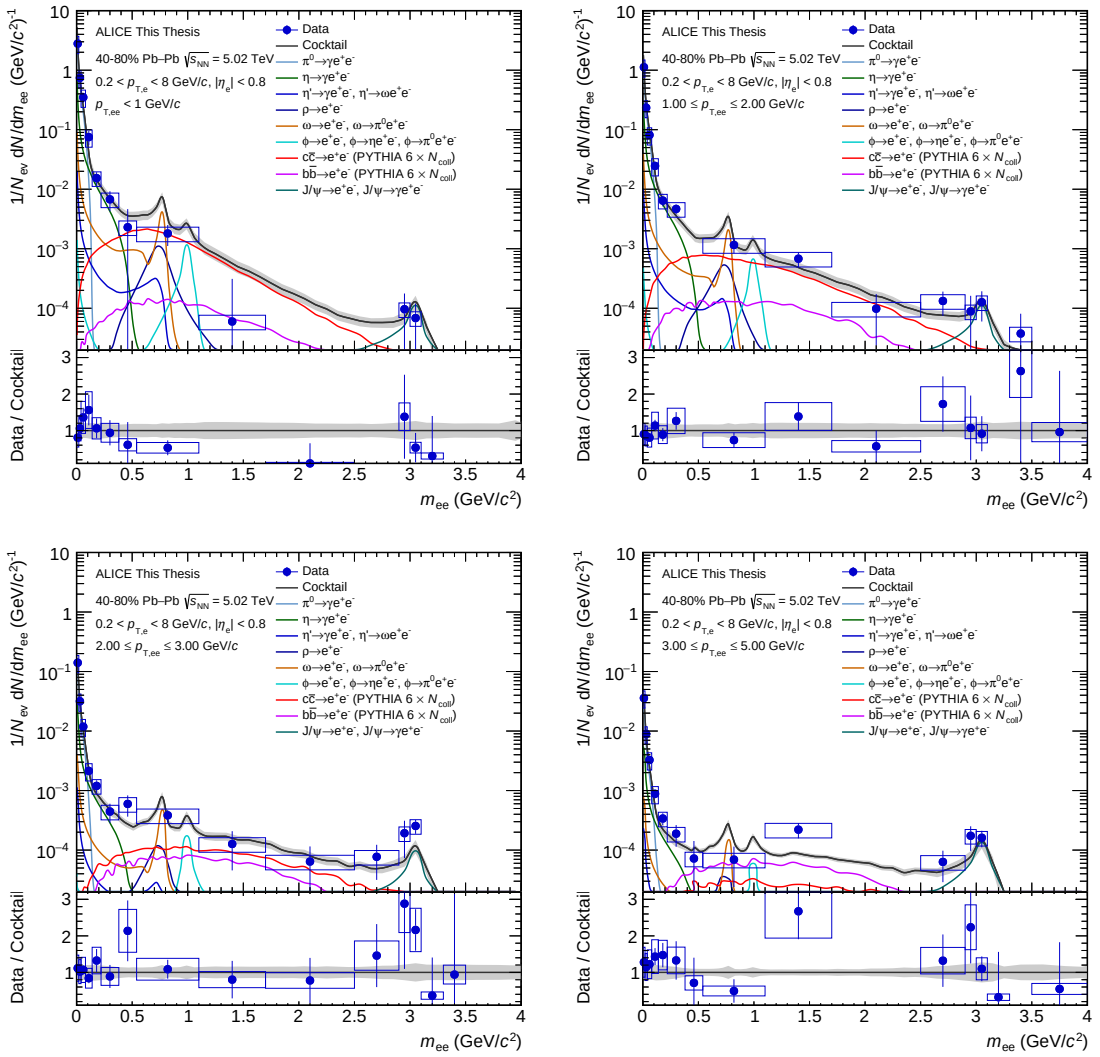

Figure G.8.: Fully corrected dielectron yield as a function of invariant mass m_{ee} in several pair transverse momentum $p_{\mathrm{T,ee}}$ ranges in the most 40-80% central Pb-Pb collisions, similar to figure G.1.

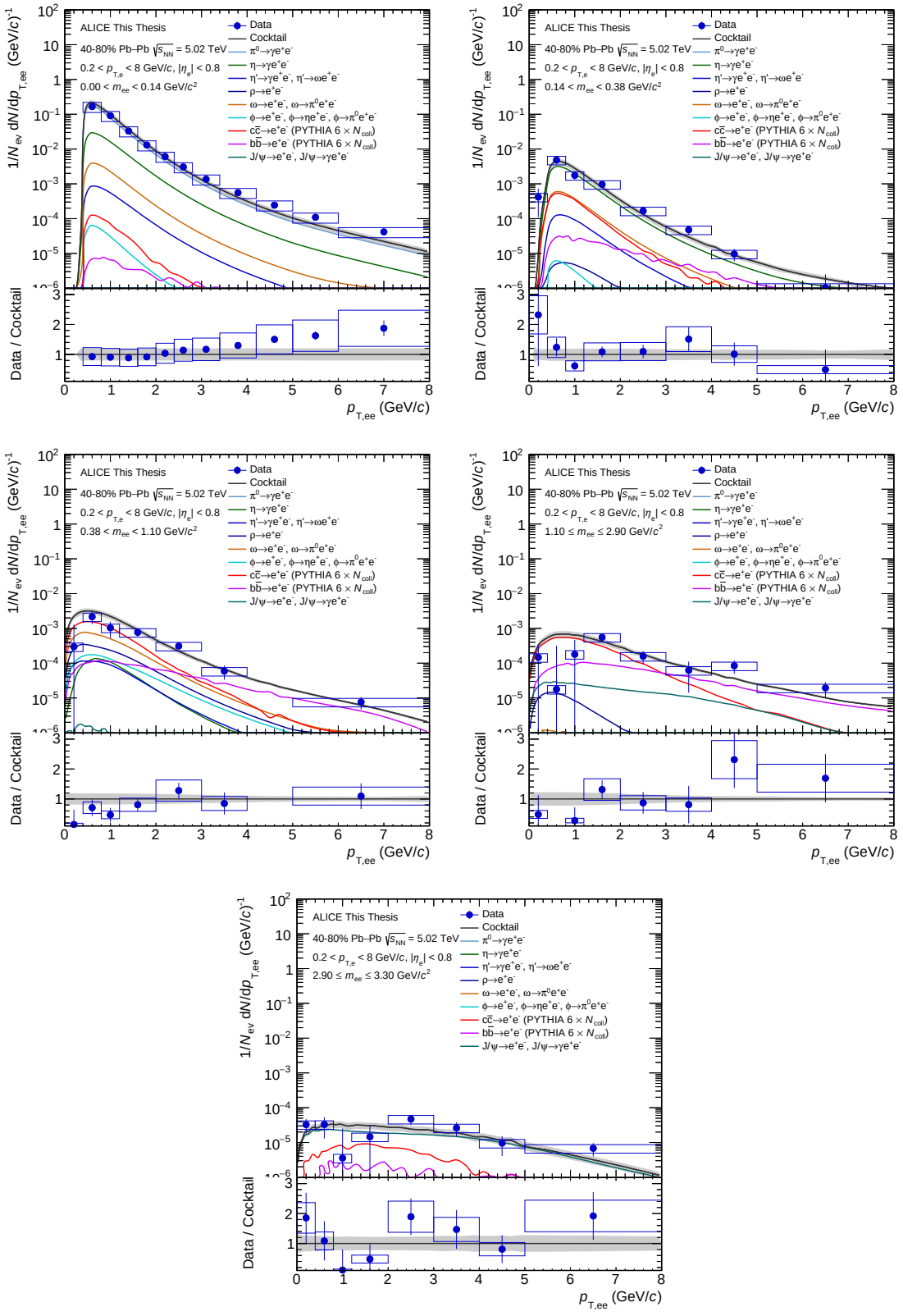

Figure G.9.: Fully corrected dielectron yield as a function of pair transverse momentum $p_{\mathrm{T,ee}}$ in several invariant mass m_{ee} ranges in the most 40-80% central Pb-Pb collisions, similar to figure G.1.

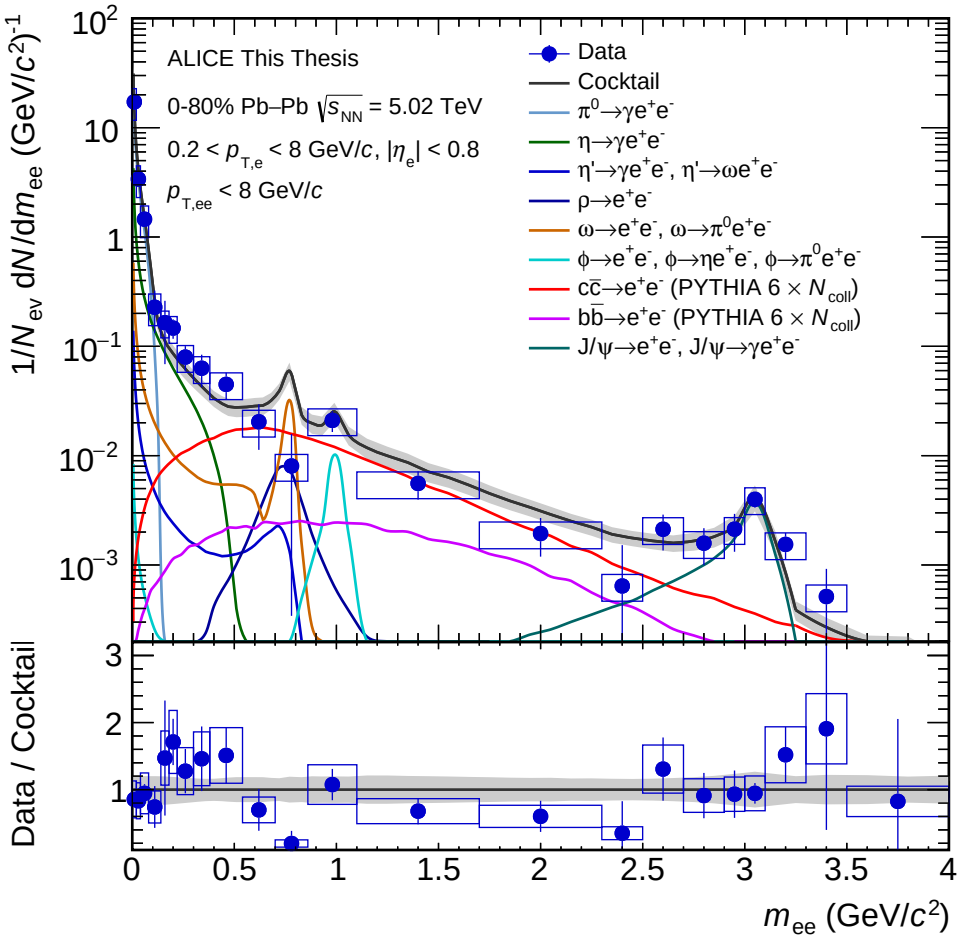

Figure G.10.: Fully corrected dielectron yield as a function of invariant mass m_{ee} integrated over pair transverse momentum $p_{T,ee}$ in the most 0-80% central Pb-Pb collisions at $\sqrt{s_{NN}} = 5.02\,\text{TeV}$ in the ALICE acceptance compared to the hadronic cocktail expectations. While error bars describe statistical uncertainties, boxes depict systematic uncertainties. The grey band around the total cocktail expectation represents systematic uncertainties of the cocktail. The lower panel shows the ratio between data and cocktail.

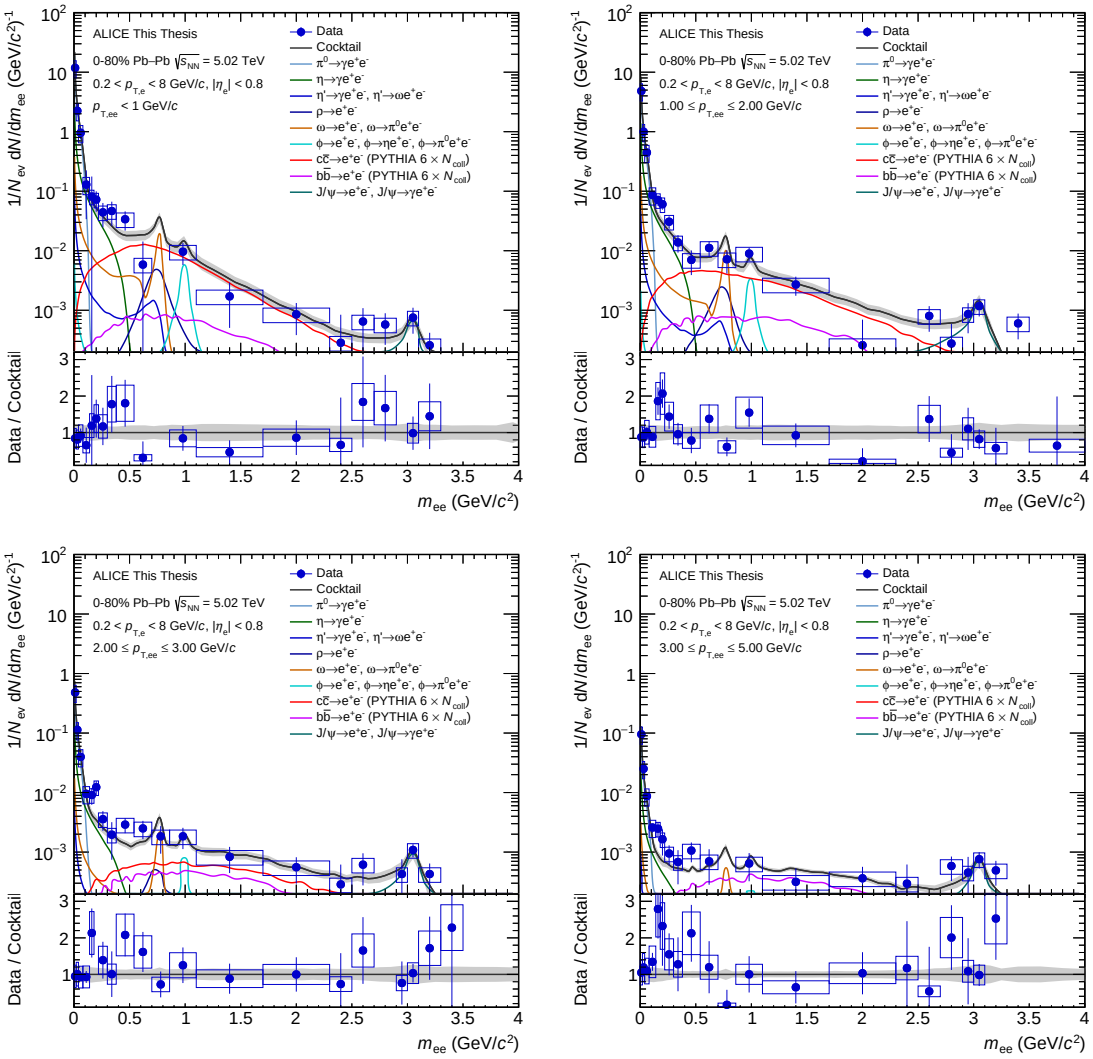

Figure G.11.: Fully corrected dielectron yield as a function of invariant mass m_{ee} in several pair transverse momentum $p_{\mathrm{T,ee}}$ ranges in the most 0-80% central Pb-Pb collisions, similar to figure G.1.

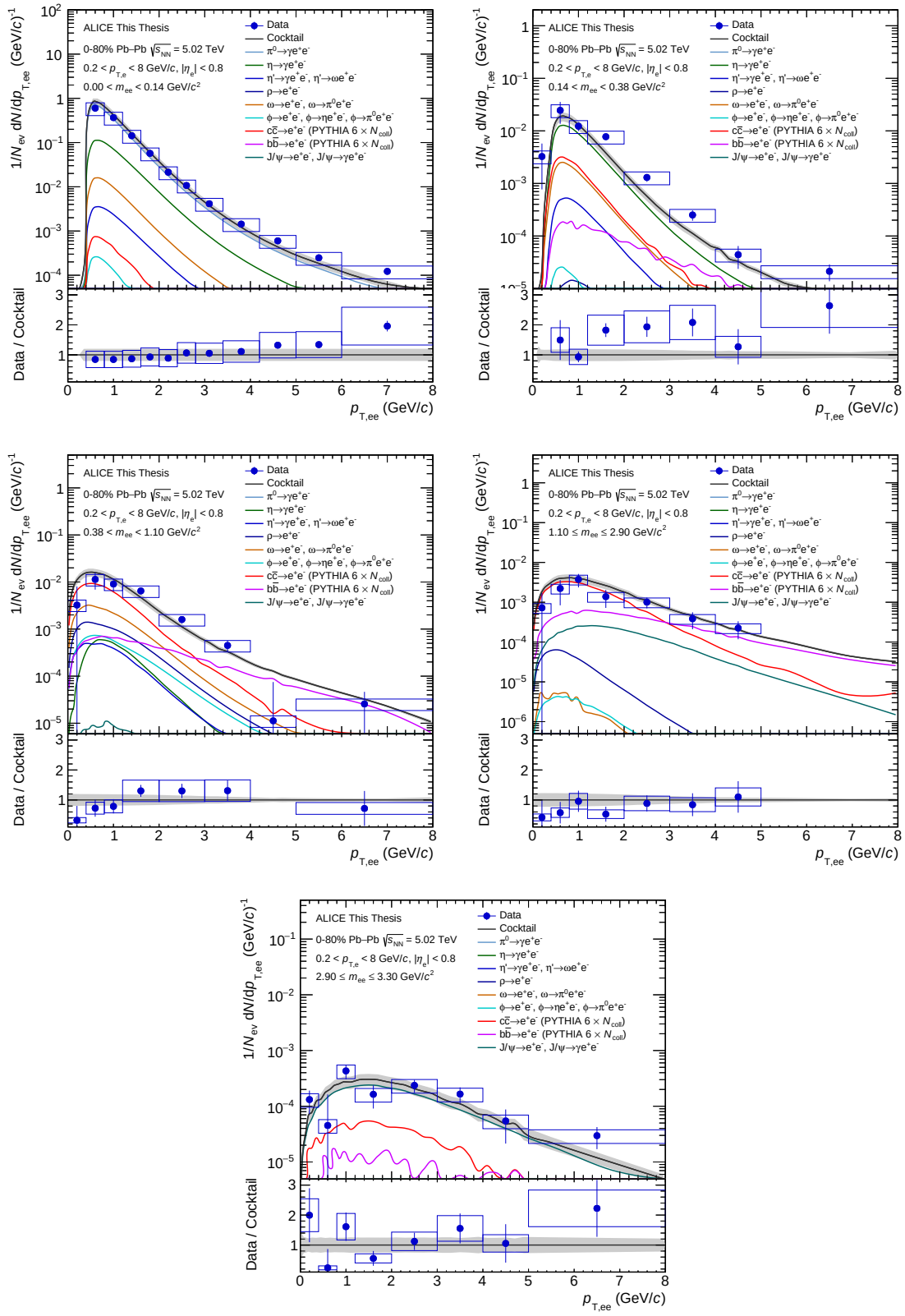

Figure G.12.: Fully corrected dielectron yield as a function of pair transverse momentum $p_{\mathrm{T,ee}}$ in several invariant mass m_{ee} ranges in the most 0-80% central Pb-Pb collisions, similar to figure G.1.

Bibliography

[1] P. A. R. Ade et al. 'Planck 2015 results. XIII. Cosmological parameters'. In: *Astron. Astrophys.* 594 (2016), A13.

[2] L. Yu. Abramova et al. *ALICE: Technical proposal for A Large Ion Collider Experiment at the CERN LHC*. LHC Tech. Proposal. Geneva: CERN, 1995.

[3] K. Aamodt et al. 'The ALICE experiment at the CERN LHC'. In: *JINST* 3 (2008), S08002.

[4] M. Tanabashi et al. 'Review of Particle Physics'. In: *Phys. Rev. D* 98 (3 2018), p. 030001.

[5] H. Fritzsch, Murray Gell-Mann and H. Leutwyler. 'Advantages of the Color Octet Gluon Picture'. In: *Phys. Lett.* 47B (1973), pp. 365–368.

[6] F. Yndurain. *The Theory of Quarks and Gluon interactions*. 2006.

[7] V. Khachatryan et al. 'Measurement of the inclusive 3-jet production differential cross section in proton-proton collisions at 7 TeV and determination of the strong coupling constant in the TeV range'. In: *The European Physical Journal C* 75.5 (May 2015), p. 186. ISSN: 1434-6052.

[8] Volker Koch. 'Aspects of chiral symmetry'. In: *Int. J. Mod. Phys.* E6 (1997), pp. 203–250.

[9] Rupert Millard, ed. *Mexican hat potential*. 2009.

[10] G. E. Brown and Mannque Rho. 'Scaling effective Lagrangians in a dense medium'. In: *Phys. Rev. Lett.* 66 (21 May 1991), pp. 2720–2723.

[11] Paul M. Hohler and Ralf Rapp. 'Is Rho-Meson Melting Compatible with Chiral Restoration?' In: *Physics Letters B* 731 (Nov. 2013).

[12] Irene Rodriguez Amado. 'Applications of Holography to Strongly Coupled Hydrodynamics'. PhD thesis. Madrid, Autonoma U., 2010.

[13] Simon Hands. 'The phase diagram of QCD'. In: *Contemporary Physics* 42.4 (2001), pp. 209–225.

[14] Julian Book. 'J/Ψ Production in Pb-Pb Collisions with ALICE at the LHC'. PhD thesis. Goethe Universität Frankfurt, 2014.

[15] Anton Andronic et al. 'Decoding the phase structure of QCD via particle production at high energy'. In: *Nature* 561.7723 (2018), pp. 321–330. arXiv: 1710.09425 [nucl-th].

[16] Albert M Sirunyan et al. 'Nuclear modification factor of D^0 mesons in PbPb collisions at $\sqrt{s_{NN}} = 5.02$ TeV'. In: *Phys. Lett.* B782 (2018), pp. 474–496. arXiv: 1708.04962 [nucl-ex].

[17] Jaroslav Adam et al. 'Transverse momentum dependence of D-meson production in Pb-Pb collisions at $\sqrt{s_{NN}} = 2.76$ TeV'. In: *JHEP* 03 (2016), p. 081. arXiv: 1509.06888 [nucl-ex].

[18] B. Abelev et al. 'D meson elliptic flow in non-central Pb-Pb collisions at $\sqrt{s_{NN}} = 2.76$TeV'. In: *Phys. Rev. Lett.* 111 (2013), p. 102301. arXiv: 1305.2707 [nucl-ex].

[19] R. Nouicer. 'New State of Nuclear Matter: Nearly Perfect Fluid of Quarks and Gluons in Heavy Ion Collisions at RHIC Energies'. In: *Eur. Phys. J. Plus* 131.3 (2016), p. 70. arXiv: 1512.08993 [nucl-ex].

[20] Chun Shen et al. 'Radial and elliptic flow in Pb+Pb collisions at the Large Hadron Collider from viscous hydrodynamic'. In: *Phys. Rev.* C84 (2011), p. 044903. arXiv: 1105.3226 [nucl-th].

[21] Jean-Yves Ollitrault. 'Anisotropy as a signature of transverse collective flow'. In: *Phys. Rev. D* 46 (1 July 1992), pp. 229–245.

[22] Peter F. Kolb and Ulrich W. Heinz. 'Hydrodynamic description of ultra-relativistic heavy ion collisions'. In: (2003), pp. 634–714. arXiv: nucl-th/0305084 [nucl-th].

[23] M. Gyulassy, I. Vitev and X. N. Wang. 'High p(T) azimuthal asymmetry in noncentral A+A at RHIC'. In: *Phys. Rev. Lett.* 86 (2001), pp. 2537–2540. arXiv: nucl-th/0012092 [nucl-th].

[24] E. V. Shuryak. 'The Azimuthal asymmetry at large p(t) seem to be too large for a 'jet quenching''. In: *Phys. Rev.* C66 (2002), p. 027902. arXiv: nucl-th/0112042 [nucl-th].

[25] Betty Bezverkhny Abelev et al. 'Azimuthal anisotropy of D meson production in Pb-Pb collisions at $\sqrt{s_{NN}} = 2.76$ TeV'. In: *Phys. Rev.* C90.3 (2014), p. 034904. arXiv: 1405.2001 [nucl-ex].

[26] ALICE Collaboration. 'Multi-strange baryon production in p-Pb collisions at $\sqrt{s_{NN}} = 5.02$ TeV'. In: *Physics Letters B* 758 (2016), pp. 389–401. ISSN: 0370-2693.

[27] Johann Rafelski and R. Hagedorn. 'From Hadron Gas to Quark Matter. 2.' In: *International Symposium on Statistical Mechanics of Quarks and Hadrons Bielefeld, Germany, August 24-31, 1980.* 1980, pp. 253–272.

[28] Johann Rafelski and Berndt Muller. 'Strangeness Production in the Quark - Gluon Plasma'. In: *Phys. Rev. Lett.* 48 (1982). [Erratum: Phys. Rev. Lett. 56,2334(1986)], p. 1066.

[29] Betty Bezverkhny Abelev et al. 'Multi-strange baryon production at mid-rapidity in Pb-Pb collisions at $\sqrt{s_{NN}} = 2.76$ TeV'. In: *Phys. Lett.* B728 (2014). [Erratum: Phys. Lett.B734,409(2014)], pp. 216–227. arXiv: 1307.5543 [nucl-ex].

[30] J. Book. 'J/ψ production in Pb–Pb collisions at $\sqrt{s_{NN}} = 2.76$ TeV'. In: *Nucl. Phys.* A931 (2014), pp. 591–595.

[31] T. Matsui and H. Satz. 'J/ψ Suppression by Quark-Gluon Plasma Formation'. In: *Phys. Lett.* B178 (1986), pp. 416–422.

[32] P. Braun-Munzinger and J. Stachel. '(Non)thermal aspects of charmonium production and a new look at J/psi suppression'. In: *Phys. Lett.* B490 (2000), pp. 196–202.

[33] Munshi G. Mustafa, Markus H. Thoma and Purnendu Chakraborty. 'Screening of a moving parton in the quark gluon plasma'. In: *Phys. Rev.* C71 (2005), p. 017901. arXiv: hep-ph/0403279 [hep-ph].

[34] Peter Braun-Munzinger and Johanna Stachel. 'The quest for the quark-gluon plasma'. In: *Nature* 448 (2007), pp. 302–309.

[35] Jean-Francois Paquet et al. 'Production of photons in relativistic heavy-ion collisions'. In: *Phys. Rev.* C93.4 (2016), p. 044906. arXiv: 1509.06738 [hep-ph].

[36] S. Acharya et al. 'Direct photon elliptic flow in Pb–Pb collisions at $\sqrt{s_{\mathrm{NN}}} = 2.76$ TeV'. In: *Physics Letters B* 789 (2019), pp. 308–322. ISSN: 0370-2693.

[37] Petja Paakkinen. 'Nuclear parton distribution functions'. In: *Proceedings, Old and New Strong Interactions from LHC to Future Colliders (LFC17): Trento, Italy, September 11-15, 2017*. 2017, pp. 33–40. arXiv: 1802.05927 [hep-ph].

[38] R. Vogt. 'Cold Nuclear Matter Effects on Open and Hidden Heavy Flavor Production at the LHC'. In: *Proceedings, 7th International Workshop on Charm Physics, CHARM 2015: Detroit, USA, May 18-22, 2015*. 2015. arXiv: 1508.01286 [hep-ph].

[39] J. W. Cronin et al. 'Production of hadrons at large transverse momentum at 200, 300, and 400 GeV'. In: *Phys. Rev. D* 11 (11 June 1975), pp. 3105–3123.

[40] Wikimedia Commons. *Processo Drell-Yan*. 2006. URL: https://commons.wikimedia.org/wiki/File:Drell-Yan.svg.

[41] Sidney D. Drell and Tung-Mow Yan. 'Massive Lepton-Pair Production in Hadron-Hadron Collisions at High Energies'. In: *Phys. Rev. Lett.* 25 (13 Sept. 1970), pp. 902–902.

[42] J. H. Christenson et al. 'Observation of Massive Muon Pairs in Hadron Collisions'. In: *Phys. Rev. Lett.* 25 (21 Nov. 1970), pp. 1523–1526.

[43] Serguei Chatrchyan et al. 'Measurement of the Drell-Yan Cross Section in pp Collisions at $\sqrt{s} = 7$ TeV'. In: *JHEP* 10 (2011), p. 007.

[44] Shreyasi Acharya et al. 'Dielectron production in proton-proton collisions at $\sqrt{s} = 7$ TeV'. In: *JHEP* 09 (2018), p. 064.

[45] Norman M. Kroll and Walter Wada. 'Internal Pair Production Associated with the Emission of High-Energy Gamma Rays'. In: *Phys. Rev.* 98 (5 June 1955), pp. 1355–1359.

[46] NA60 Collaboration. 'Precision study of the $\eta \to \mu^+\mu^-\gamma$ and $\omega \to \mu^+\mu^-\pi^0$ electromagnetic transition form-factors and of the $\rho \to \mu^+\mu^-$ line shape in NA60'. In: *Physics Letters B* 757 (2016), pp. 437–444.

[47] R. Rapp, J. Wambach and H. van Hees. 'The Chiral Restoration Transition of QCD and Low Mass Dileptons'. In: *Landolt-Bornstein* 23 (2010), p. 134.

[48] Shreyasi Acharya et al. 'Measurement of D-meson production at mid-rapidity in pp collisions at $\sqrt{s} = 7$ TeV'. In: *Eur. Phys. J.* C77.8 (2017), p. 550. arXiv: 1702.00766 [hep-ex].

[49] Jerome Jung. private communication. 5th Aug. 2019.

[50] A. Andronic et al. 'Heavy-flavour and quarkonium production in the LHC era: from proton–proton to heavy-ion collisions'. In: *The European Physical Journal C* 76.3 (Feb. 2016), p. 107.

[51] Mariola Kłusek-Gawenda et al. 'Dilepton Radiation in Heavy-Ion Collisions at Small Transverse Momentum'. In: *Phys. Lett.* B790 (2019), pp. 339–344. DOI: 10.1016/j.physletb.2019.01.035. arXiv: 1809.07049 [nucl-th].

[52] J. Adam et al. 'Low-p_T e^+e^- Pair Production in Au + Au Collisions at $\sqrt{s_{NN}} = 200$ GeV and U + U Collisions at $\sqrt{s_{NN}} = 193$ GeV at STAR'. In: *Phys. Rev. Lett.* 121 (13 Sept. 2018), p. 132301.

[53] L.D. Landau and E.M. Lifshitz. In: *Phys. Zs. Sowjet* 244.6 (1934).

[54] Carlos A. Bertulani, Spencer R. Klein and Joakim Nystrand. 'Physics of ultra-peripheral nuclear collisions'. In: *Ann. Rev. Nucl. Part. Sci.* 55 (2005), pp. 271–310. arXiv: nucl-ex/0502005 [nucl-ex].

[55] M. G. Ryskin. 'Diffractive J/ψ electroproduction in LLA QCD'. In: *Z. Phys.* C57 (1993), pp. 89–92.

[56] Shreyasi Acharya et al. 'Coherent J/ψ photoproduction at forward rapidity in ultra-peripheral Pb-Pb collisions at $\sqrt{s_{\mathrm{NN}}} = 5.02$ TeV'. In: (2019). arXiv: 1904.06272 [nucl-ex].

[57] Carlos A. Bertulani and Gerhard Baur. 'Electromagnetic processes in relativistic heavy ion collisions'. In: *Physics Reports* 163.5 (1988), pp. 299–408. ISSN: 0370-1573.

[58] Spencer R. Klein. 'Two-photon production of dilepton pairs in peripheral heavy ion collisions'. In: *Phys. Rev. C* 97 (5 May 2018), p. 054903.

[59] W. Zha et al. 'Coherent lepton pair production in hadronic heavy ion collisions'. In: *Phys. Lett.* B781 (2018), pp. 182–186. arXiv: 1804.01813 [hep-ph].

[60] CERES Collaboration. 'Modification of the ρ meson detected by low-mass electron-positron pairs in central PbAu collisions at 158A GeV'. In: *Physics Letters B* 666.5 (2008), pp. 425–429. ISSN: 0370-2693.

[61] CERES Collaboration. 'First results of the CERES electron pair spectrometer from p + Be, p + Au and S + Au collisions'. In: *Nuclear Physics A* 566 (1994), pp. 87–94. ISSN: 0375-9474.

[62] 'Enhanced Production of Low-Mass Electron Pairs in 200 GeV/Nucleon S-Au Collisions at the CERN Super Proton Synchrotron'. In: *Phys. Rev. Lett.* 75 (7 Aug. 1995), pp. 1272–1275.

[63] CERES Collaboration. 'Low-mass e^+e^- pair production in 158 A GeV Pb-Au collisions at the CERN SPS, its dependence on multiplicity and transverse momentum'. In: *Physics Letters B* 422.1 (1998), pp. 405–412. ISSN: 0370-2693.

[64] G.E. Brown and Mannque Rho. 'Chiral restoration in hot and/or dense matter'. In: *Physics Reports* 269.6 (1996), pp. 333–380. ISSN: 0370-1573.

[65] G.E. Brown and Mannque Rho. 'On the manifestation of chiral symmetry in nuclei and dense nuclear matter'. In: *Physics Reports* 363.2 (2002), pp. 85–171. ISSN: 0370-1573.

[66] Hendrik van Hees and Ralf Rapp. 'Comprehensive Interpretation of Thermal Dileptons Measured at the CERN Super Proton Synchrotron'. In: *Phys. Rev. Lett.* 97 (10 Sept. 2006), p. 102301.

[67] R. Arnaldi et al. 'NA60 results on thermal dimuons'. In: *Eur. Phys. J.* C61 (2009), pp. 711–720.

[68] A. Adare et al. 'Dielectron production in Au + Au collisions at $\sqrt{s_{NN}} = 200$ GeV'. In: *Phys. Rev. C* 93 (1 Jan. 2016), p. 014904.

[69] A. Adare et al. 'Dilepton mass spectra in p+p collisions at $\sqrt{s_{\mathrm{NN}}} = 200$ GeV and the contribution from open charm'. In: *Phys. Lett.* B670 (2009), pp. 313–320.

[70] 'Cross section for $b\bar{b}$ production via dielectrons in d + Au collisions at $\sqrt{s_{NN}} =$ 200 GeV'. In: *Phys. Rev. C* 91 (1 Jan. 2015), p. 014907.

[71] Torbjorn Sjostrand, Stephen Mrenna and Peter Z. Skands. 'PYTHIA 6.4 Physics and Manual'. In: *JHEP* 05 (2006), p. 026. arXiv: `hep-ph/0603175 [hep-ph]`.

[72] R. Rapp. 'Signatures of thermal dilepton radiation at RHIC'. In: *Phys. Rev.* C63 (2001), p. 054907.

[73] L. Adamczyk et al. 'Measurements of Dielectron Production in Au+Au Collisions at $\sqrt{s_{\mathrm{NN}}} = 200$ GeV from the STAR Experiment'. In: *Phys. Rev.* C92.2 (2015), p. 024912.

[74] Patrick Huck. 'Beam energy dependence of dielectron production in Au+Au collisions from STAR at RHIC'. In: *Nuclear Physics A* 931 (2014). QUARK MATTER 2014, pp. 659–664. ISSN: 0375-9474.

[75] L. Adamczyk et al. 'Dielectron Mass Spectra from Au+Au Collisions at $\sqrt{s_{\mathrm{NN}}} = 200$ GeV'. In: *Phys. Rev. Lett.* 113.2 (2014). [Addendum: Phys. Rev. Lett.113, no.4, 049903(2014)], p. 022301.

[76] Spencer R. Klein et al. 'STARlight: A Monte Carlo simulation program for ultra-peripheral collisions of relativistic ions'. In: *Comput. Phys. Commun.* 212 (2017), pp. 258–268. arXiv: 1607.03838 [hep-ph].

[77] Shreyasi Acharya et al. 'Dielectron and heavy-quark production in inelastic and high-multiplicity proton–proton collisions at $\sqrt{s} = 13$ TeV'. In: *Phys. Lett.* B788 (2019), pp. 505–518.

[78] Shreyasi Acharya et al. 'Measurement of dielectron production in central Pb-Pb collisions at $\sqrt{s_{\mathrm{NN}}} = 2.76$ TeV'. In: (2018). arXiv: 1807.00923 [nucl-ex].

[79] ALICE Collaboration. *Low $p_{T,ee}$ spectrum in 70-90% centrality*. 2019. URL: http://alice-figure.web.cern.ch/node/15006.

[80] Jerome Jung. 'Dielectron Production in pp Collisions at $\sqrt{s} = 13$ TeV Measured in a Dedicated Low Magnetic-Field Setting with ALICE'. In: *MDPI Proc.* 10.1 (2019), p. 50.

[81] Jerome Jung. 'Dielectron production in pp collisions at $\sqrt{s} = 13$ TeV measured in a dedicated low magnetic-field setting with ALICE'. Master thesis. Goethe Universität Frankfurt, 2019.

[82] W. Cassing and E. L. Bratkovskaya. 'Parton transport and hadronization from the dynamical quasiparticle point of view'. In: *Phys. Rev.* C78 (2008), p. 034919. arXiv: 0808.0022 [hep-ph].

[83] W. Cassing and E. L. Bratkovskaya. 'Parton-Hadron-String Dynamics: an off-shell transport approach for relativistic energies'. In: *Nucl. Phys.* A831 (2009), pp. 215–242. arXiv: 0907.5331 [nucl-th].

[84] Taesoo Song, Wolfgang Cassing and Elena Moreau Pierre and Bratkovskaya. 'Open charm and dileptons from relativistic heavy-ion collisions'. In: *Phys. Rev.* C97.6 (2018), p. 064907.

[85] Ralf Rapp. 'Dilepton Spectroscopy of QCD Matter at Collider Energies'. In: *Adv. High Energy Phys.* 2013 (2013), p. 148253.

[86] Lyndon Evans and Philip Bryant. 'LHC Machine'. In: *Journal of Instrumentation* 3.08 (Aug. 2008), S08001–S08001.

[87] A Beuret et al. 'The LHC Lead Injector Chain'. In: LHC-Project-Report-776. CERN-LHC-Project-Report-776 (Aug. 2004). revised version submitted on 2004-09-23 14:33:06, 4 p.

[88] John Jowett et al. 'The 2015 Heavy-Ion Run of the LHC'. In: *Proceedings, 7th International Particle Accelerator Conference (IPAC 2016): Busan, Korea, May 8-13, 2016*. 2016, TUPMW027.

[89] Lyndon Evans. 'The Large Hadron Collider'. In: *New Journal of Physics* 9.9 (2007), p. 335.

[90] CERN. *LHC Injector Chain*. 2010. URL: `http://maalpu.org/lhc/LHC.main.htm` (visited on 01/10/2018).

[91] ALICE Collaboration. *3D ALICE Schematic RUN2 - with Description*. 2017. URL: `https://alice-figure.web.cern.ch/node/11218`.

[92] Collaboration Alice. 'ALICE: Physics Performance Report, Volume I'. In: *Journal of Physics G: Nuclear and Particle Physics* 30.11 (2004), p. 1517.

[93] Collaboration ALICE. 'ALICE: Physics Performance Report, Volume II'. In: *Journal of Physics G: Nuclear and Particle Physics* 32.10 (2006), p. 1295.

[94] Betty Bezverkhny Abelev et al. 'Performance of the ALICE Experiment at the CERN LHC'. In: *Int. J. Mod. Phys.* A29 (2014), p. 1430044.

[95] The ALICE collaboration. 'Performance of the ALICE VZERO system'. In: *Journal of Instrumentation* 8.10 (2013), P10016.

[96] K Aamodt et al. 'Alignment of the ALICE Inner Tracking System with cosmic-ray tracks'. In: *JINST* 5 (2010), P03003.

[97] The ALICE collaboration. 'Technical Design Report for the Upgrade of the ALICE Inner Tracking System'. In: *J. Phys. G: Nucl. Part. Phys.* 41.087002 (2014).

[98] J. Alme et al. 'The ALICE TPC, a large 3-dimensional tracking device with fast readout for ultra-high multiplicity events'. In: *Nuclear Instruments and Methods in Physics Research Section A: Accelerators, Spectrometers, Detectors and Associated Equipment* 622.1 (2010), pp. 316–367.

[99] R. Brun et al. 'GEANT3'. In: (1987).

[100] Miklos Gyulassy and Xin-Nian Wang. 'HIJING 1.0: A Monte Carlo program for parton and particle production in high-energy hadronic and nuclear collisions'. In: *Comput. Phys. Commun.* 83 (1994), p. 307.

[101] R.J. Glauber and G. Matthiae. 'High-energy scattering of protons by nuclei'. In: *Nuclear Physics B* 21.2 (1970), pp. 135–157. ISSN: 0550-3213.

[102] ALICE Collaboration. 'Centrality determination in heavy ion collisions'. In: *ALICE Public Note* (Aug. 2018).

[103] ALICE Collaboration. 'Centrality determination in heavy ion collisions'. Unpublished Analysis Note. 2018.

[104] The ALICE Collaboration, ed. *The ALICE definition of primary particles*. 2017.

[105] Donald E. Groom, Nikolai V. Mokhov and Sergei I. Striganov. 'Muon Stopping Power and Range Tables'. In: *Atomic Data and Nuclear Data Tables* 76 (2001).

[106] Elena Botta. 'Particle identification performance at ALICE'. In: *5th Large Hadron Collider Physics Conference (LHCP 2017) Shanghai, China, May 15-20, 2017*. 2017.

[107] Francesca Carnesecchi. 'Performance of the ALICE Time-Of-Flight detector at the LHC'. In: *14th Workshop on Resistive Plate Chambers and Related Detectors (RCP2018) Puerto Vallarta, Jalisco State, Mexico, February 19-23, 2018*. 2018. eprint: 1806.03825.

[108] Stefan Rosegger. 'Simulation and Calibration of the ALICE TPC including innovative Space Charge Calculations'. Ph.D. thesis. Technische Universität Graz, 2009.

[109] Alberto Caliva. 'Low-mass dielectron measurement in Pb-Pb collisions at $\sqrt{s_{\mathrm{NN}}} = 2.76\,\mathrm{TeV}$ with ALICE at the LHC'. PhD thesis. Utrecht University, 2017.

[110] Patrick Reichelt. 'Private Communication'. 2019.

[111] Ivan Vorobyev. 'Low-mass dielectron production proton–proton collisions at $\sqrt{s} = 13\,\mathrm{TeV}$ with ALICE'. Ph.D. thesis. TU München, 2018.

[112] PHENIX Collaboration. 'Detailed measurement of the e^+e^- pair continuum in $p+p$ and Au + Au collisions at $\sqrt{s_{NN}} = 200$ GeV and implications for direct photon production'. In: *Phys. Rev. C* 81 (3 Mar. 2010), p. 034911.

[113] G. J. Gounaris and J. J. Sakurai. 'Finite-Width Corrections to the Vector-Meson-Dominance Prediction for $\rho \to e^+e^-$'. In: *Phys. Rev. Lett.* 21 (4 1968), pp. 244–247.

[114] ALICE Collaboration. 'Production of π, K, p in pp and Pb-Pb collisions at $\sqrt{s_{\mathrm{NN}}} = 5.02\,\mathrm{TeV}$'. In: *ArXiv* (2017).

[115] Dmitri Peressounko Daiki Sekihata Yuri Kharlo. 'Measurement of neutral mesons in pp and Pb–Pb collisions at $\sqrt{s_{\mathrm{NN}}} = 5.02$ TeV with the PHOS detector'. Unpublished Analysis Note. 2018.

[116] R. Hagedorn. 'Statistical thermodynamics of strong interactions at high-energies'. In: *Nuovo Cim. Suppl* 3 (1965), pp. 147–186.

[117] V. Riabov. '$\rho \to \pi\pi$ production in pp collisions at $\sqrt{s} = 2.76$ TeV with TPC-PID'. In: *ALICE Analysis Note ALICE-ANA-2179* (2014).

[118] B. Abelev et al. (ALICE). 'Production of $\omega(782)$ in pp collisions at $\sqrt{s} = 7$ TeV'. In: *ALICE-PUBLIC-2018-004* (2012).

[119] B. Abelev et al. (ALICE). 'Production of K^* (892) and $\phi(1020)$ in pp collisions at $\sqrt{s} = 7$ TeV'. In: *Eur. Phys. J. C 72, 2183* (2012).

[120] Peter Zeiler Skands. 'Tuning Monte Carlo Generators: The Perugia Tunes'. In: *Phys. Rev.* D82 (2010), p. 074018.

[121] The LHCb Collaboration et al. 'Measurement of J/Ψ production in pp collisions at $\sqrt{s} = 7$ TeV'. In: *The European Physical Journal C* 71.5 (May 2011), p. 1645. ISSN: 1434-6052.

[122] M. Cacciari, M. Greco and P. Nason. 'The p_{T} Spectrum in Heavy Flavor Hadroproduction'. In: *JHEP 9805* (1998).

[123] Matteo Cacciari, Stefano Frixione and Paolo Nason. 'The p(T) spectrum in heavy flavor photoproduction'. In: *JHEP* 03 (2001), p. 006. arXiv: `hep-ph/0102134 [hep-ph]`.

[124] R. Averbeck et al. '"Reference heavy flavour cross sections in pp collisions at $\sqrt{s} = 2.76$ TeV, using a pQCD-driven $\sqrt{s}$-scaling of ALICE measurements at $\sqrt{s} = 7$ TeV"'. In: *arXiv:1107.3243 [hep-ph]* (2011).

[125] Matteo Cacciari et al. 'Theoretical predictions for charm and bottom production at the LHC'. In: *JHEP* 10 (2012), p. 137. arXiv: `1205.6344 [hep-ph]`.

[126] Matteo Cacciari, Michelangelo L. Mangano and Paolo Nason. 'Gluon PDF constraints from the ratio of forward heavy-quark production at the LHC at $\sqrt{S} = 7$ and 13 TeV'. In: *Eur. Phys. J.* C75.12 (2015), p. 610. arXiv: `1507.06197 [hep-ph]`.

[127] The ALICE collaboration. 'Λ_c production in pp collisions at $\sqrt{s} = 7$ TeV and in p-Pb collisions at $\sqrt{s_{\mathrm{NN}}} = 5.02$ TeV'. In: *Journal of High Energy Physics* 2018.4 (Apr. 2018), p. 108.

[128] L. Gladilin. 'Fragmentation fractions of c and b quarks into charmed hadrons at LEP'. In: *The European Physical Journal C* 75.1 (Jan. 2015), p. 19.

[129] A. Beraudo et al. 'Extraction of Heavy-Flavor Transport Coefficients in QCD Matter'. In: *Nucl. Phys.* A979 (2018). Ed. by R. Rapp et al., pp. 21–86.

[130] Hung-Liang Lai et al. 'New parton distributions for collider physics'. In: *Phys. Rev. D* 82 (7 2010), p. 074024.

[131] Kari J. Eskola et al. 'EPPS16: nuclear parton distributions with LHC data'. In: *The European Physical Journal C* 77.3 (2017), p. 163. ISSN: 1434-6052.

[132] Jonathan Pumplin et al. 'New Generation of Parton Distributions with Uncertainties from Global QCD Analysis'. In: *Journal of High Energy Physics* 2002.07 (2002), p. 012.

[133] K.J. Eskola, H. Paukkunen and C.A. Salgado. 'EPS09 - A new generation of NLO and LO nuclear parton distribution functions'. In: *Journal of High Energy Physics* 2009.04 (2009), p. 065.

[134] Jaroslav Adam et al. 'D-meson production in p-Pb collisions at $\sqrt{s_{NN}}$ =5.02 TeV and in pp collisions at $\sqrt{s}$ =7 TeV'. In: *Phys. Rev.* C94.5 (2016), p. 054908. arXiv: `1605.07569 [nucl-ex]`.

[135] Roel Aaij et al. 'Study of prompt D^0 meson production in pPb collisions at $\sqrt{s_{NN}} = 5$ TeV'. In: *JHEP* 10 (2017), p. 090. arXiv: 1707.02750 [hep-ex].

[136] ALICE Collaboration. 'Measurement of electrons from heavy-flavour hadron decays at mid-rapidity in pp collisions at $\sqrt{s} = 5.02$ TeV and Pb–Pb collisions at $\sqrt{s_{NN}} = 5.02$ TeV'. In: *To be published* ().

[137] ALICE Collaboration. *Preliminary J/Ψ transverse momentum spectrum*. 2017. URL: https://alice-figure.web.cern.ch/node/11636.

[138] Shreyasi Acharya et al. 'Direct photon production at low transverse momentum in proton-proton collisions at $\sqrt{s} = 2.76$ and 8 TeV'. In: (2018). arXiv: 1803.09857 [nucl-ex].

[139] ALICE Collaboration. 'Direct photon production in Pb–Pb collisions at $\sqrt{s_{NN}} = 2.76$ TeV'. In: *Physics Letters B* 754 (2016), pp. 235–248. ISSN: 0370-2693.

[140] L. E. Gordon and W. Vogelsang. 'Polarized and unpolarized prompt photon production beyond the leading order'. In: *Phys. Rev.* D48 (1993), pp. 3136–3159.

[141] K Aamodt et al. 'Charged-particle multiplicity density at mid-rapidity in central Pb-Pb collisions at $\sqrt{s_{NN}} = 2.76$ TeV'. In: *Phys. Rev. Lett.* 105 (2010), p. 252301.

[142] W. Cassing. 'Dynamical quasiparticles properties and effective interactions in the sQGP'. In: *Nucl. Phys.* A795 (2007), pp. 70–97.

[143] *Upgrade of the ALICE Time Projection Chamber*. Tech. rep. CERN-LHCC-2013-020. ALICE-TDR-016. Oct. 2013.

[144] Philipp Lüttig. 'Charged Particle Production in pp and Pb–Pb Collisions measured with ALICE at the LHC'. PhD thesis. Goethe Universität Frankfurt, 2017.

[145] Rene Brun and Fons Rademakers. *ROOT - An Object Oriented Data Analysis Framework*. 2018. URL: http://root.cern.ch/.